Washington University in St. Louis
Washington University Open Scholarship

Arts & Sciences Electronic Theses and Dissertations

Arts & Sciences

Summer 8-15-2013

Biological Applications of Extraordinary Electroconductance and Photovoltaic Effects in Inverse Extraordinary Optoconductance

Lauren C. Tran
Washington University in St. Louis

Follow this and additional works at: https://openscholarship.wustl.edu/art_sci_etds

Part of the Physics Commons

Recommended Citation

Tran, Lauren C., "Biological Applications of Extraordinary Electroconductance and Photovoltaic Effects in Inverse Extraordinary Optoconductance" (2013). *Arts & Sciences Electronic Theses and Dissertations*. 1041.
https://openscholarship.wustl.edu/art_sci_etds/1041

This Dissertation is brought to you for free and open access by the Arts & Sciences at Washington University Open Scholarship. It has been accepted for inclusion in Arts & Sciences Electronic Theses and Dissertations by an authorized administrator of Washington University Open Scholarship. For more information, please contact digital@wumail.wustl.edu.

WASHINGTON UNIVERSITY IN ST. LOUIS

Department of Physics

Dissertation Examination Committee:

Stuart A. Solin, Chair
Tyrone L. Daulton
Viktor Gruev
Zohar Nussinov
James S. Schilling
Jung-Tsung Shen

Biological Applications of Extraordinary Electroconductance and Photovoltaic Effects in Inverse Extraordinary Optoconductance

by

Lauren Christine Tran

A dissertation presented to the
Graduate School of Arts and Sciences
of Washington University in
partial fulfillment of the
requirements for the degree
of Doctor of Philosophy

August 2013
St. Louis, Missouri

Table of Contents

List of Figures vi
List of Abbreviations xi
ACKNOWLEDGEMENTS xii
ABSTRACT OF THE DISSERTATION xv

Chapter 1 Introduction 1
Section 1.1 Extraordinary Magnetoresistance 1
Section 1.2 Extraordinary Piezoconductance 4
Section 1.3 Extraordinary Optoconductance 5
Section 1.4 Extraordinary Electroconductance 6

Chapter 2 Basic Principles of Solid State Physics 9
Section 2.1 Free Electron Model: Quantum Theory for Metals 9
Section 2.1.1 Free Electrons in Metal – Hamiltonian, Wave Functions 9
Section 2.1.2 Fermi Energy and Density of States 12
Section 2.1.3 Effective Mass 15
Section 2.2 Modulated Electron (Bloch) Model: Quantum Theory for Semiconductors 16
Section 2.2.1 Band Theory 16
Section 2.2.3 Band Gaps for Real Materials 19
Section 2.3 Conductivity in Semiconductors 21
Section 2.3.1 Intrinsic Carrier Concentration and Fermi Energy in a Semiconductor 21
Section 2.3.2 Equivalence of Fermi Energy and Chemical Potential 24
Section 2.3.4 Drift and Diffusion Current in Mesoscopic Samples Exhibiting Diffusive Transport 26
Section 2.4 Behavior of Material Interfaces 27
Section 2.4.1 P-N Junction and Metal-Semiconductor Junction 27
Section 2.4.2 Schottky Barriers and Ohmic Contacts 31

Chapter 3 Semiconductor and EXX Sensors Structure, Fabrication, and Function 34
Section 3.1 Manufacturing and Fabrication of Sensors 34

Section 3.1.1 Materials 35
Section 3.1.2 Sensor Fabrication Overview 35
Section 3.1.2.1 Sensor Patterning 36
Section 3.1.2.2 Photoresist Profile and Metal Lift-Off 40
Section 3.1.2.2 Insulator Deposition 41
Section 3.2 Structure and Function of EXX Sensors 43
Section 3.2.1 Shunt: Ohmic or Schottky Interface 43
Section 3.2.2 Conductivity of EXX 44

Chapter 4 A nano-scale Ti/GaAs metal-semiconductor hybrid sensor for room temperature light detection 47
Abstract 47
Section 4.1 Introduction 47
Section 4.2 Device Description 48
Section 4.3 Optical Experimental Methods 49
Section 4.4 Results and Discussion 53

Chapter 5 Photon Induced Schottky Barrier Effects in Inverse Extraordinary Optoconductance Structures 57
Section 5.1 Introduction 57
Section 5.2 Experiment 58
Section 5.3 Results 59

Chapter 6 Photon Induced Asymmetric Resistance Response in Extraordinary Optoconductance Structures 63
Section 6.1 Introduction 63
Section 6.2 Experimental Methods 63
Section 6.2.1 Sensor geometry 63
Section 6.2.2 Open circuit voltage and sensor resistance 64
Section 6.2.3 Optical Apparatus 65
Section 6.3 Results 66
Section 6.3.1 Gaussian response 66

Section 6.3.2 Asymmetric response and lead configuration 68
Section 6.4 Discussion 70
Section 6.4.1 Lateral photovoltaic effect at Ohmic contacts 70
Section 6.4.2 Lateral photovoltage at Schottky contacts 72
Section 6.4.3 Asymmetry and sensitivity of R_{4pt} and EOC measurements 73

Chapter 7 Extraordinary Electroconductance Sensors as Electrochemical Biosensors 74
Section 7.1 Expected Change in Electric Field Due to DNA Binding at Sensor Surface: A Calculation of Molecular Detection Lower Limit 74
Section 7.1.1 Defining physical system parameters 75
Section 7.1.1.1 Charge on DNA in solution 75
Section 7.1.1.2 Charge on Biotin/Streptavidin/Captavidin in solution 76
Section 7.1.1.3 Thickness of functionalization and binding site layer 79
Section 7.1.1.4 Dielectric Constant for Water 81
Section 7.1.1.5 Sensor Spatial Dimensions 81
Section 7.1.2 Simple Dielectric Fluid Model for 20, 40 base pair DNA 81
Section 7.1.3 Simple Dielectric Fluid Model for Biotin and Captavidin 85
Section 7.1.4 Effects of Fluid Ionic Strength and Debye Screening 88
Section 7.1.5 Ionic and Dielectric Fluid Model for 20 and 40 base pair DNA 91
Section 7.1.6 Ionic and Dielectric Fluid Model for Biotin and Streptavidin 95
Section 7.2 Fabrication Process and Experimental Methods 102
Section 7.2.1 Sensor Design Parameters 102
Section 7.2.2 Functionalization of Aluminum Oxide 103
Section 7.2.3 Dilution Curve and Protein Binding Experiment 105
Section 7.3 Experimental Results 107
Section 7.3.1 Characterization of Sensors 107
Section 7.3.2 Captavidin Serial Dilution Curve and Protein Binding Experiment 110
Section 7.3.2.1 Results – Bare Device Binding Signal 110
Section 7.3.2.2 Results – Shunted Device Binding Signal 113
Section 7.3.2.3 Calculations of Sensitivity 117
Section 7.3.2.4 Two-Point versus Four-Point: Discussion 119

Section 7.3.2.5 Bare versus Shunted: Discussion 122
Section 7.3.3 Streptavidin Serial Dilution Curve 123
Section 7.3.3.1 Temperature Fluctuations and Evaporative Cooling 123

Concluding statements 126
Appendix 127
References 161

List of Figures

Figure 1.1 Inset: GaAs substrate with InSb mesa and Au concentric shunt. Indication of the four point resistance measurement wire configuration and orientation of the magnetic field. Plot: Four point resistance as a function of magnetic field strength for filling factors:16α = 0, □; 6, ■; 8, ∇; 9, ▼; 10, Δ; 11, ▲; 12, ○; 13, ●; 14, ◊; 15, ♦. From Solin et al. (2000) Ref [1] 2
Figure 1.2 Geometric dependence of EMR for magnetic field strengths, H, ranged between 0.05-5.0 T. From Solin et al. (2000) Ref [1] 3
Figure 1.3 Inset is a schematic of the four point resistance lead configuration and device dimensions. The EPC is % change in conductivity with applied strain transverse to the interface. The symbols 16α= 0, ○; 6, □; 8, ◊; 9, ×; 12, Δ; 13, ∇; 15, +. The solid line is the semiconductor only. 4
Figure 1.4 From Weiland et al. (2006), y = 0.2 mm, ○; y = 0.7 mm, □; (a) Scanned response from bare In (b) Scanned response from In/GaAs EOC sensor (c) Schematic of EOC sensor 5
Figure 1.5 From Newaz et al. (2009) (a) CAD design of 100 μm mesa EEC detector (b) SEM image of a bare device, α = 0, without shunt (c) a cutaway of the EEC layer structure showing the EEC sensor AuGe/Ti/GaAs Schottky interface at the center, surrounded by the insulating GaAs and dielectric Si3N4, and finally the top and bottom AuGe capacitor plate layers..... 7
Figure 1.6 From Newaz et al. (2009) (a) Four point resistance dependence on externally applied electric field via the applied voltage across the capacitor plates with no internal biasing (b) The sensitivity to external electric field for several shunt bias voltages (internally applied field biases) (c) EEC percent change in resistance for alpha values of 1/16, 5/16, 10/16, and 14/16 and no internal bias. 8

Figure 2.1 (a) The Fermi function at T = 0 (b) Fermi function - density of states product at T = 0 (c) The Fermi function at T ≠ 0 (d) Fermi function - density of states product at T ≠ 0 14
Figure 2.2 The origin of an energy band gap: the transcendental equation for $\boldsymbol{\beta a}$ between the allowed values of ±1. The pink shaded regions are the allowed values projected onto the $\boldsymbol{\beta a}$ axis. Created using Kronig and Penny[9]. Recall that $\boldsymbol{\beta = 2me\hbar 2E}$ and *a* is the lattice spacing. 19
Figure 2.3 Band structure for common semiconductors taken from Cohen and Bergstresser[10] or Chelikowsky and Cohen 20
Figure 2.4 Graphs of the charge density, ρ, the electrostatic field, E, and the electrostatic potential, V, on either side of a p-n junction. Reproduced from Burns[16] 30
Figure 2.5 Cartoon depictions of the band diagrams for Ohmic and Schottky contacts..... 32

Figure 3.1 Top view of three standard structures: Bare sensor without shunt, standard EXX sensor with shunt, nonstandard EXX sensor with shunt contacted. 34
Figure 3.2 Cross section of EXX sensor to demonstrate layered structure. The lateral dimensions are not to scale. 35

Figure 3.3 The photolithographic fabrications steps to form macroscopic integrated circuit devices such as EEC and EOC sensors. The unexposed photoresist is dark red (1-4), the vacuum chuck is brown (1), the glass of the photo-mask is light blue and the photo-mask chrome pattern is gold (3), the UV-exposed resist is light pink (4-5), the UV-exposed and heated resist is blue (5-7), and the metal evaporated layer is yellow (7-8) 37
Figure 3.4 Glass photo-mask in plastic protective case. The left hand of the mask is "bright field" chrome patterning (clear background, chrome pattern) and the right hand of the mask is "dark field" chrome patterning (chrome background, clear pattern) 39
Figure 3.5 Profiles of positive and negative photoresist patterning. Black is the metal chrome pattern, red is unexposed photoresist, pink is exposed resist and yellow is deposited gold film. 41
Figure 3.6 (a) Beginning of exposure with e- beam spreading (b) Exposure complete (c) Developed positive resist. Red is unexposed photoresist, pink is exposed resist, and grey is the substrate. 41
Figure 3.7 From Newaz et al. (2009) (a) Schematic of dual layer model for conductivity. Yellow are the contacts, grey is GaAs, pink is GaAs that has been depleted of carriers. (b) Labels of radii used to define fill factor, α. 46

Figure 4.1 A cross-sectional view of the structure of the SDPP device. 48
Figure 4.2 SEM images (top panel) and resistance image plots (bottom panel) of the 5 μm device (a) and 250 nm device (b). Panel (a) shows the contact labeling scheme. All image plots were acquired with an AC bias of peak current I_{34} = 100 nA. 50
Figure 4.3 The intensity dependence of the 2-point I-V characteristic of the Schottky diode component of a 5 μm SDPP device (I_0 = 1W/cm^2). 51
Figure 4.4 The dynamic responses of SDPP devices of different sizes to illumination by 632.8 nm radiation. Device size: ◆ - 5 μm, ■ - 1 μm, ● - 500 nm, ▼ - 250 nm. 54

Figure 5.1 100 μm EOC device 58
Figure 5.2 5 μm EOC sensor's Schottky barrier reduced by laser intensity a) positive photovoltage b) negative photovoltage c) similar reverse bias resistance for both positive and negative photovoltage offset 60
Figure 5.3 Laser rastering across 100 μm EOC sensors V_{oc} (x,y) map of the Schottky interface at I_0, without epoxy (a) and a schematic of sensor's electrical connection (b). (c) V_{oc} (x,y) with epoxy and (d) R_{4pt}(x,y) with epoxy. (e) Intensity dependence of V_{oc} at 4 laser locations. 61
Figure 6.1 Schematic of the sensors and the active (+) and passive (-) contact configuration; red is Ti, yellow is n-GaAs, orange is Au/Ge/Ni, and black is insulating GaAs substrate 64
Figure 6.2 Schematic of epoxy covering the wires and identification of the epoxied sensors as "A," "B," "C," and "D" 66
Figure 6.4 Red line indicates location of a shunt tab,+ indicates active leads, and – indicates ground (A) Laser rastering map: four terminal resistance response (B) Laser rastering map: DC voltage offset of resistance measurement, V_{off} 69

Figure 6.5 (A) Plot of the lateral photovoltage induced by scanning illumination inhomogeneity between two Ohmic contacts of the p-n photo detector (B) Lateral photo detector, Schematic of the Germanium substrate, Indium Dot, two Ohmic contacts, and illumination point. From Reference [44] 71
Figure 6.6 Plot of V_{off} data along line X = 1.7 mm for EOC sensor B in Figure 6.3 (d)..... 71
Figure 7.1 The above structure is a streptavidin monomer rather than the tetramer used in the experiments discussed later. The biotin section of probe (spheres) is bound to one of the four monomers in the target, streptavidin, (blue ribbon structure). Image from Integrated DNA Technologies© website. Image is a recreation on modern molecular modeling software of the published work by Weber PC, Ohlendorf DH, et al (1989)..... 77
Figure 7.2 Functional dependence of charge on avidin and streptavidin on pH of surrounding solution[54] 78
Figure 7.3 Linear regression of charge on (A) avidin and (B) streptavidin as a function of pH of salt solution. 78
Figure 7.4 From reference [56], Dorvel et al. 2010. The thickness of the self-assembling monolayer and the amount of adsorbed mass is plotted versus vapor exposure time for APDMS. The red line is a fit to the diffusion limited Langmuir equation. 79
Figure 7.5 a) An example of biotin probe with variable spacer arm available from Thermo Scientific. Figure from chemical information documentation. b) The chemical structure of biotin as defined and pictured by the CAS registry. 80
Figure 7.6 The schematic layout for the simple DNA model. The green section of the z-axis indicates the thickness of the functionalization layer, f_o. The tick marks on the z-axis indicate positions of discrete 0.5 e^- charges at each base pair location with spacing, a, for a total of n base pairs. The blue bar indicates the vertical extent of the continuous-charge, smeared distribution. 82
Figure 7.7 Sampled values of the discrete sphere model (green dots) and the smeared, continuous charge distribution model (blue line). (A) Electric field magnitude in Z direction and (B) X direction for n = 20 DNA base pairs attached to a functionalization layer 1 nm thick. In A and B, the lower bound of the E field axis is the detection limit of 3.05 V/cm (C) % difference between E field magnitude due to 40 base pairs at 1nm and 20 base pairs at 2nm 84
Figure 7.8 Electric field magnitude in Z direction (transverse to interface) along line in sensor plane (x, 0, 0). Avidin modeled as a single charged ion at position (0, 0, Binding Height) in dielectric water. 87
Figure 7.9 Electric field magnitude in X direction (parallel to interface plane) along line in sensor plane (x, 0, 0). Avidin modeled as a single charged ion at position (0, 0, Binding Height) in dielectric water. 87
Figure 7.10 Functional dependence of electric field in Z direction at the origin from a proton at a fixed location (0, 0, 5nm) on the concentration of PBS. This demonstrates signal quenching due to ionic shielding. The highlighted values are: 0 mM PBS (no salt, equivalent to the simple dielectric), 10 mM PBS (the concentration used in the following experiments), and 44 mM PBS (at detection limit)..... 92

Figure 7.11 Functional dependence of electric field (A) in the Z and (B) in the X directions from a 20 base pair DNA strand under identical parameters to the discrete model of section 7.1.2 but with the introduction of 10mM concentration of PBS. This figure also demonstrates signal quenching due to functionalization layer thickness (increasing binding height)..... 93
Figure 7.12 The average field in the Z direction for 20 base pair DNA at various binding heights as a function of *d* (which dictates the integrated area). The lower bound of the field axis is 3.05 V/cm. Note that 11 nm is below the limit and is off the range of this plot..... 95
Figure 7.13 Functional dependence of electric field (A) in the Z direction (B) in the X direction from avidin with parameters identical to the dielectric model of section 7.1.3 but with the introduction of 10mM concentration of PBS and a_{Bohr}. This figure also demonstrates signal quenching due to functionalization layer thickness (increasing binding height)..... 96
Figure 7.14 The averaged electric field in the Z direction for 10 mM PBS and aBohr. The spacing of proteins would be every 2*d*. The lower bound of the field axis is 3.05 V/cm. Note that 9 and 11 nm are below the limit and are off the range of this plot. 98
Figure 7.15 Electric field magnitude in the z direction (A) and the x direction (B) from avidin in 10 mM PBS and aavidin. Notice that binding distance of 13 nm is below the 3 V/cm threshold and is off the range of the plots..... 99
Figure 7.16 Averaged electric field in the z direction from avidin in 10 mM PBS and a_{avidin}. To estimate necessary binding density, proteins would be bound every 2*d*. Binding heights 13 nm and 15 nm are below the detectable range. 100
Figure 7.17 Functional dependence of electric field from avidin with parameters identical to the dielectric model of section 7.1.3 but with the introduction of 1 mM concentration of PBS, or 1/10 that used in experiment and a_{avidin}. This figure also demonstrates signal quenching due to functionalization layer thickness (increasing binding height). 101
Figure 7.18 The above sensor photographs were taken by camera through a microscope objective under 100x magnification..... 103
Figure 7.19 (A) Structure of APMDES (B) PEG_4, Ref[] (C) PEG_4-biotin, Ref[57] 104
Figure 7.20 Schematic of reaction attaching PEG_4 and PEG_4-biotin to amine group of APMDES. Adapted from the structures provided by ThermoScientific and Gelest molecular data sheets. 104
Figure 7.21 Schematic of attached APMDES, PEG_4 and PEG_4-biotin on aluminum oxide. This is a proposed attachment outcome. Documentation of the attachment mechanism for APMDES to oxide surfaces has not been proposed in published literature, to the author's knowledge. The chemical changes that occur at the oxide surface for a dimethyl silane (DMS) are a substitution of carbon for available oxygen at the surface and from neighboring silanes. However, it is unconfirmed whether the two carbons in the ethyl groups of diethyl silane, APM(DES), such as we used would detach differently than the single carbon methyl groups of APMDMS. The figure demonstrates an APMDMS-like attachment. 105
Figure 7.22 Detector photographs with measurement configuration overlaid. White (I,V) = Four Point Resistance, Red (I,V) = Two Point Resistance, A, Blue (I,V) = Two Point Resistance, B 106

Figure 7.23 Shunt connected device with Ohmic, ground pins identified for the I-V characteristic curves and the fifth lead the positive reference 107
Figure 7.24 Current-Voltage behavior across Schottky interface of five-lead sensors after fabrication. 108
Figure 7.25 Current-Voltage behavior across Schottky interface of five-lead sensors prior to functionalization and captavidin competitive assay. 109
Figure 7.26 Four point resistance of three bare devices (pink, yellow, blue data with error bars). Time 0-1.5 hours shows the competitive binding assay of captavidin. Time 5.8-7.4 hours shows the serial dilution of captavidin and the distinct response to bound proteins. The color bars are marked with the biochemical droplet label applied at a particular point in time. 110
Figure 7.27 Two point resistance configuration (A) and (B) of three bare devices (pink, yellow, blue data with error bars) for the competitive binding assay and the serial dilution of captavidin. The color bars are marked with the biochemical droplet name. 111
Figure 7.28 Four point resistance configuration for four lead (A) and five lead (B) sensors for the competitive binding assay and the serial dilution of captavidin. The color bars are marked with the biochemical droplet name. 114
Figure 7.29 Four lead sensors: Two point resistance configuration (A) and (B) for the competitive binding assay and the serial dilution of captavidin. The color bars are marked with the biochemical droplet name. 115
Figure 7.30 Five lead sensors: Two point resistance configuration (A) and (B) for the competitive binding assay and the serial dilution of captavidin. The color bars are marked with the biochemical droplet name. 116
Figure 7.31 Overview of Sensitivity. The blue data is the first sequence, competitive assay, with minimal binding, while the red data of each graph is the second assay, with binding to the surface. 118
Figure 7.32 Atomic force microscopy image of APMDES layers deposited on silicon dioxide by (A) solution phase in 1% toluene (B) vapor phase deposition at ~125 Torr. From Anderson, et al. (2008)[67] 120
Figure 7.33 Example of four point resistance response from a bare sensor undergoing a streptavidin dilution curve. Two droplets of each chemical were applied correlating to the two downward spikes in each color bar. The dashed lines connecting the data points of a droplet are meant as a guide for the eye only 124

List of Abbreviations

EXX	Extraordinary “XX”
EMR	Extraordinary Magnetoresistance
EPC	Extraordinary Piezoconductance
EOC	Extraordinary Optoconductance
EEC	Extraordinary Electroconductance
MSH	metal semiconductor heterostructure
I-V	Current-Voltage
ALD	atomic layer deposition
PECVD	plasma enhanced chemical vapor deposition
SDPP	scale-dependent positive photoresistance
DMF	dimethylformamide
PBS	phosphate buffered saline
APMDES	3-aminopropylmethyldiethoxysilane
APMDMS	3-aminopropylmethyldimethoxysilane
PEG_4 Ester)	Methyl-PEG_4-NHS Ester (Methyl-polyethylene glycol$_4$-*N*-Hydroxysuccinimide
NHS	*N*-Hydroxysuccinimide
PEG_4-biotin	EZ Link NHS-PEG_4-Biotin
DMSO	dimethyl sulfoxide

ACKNOWLEDGEMENTS

I am grateful to everyone who has supported this work and helped so greatly in its accomplishment. First, I thank my advisor, Stuart Solin, for his guidance and insight into physics, research, and via lively lunch discussions, my informal education in finance, the legal system, and politics. In him I have witnessed the standard of detailed, methodical physics, of ethical, unbiased scientific method and of high quality research. His Socratic method of systematic questions got to the heart of any problem and proved an unequaled guidance in my thesis work.

I would like to thank Fletcher Werner for his contributions to the biological measurement apparatus and his indispensable help in discussion and debate. I would like to thank Dr. Ken Bradley and Dr. Renee Carder of PixelEXX for their funding support, for their contributions to the biological sensing experiments and their illuminating discussions. I thank Woo-Jin Chang for training me in cleanroom fabrication processes and his sustained advice on device manufacturing. I would like to thank Dr. A. K. M. Newaz, Dr. Kirk Wallace, and Dr. Samuel Wickline for their contributions to Inverse Extraordinary Electroconductance, and to Dr. Adam Gilbertson and Dr. Lesley Cohen for their measurements of mean free path length in room temperature GaAs.

Finally, I would like to thank my grandfather, Dr. Ronald Edge and my father, Dr. Christopher Edge, for fostering a young enthusiasm for physics. With the achievement of this doctorate, I am proud to be the third generation of the "family business." For their love and support in every moment, I thank both my parents Chris and Karen Edge, my brothers, David, Peter, and Michael Edge, and my newest family Tu, Thanh, Phong, David, and Christina Tran. Lastly, in the place of highest honor and with great love, I dedicate this thesis to my husband, Vy

Tran. You challenge me to better myself, to reject excuses, and to commit to excellence. I am inspired by you and I thank you for standing with me these past four years.

Disclosure of Previously Published Material

Some chapters have been published, specifically:

Chapter 4: "A nano-scale Ti/GaAs metal-semiconductor hybrid sensor for room temperature light detection" A. K. M. Newaz,[1] W. - J. Chang,[2] K. D. Wallace,[3] L. C. Edge,[1] S. A. Wickline,[3] R. Bashir,[2,4] A. M. Gilbertson,[5] L. F. Cohen,[5] and S. A. Solin,[1,5] *Applied physics letters* 97.8 (2010): 082105-082105.

[1] *Center for Material Innovations and Department of Physics, Washington University in St. Louis, USA*

[2] *Micro and Nanotechnology Laboratory, University of Illinois at Urbana-Champaign, USA*

[3] *Department of Medicine, Washington University in St. Louis, USA*

[4] *Department of Electrical and Computer Engineering & Bioengineering, University of Illinois at Urbana-Champaign, USA*

[5]*Blackett Laboratory, Imperial College, UK*

(Note for incorporation into doctoral thesis: This was published under L. C. Edge's maiden name, later changed to L. C. Tran after her marriage in 2010)

Chapter 5: "Photon Induced Schottky Barrier Effects in Inverse Extraordinary Optoconductance Structures," L. Tran,[1] S. A. Solin,[1] A. Gilbertson,[2] L. F. Cohen[2], Proceedings of the 31st International Conference on the Physics of Semiconductors, Zurich, Switzerland, 2012.

[1]*Department of Physics, Washington University in St. Louis, St. Louis, Missouri 63130, USA*

[2]*Blackett Laboratory, Imperial College London, SW7 2BZ, UK*

ABSTRACT OF THE DISSERTATION

Biological Applications of Extraordinary Electroconductance
and Photovoltaic Effects in Inverse Extraordinary Optoconductance

by

Lauren Christine Tran

Doctor of Philosophy in Physics

Washington University in St. Louis, 2013

Professor Stuart Solin, Chair

The Extraordinary Electroconductance (EEC) sensor has been previously demonstrated to have an electric field sensitivity of 3.05V/cm in a mesoscopic-scale structure fabricated at the center of a parallel plate capacitor. In this thesis, we demonstrate the first successful application of EEC sensors as electrochemical detectors of protein binding and biological molecule concentration. Using the avidin derivative, captavidin, in complex with the vitamin biotin, the change in four-point measured resistance with fluid protein concentration of bare EEC sensors was shown to increase by a factor of four in the presence of biomolecular binding as compared to baseline. Calculations for approximate field strengths introduced by a bound captavidin molecule are also presented.

The development of Inverse-Extraordinary Optoconductance (I-EOC), an effect which occurs in nanoscale sensors, is also discussed. In the I-EOC effect, electron transport transitions from ballistic to diffusive with increasing light intensity. In these novel, room temperature optical detectors, the resistance is low at low light intensity and resistance increases by 9462% in

a 250nm device mesa upon full illumination with a 5 mW HeNe laser. This is the inverse of bulk and mesoscopic device behavior, in which resistance decreases with increasing photon density.

Chapter 1 Introduction

Developed by the Solin group, "extraordinary effects"-based sensors are a family of room temperature, metal-semiconductor heterostructures (MSH) that utilize device geometry to enhance intrinsic, material-based sensitivity to external perturbations. "EXX" is the abbreviation for this class of MSH where "E" stands for Extraordinary and the "XX" stands for the perturbative effect a particular structure is designed to detect. Thus, XX can be "MR" for Magnetoresistance, "PC" for Piezoconductance, "OC" for Optoconductance, or "EC" for Electroconductance. Summaries of published research for each type are presented in the following sections.

In this thesis, the following definitions are used for the device components. The semiconducting section of a detector is termed the *mesa*. The metallic section is termed the *shunt* since the metal makes intimate contact with the mesa and can be an alternate conductance path to "shunt" carriers away from the mesa. The wires patterned to contact the mesa can also be referred to as *leads*.

Section 1.1 Extraordinary Magnetoresistance

Solin and collaborators[1] first discovered the extraordinary, geometry-based effects in application to magnetoresistance in 2000 as a development of their work in layered, crystalline, quantum-well structures. The most immediately striking aspect of the Extraordinary Magnetoresistance (EMR) detector is that it is based on non-magnetic materials, specifically high mobility, narrow band gap semiconductors. Such materials have included an InSb mesa with Au shunt[1] and an InSb/$Al_{0.09}In_{0.1}Sb$ quantum well mesa with Au shunt[2].

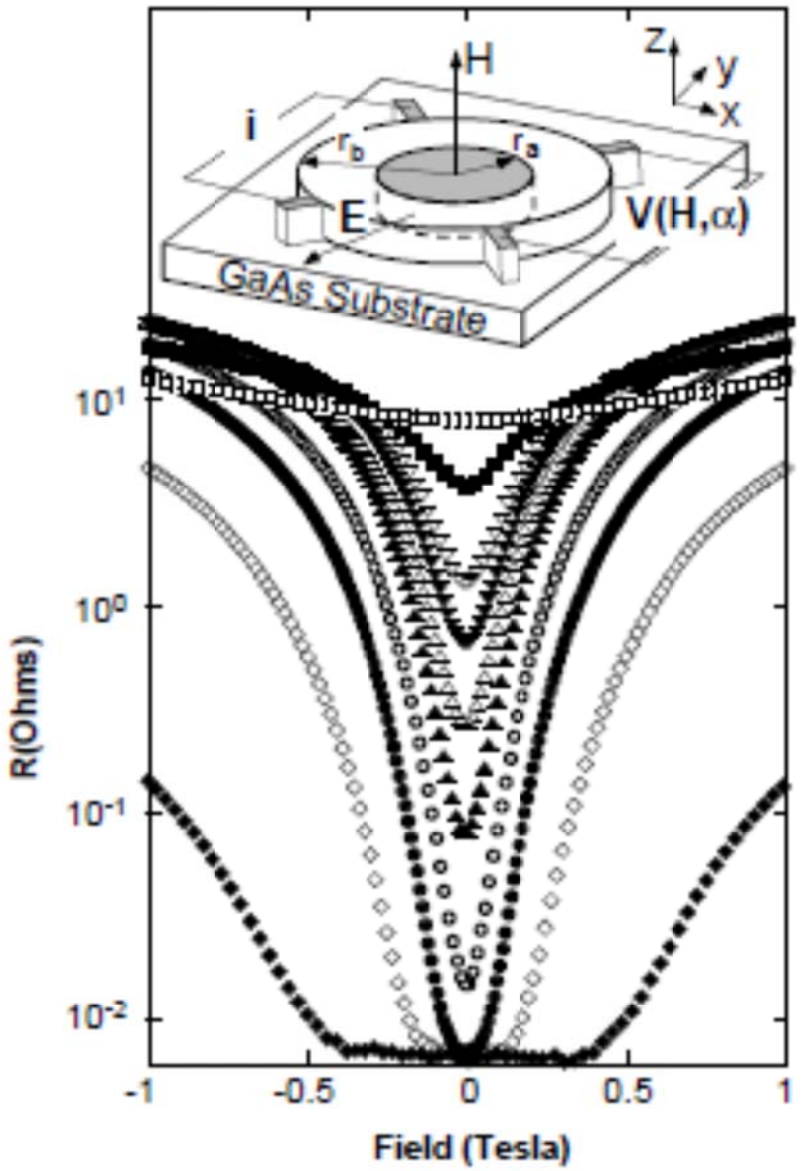

Figure 1.1 Inset: GaAs substrate with InSb mesa and Au concentric shunt. Indication of the four point resistance measurement wire configuration and orientation of the magnetic field. Plot: Four point resistance as a function of magnetic field strength for filling factors:16α = 0, □; 6, ■; 8, ∇; 9, ▼; 10, Δ; 11, ▲; 12, ○; 13, ●; 14, ◊; 15, ♦. From Solin et al. (2000) Ref [1]

The structure of EMR devices from Solin et al. (2000) can be seen from the inset of Figure 1.1 to be a cylindrical GaAs mesa with a Au shunt imbedded in the center. External magnetic fields deflect current between the shunt and mesa, following the boundary conditions for current flow in the MSH. At low field, the shunt acts like a short, but for high fields, the

interface becomes a very high resistance barrier and the shunt acts like an open circuit. Thus in Figure 1.1, the resistance of the EMR sensor is low at low fields and increases with higher fields. A geometric parameter, α, was defined as the ratio of the shunt radius to the mesa radius. It may also be referred to as the *filling factor*. The sheet resistance is calculated from a van der Pauw, four-point resistance measurement. Since the leads are symmetrically placed around the sample perimeter, only one measurement is needed rather than the typical average of two measurements with permuted contacts.

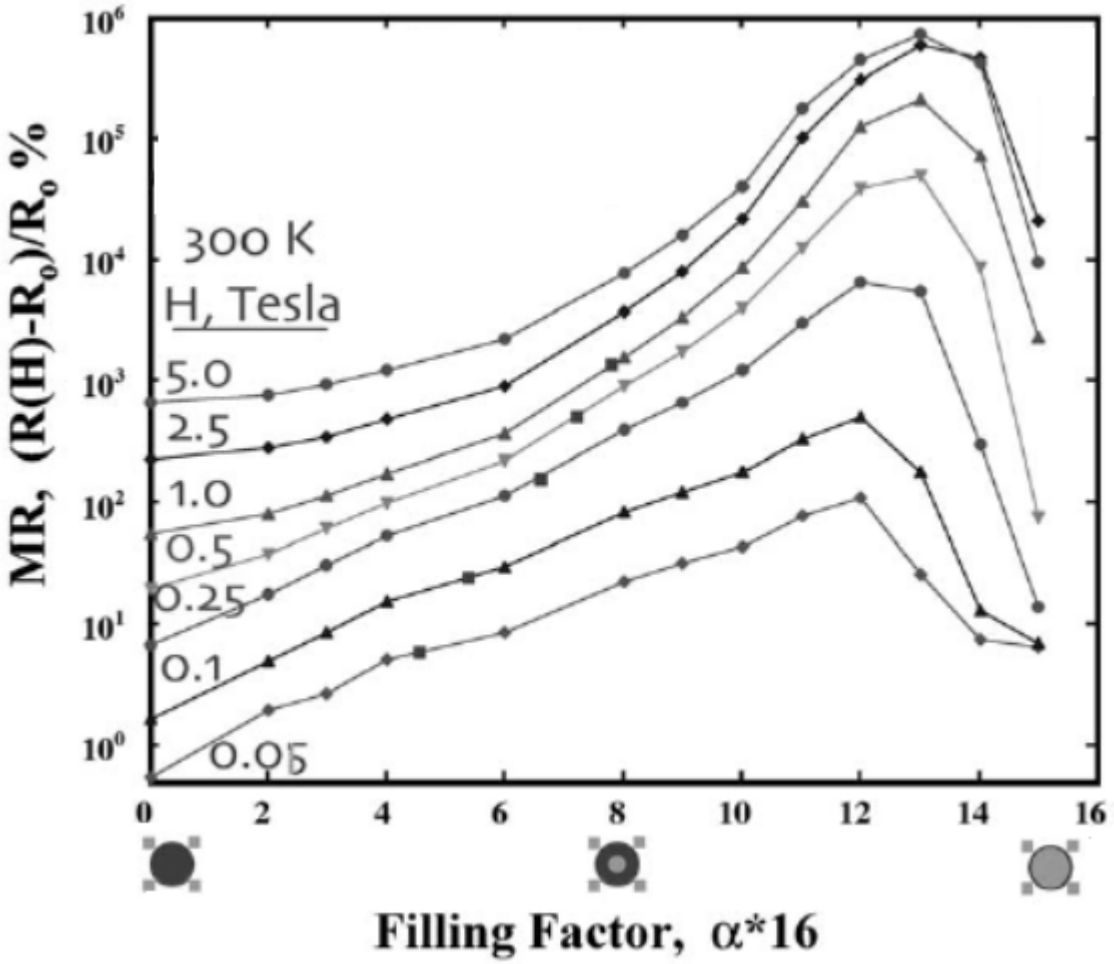

Figure 1.2 Geometric dependence of EMR for magnetic field strengths, H, ranged between 0.05-5.0 T. From Solin et al. (2000) Ref [1]

MR and EMR are usually measured as a percent change in resistance, or $(R(H) - R_0)/R_0$ %. Varying the filling factor demonstrates the geometry dependence of EMR, which at an α of 13/16 and 5T field, has a maximum value of 10^6 % as shown in Figure 1.2.

Section 1.2 Extraordinary Piezoconductance

EPC was first demonstrated in 2003 and shows applications as an ultrasound transducer or other strain-based detection applications[3]. The addition of the metal shunt increased the response of a homogeneous, bare mesa by five times the sensitivity for a maximum change of 10% (Figure 1.3).

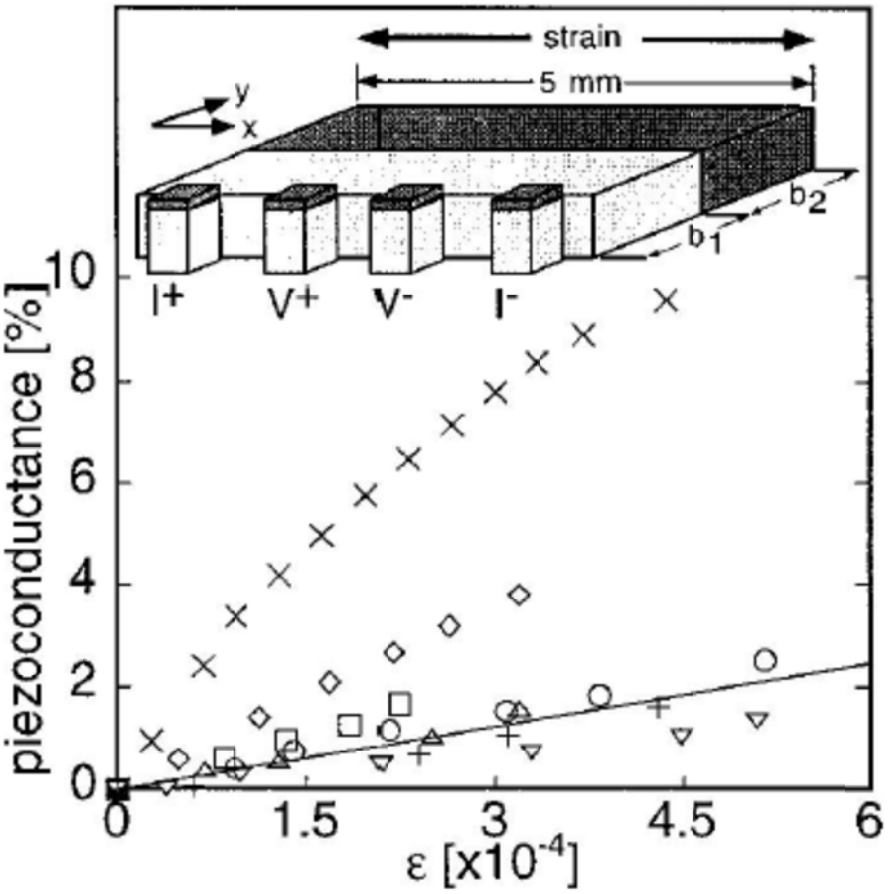

Figure 1.3 Inset is a schematic of the four point resistance lead configuration and device dimensions. The EPC is % change in conductivity with applied strain transverse to the interface. The symbols 16α= 0, ○; 6, □; 8, ◊; 9, ×; 12, Δ; 13, ∇; 15, +. The solid line is the semiconductor only.

Section 1.3 Extraordinary Optoconductance

In 2005, the first In/GaAs EOC detectors [4] were documented. The behavior and augmentation in sensitivity was well explained with a model of differential mobility between photo generated holes and electrons. Electrons have a much higher mobility and will tend to diffuse away from the laser excitation spot (Figure 1.4(c)), leaving behind the less mobile holes as a positive point-perturbation. The temperature behavior of the Ohmic EOC structure was also studied and was found to peak at 500% at 30K.

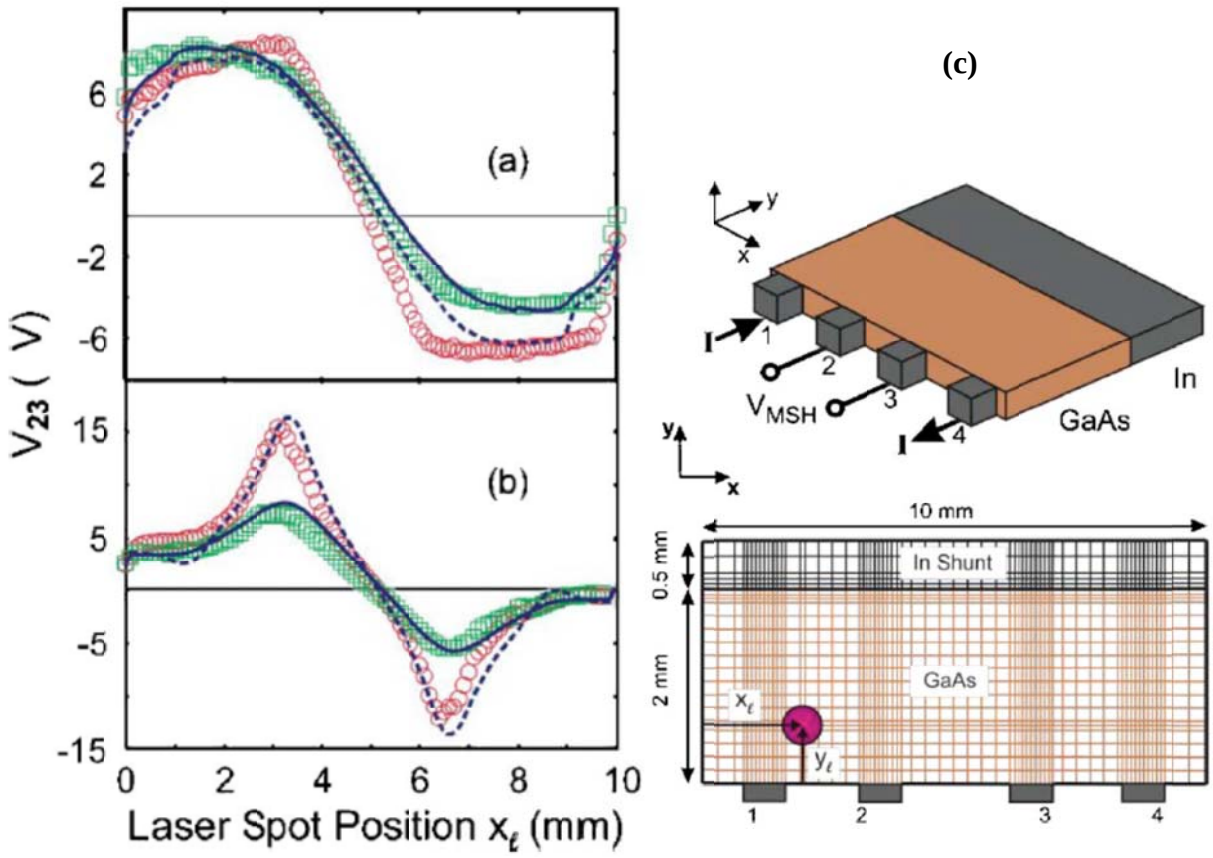

Figure 1.4 From Weiland et al. (2006), y = 0.2 mm, ○; y = 0.7 mm, □; (a) Scanned response from bare In (b) Scanned response from In/GaAs EOC sensor (c) Schematic of EOC sensor

As you can see if Figure 1.4(a) and(b), the structures demonstrates a positive voltage deflection when the hole-concentration passes the positive voltage terminal (lead 2 in if Figure 1.4C) following the location of the laser spot and a negative deflection when passing terminal 3.

Section 1.4 Extraordinary Electroconductance

In 2008, the Solin group first published results from EEC sensors.[5,6] This was the first generation of EXX detectors to incorporate a Schottky MSH junction rather than a non-rectifying junction. The details of such junctions, the built-in voltage, and depletion region are dealt with in Section 2.4.1.

As seen in Figure 1.5 (a) and (c) the EEC detectors utilize a stacked structure to maximize the interfacial area. A range of α ratios were studied to determine the geometry with the highest enhanced sensitivity, varying from $\alpha = 0$, implying no shunt as in Figure 1.5 (b), to $\alpha = 15/16$, in steps of 1/16.

Two methods of probing the heterostructure sensitivity to electric field were described: internal and external biasing. “Internal biasing” was implemented by directly applying a voltage bias to the shunt metal with respect to the grounded four point measurement leads, for example across lead 5 and grounding lead 1 in Figure 1.5 (a). Since the shunt metal was connected to a voltage source, this method internally manipulated the charge density and electric field at the interface, acting as a charge source or sink. This was in contrast to “external biasing” in which the shunt lead 5 is disconnected. The shunt was an electrically floating metal layer. The external field was then applied by a voltage bias across the capacitor plate layers identified in the cutaway of Figure 1.5 (c).

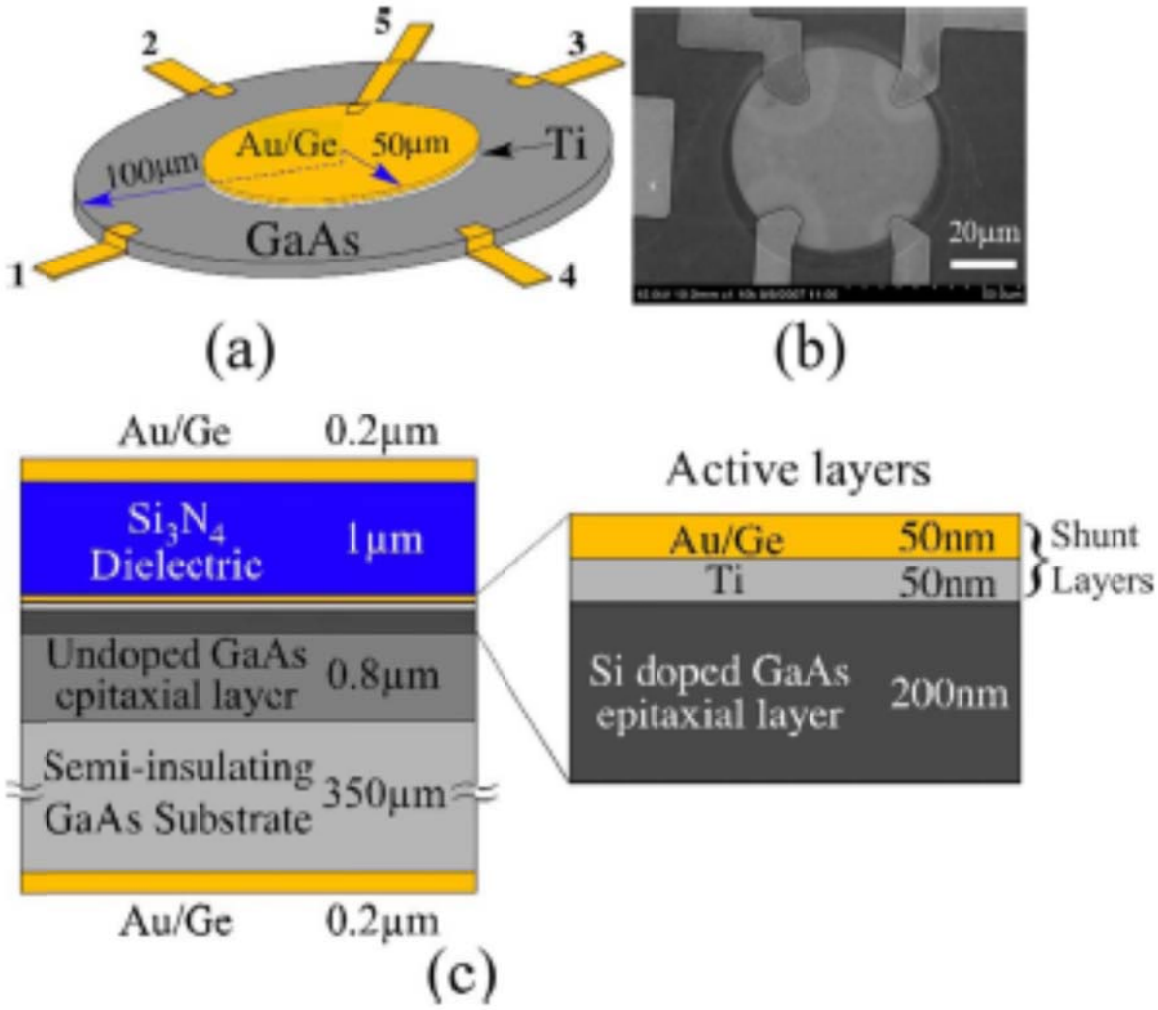

Figure 1.5 From Newaz et al. (2009) (a) CAD design of 100 μm mesa EEC detector (b) SEM image of a bare device, α = 0, without shunt (c) a cutaway of the EEC layer structure showing the EEC sensor AuGe/Ti/GaAs Schottky interface at the center, surrounded by the insulating GaAs and dielectric Si3N4, and finally the top and bottom AuGe capacitor plate layers

As can be seen in Figure 1.6 (a) and (b) the sensitivity of EEC response to externally applied fields larger than -1.5 kV/cm is not affected by the internally applied field. The EEC sensitivity to externally applied fields smaller than -1.5 kV/cm is increased by negative internally applied fields. This increase in sensitivity for negative fields correlates to an increase in the depletion region and a significant variation in available charge carriers in the mesa. Figure 1.6 (c) demonstrated the geometric dependence of the EEC effect and that the smallest shunt α = 1/16

was the most significant in percent change of resistivity. Using the maximum sensitivity of 4% in Figure 1.6 (b) and the resolution of the voltage and current equipment, the Solin group established a minimum field resolution of 3.05 V/cm. This field resolution limit will be referenced again in Chapter 7 to determine the viability of EEC sensors for biochemical concentration detection.

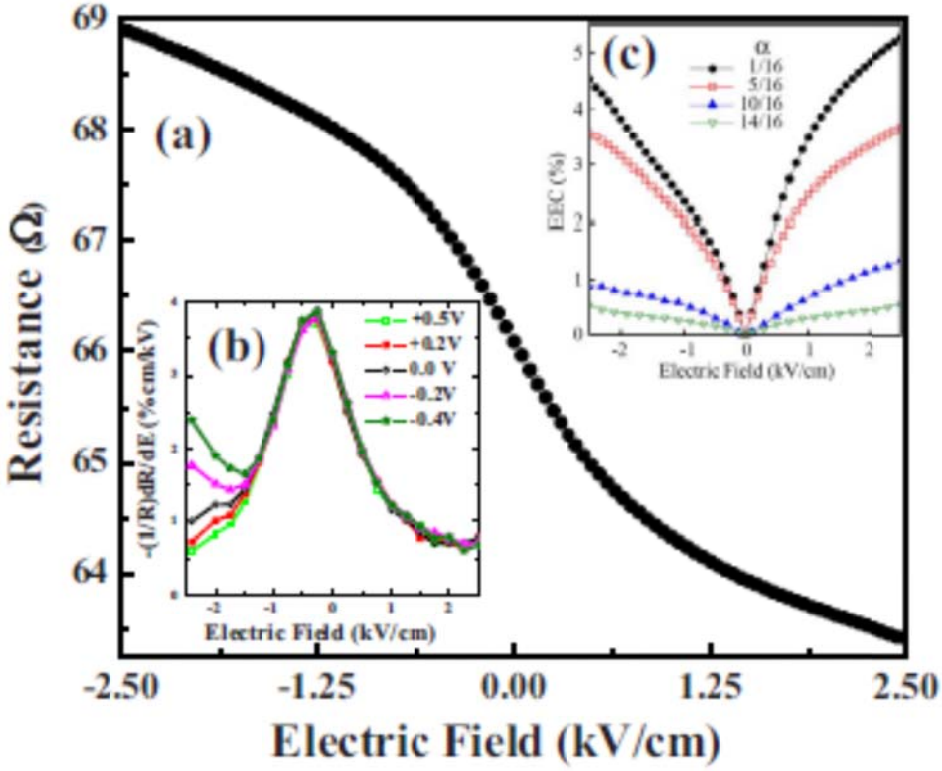

Figure 1.6 From Newaz et al. (2009) (a) Four point resistance dependence on externally applied electric field via the applied voltage across the capacitor plates with no internal biasing (b) The sensitivity to external electric field for several shunt bias voltages (internally applied field biases) (c) EEC percent change in resistance for alpha values of 1/16, 5/16, 10/16, and 14/16 and no internal bias.

Chapter 2 Basic Principles of Solid State Physics

Section 2.1 Free Electron Model: Quantum Theory for Metals

Electrical *conductivity* is a measure of how easily charge carriers can move through a material. Materials can be categorized by decreasing conductivity into three classes: metals, semiconductors, and insulators. The conductivity of metals and semiconductors depends upon temperature in an inverse manner. The conductivity of metals is proportional to the negative change in temperature since the cooler temperature reduces scattering. Semiconductors on the other hand, typically increase conductivity with increasing temperature since higher temperatures thermally excite more free carriers across the band gap. In this chapter, I will discuss the physical concepts that influence the conductivity of a solid material.

Section 2.1.1 Free Electrons in Metal – Hamiltonian, Wave Functions

Let us first examine conductivity in a metal where the dominant charge carrier is the "free" electron, one that is not tightly bound to an atomic nucleus. To develop the simplest, quantum mechanics-based model for free electrons in a metal lattice, we assume that the electrons are non-interacting and behave independently of one another. This system of non-interacting electrons is located in a lattice of positive atomic nuclei. The electron will be electrostatically attracted to the positive nuclei; that is, there is a high energy barrier to the electron leaving the boundary of the crystal. The simplest model of this energy barrier is an infinite-well potential, with some finite potential inside the volume of the metal and an infinite potential outside the volume. To first order, the electrostatic potential inside the well can be

assumed constant – some averaged value of the background positive atomic nuclei and the negative free electrons. This value can be set to zero without loss of generality.

The Schrödinger equation is

$$\vec{H}\psi(\vec{x}) = \frac{-\hbar^2}{2m_e}\vec{\nabla}^2\psi(\vec{x}) + V(\vec{x})\psi(\vec{x}) = E\psi(\vec{x}) \qquad 2.1.$$

where m_e is the mass of the electron, $\hbar$ is the reduced Plank constant, H is the Hamiltonian, ψ is the wave function, V is the electric potential, and E is the energy. The potential discussed above can be written

$$V(\vec{x}) = \begin{Bmatrix} 0 & \text{for } \vec{x} \in \text{Volume} \\ \infty & \text{for } \vec{x} \notin \text{Volume} \end{Bmatrix} \qquad 2.2.$$

Approximating the electrons as non-interacting, the corresponding Hamiltonian for each electron is independent of the coordinates of the other electrons in the system, leading to

$$\vec{H} = \vec{H}(\vec{x}_1, \vec{x}_2, \vec{x}_3, \vec{x}_4, \dots) \approx \vec{H}(\vec{x}_1) + \vec{H}(\vec{x}_2) + \vec{H}(\vec{x}_3) \dots \stackrel{\text{def}}{=} \tilde{H} \qquad 2.3.$$

$$\psi(\vec{x}_1, \vec{x}_2, \vec{x}_3, \vec{x}_4, \dots) \approx \prod_{j=1}^{N} \psi_j(\vec{x}_j) \stackrel{\text{def}}{=} \tilde{\psi} \qquad 2.4.$$

The second line describing $\tilde{\psi}$ can be intuitively understood for a non-interacting system since the probability density function, $\psi_j^*\psi_j$, of a particular particle *j* should be the same independent of the location or existence of another particle *i* with probability density function, $\psi_i^*\psi_i$. This property is a direct consequence of constructing $\tilde{\psi}$ as the product of individual wave functions which can be seen by considering $\tilde{\psi}^*\tilde{\psi}$. The action of the Hamiltonian reduces to a sum over energies as shown:

$$\tilde{H}\tilde{\psi} = \sum_{i=1}^{N} \vec{H}_i \left(\psi_i(\vec{x}_i) \prod_{j \neq i}^{N} \psi_j(\vec{x}_j) \right)$$

$$= \sum_{i=1}^{N} E_i \psi_i(\vec{x}_i) \prod_{j \neq i}^{N} \psi_j(\vec{x}_j) = \sum_{i=1}^{N} E_i \prod_{j=1}^{N} \psi_j(\vec{x}_j) = \sum_{i=1}^{N} E_i \, \tilde{\psi} \qquad 2.5.$$

The form of the differential equation (second derivative of $\tilde{\psi}$ proportional to $\tilde{\psi}$) suggests exponential, plane wave solutions for $\tilde{\psi}$.

$$\tilde{\psi} = \prod_{j=1}^{N} \psi_{jo} e^{-i\,\vec{k}_j \cdot \vec{x}_j} \tag{2.6.}$$

$$\sum_{i=1}^{N} \frac{-\hbar^2}{2m_e} \vec{\nabla}^2\, \tilde{\psi} = \sum_{i=1}^{N} \frac{\hbar^2}{2m_e} \vec{\mathrm{k}}_i^2 \tilde{\psi} = \sum_{i=1}^{N} E_i\, \tilde{\psi} = \sum_{i=1}^{N} \frac{\vec{\mathrm{p}}_i^2}{2m_e}\, \tilde{\psi} \tag{2.7.}$$

which of course leads to the familiar De Broglie relation, $\hbar^2 \vec{\mathrm{k}}_i^2 = \vec{\mathrm{p}}_i^2$ and since the wave number $|\vec{\mathrm{k}}_i| = \frac{2\pi}{\lambda_i}$, and the momentum $|\vec{\mathrm{p}}_i| = \frac{h}{\lambda_i}$. In this instance, λ_i can be thought of as the wavelength of the plane wave of the i[th] electron.

I apply the Born-Von Karman boundary conditions, i.e. that the wave functions be periodic with the length of the sample, L, then in one dimension, $\tilde{\psi}(x) = \tilde{\psi}(x + L)$ and

$$\tilde{\psi}(0) = \tilde{\psi}(0 + L) = \prod_{j=1}^{N} \psi_{jo} \cdot 1 = \prod_{j=1}^{N} \psi_{jo} e^{-ik_j L} \tag{2.8.}$$

This implies that $e^{-ik\,L} = 1$ which is true for $kL = m\,2\pi$, where m is 0, ±1, ±2… It also follows that $E_m = \frac{\hbar^2}{2m_e}(\frac{m\,2\pi}{L})^2$. It is straightforward to extend the argument to three dimensions and in that case, $E_m = \frac{\hbar^2}{2m_e}\left(\frac{2\pi}{L}\right)^2 (m_x^2 + m_y^2 + m_z^2)$ where m_x, m_y, and m_z are intergers. Since "m" increments by 1, a unit volume of "m-space" has volume (Δm)(Δm)(Δm) = 1. Similarly, "k" increments by $\frac{2\pi}{L}$, a unit volume of "k-space" has volume (Δk)(Δk)(Δk) = $(\frac{2\pi}{L})^3 = \frac{(2\pi)^3}{V}$, where V is the volume of the metal.

"Degeneracy" is defined as multiple states with distinct quantum numbers having the same energy. The Pauli exclusion principle states that no two particles can exist in the same location with the same set of quantum numbers. Energy is not a quantum number; therefore two particles with the same energy may exist in the same location provided they have different quantum numbers. The Pauli exclusion principle applied to the approximation of free electrons in an infinite well is the basis for the development of the "Fermi energy" and the "Fermi level" in a material.

Section 2.1.2 Fermi Energy and Density of States

To develop the notion of the Fermi energy, consider a metal at T = 0 and let us then determine the minimal energy configuration of the electrons. Since $E \propto {m_x}^2 + {m_y}^2 + {m_z}^2$ where *m* is a quantum number, at low temperature the lowest energy states will be filled first, with two electrons of opposite spin having identical m-quantum numbers. Thus as the lowest m-numbers are filled they form a "sphere" around the origin in m-space, with the largest m-value defined as the Fermi number, m_F. The volume of the sphere is $\frac{4}{3}\pi\, m_F^3$ which contains $2\frac{4}{3}\pi\, m_F^3$ distinct sets of quantum numbers since the volume in m-space per quantum number is ½ (the volume of 1 mentioned above can now sustain two distinct electrons of different spin). Obviously, the number of distinct sets of quantum numbers must equal the number of particles, N. Then, the Fermi energy is the maximum energy of an electron that is, the energy of an electron in the highest quantum state, or

$$\varepsilon_F(T=0) = \frac{\hbar^2}{2m_e}\left(\frac{m_F\, 2\pi}{L}\right)^2$$

$$= \frac{\hbar^2}{2m_e}\left(\frac{2\pi}{L}\right)^2\left(\frac{3N}{8\pi}\right)^{2/3} = \frac{\hbar^2}{2m_e}\left(\frac{3\pi^2 N}{V}\right)^{2/3} \qquad 2.9.$$

The "density of states," g(ε), is defined as the number of states that have energy between ε and ε + dε such that the number of states than have energy less than E is

$$\int_0^E g(\varepsilon)d\varepsilon = 2\frac{4}{3}\pi\, m_E^3 = \frac{V}{3\pi^2}\left(\frac{2mE}{\hbar^2}\right)^{3/2} \quad 2.10.$$

$$g(E) = \frac{d}{dE}\left[\frac{V}{3\pi^2}\left(\frac{2mE}{\hbar^2}\right)^{3/2}\right] = \frac{V}{2\pi^2}\left(\frac{2m}{\hbar^2}\right)^{3/2}E^{1/2} \propto E^{1/2} \quad 2.11.$$

If the T = 0 constraint is relaxed, the definition of the Fermi energy must be extended to account for the thermal distribution of energies. As should be obvious from the above discussion, at T = 0 the probability of an energy state being occupied is 1 for energies less than the Fermi energy and the probability of an energy state being occupied is 0 for energies greater than the Fermi energy. The probability distribution displays a sharp cutoff as demonstrated in Figure 2.1(a). At temperatures intermediate between 0 and high temperature, the energy distribution of a spin ½ particle like an electron follows Fermi-Dirac statistics. From statistical mechanics, a large system in contact with a heat reservoir at temperature, T, will exchange energy and particles with the reservoir. The available energy states will be occupied with probability

$$P(E_i) = \frac{e^{-\frac{E_i}{kT}}}{Z} = \frac{e^{-\frac{E_i}{kT}}}{\sum_{n=0}^{\infty} e^{-\frac{E_n}{kT}}} \quad 2.12.$$

where k is now Boltzmann's constant, not the wave number and Z is the grand canonical ensemble. Since Fermionic energy states are independent only one fermion can occupy a particular state. Each state has an associated canonical ensemble, Z. There are only two possibilities for the total energy of the system– an empty state implying the system's energy is zero or an occupied state implying the system's energy is E. Applying the definitions of the

canonical ensemble and the occupation probability to each independent state results in the Fermi function which is defined as

$$f(\varepsilon) = \frac{e^{-\frac{(\varepsilon-\varepsilon_F)}{kT}}}{e^0 + e^{-\frac{(\varepsilon-\varepsilon_F)}{kT}}} = \frac{1}{e^{\frac{(\varepsilon-\varepsilon_F)}{kT}} + 1} \qquad 2.13.$$

Then, we have a found a definition of the Fermi energy for T > 0. The Fermi energy is the energy level at which there is a ½ probability of the state being occupied. In most metals, the Fermi energy is of the order of $k_B * T_{Fermi} = k_B * 10{,}000$ K and the room temperature Fermi distribution is well approximated with the zero temperature step function.

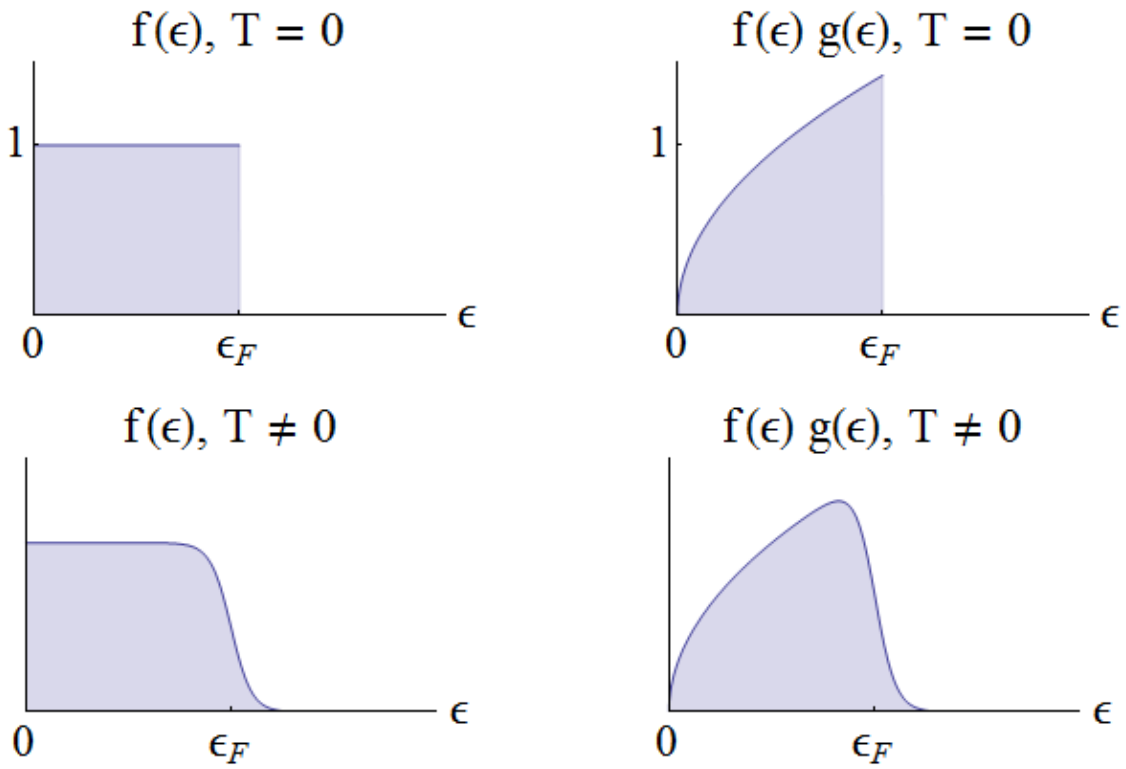

Figure 2.1 (a) The Fermi function at T = 0 (b) Fermi function - density of states product at T = 0 (c) The Fermi function at T ≠ 0 (d) Fermi function - density of states product at T ≠ 0

Any deviation from the step function will only be in the region where $\varepsilon \approx \varepsilon_F$. Qualitatively, this can be justified since the variation in a particular electron's energy will be on the order of the average thermal energy, $\frac{3}{2}$kT.

If an electron is far below the Fermi energy, each energy state within kT of the electron's current energy state will already have an electron occupying it. By the Pauli exclusion principle, the electron will be constrained to stay at its current energy. Only electrons within ≈ kT of ε_F will have available, empty energy states into which they could thermally excite with high probability.

The Fermi function can also be show to match the distributions for the T = 0 and high temperature limit. If the Fermi function in Equation 2.13 is studied in the low temperature limit, the sharp step function is recovered. For $\varepsilon - \varepsilon_F < 0$, $\lim_{T\to 0} e^{\frac{(\varepsilon-\varepsilon_F)}{kT}} = 0$ and $f(\varepsilon) = 1$. For $\varepsilon - \varepsilon_F > 0$, $\lim_{T\to 0} e^{\frac{(\varepsilon-\varepsilon_F)}{kT}}$ approaches ∞ and $f(\varepsilon) \to 0$.

At high temperatures, the energy distribution of many particles follows Maxwell-Boltzmann statistics, $e^{-E/kT}$. In the high temperature limit, $1 + e^{-\frac{(\varepsilon-\varepsilon_F)}{kT}} \to 1$, and $f(\varepsilon) \approx e^{\frac{-(\varepsilon-\varepsilon_F)}{kT}}$ or the Maxwell-Boltzmann limit.

Section 2.1.3 Effective Mass

In a semiconductor, it has been useful to define an electron vacancy as a "hole", which can be treated as a particle with charge equal and opposite to an electron. When an electron in the semiconductor fills a vacancy, the electron leaves a vacancy behind at its original atom. In this way the hole can be thought of as mobile between atomic centers and a contributor to conductivity.

The "effective mass" of an electron or hole, like the classical counterpart, describes the ratio of acceleration to an applied force. However, since the electron interacts with the crystal structure and the potential, V(x), this alters the ratio to be greater or less than the free electron mass. The effective mass can even be found to be negative. Rather than the simple ratio of force to acceleration, effective mass is defined most generally as a tensor since the potential and thus the interaction can be different based upon the direction of interest in the crystal.

$$\frac{1}{m^*_{ij}} = \frac{1}{\hbar^2}\frac{d}{dk_i}\frac{d}{dk_j}[E] \qquad 2.14.$$

For the free electron, $E = \frac{\hbar^2}{2m_e}\vec{k}^2$ and since all k-directions are equivalent, $\frac{1}{\hbar^2}\frac{d^2E}{dk^2} = \frac{1}{m_e}$ and the effective mass is simply the scalar, free mass.

Section 2.2 Modulated Electron (Bloch) Model: Quantum Theory for Semiconductors

Section 2.2.1 Band Theory

The next higher order approximation for the behavior of an electron in a material is to introduce the periodic nature of the positive nuclei into the potential, V($\vec{x}$), in the Schrodinger equation. For simplicity, consider a one dimensional lattice, V(x) = V(x + a), where "*a"* is the lattice spacing of the atomic nuclei[7]. The Born Von Karmen periodic boundary conditions for the edges of the crystal still hold and mandate that $\tilde{\psi}(x) = \tilde{\psi}(x + L)$. Consider the charge density of $\tilde{\psi}^*\tilde{\psi}$. The density should be translationally invariant with respect to the periodicity of the lattice: $\tilde{\psi}^*(x)\tilde{\psi}(x) = \tilde{\psi}^*(x + m\,a)\tilde{\psi}(x + m\,a)$, where "m" is an integer. From this, ψ must have a periodicity identical to that of the lattice and any modification to the wave function due to

translation must be in a complex phase factor, C, whose magnitude must satisfy the condition $C^*C = 1$. Another phase factor is accrued for each unit "m" moved. Therefore,

$$\psi(x + Na) = C^N \psi(x) \qquad 2.15.$$
$$1 = C^N \leftrightarrow C = e^{\frac{2\pi i d}{N}} \text{ for d} = 0, \pm 1, \pm 2\ldots$$

Thus, the wave functions $\psi(x)$ meet the "Bloch condition" that they be a two part function

$$\psi(x) = e^{i\vec{k}\cdot\vec{x}} u_{\vec{k}}(\vec{x}), \qquad 2.16.$$

the first term $e^{i\vec{k}\cdot\vec{x}}$ being the plane wave form of the free electron solution and the second part $u_{\vec{k}}(\vec{x})$ is periodic and modulates the amplitude of the wave function with the periodicity of the lattice[8]. Since $\psi(x + a) = e^{ika}\psi(x)$, $e^{ika} = C = e^{\frac{2\pi i d}{N}}$ and thus $k = \frac{2\pi i d}{N \cdot a}$.

Applying the Schrodinger equation to the Bloch function $\psi(x) = e^{i\vec{k}\cdot\vec{x}} u_{\vec{k}}(\vec{x})$, the $\vec{\nabla}^2$ must be applied to both $e^{i\vec{k}\cdot\vec{x}}$ and $u_{\vec{k}}(\vec{x})$. The Schrodinger equation becomes:

$$\frac{-\hbar^2}{2m_e} e^{i\vec{k}\cdot\vec{x}} \left[\vec{\nabla}^2 + 2i\vec{k}\,\vec{\nabla} + \vec{k}^2\right] u_{\vec{k}}(\vec{x}) + e^{i\vec{k}\cdot\vec{x}} V(\vec{x}) u_{\vec{k}}(\vec{x}) = E e^{i\vec{k}\cdot\vec{x}}\, u_{\vec{k}}(\vec{x}) \qquad 2.17.$$

$$\frac{-\hbar^2}{2m_e} \left[\vec{\nabla}^2 + 2i\vec{k}\,\vec{\nabla} + \vec{k}^2\right] u_{\vec{k}}(\vec{x}) + V(\vec{x}) u_{\vec{k}}(\vec{x}) = E\, u_{\vec{k}}(\vec{x}) \qquad 2.18.$$

Section 2.2.2 Origin of Band Gap: Kronig-Penny Model

Shortly after Bloch presented the form of an electron wave function in a periodic crystal potential, Kronig and Penny proposed the solution for the wave function and the energy in the limit of a delta function potential at each atomic lattice site[9]. To begin, the potential is modeled as finite with height, V_o, with a non-zero width, b, and lattice spacing, a. Limits are applied to

transform the finite potential to the infinite potential, delta functional form. The one-dimensional differential equation is

$$\frac{-\hbar^2}{2m_e}\left[\frac{d^2u_{\vec{k}}(x)}{dx^2}+2i\vec{k}\,\frac{du_{\vec{k}}(x)}{dx}+k^2\right]+V(x)u_{\vec{k}}(x)=E\,u_{\vec{k}}(x). \qquad 2.19.$$

If we define

$$\gamma=\sqrt{\frac{2m_e}{\hbar^2}(V_o-E)}\ \text{ and }\ \beta=\sqrt{\frac{2m_e}{\hbar^2}E}, \qquad 2.20.$$

then equation (2.19) has solution $u_{\vec{k}}(x)=Ae^{(-ik+\gamma)x}+Be^{(-ik-\gamma)x}$ in the high potential area, and solution $u_{\vec{k}}(x)=Ce^{(-ik+\beta)x}+De^{(-ik-\beta)x}$ in the zero potential area. With the restriction that the wave function and the first derivative (i.e. the momentum) must be continuous, the four resulting equations eliminate the coefficients A, B, C, and D. Then, by taking the limit of the potential such that V→∞ as b→0 in such a way that

$$\lim_{\substack{b\to 0\\ \gamma\to\infty}}\frac{\gamma^2 ab}{2}=P \qquad 2.21.$$

the solution for the wavefunction is constrained by

$$P\,sinc\beta a+cos\beta a=cos\,ka \qquad 2.22.$$

This has several important consequences. Since *ka* is real, $-1\le cos\,ka\le 1$, and this also limits the transcendental function $-1\le P\,sinc\beta a+cos\beta a\le 1$ which, from the definition of β, limits the energy. Thus, this simple model predicts that the allowed energies are restricted with "forbidden bands" or forbidden regions in between, as shown in Figure 2.2. These forbidden regions are termed *band gaps*.

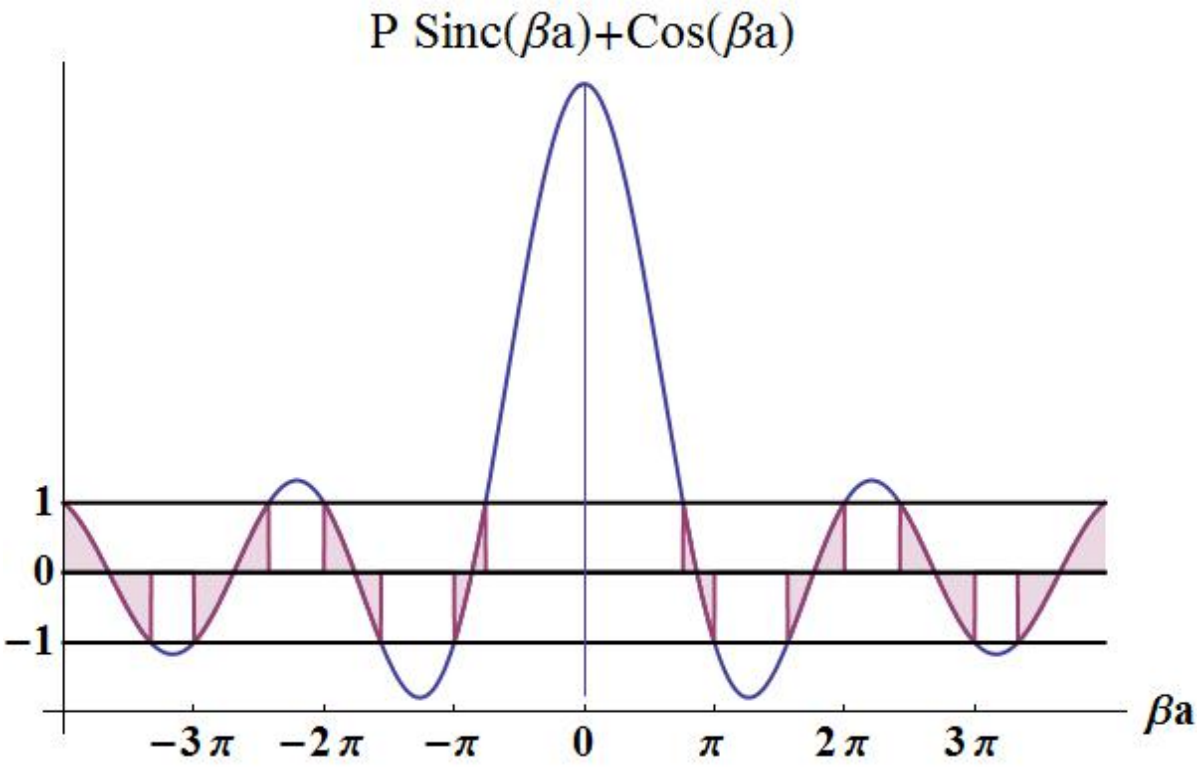

Figure 2.2 The origin of an energy band gap: the transcendental equation for $\boldsymbol{\beta a}$ between the allowed values of ±1. The pink shaded regions are the allowed values projected onto the $\boldsymbol{\beta a}$ axis. Created using Kronig and Penny[9]. Recall that $\boldsymbol{\beta} = \sqrt{\frac{2m_e}{\hbar^2}\boldsymbol{E}}$ and a is the lattice spacing.

Section 2.2.3 Band Gaps for Real Materials

From the Kronig-Penny model, it is evident that the energy and the lattice constant will be involved in the equation of the forbidden zones, that is, differences in lattice spacing and crystal structure can be expected to impact the electrostatic potential V(x) as well as the size of the forbidden energy region. Many theoretical and experimental studies have been carried out to map the band structures of semiconductors which are obviously more complex than the results of the simple one dimensional model presented in the previous section. The band structure of a real material depends heavily on the direction in the lattice and in reciprocal k-space. Some example band structure diagrams from the work of Cohen and Bergstresser[10] are pictured in Figure 2.3.

The energy surface spans three dimensions, but intersections of the energy surface along specific crystallographic planes can represent slices of the three dimensional surfaces in a two dimensional format. The Greek letters along the horizontal axis indicate the points in the k-space of the unit cell. The plane of intersection is defined by moving between the two points in the unit cell.

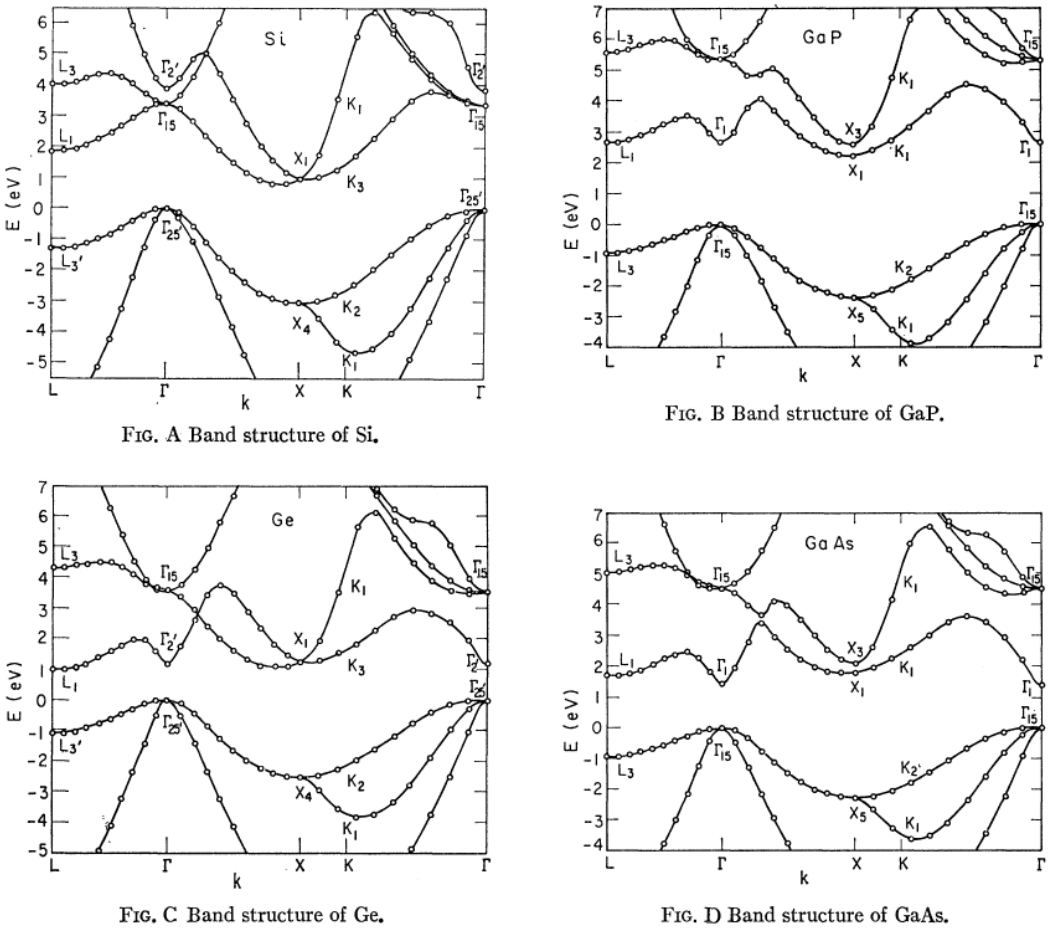

FIG. A Band structure of Si.

FIG. B Band structure of GaP.

FIG. C Band structure of Ge.

FIG. D Band structure of GaAs.

Figure 2.3 Band structure for common semiconductors taken from Cohen and Bergstresser[10] or Chelikowsky and Cohen[11]

If the highest point in the valence band is at the same value of *k* as the lowest point in the conduction band, the semiconductor is classified as a "direct band gap" semiconductor. The band structure of GaAs displays this feature at the Γ-point, k = (0, 0, 0) with a 1.5 eV gap (Figure 2.3 (d)). If the highest point in the valence band is at a different value of *k* than the lowest point in

the conduction band, the semiconductor is classified as an "indirect band gap" semiconductor. The band structure of Si displays this feature (Figure 2.3 (a)) with a gap energy of 1.17 eV.

Conservation laws imply that for an excitation of an electron using the minimum gap energy in an indirect band gap material, the electron will excite to a virtual state, de-excite to the conduction band at a new *k* with the generation of a phonon, to conserve momentum. In a direct band gap semiconductor, there is no change in *k*; therefore, phonon mediation is unnecessary to conserve momentum. Direct band gap semiconductors like GaAs (Figure 2.3 (d)) will tend to have higher optical absorption since the transition does not involve excitations through forbidden states. This is one reason to select GaAs for use in optoelectronic sensors, like Extraordinary Optoconductance (EOC) sensors.

Section 2.3 Conductivity in Semiconductors

Section 2.3.1 Intrinsic Carrier Concentration and Fermi Energy in a Semiconductor

Thus far, we have developed the notion of the quantum mechanical nature of electronic states, the band gap, the Fermi energy, and the density of states. It now remains to outline how these fundamental constructs manifest in measurable characteristics like conductivity, carrier concentrations, and the magnitude of the gap.[12] The number of electrons in the conduction band is the integral of the probability of occupation (the Fermi distribution) and the density of states from the bottom, ε_c, to the top of the conduction band, ε_{top}. The density of electrons $n \equiv$ N/V is,

$$n = \int_{\varepsilon_c}^{\varepsilon_{top}} f(\varepsilon) g(\varepsilon) d\varepsilon$$

$$n = \int_{\varepsilon_c}^{\varepsilon_{top}} \frac{C\ (\varepsilon - \varepsilon_F)^{1/2}}{e^{\frac{(\varepsilon - \varepsilon_F)}{kT}} + 1} d\varepsilon \qquad 2.23.$$

where we collect the remaining multiplicative constants from equation 2.11 and define:

$$C = \frac{1}{2\pi^2}\left(\frac{2m_{ds}}{\hbar^2}\right)^{3/2}$$

since we divided by volume to calculate number density. Notice that the band structures in Figure 2.3 have multiple local minima some of which may be equal in value. The density of states mass for electrons, $m_{ds}^3 = N_{min}^2 m_1^* m_2^* m_3^*$, is a product of the effective masses in the three spatial directions and the number of equal-valued, global conduction band minima. The substitution $x = \frac{(\varepsilon - \varepsilon_C)}{kT}$ alters the integral to $n = C \cdot (kT)^{3/2} \cdot F[\frac{(\varepsilon_F - \varepsilon_c)}{kT}]$ where $F[x] = \int_0^\infty \frac{x^{1/2}}{e^{x-(\varepsilon_F-\varepsilon_C)/kT}+1} dx$ is the Fermi Dirac integral. $F[x]$ does not have a closed form solution and must be evaluated numerically. An approximation can be made for the case of non-degenerate energy states, where ε_F is mid-gap, and more than 3kT away from either band edge, implying that the total band gap be more than 0.14 eV at room temperature (both GaAs and Si fit this requirement). Then the electron density simplifies to $n = N_c e^{-\frac{(\varepsilon_C - \varepsilon_F)}{kT}}$, where $N_c = 2(\frac{2\pi\, kT\, m_{eds}}{\hbar^2})^{3/2}$ is the effective density of states at the conduction band and m_{eds} is the "density of states mass" in the conduction band. Similar treatment of the hole density, *p*, can derive the effective density of states at the valence band energy from the integral of $f(\varepsilon)g(\varepsilon)$ evaluated between the top of the valence band, ε_v, to the bottom of the energy band. The effective density of states at the valence band energy is $N_v = 2(\frac{2\pi\, kT\, m_{hds}}{\hbar^2})^{3/2}$ and m_{hds} is the "density of states mass" in the valence band.

$$n = N_c e^{-\frac{(\varepsilon_c - \varepsilon_F)}{kT}} \qquad 2.24.$$

$$p = N_v e^{-\frac{(\varepsilon_F - \varepsilon_v)}{kT}} \qquad 2.25.$$

$$n_i^2 \equiv n \cdot p = N_c N_v \, e^{-\frac{(\varepsilon_c - \varepsilon_v)}{kT}} \tag{2.26.}$$

The critical feature of the defined quantity, n_i or the *intrinsic carrier density*, is that it is independent of the Fermi level and depends only on the band gap, the effective masses, and the temperature. Also, in the derivation from the Fermi function and the density of states, there were no assumptions made about the source of the carriers: intrinsic, doped, or injected. Therefore the result is general and the product $n \cdot p$ can be considered a constant for any semiconductor whose Fermi level and band gap satisfies the simplifying assumptions used to evaluate $F[\frac{(\varepsilon_F - \varepsilon_c)}{kT}]$ mentioned above.

Furthermore, if the semiconductor is intrinsic and no dopant atoms are added, then the volume density of electrons must equal the density of holes, since each electron excited thermally across the band gap will leave a hole behind in the valence band.

$$n = p = N_c e^{-\frac{(\varepsilon_c - \varepsilon_F)}{kT}} = N_v e^{-\frac{(\varepsilon_F - \varepsilon_v)}{kT}} \tag{2.27.}$$

$$\frac{N_c}{N_v} = e^{\frac{(\varepsilon_c + \varepsilon_v - 2\varepsilon_F)}{kT}} \tag{2.28.}$$

$$\left(\frac{m_{eds}}{m_{hds}}\right)^{3/2} = e^{\frac{(\varepsilon_c + \varepsilon_v - 2\varepsilon_F)}{kT}} \tag{2.29.}$$

$$\varepsilon_F = -\frac{3\,kT}{4} \ln\left(\frac{m_{eds}}{m_{hds}}\right) + \frac{(\varepsilon_c + \varepsilon_v)}{2} \tag{2.30.}$$

Therefore, in the special case where the electron and hole effective masses are identical, the first term disappears and the Fermi level of an intrinsic semiconductor will fall exactly between $\varepsilon_c + \varepsilon_v$ in the center of the band gap.

If the semiconductor is not intrinsic, but has been doped with a concentration of atoms which can donate an electron, the semiconductor is called “n-type”, for instance, when a silicon

($1s^2 2s^2 2p^2$) crystal is doped with arsenic ($1s^2 2s^2 2p^3$). A semiconductor that has been doped such that the dopants accept or trap an electron are called "p-type" and can be modeled as "donating" holes, for instance if a silicon ($1s^2 2s^2 2p^2$) crystal is doped with boron ($1s^2 2s^2 2p^1$).

Consider an n-type semiconductor at T = 0. All the donated electrons will be in the vicinity of the dopant atom's attractive potential well and have energy ε_D. From the definition of the Fermi energy in the Fermi function as the energy at which there is a ½ probability of the state being filled, at zero temperature the relation $\varepsilon_D < \varepsilon_F < \varepsilon_C$ must be true. Thus, since generally it is true that $\varepsilon_V < \varepsilon_D$, adding donors will tend to increase the Fermi energy of a sample, while adding acceptors will tend to decrease the Fermi energy, bringing it closer to the valence band. As the temperature is increased, the dopant carriers will be excited above the band gap and there exists a regime where the carrier concentration can be assumed equal to the dopant concentration. In the case of either type of dopant, when the temperature is high enough to excite a population of intrinsic carriers higher than the concentration of donor carriers, the Fermi energy will return to mid-gap, intrinsic behavior.

Section 2.3.2 Equivalence of Fermi Energy and Chemical Potential

The distribution of carriers at a junction of two distinct materials and the spontaneous formation of regions of high internal electric fields result in the phenomena of rectification that allows easy current flow in one direction and is utilized in semiconductor integrated circuit technology. To understand the operation of semiconductor devices in general and EXX sensors in particular, it is necessary to understand the origins of the junction phenomena.

Following Swalin[13], imagine a crystal with N(ε) electrons on Z sites. The fraction of occupied states at system energy "ε" is

$$f(\varepsilon) = \frac{1}{e^{\frac{\varepsilon-\varepsilon_F}{kT}}+1} = \frac{N}{Z}. \quad 2.31.$$

Now, if one electron is added to the crystal, the change in the system entropy, S, will relate to the number of microstates, W, by the Boltzmann relation, and employing Sterling's approximation for $W = \frac{Z!}{N!(Z-N)!}$:

$$\frac{dS}{dN} = k_B \frac{d\ln(W)}{dN} \quad 2.32.$$

$$\frac{dS}{dN} = k_B \frac{d\,[Z(ln(Z)-1) - (Z-N)(ln(Z-N)-1) - N(\ln(N)-1)]}{dN} \quad 2.33.$$

$$\frac{dS}{dN} = k_B \ln(\frac{Z}{N} - 1) \quad 2.34.$$

$$\frac{dS}{dN} = k_B \ln\left(e^{\frac{\varepsilon-\varepsilon_F}{k_B T}} + 1 - 1\right) = \frac{\varepsilon}{T} - \frac{\varepsilon_F}{T} \quad 2.35.$$

Then recall from the definition of a full differential in terms of the partial derivatives of its arguments:

$$\frac{dS}{dN} = \left(\frac{\partial S}{\partial N}\right)_{\varepsilon,V} + \left(\frac{\partial S}{\partial \varepsilon}\right)_{N,V} \frac{d\varepsilon}{dN} \quad 2.36.$$

The added electron gains the average energy of the system, ε, implying that I may define $\frac{d\varepsilon}{dN}$ as equal to ε/electron or $\frac{d\varepsilon}{dN} \equiv \varepsilon$. With this definition inserted into equation 2.36 and by equating like coefficients in Eq. 2.35 and 2.36 we see that

$$\left(\frac{\partial S}{\partial \varepsilon}\right)_{N,V} = \frac{1}{T} \qquad \left(\frac{\partial S}{\partial N}\right)_{\varepsilon,V} = -\frac{\varepsilon_F}{T}.$$

From thermodynamics and the definition of the Helmholtz free energy, $F = U - TS$, the chemical potential, μ, can be shown to be

$$\left(\frac{\partial S}{\partial N}\right)_{\varepsilon,V} = -\frac{\mu}{T} \qquad 2.37.$$

Thus it can be seen that for the case of electrons in a crystal, the Fermi energy, ε_F, equals the chemical potential, μ, and the difference in the Fermi energies in a junction of a p-type and an n-type doped material will drive diffusion of electrons and holes across the barrier until the Fermi level is flat across the junction.

Section 2.3.4 Drift and Diffusion Current in Mesoscopic Samples Exhibiting Diffusive Transport

An electric field applied to a metal or semiconductor will cause a "drift current," *J*, from the electric force applied to the electrons and holes in the material as they then scatter off the lattice, or off ionized atomic nuclei, randomly reorienting the direction of their motion. Thus, there will be a general "drift" of net charge in the direction of the field. The drift current is

$$\vec{J}_{drift} = pe\mu_h\vec{E} + ne\mu_n\vec{E} \qquad 2.38.$$

For low electric fields, less than about 2 kV/cm, the "mobility," μ, of an electron or hole can be defined as the ratio of the drift velocity to the electric field[14], $\mu = \frac{v_d}{E}$. From the definition of the drift velocity as the applied acceleration, $\frac{eE}{m_e}$, multiplied by the average time between collisions (the average time the electron is accelerated without interruption), τ_{avg}, then it can also be stated that $\mu = \frac{v_d}{E} = \frac{e\tau_{avg}}{m_e}$. Thus, the mobility will increase as the average scattering time increases and will decrease as the effective mass increases.

In addition to the drift current, there can also be a current from a concentration gradient, like at a junction of a p-type and an n-type doped material. Recall the equality of the chemical potential and the Fermi level which explains how an uneven concentration of charge will

spontaneously smooth itself by generating a current. The direction of motion of holes is considered "positive" as is typical. Following Fick's first law, the holes will move away from the high concentration, that is, in the direction opposite the gradient of the concentration.

$$\vec{J}_{diffusion} = eD_N \nabla n - eD_H \nabla p \qquad 2.39.$$

where D_N and D_H are the diffusion coefficients for electrons and holes. If only the electrons are considered, such as in an n-type material, then at thermal equilibrium, both currents should balance. Thus, for one dimension and a constant electric field,

$$-ne\mu_n E = eD_N \nabla n = eD_N \frac{dn}{dx} \qquad 2.40.$$

$$-e\mu_n Ex + c = eD_N \ln(n) \qquad 2.41.$$

$$n = n_o e^{\frac{-\mu_n Ex}{D_N}} \qquad 2.42.$$

Then from Boltzmann statistics, for a potential energy q·V = q·E·x, the thermal distribution *n* would have the same form.

$$n = n_o e^{\frac{-eEx}{kT}} \qquad 2.43.$$

Equating the arguments of the exponentials 2.42 and 2.43, we derive the Einstein-Nernst equation[15]:

$$\frac{\mu_n}{D_N} = \frac{e}{kT} . \qquad 2.44.$$

Section 2.4 Behavior of Material Interfaces

Section 2.4.1 P-N Junction and Metal-Semiconductor Junction

The p-n junction is a critically important semiconductor construct in industrial applications consisting of a single crystal with a doped p-type section in contact with an n-type

section. The doping profiles can vary depending upon the application and the cost-effectiveness of the manufacturing process. For instance, an alloyed junction consists of heating an overlaid metal layer which melts into the substrate and the semiconductor-metal blend recrystallizes upon cooling creating a doped region between the metal and semiconductor. This is a common method of creating a highly robust, Ohmic contact to semiconductor sensors. A diffused junction is similar except that the doping occurs by exposing the semiconductor to a hot gas in a furnace. The location of doping is isolated by laying down a mask of an insulating material such as an oxide or nitride that can withstand the high temperatures. Ion implantation is another method for doping a semiconductor which has the benefit of operating at lower temperatures than the diffusion or alloying methods. Thus it will not damage previously patterned junctions. However, the ion implantation process will damage the crystal structure of the bombarded region, which may be undesirable.

Under equilibrium, in an n-type material, the electrons outnumber holes and are termed "majority carriers" while holes are termed "minority carriers". The thermodynamics of the concentration gradient across the junction will drive electron and hole diffusion. Recombination on either side of the junction will occur with some probability distribution.

The "depletion region" is defined as the volume of semiconductor whose donor/acceptor static atomic nuclei lose/gain an electron upon diffusion. The length of the depletion region is the sum of the depletion lengths in the p and n regions, $d_p + d_n = d$. The doping concentrations in the two sections need not be equal; so naturally the depletion lengths need not be equal.

A calculation of the depletion length of a p-n junction is applicable to other technologically important situations. The metal-n-semiconductor junction can be modeled as a p-n junction whose p doped region (the metal) is an infinite source of holes and an infinite acceptor

of electrons. As will be shown, when this limit is applied to the p-n junction, the depletion region in the metal is zero with a surface charge of electrons collected on the boundary.

Following Burns[16] for this model, the doping profile is assumed to be abrupt, as shown in Figure 2.4. Also to simplify the model, it is assumed that all the available donors and acceptors in the depletion region combine with the diffused charges – in other words, that all atomic nuclei within the depletion region are ionized. In the bulk outside the depletion region, charges are assumed to balance for a charge density equal to zero. The crystal is assumed to be much larger in the two dimensions parallel to the interface. Therefore the problem reduces to one dimension, since the charge density, potential and electric field will be constant at any plane parallel to the junction interface. We define the volume density of acceptor dopants as N_A and the volume density of donor dopants as N_D. The depleted charge regions have a charge density, ρ, that is

$$\rho(x) = \begin{cases} -eN_A \; for \; -d_p \le x \le 0 \\ eN_D \; for \quad 0 \le x \le d_n \end{cases} \qquad 2.45.$$

The electric field is related to the charge density by $\nabla\vec{E} = \frac{-\rho}{\epsilon}$ which in one dimension reduces to

$$\frac{dE}{dx} = \frac{d^2V}{dx^2} = \frac{-\rho(x)}{\epsilon} \qquad 2.46.$$

$$E = -\frac{dV}{dx} \qquad 2.47.$$

where ϵ is the electric permittivity. We expect E = 0 outside the depletion region since we are assuming equilibrium. Charge has stopped redistributing at the junction implying that the potential should be a constant where there was no charge displacement. Since $\rho(x)$ is a constant, $\frac{dE}{dx}$ is a constant, and the electric field has the form: $\epsilon\, E(x) = C\, x + \epsilon\, E_o$. Using the boundary conditions at d_p and d_n,

$$0 = eN_A d_p + E_{o(p)} = eN_D d_n + E_{o(n)} \qquad 2.48.$$

$$\epsilon E = \begin{Bmatrix} -eN_A(x + d_p)\ for - d_p \le x \le 0 \\ eN_D(x - d_n)\ for\ 0 \le x \le d_n \end{Bmatrix} \quad 2.49.$$

We require charge conservation i.e. $eN_A d_p * Area = |q_p| = eN_D d_n * Area = |q_n|$. For every electron that crossed the interface leaving a hole in the n-type, one acceptor in the p-type took that electron; on an intuitive level this is an obvious result. It also has the effect that the electric field is continuous at the origin, x = 0. We have an additional freedom to choose that $V(-d_p) = 0$ and $V(d_n) = V_C$, the "built in potential". In addition, the potential should be continuous at zero since the electric field was continuous at zero.

$$V = \frac{1}{\epsilon}\begin{Bmatrix} eN_A\dfrac{(x + d_p)^2}{2}\ for - d_p \le x \le 0 \\ -eN_D\left(\dfrac{x^2}{2} - d_n x - \dfrac{N_A}{N_D}\dfrac{{d_p}^2}{2}\right)\ for\ 0 \le x \le d_n \end{Bmatrix} \quad 2.50.$$

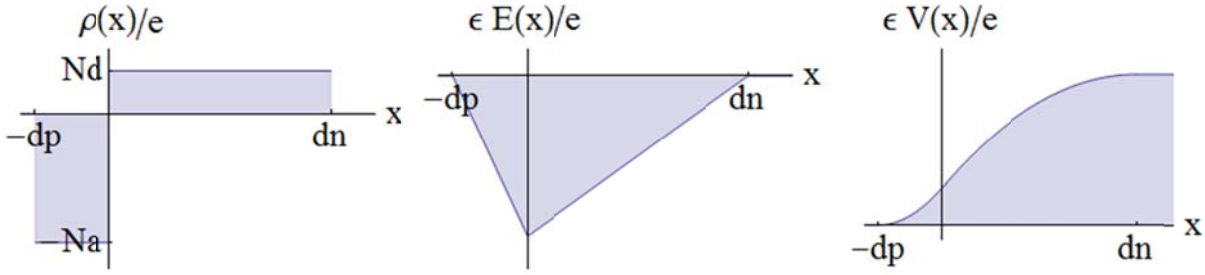

Figure 2.4 Graphs of the charge density, ρ, the electrostatic field, E, and the electrostatic potential, V, on either side of a p-n junction. Reproduced from Burns[16].

Using the equation for charge neutrality and the definition:

$$V_C = \frac{eN_D d_n}{2\epsilon}(d_n + d_p), \quad 2.51.$$

$$d = d_p + d_n = \left[\frac{2 \in V_C(N_D + N_A)}{eN_D N_A}\right]^{1/2} \quad 2.52.$$

$$d_{n-metal} = \lim_{N_A \to \infty}\left[\frac{2 \in V_C(N_D + N_A)}{eN_D N_A}\right]^{1/2} = \left[\frac{2 \in V_C}{eN_D}\right]^{1/2} \quad 2.53.$$

The final line is the expression for the depletion region in the semiconductor for an n-type to metal interface. The identical treatment can be taken for a junction with an externally applied voltage bias. In that case $V_C \rightarrow V_C + V_{Applied}$ and the depletion region is modulated accordingly. For instance, when $V_C = -V_{Applied}$, the region is eliminated altogether.

To get an idea of the internal field strength experienced at the junction of n-GaAs and a Ti interface, where $N_D = 4 \cdot 10^{17}$ cm^{-3}, $\epsilon = 12.9\ \epsilon_o$, and $V_C \sim 0.8$ V [17], then the electric field would be $E \approx 3 \cdot 10^6$ V/cm. It will be shown in Chapter 7 that this is the equivalent order of magnitude induced by a bound protein at the surface of an EEC sensor, further justifying the appropriateness of the application.

Section 2.4.2 Schottky Barriers and Ohmic Contacts

Metal semiconductor interfaces are divided into two categories based upon whether the interface is rectifying (allowing current flow in only one direction) or linear (allowing current flow in both directions). These two situations are based on the relative Fermi levels of the materials. If the Fermi level of the metal is higher than the level of the semiconductor, an Ohmic contact is formed, where carriers can directly pass to the conduction band. Applying an external voltage will manipulate the relative levels, but a wide enough range of band to band contact leads to a corresponding linear region of current-voltage dependence. If the Fermi level of the semiconductor is higher than that of the metal, the electrons in the nearby semiconductor will be depleted. Rather than the continuous potential and electron volume density of the p-type semiconductor, the charges in the metal will form a surface charge layer at x = 0 on the interface as can be seen by the discontinuity of the semiconductor conduction band

to the metal conduction band in Figure 2.5 (recall $\frac{d^2V}{dx^2} = \frac{-\rho(x)}{\epsilon}$) characterized by an energy barrier, eφ.

Applying an external voltage manipulates the relative Fermi level across the interface. A forward bias lowers the level in the semiconductor, reducing the barrier and finally aligning the metal band with the conduction band; then current flows freely. If a bias is applied with the opposite polarity, a reverse bias, the Fermi level of the semiconductor is increased, the barrier height is increased, and electrons are further limited from crossing the interface. Thus the behavior is assymetric with respect to the amount of current flow in response to an applied voltage. This is an example of a Schottky interface.

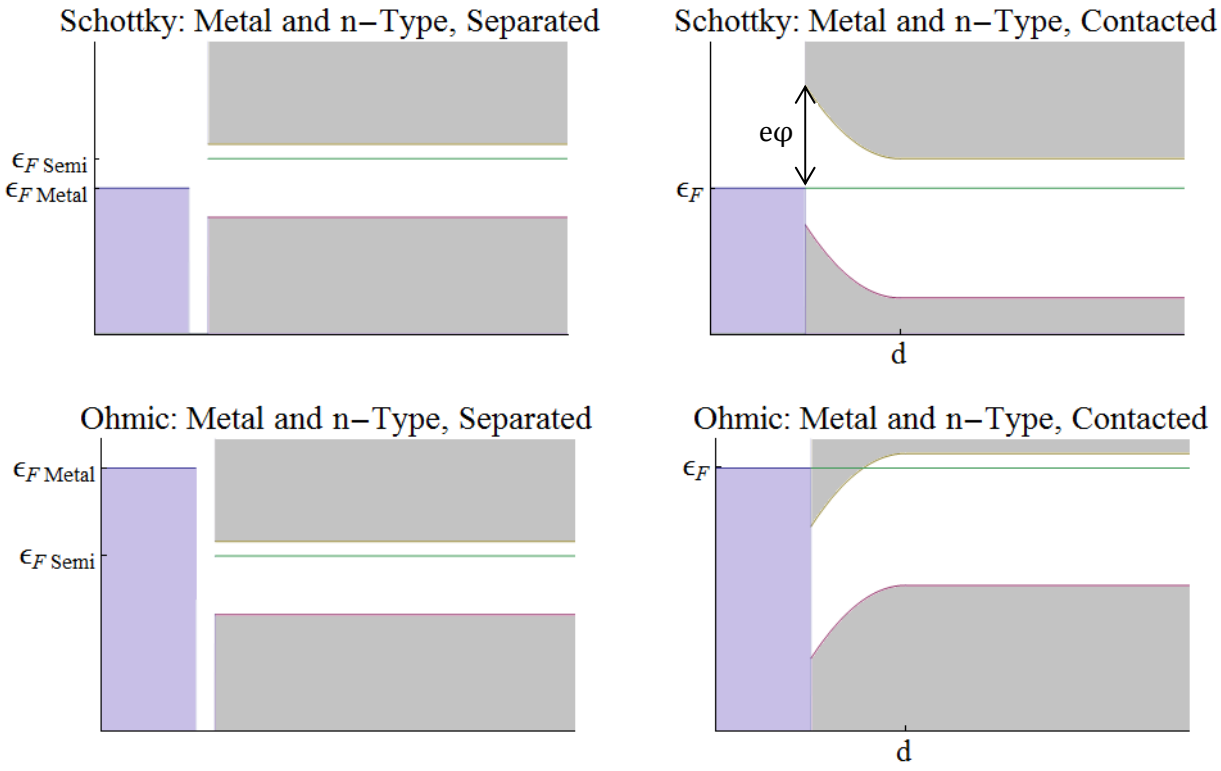

Figure 2.5 Cartoon depictions of the band diagrams for Ohmic and Schottky contacts.

The I-V characteristic curve for a Schottky barrier at a metal-semiconductor junction can be derived from thermionic emission theory[18]. As depicted above, there is a barrier to transversing the junction which can be modulated by an applied external voltage bias, $V_T = \varphi_B - V_{ap}$. For an electron to start at the Fermi level of either material, it will have to traverse a point that is φ_B above the Fermi level. Then, for doped GaAs such that 10^{15} $cm^{-3} < N_D < 10^{16}$ cm^{-3}, interfacial barriers that are larger than kT, and assuming that φ_B is not a function of V_{ap}, thermal excitation across the barrier plays the dominant role in conduction. The I-V characteristic derived from the probabilities of thermal excitation across the barrier in either direction is

$$I = SA^*T^2\left(e^{-\frac{e(\varphi_B - V_{ap})}{kT}} - e^{-\frac{e\varphi_B}{kT}}\right) = SA^*T^2e^{-\frac{e\varphi_B}{kT}}\left(e^{\frac{eV_{ap}}{kT}} - 1\right) \qquad 2.54.$$

$$A^* = \frac{4\pi\, e\, m^* k^2}{h^3}$$

where S is the junction interfacial area, A^* is the Richardson constant, T is the temperature, I is the current, and V_{ap} is the applied voltage.

If the barrier is high, but the depletion region does not extend far into the semiconductor by virtue of higher doping concentrations, electrons can tunnel quantum mechanically across the barrier, a process called field emission. At doping levels intermediate between the two, both mechanisms contribute to conduction referred to as thermionic field emission.

Chapter 3 Semiconductor and EXX Sensors Structure, Fabrication, and Function

Section 3.1 Manufacturing and Fabrication of Sensors

The EXX structures have three standard forms: bare mesa semiconductor with no shunt metal, mesa with shunt for augmented sensitivity, and mesa with shunt and a fifth lead that contacts the shunt metal. The bare devices provide the control and comparison for many other semiconductor devices and allow the heightened sensitivity of shunted devices to be demonstrated. The shunted devices are the simplest version of an EXX MSH structure. The shunted device is simpler than shunt contacted in that there is one fewer lead to pattern. The shunt connected devices have become particularly important for EEC structures in order to verify the integrity of the rectifying interface. All three structures are shown in Figure 3.1.

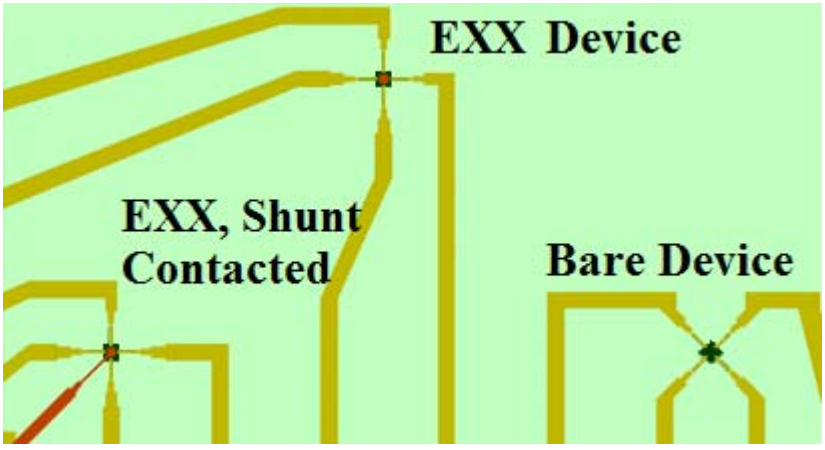

Figure 3.1 Top view of three standard structures: Bare sensor without shunt, standard EXX sensor with shunt, nonstandard EXX sensor with shunt contacted.

Section 3.1.1 Materials

Most recently, and for all sensors discussed in the following experiments, EEC and EOC sensors are fabricated from 100 nm thick, Si-doped GaAs epitaxial layers (μ =3225 $cm^2\ V^{-1}\ s^{-1}$, N_D=4 10^{17} cm^{-3}) grown by molecular beam epitaxy. The epilayer was grown on an 800 nm thick insulating GaAs layer over the bulk semi-insulating GaAs wafer. Schottky contacts at the shunt were manufactured from a layer of 40nm titanium overlaid with 40 nm gold to prevent titanium diffusion into the insulator over layer. Ohmic contacts were formed by evaporating 88:12 gold:germanium alloy, nickel as a wetting agent (the contacts are annealed at 450°C), and gold. The sensors were covered with an insulator over layer of either Si_3N_4 or Al_2O_3. The cross section of the completed sensor layering is shown in Figure 3.2.

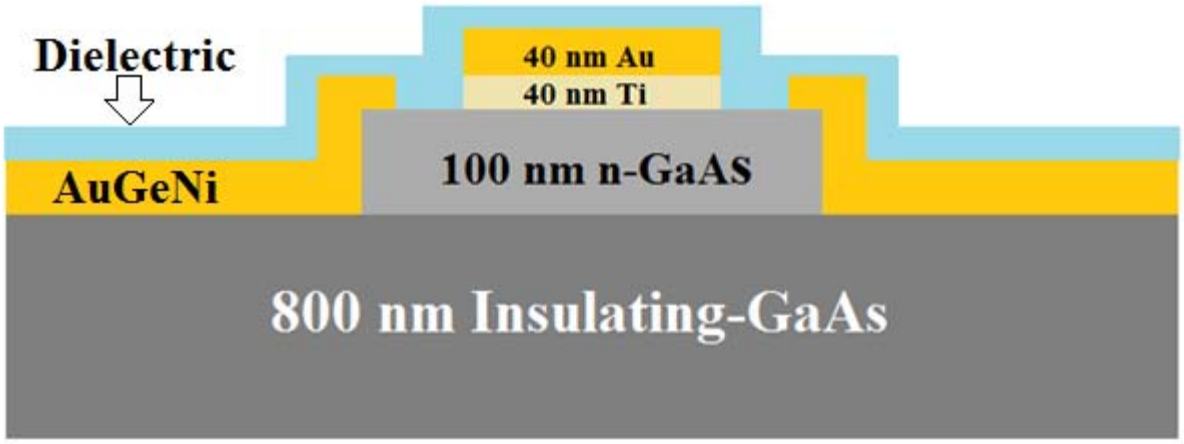

Figure 3.2 Cross section of EXX sensor to demonstrate layered structure. The lateral dimensions are not to scale.

Section 3.1.2 Sensor Fabrication Overview

In the following discussion, the photoresist is assumed to be a dual-mode, positive or negative photoresist, such as AZ 5214E from AZ Electronic Materials. However, much of the

process is quite general to the majority of single-mode resists available for semiconductor processing today. The photoresist developer mentioned in this text is AZ 327 MIF Developer.

Section 3.1.2.1 Sensor Patterning

Fabrication of EXX macro scale sensors involves patterning, etching, and deposition. Every stage involves photolithographic patterning. In brief, first the mesa structure is patterned in photoresist and the exposed, doped epitaxial layer is etched away leaving the isolated mesa structure. Then the Ohmic contacts are patterned in photoresist, the native oxide on the n-GaAs mesa from exposure to atmosphere is thinned by dipping in diluted HCl, and AuGeNi alloy evaporated over the pattern. The photoresist is removed and the metal contacts are annealed to the GaAs at 450°C, forming an Ohmic interface by Ge diffusion into the GaAs crystal and Ga diffusion into the metal melt[19]. Schottky shunt contacts are photolithographically patterned, the surface oxide is thinned by submersion in HCl, Ti is deposited followed by Au, and the photoresist removed. From this point forward the sensors are never heated to more than 150-200C. The Schottky Ti-GaAs shunt interface is intended to be abrupt and to minimize interfacial diffusion, exposure to heat is restricted. Finally, once the metal and semiconductor structures are complete, an insulating layer is deposited over the entire sensor, typically SiO_2, Si_3N_4, or Al_2O_3. The insulator is photolithographically patterned and then etched to expose the metal pads for external electrical contact. Figure 3.3 is a diagram of the photolithographic patterning steps.

As in Figure 3.3.1, first the wafer is attached to a chuck by vacuum. Photoresist is applied to the top surface and then the chuck rotates at several thousand revolutions per minute. When a viscous liquid is spun on a flat surface, the central region will reach a uniform thickness dependent on the viscosity of the fluid, while the edges will be thicker because of surface tension

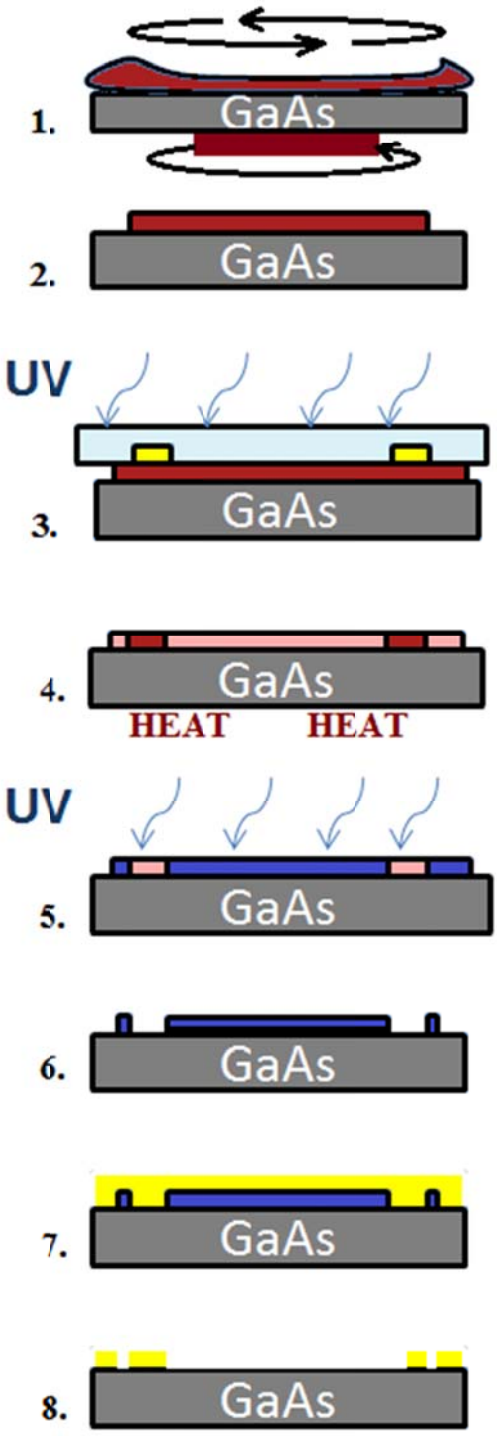

Figure 3.3 The photolithographic fabrications steps to form macroscopic integrated circuit devices such as EEC and EOC sensors. The unexposed photoresist is dark red (1-4), the vacuum chuck is brown (1), the glass of the photo-mask is light blue and the photo-mask chrome pattern is gold (3), the UV-exposed resist is light pink (4-5), the UV-exposed and heated resist is blue (5-7), and the metal evaporated layer is yellow (7-8)

The color of the film indicates thickness and the edges will be darker in color than the central film.

If the thick sections are left around the edge, it will be impossible for the flat photo-mask to make contact with every point on the surface of the resist. If the glass and chrome patterns on the photo-mask are at different distances from the surface of the photoresist, then the shadow-image pattern in the resist will not be sharp. The thick edges can be removed with a solvent like acetone and a swab to achieve a uniform film as seen in Figure 3.3.2. Alternatively, the central, flat area can be covered, the edges exposed to UV and then the thick section will dissolve away in photoresist developer.

The glass and chrome photo-mask is lowered using micrometers until it applies a gentle pressure, contacting the surface of the resist as in Figure 3.3.3. Full contact is judged by evenly spaced Newton's rings as the pressure of the glass plate modulates the thickness of the photoresist film. Ultra violet light interacts with the resist at every location that is not blocked by the metal chrome pattern (yellow regions in Figure 3.3.3). Figure 3.4 is a photograph of a photo-mask with bright field and dark field patterns.

At this point in the process, the exposed resist could be washed in the developer to achieve "positive" photolithography. That is, everywhere that was exposed will be dissolved by the developer (pink in Figure 3.3.4) and the shapes that were blocked (identical to the chrome) will remain on the substrate (red in Figure 3.3.4). The process is referred to as "positive" because the shape of the unexposed resist remaining on the substrate after development is identical to the shape of the chrome.

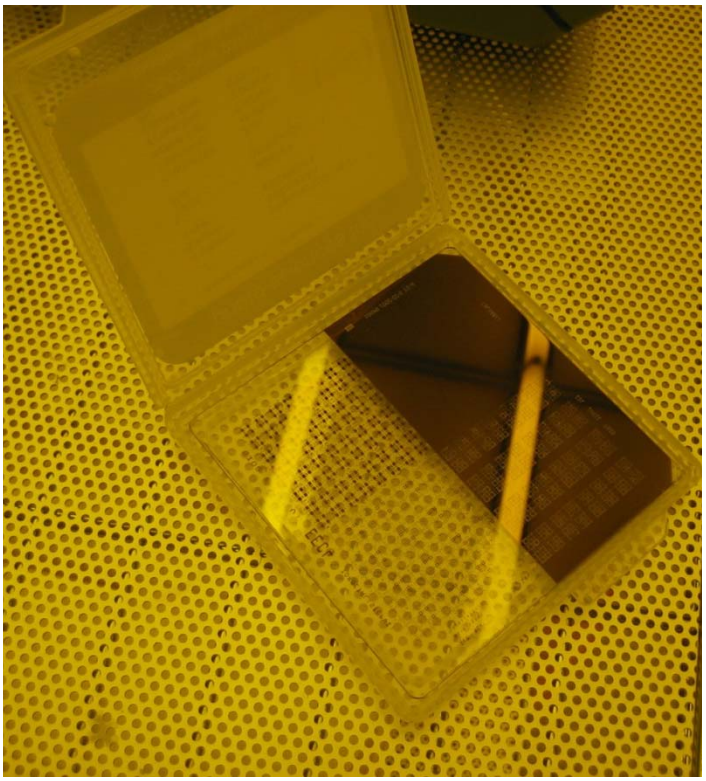

Figure 3.4 Glass photo-mask in plastic protective case. The left hand of the mask is "bright field" chrome patterning (clear background, chrome pattern) and the right hand of the mask is "dark field" chrome patterning (chrome background, clear pattern)

Alternatively, the exposed resist can be further processed to achieve "negative" photolithography. The UV light exposure ionizes active groups in the photoresist polymer changing the acidity and the propensity to dissolve in the basic (as in non-acidic) developer. When heat is applied to the exposed resist in Figure 3.3.4, the heat crosslinks the ionized polymers by overcoming the activation energy for binding. The heat does not crosslink the photoresist that was not exposed and ionized. The entire wafer is then flood exposed with ultraviolet light and no mask as in Figure 3.3.5. The cross-linked regions are left intact and the regions that were chrome covered are now ionized. Thus, the regions that were covered by chrome will dissolve away in the photoresist developer, indicated in Figure 3.3.6. The process is

termed “negative” photolithography, or “image reversal”, since after development the cross-linked resist remains in the inverse image of the chrome pattern.

Once the photoresist pattern is formed, the process divides into etching (of semiconductor and insulators) or evaporation patterning (of metals). For instance, a wet chemistry method is used to etch the GaAs mesa structure. The patterned substrate is submerged in a chemical bath of 20: 1 volume ratio of citric acid:30% hydrogen peroxide.

When patterning metal contacts, the wafer surface is typically cleaned with a hydrochloric acid solution immediately before being mounted in the evaporation chamber. As mentioned before, this removes any “native oxide” on the semiconductor produced from exposure to atmospheric oxygen. The substrate and the metal source are separated by some distance in a vacuum chamber so that no gas atoms will contaminate the composition of the growing metal film, as in Figure 3.3.7. The metal source may be evaporated by thermal evaporation (driving a high current, ~150A, through low melting point source metal sitting in a high melting point boat until the source melts) or by electron beam evaporation (high energy electron beam impacting a crucible full of source metal).

Undesired regions of the metal layer are removed by soaking the wafer in a solvent such as warmed acetone which dissolves the cross-linked photoresist. Only regions where the metal made contact with the wafer substrate rather than the photoresist will remain. This process is named “lift-off” and the result is demonstrated in Figure 3.3.8.

Section 3.1.2.2 Photoresist Profile and Metal Lift-Off

Metal evaporation is typically paired with the image reversal patterning process. This is due to the fact that the chrome of the mask casts a shadow in the photoresist. The photoresist at the edge will be exposed a varying amount. This changes the photoresist cross-sectional profile

to be trapezoidal. In positive patterning the contact angle with respect to the substrate plane is obtuse (Figure 3.5(b)) while in negative patterning the contact angle is acute (Figure 3.5(c)). Upon metal deposition, a continuous layer is often deposited on the positive pattern without breaks or defects at the patterned edge. If the acetone is not able to access the cross-linked resist, the resist cannot be dissolved. However, if an inverted profile is used, there is a high probability that there will be a gap in the metal deposition in the region of the pattern edge where an overhang is present. Metal liftoff is swift and effective as acetone can easily access the breaks. This is particularly critical for patterning delicate wires or alignment marks which can be less than 2 μm in width.

Figure 3.5 Profiles of positive and negative photoresist patterning. Black is the metal chrome pattern, red is unexposed photoresist, pink is exposed resist and yellow is deposited gold film.

Consideration of resist profile for metal liftoff is more critical for electron beam lithography when the feature sizes such as wire traces can be far smaller, on the order of 10 nm. In electron beam lithography, beam spreading from electrons scattering in the resist causes overhangs in positive resists.

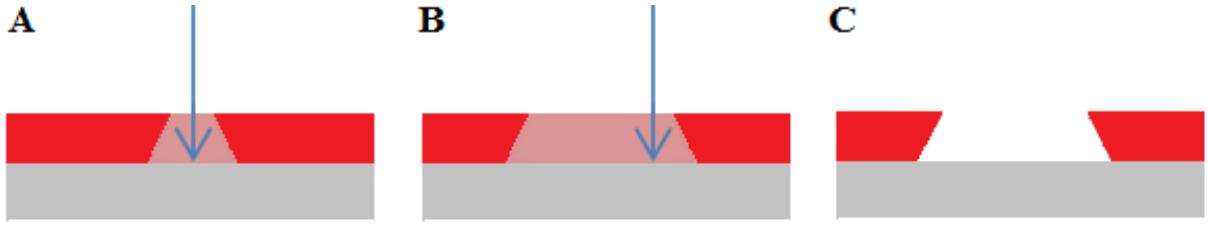

Figure 3.6 (a) Beginning of exposure with e- beam spreading (b) Exposure complete (c) Developed positive resist. R**ed is unexposed photoresist, pink is exposed resist**, **and** grey is the substrate.

Section 3.1.2.2 Insulator Deposition

Two common methods of depositing insulators are plasma enhanced chemical vapor deposition (PECVD) and atomic layer deposition (ALD). Silicon dioxide and silicon nitride are typically deposited by PECVD and aluminum oxide lends itself well to ALD. PECVD mixes the component gasses in a vacuum chamber and creates plasma in the gases. The hot gases condense on the cooler sample below the plasma cloud. Two primary strengths of PECVD are significantly faster growth rates of films from the high energy of plasma reactions and control over stress and compression in a film by adjusting the applied power and frequency of the plasma. The drawbacks are high velocity ion bombardment (which may cause ion implantation and lattice damage) and potentially higher sample temperature (which could anneal and drive diffusion). The high growth rate can also be a drawback since this makes thin films of 20 nm thickness or less difficult to manufacture reliably and this will hinder development of smaller scale sensor.

Atomic layer deposition on the other hand is a discrete process. The vacuum chamber is pumped down to a moderate vacuum and heated moderately (~150^{o} C). ALD can be done either thermally, as with our sensors, or by ALD plasma. Thermal ALDs such as the Cambridge Nanotech "Savannah" controls a single species of gas to flow through the chamber, wait, remove, and then flow the companion species of gas, wait, and remove for the completion of a single cycle. The waiting period has been determined by the diffusion limiting surface reactions. For instance, in aluminum oxide growth, the aluminum precursor is released, it reacts with any native oxide on the surface of the semiconductor until the surface is saturated, the aluminum precursor is removed, and the oxide precursor is introduced. The two reactants never exist in the chamber at the same moment, thus the description of the process as "discrete." ALD films are extremely slow growing (Savannah rate ≈ 2 atomic layers pre minute), making them impractical for

commercial fabrication that does not require precise thickness control. However, they are perfectly suited to applications that require highly precise thickness control of nm-scale films. In addition, the film is amorphous and conforms excellently to any aspect ratio of sensor structures.

Section 3.2 Structure and Function of EXX Sensors

Section 3.2.1 Shunt: Ohmic or Schottky Interface

Both Ohmic and Schottky interfaces have been utilized for EXX sensor shunts. Of these, EEC sensors were the first sensors to be fabricated with a Schottky interface. As was outlined in Section 2.4.2, a Schottky interface will have a depletion region in the semiconductor the width of which can be modulated by an applied voltage or an external electric field. In the case of an EEC sensor, the mesa's conductivity will be highly sensitive to the depletion region and the density of carriers in the GaAs. For n-type GaAs, an Ohmic interface will behave similarly in sensitivity to a Schottky interface when the depletion region is eliminated through the application of a high forward bias. In addition to the Ohmic like mode, the rectifying contact can also deplete the semiconductor by application of negative biases. For this reason, the rectifying shunt is preferable to an Ohmic shunt in an EEC sensor. To characterize the Schottky interface of the EEC sensors, the sensors were fabricated with have an additional fifth lead that directly contacts the shunt metal. The rectifying current-voltage dependence of the interface was characterized by a straightforward two-terminal measurement. The high contacts on a current source (Keithley 6221) and nanovoltmeter (Keithley 2182a) were connected to the shunt while one of the Ohmic leads on the periphery of the mesa served as the common ground for the low contacts on the source and meter. A direct current was applied though two of the unused leads of the sensor and the resulting voltage recorded.

Although EOC sensors were originally designed with an Ohmic shunt, EOC sensors can also be designed with a Schottky interface of Ti-GaAs. These are discussed in chapters 4-6. If the optical behavior of the interface is measured in the configuration described above, it is identical in most respects to a traditional photodiode.

Section 3.2.2 Conductivity of EXX

EXX sensor performance was characterized by four terminal resistance measurements of the conductivity of the metal semiconductor heterostructure. The four terminal (or four point) method has the important advantage that it eliminates contact resistance from the measurement. By separating the current sourcing and voltage sensing loops, the high internal resistance voltmeter will have theoretically zero current flow in its loop. The only induced voltage drop will occur at the small section of heterostructure that has the source forcing current through it. This allows for specific and sensitive monitoring of the heterostructure's resistance which becomes particularly critical when EXX sensors are shrunk to the nanoscale. As the critical dimensions and cross sections of the four leads used to make the measurement are reduced, the current density increases dramatically. The interface and spreading resistance of the contacts can entirely dominate two terminal measurements.

The conductivity of van der Pauw[20] disk sensors has been well developed analytically in previous work in the group[5] and is summarized briefly here since the same geometry of sensor is discussed in chapters 5 and 6.

The semiconductor has a total thickness of t. The metal is assumed to deplete all charges in the region below it. This creates a cylindrical depletion region that has width, W (pink in Figure 3.7 (a)). The cylindrical GaAs consists of two components: first base cylinder (thickness

= t-W) and second an annular layer formed from semiconductor with a concentric depletion region (thickness = W). Then, the apparent resistivity is calculated by Wang, et al. (2008) to be

$$\rho_{app}(\alpha,\gamma) = \frac{1}{\sigma ln2}\sum_{n=1}^{\infty}\left[\frac{2(1-\gamma\alpha^{2n})}{1+\gamma\alpha^{2n}} - \frac{1-\gamma\alpha^{4n}}{1+\gamma\alpha^{4n}}\right]\frac{(-1)^{n+1}}{n} \quad 3.1.$$

where $\alpha = r_{shunt}/r_{mesa}$, the ratio of the shunt radius to mesa radius(see Figure 3.6 (b)), and $\gamma = (\sigma_{GaAs}^2 - \sigma_{dep}^2)/(\sigma_{GaAs} + \sigma_{dep})^2$, depends on the conductivity of the n-GaAs, σ_{GaAs}, and the depletion region, σ_{dep}. Applying the same assumptions as in Section 2.4.1 that all the donors in the depletion region have in fact ionized, the conductivity of the region should be very low. This leads to $\gamma \approx 1$. The resistivity of the bottom cylinder is also given by equation 3.1 in the limit that $\alpha=0$. The van der Pauw resistance is related to the resistivity by

$$R = \frac{V_{23}}{I_{14}} = \frac{\rho_{app} ln2}{\pi T} \quad 3.2.$$

where T is the thickness of the object. The resistance of the two sections is then

$$R_{Bottom} = \frac{ln2}{\pi\sigma(t-W)} \quad 3.3.$$

$$R_{Top} = \frac{1}{\sigma\pi W}\sum_{n=1}^{\infty}\left[\frac{2(1-\alpha^{2n})}{1+\alpha^{2n}} - \frac{1-\alpha^{4n}}{1+\alpha^{4n}}\right]\frac{(-1)^{n+1}}{n} \quad 3.4.$$

where W is the width of the depletion region derived previously as

$$W = d_{n-metal} = \left[\frac{2\varepsilon\,(\varphi_B - V_{Applied})}{eN_D}\right]^{1/2} \quad 3.5.$$

Since the top and bottom can be modeled as two resistors in parallel, the total resistance can be calculated as $1/R_{total} = 1/R_{top} + 1/R_{bottom}$.

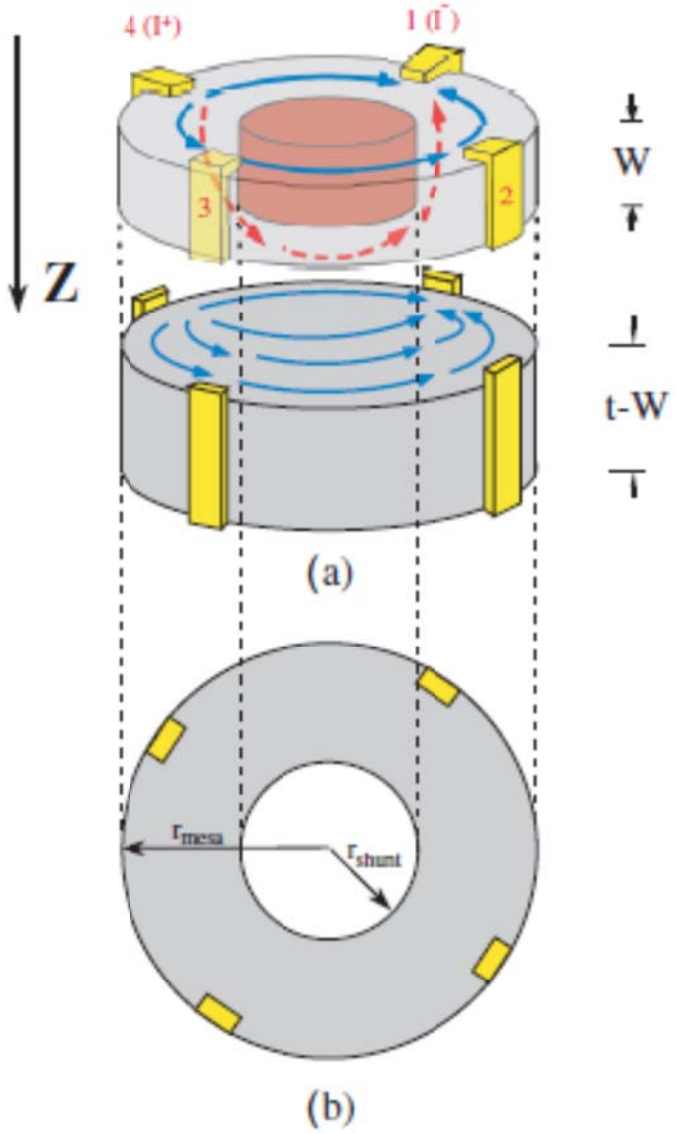

Figure 3.7 From Newaz et al. (2009) (a) Schematic of dual layer model for conductivity. Yellow are the contacts, grey is GaAs, pink is GaAs that has been depleted of carriers. (b) Labels of radii used to define fill factor, α.

These equations give an idea of the dependence of the resistance on the external electric field. However, the EEC sensors discussed for biochemical sensing applications in Chapter 7 are square. The change in geometry can be expected to alter the proportionality factors, but the functional dependence on voltage, electric field and depletion region may be expected to be similar. For the van der Pauw disk EOC sensors discussed in chapters 5 and 6, upon optical excitation an effective Schottky barrier may be defined that should follow the functions described above.

Chapter 4 A nano-scale Ti/GaAs metal-semiconductor hybrid sensor for room temperature light detection

Abstract

We report an individually addressable Ti/GaAs metal-semiconductor hybrid optical nano-sensor with positive photoresistance and a sensitivity that *increases* as the sensor dimensions shrink. The underlying physics relates to the crossover from ballistic to diffusive transport of the photoinduced carriers and the geometric enhancement of the effect associated with a Schottky-barrier-coupled parallel metal shunt layer. For a 250nm device under 633 nm illumination we observe a specific detectivity of $D^* = 5.06\times10^{11}$ cm$\sqrt{\text{Hz}}$/W with a dynamic response of 40 dB.

Section 4.1 Introduction

The ongoing effort to develop inexpensive optical sensors with high sensitivity and reduced size in the sub-micron regime is driven by the positive impact they would have on a number of disciplines ranging from medical instrumentation to consumer electronics.[21] While much progress has been made[22] and sensors as small as 100 nm have been reported,[23] structures with dimensions below 500 nm are typically incompatible with the fabrication methods that stimulate commercialization. In this letter we describe an individually addressable 250 nm positive photoresistance optical sensor that exhibits significant room temperature sensitivity in the visible spectral region and can be fabricated using conventional methods. Positive photoresistance (negative photoconductivity) has been observed in macroscopic semiconductor heterostructures [24] and nanoparticle films. [25] However, the nano-scale Ti/GaAs

metal/semiconductor hybrid structures (MSH) we describe here function via a fundamentally distinct principle; the photoinduced switching from ballistic[26] to diffusive transport of carriers. This results in a scale-dependent positive photoresistance (SDPP) that *increases with decreasing* dimensions. The photoresistive effect in an MSH, results from photocarrier-induced electrical current reallocation between the semiconductor and metal that changes the effective resistance.

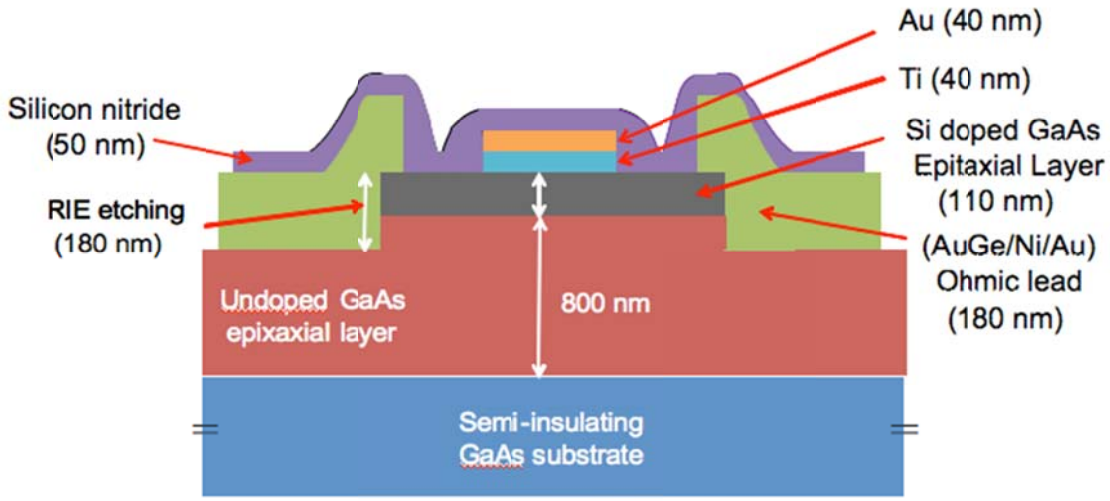

Figure 4.1 A cross-sectional view of the structure of the SDPP device.

Section 4.2 Device Description

The MSH structures we study, consist of a Au/Ti top surface layer that makes a Schottky contact to the underlying GaAs. We refer hereafter to the Au/Ti layer as the shunt (see below.) The details of the structure are shown in Fig. 4.1. Our devices were prepared on lattice-matched 90 nm thick Si-doped GaAs epitaxial layers (μ = 3225 $cm^2 V^{-1}S^{-1}$, N_D = 4 x 10^{17} cm^{-3})[27] grown by molecular beam epitaxy. All MSH we prepared had a fixed geometrical arrangement of the mesa, shunt, and metal leads but varied in scale/size from macroscopic (5 μm, 1 μm) to

nanoscopic (500 nm, 250 nm) as shown for the largest and smallest devices in the electron micrographs of Fig. 4.2. To directly ascertain the effect of the shunt, equivalent but shuntless reference devices were also studied. A minimum of 4 devices for each device size has been studied; all devices of a specific size show equivalent results. Details of the device fabrication procedures are described elsewhere[6].

Section 4.3 Optical Experimental Methods

All optical and transport measurements presented here were carried out at room temperature. Our devices employ a modified van der Pauw (VdP) mesa structure in which current is applied between leads 1 and 2 and voltage is measured between leads 3 and 4 [see Fig. 4.2(a)]. The 4-point resistance is defined as $R = V_{34}/I_{12}$. The spatial sensitivity of the SDPP devices has been measured by recording the lateral positional dependence of R (image plot) as an unfocused He-Ne laser beam (TEM_{00} mode, beam waist diameter 800 μm, output 5 mW, wavelength 632.8 nm) traverses the sensor area in steps, down to 10 μm.

The Ti/GaAs interface forms a well-characterized Schottky barrier while the Au/Ti layer acts as a shunt for current crossing the barrier (hence, the name).[6] Thus, in contrast to typical top-gated structures such as FET's, the shunt provides an important and intended current path. Moreover, even though the shunt is essentially opaque at 633 nm, illumination of the exposed GaAs mesa at that wavelength is sufficient to promote current flow through it as demonstrated

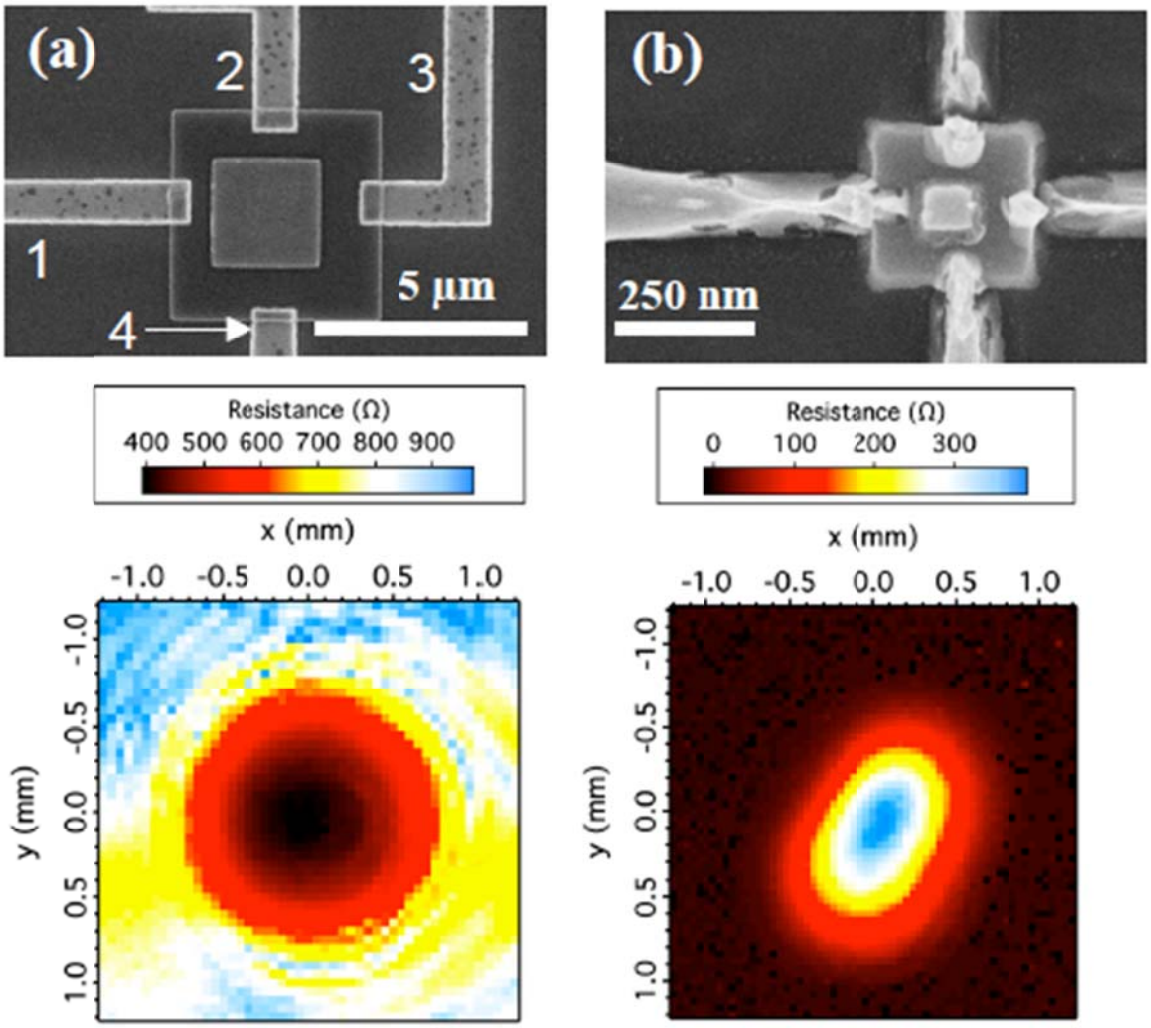

Figure 4.2 SEM images (top panel) and resistance image plots (bottom panel) of the 5 µm device (a) and 250 nm device (b). Panel (a) shows the contact labeling scheme. All image plots were acquired with an AC bias of peak current I_{34} = 100 nA.

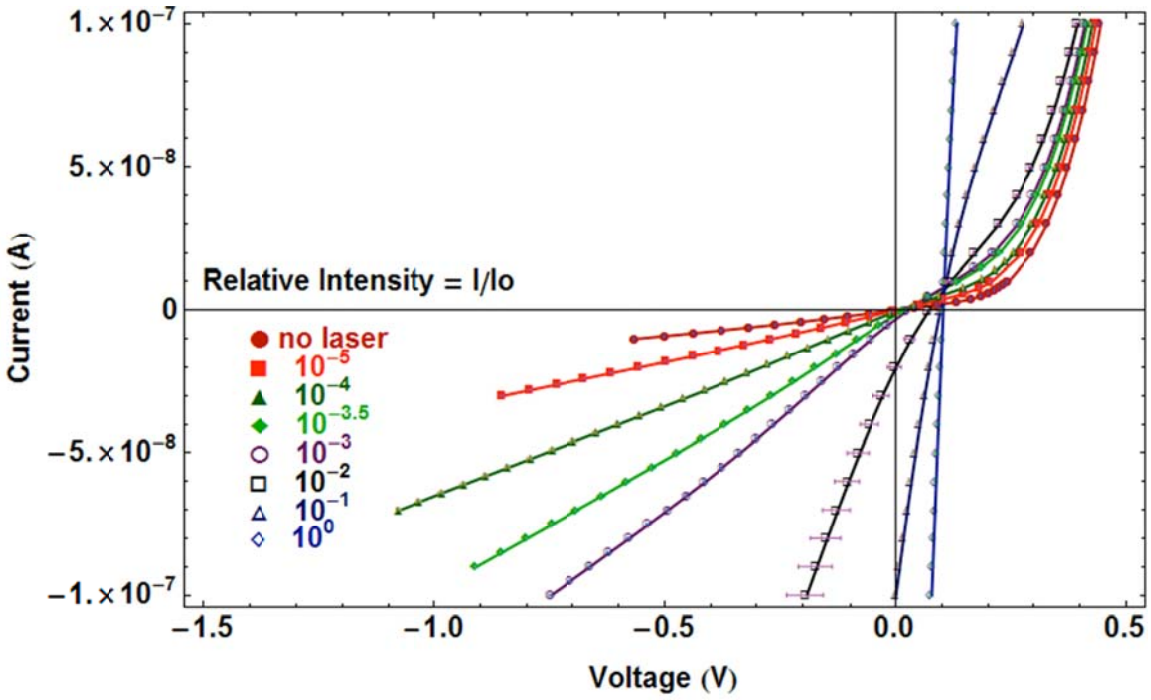

Figure 4.3 The intensity dependence of the 2-point I-V characteristic of the Schottky diode component of a 5 μm SDPP device (I_0 = 1W/cm^2).

by the direct I-V measurements shown in Fig. 4.3. The I-V characteristic changes from Schottky-like to Ohmic at high illumination. This is accompanied by a reduction in the zero bias resistance by a factor of 209 with an illumination intensity change of 10^{-5} I_0 to I_0, where I_0 is 1W/cm^2. The intensity-dependent open circuit voltage seen in Fig. 3 is characteristic of illuminated Schottky barriers[28] and in our case is no doubt caused by the migration of photogenerated carriers into the interface/depletion region.

A 2D image plot for the 5 μm device is shown in Fig. 4.2(a). The general features observed for the image plot of the 1 μm device are similar. The resistances of these devices are large when the laser spot is far from the device center (minimum illumination intensity) and smallest when the laser is approximately centered on the device (maximum illumination intensity). If we define the relative photoresistance as $\delta R(P,\lambda) = |[R(P) - R_0]/R_0|_\lambda$ x 100%

where R_0 is the dark resistance, P is the total power illuminating the active region, and λ is the wavelength then the maximum $\delta R(P,\lambda)$ values for the 5 μm (R_0 = 978 Ohm) and 1 μm (R_0 = 1301 Ohm) devices are both 58% for maximum illumination of P = 100 nW and P = 4 nW, respectively. The optical characteristics for the 500 nm (R_0 = 40 Ohm) and 250 nm (R_0 = 6.79 Ohm) devices are also similar to each other but, remarkably, opposite to those of the 5 μm and 1 μm devices as can be seen in Fig. 4.2(b). Here the resistance *increases* drastically with increased illumination. The different physical process now prevalent must overcome the reduction in the resistance originating from non-equilibrium carriers.

Carriers traversing the semiconductor exhibit diffusive transport with resistivity $\rho = 1/(n\mu e)$, determined by the concentration (n) and mobility (μ). The product $n\mu$ increases upon illumination[29]. thus, above band-gap illumination of 5 μm and 1 μm devices reduces their 4-point resistance as do the carriers traveling through the shunt. Given the opacity of the shunt, the observed response can be clearly distinguished from the lateral photovoltaic effect.[30] These negative photoresistive results are similar to the photo response of a macroscopic In/GaAs MSH structure with an Ohmic sidewall interface that has recently been reported.[31] In both cases the photo response is amplified by the geometry of the device and the current pathway provided by a metal shunt.

A comparative study of dynamic responses for different size devices with respect to light intensity is presented in Fig. 4.4. The response curves clearly demonstrate a wide dynamic range, as high as 40 dB, for our nano-scale devices. By considering the Gaussian beam profile, the opaque shunt and contacts, and the absorbance of the illuminated region of the doped GaAs epilayer we find $\delta R(P)$ values for the 500 nm and 250 nm devices of 965% (1.0 nW) and 9462% (0.25nW), respectively. The optical characteristics of the 500 nm control device are similar to

that of devices the 5 μm and 1 μm devices but the maximum $\delta R(P)$ is only 6% (2 nW). With a maximum power density of 1 W/cm^2 of 632.8 nm radiation and radiative recombination[32] the steady state photoinduced carrier density is $n_{ph} \approx 1.5\text{x}10^{16}$ cm^{-3}.[33] This alone accounts well for the 6% $\delta R(P)$ of the control device and emphasizes the enhancement of $\delta R(P)$ by the shunt.

Section 4.4 Results and Discussion

To interpret our results, we note that if the lateral geometry and placement of the shunt and leads is preserved, the measured $R(P)$ values should depend only on the steady state resistivity. If the same recombination process is prevalent in each device, n_{ph} is fixed and the devices would have approximately equal resistances at maximum illumination. As can be seen from Fig. 4, the values of $R(P)$ for all four devices are within a factor of 2 under maximum illumination and we conclude that all devices are diffusive in this limit.

The photo response in the submicron devices can be explained by considering quasi-ballistic carrier transport in addition to the diffusive transport.[34] When the relevant length scales of the conductor become comparable to the momentum mean free path of the carriers, λ_p, electrons can travel ballistically.[26,35] Here, the resistance is determined by the contact resistance and is sensitive to interactions with the boundaries.[36]

Transport measurements of the GaAs epitaxial layer of our devices[227] have determined that 18 nm $\leq \lambda_p \leq$ 35 nm for 2 K $\leq$ T $\leq$ 300 K. Because of the space constriction for the submicron devices and fabrication limitations the actual separation of the Ohmic leads and shunt (L) varies from 20 nm to 40 nm for the 500 nm device and 15 nm to 30 nm for the 250 nm device. Hence for these devices $L \sim \lambda_p$ and $L < \lambda_p$, respectively. Thus, in the dark, the majority of the carriers travel ballistically across the gap between injector contact and shunt. This

accounts for the (counter intuitive) small value of R_0 for the nanoscopic devices. The larger $\delta R(P)$ values of the 250 nm device relative to the 500 nm device can also be attributed to the

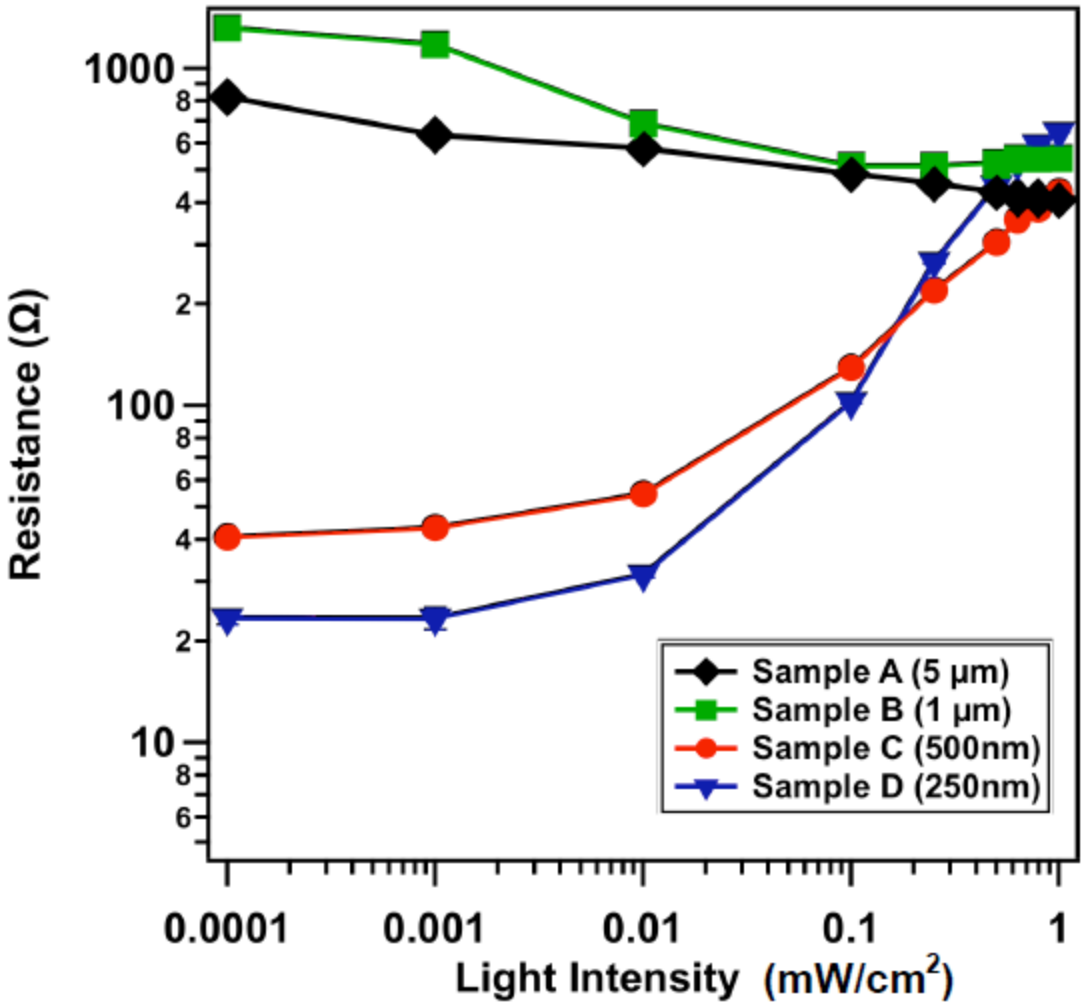

Figure 4.4 The dynamic responses of SDPP devices of different sizes to illumination by 632.8 nm radiation. Device size: ◆ - 5 μm, ■ - 1 μm, ● - 500 nm, ▼ - 250 nm.

ballistic and quasi-ballistic traversal of the carriers. For smaller separation between the lead and shunt a larger proportion of electrons travel ballistically; hence the response to illumination will be more acute for smaller gap devices. Presumably, the increase in $\delta R(P)$ with decreasing device size will ultimately be limited by boundary scattering.

Our explanation for the observed SDPP is summarized as follows: At low bias, the introduction of a sufficient density of photoinduced carriers gives rise to additional scattering (from photoionised traps or scattering centers) resulting in a transition from ballistic to diffusive transport and a corresponding increase in resistance.[37] If this increase in resistance is greater than the reduction due to the photoinduced carrier density (6%) and the influence of the shunt, a positive photoresistance will result. The exact mechanism for the conversion from ballistic to diffusive transport will depend on the specifics of the excitation and recombination mechanisms; however, the lower R_0 of the 500 nm and 250 nm devices supports the assertion that these are in the ballistic regime and the convergence of the resistance of all four devices within a factor of 2 under maximal illumination supports a size-independent final diffusive state.

To evaluate the sensitivity of SDPP sensors using a conventional figure of merit we have calculated the specific detectivity, $D^* = R_V\sqrt{A_D}/V_n$ at minimum illumination, where $R_V = \Delta V/\Delta P$ is the responsitivity, A_D is the active area of detection, V_n is the root-mean-square noise voltage per unit bandwidth, ΔP is the incident power on the active area, and ΔV is the corresponding voltage change.[38] For the 250 nm device, we find a resistance change of 16.7 Ohms for 2.5×10^{-14} W laser power after passing through a 40 dB ND filter. Since, the current through the device was 100 nA, $R_V = 6.68\times10^6$ V/W. In the Johnson noise limit, V_n can be replaced by the thermal noise voltage, $V_n = [4kTR_0]^{1/2}$ where k is Boltzman's constant.[39] For the 250 nm device, $D^* = 5.06\times10^{11}$ cm√Hz/W. This is competitive with the published D* values of much larger individually addressable photodetectors.[40,41] [The D* values for the 5 μm, 1 μm and 500 nm devices were 2.0, 1.0 and 3.3 x 10^{11} cm√Hz/W, respectively.]

This work is supported by the US NIH, the US NSF and the UK EPSRC. WJC was partially supported from the ERC for Advanced Bioseparation Technology, KOSEF, Korea. SAS

and SAW are cofounders of and have a financial interest in PixelEXX, Inc, a start-up company whose mission is to market imaging arrays. KDW and AKMN also have a financial interest in PixelEXX.

Chapter 5 Photon Induced Schottky Barrier Effects in Inverse Extraordinary Optoconductance Structures

Abstract. We expand upon our previous work and characterize the photo-dependence of the effective Schottky barrier in EOC and I-EOC heterostructures by measuring the open circuit voltage and the change in the reverse bias resistance. Under full illumination by a 5 mW, 632.8 nm HeNe laser, the barrier is effectively eliminated and the Ti-GaAs interface becomes Ohmic. The reverse bias resistance changes by a factor of 209 over an illumination intensity change of 10^{-5}:1. While this work illustrates the behavior of the Schottky interface upon illumination, it also demonstrates the effectiveness of the four-point, van der Pauw measurement fundamental to EOC/IEOC phenomena at monitoring changes in the active region of the mesa. The resistance is largely unaffected by the photovoltaic, DC offset of the surrounding leads, as indicated by the radial symmetry of 2-D resistance maps obtained by rastering the laser across EOC/IEOC devices.

Section 5.1 Introduction

To advance technology in areas such as single cell imaging, medical diagnostics, or consumer electronics, the device requirements are similar. They include inexpensive, nano-scale, VLSI-compatible, room temperature sensors. To meet these criteria, individually addressable optical sensors with critical dimensions as low as 250 nm were fabricated from metal semiconductor hybrid structures (MSH) of AuTi-GaAs Schottky interfaces. These interfaces show high sensitivity to external perturbations, such as illumination in the visible spectrum. Intriguingly, a transition occurs from resistance decreasing with intensity in micron-scale sensors (Extraordinary Optoconductance, EOC) to resistance increasing with intensity in the nano-scale

sensors (Inverse Extraordinary Optoconductance, I-EOC). This phenomenon has been attributed to an optically induced transition from ballistic to diffusive conduction and gives rise to resistance changes of up to 9462% in a 250nm device mesa.[42]

Here we discuss the dependence of the open circuit voltage (V_{oc}) on the shunt on the position of the laser location as an illustration of the diffusion of photo-generated carriers to the Schottky interface and depletion region. A comparative study of two EOC devices illustrates the photovoltaic effects from the leads on the semi-insulating GaAs substrate and from the leads contacting the Si-doped active region.

Section 5.2 Experiment

The fabrication process for the EOC device is discussed in detail elsewhere[6]. The generic device structure is shown in Fig 5.1. The GaAs mesa region is etched from a 100nm thick Si-doped epitaxial layer on an insulating GaAs substrate with a concentric AuTi shunt and four rapid annealed AuGe/Ni/Au Ohmic contacts, positioned equidistant around the circumference. A 5th lead, contacting the shunt, has been added to investigate the Schottky interface between the shunt and GaAs mesa.

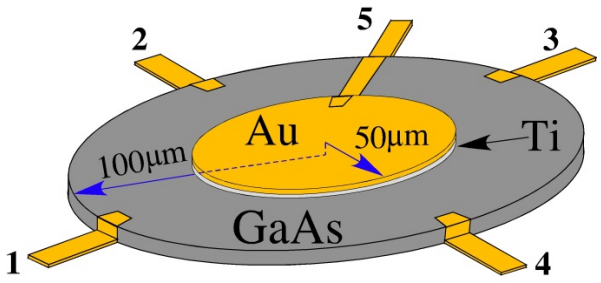

Figure 5.1 100 µm EOC device

The resistance of the EOC sensor (R_{4pt}) is determined using a four-point (Van der Pauw) measurement. A 1.3 Hz, 5 μA square wave is passed through pins 1 and 2 from a Keithley 6221 Current Source and the voltage across pins 3 and 4 was measured on a Keithley 2182A Nanovoltmeter. To study the Schottky barrier a two-point measurement was made between a contact to the shunt (pin 5) and a second grounding contact made through one of the four Ohmic leads. In one test, different Ohmic leads were used as ground on samples to test the effect of lead geometry. An Agilent 34925 MUX card allowed for sequential detection of R_{4pt} and Schottky barrier data on multiple sensors under illumination. We can then compare the response of several sensors while they were exposed to different local intensities from the Gaussian profile of the laser.

The unfocused, 5 mW, 632.8 nm HeNe laser was held stationary while the sample stage was moved by two crossed, computer controlled, linear actuators. The intensity of the beam (I) falling on the devices could be varied from its maximum value (I_0) by layering neutral density filters in the beam path.

Section 5.3 Results

Previous measurements on a 5 μm EOC sensor have verified that the effective Schottky barrier height is near zero at the full laser intensity and that the AuTi-GaAs interface is near Ohmic [shown in Fig. 5.2(a-b)]. We noticed at that time that the 5 μm sensor could be given a positive or negative offset at 0 nA (V_{oc}) depending upon the location of the laser, prompting a closer study of photo-voltage with 120 μm mesa devices. The offset V_{oc} is attributed to a steady state photo-voltage or static charge buildup in the sensor since the behavior of the reverse bias resistance is unaffected by the offset as can be seen in Fig. 5.2(c).

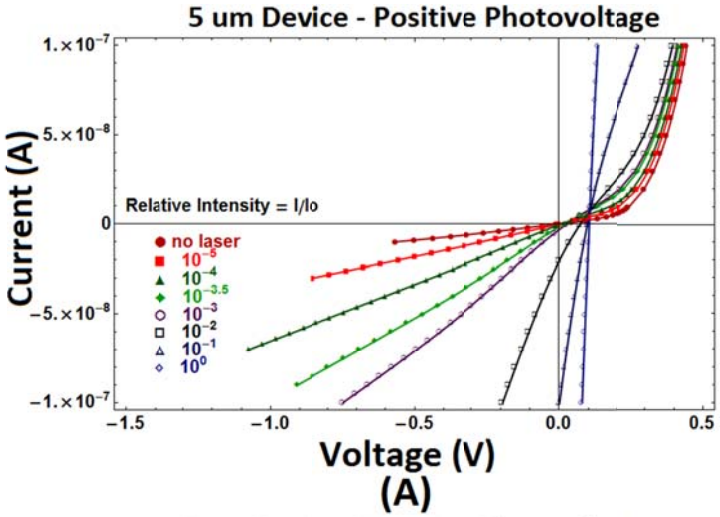

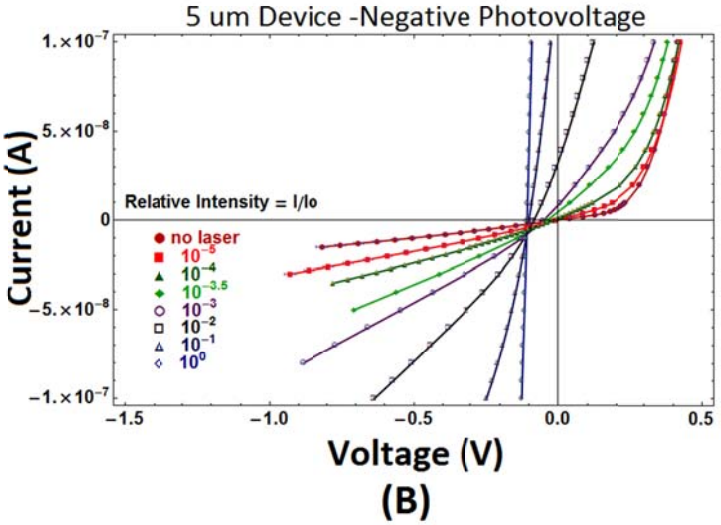

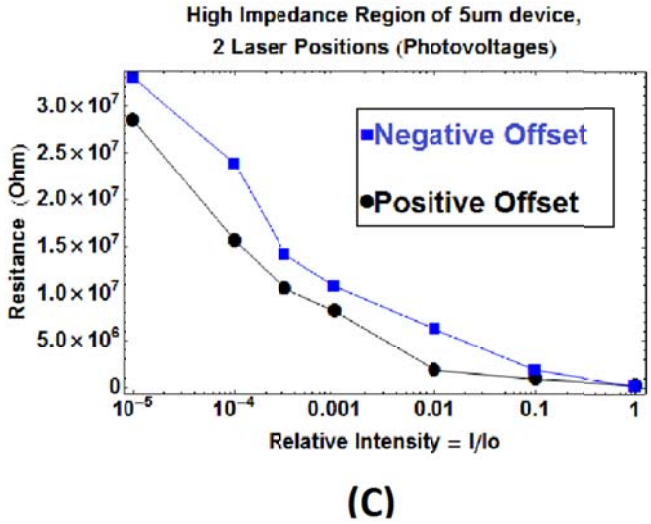

Figure 5.2 5 µm EOC sensor's Schottky barrier reduced by laser intensity a) positive photovoltage b) negative photovoltage c) similar reverse bias resistance for both positive and negative photovoltage offset

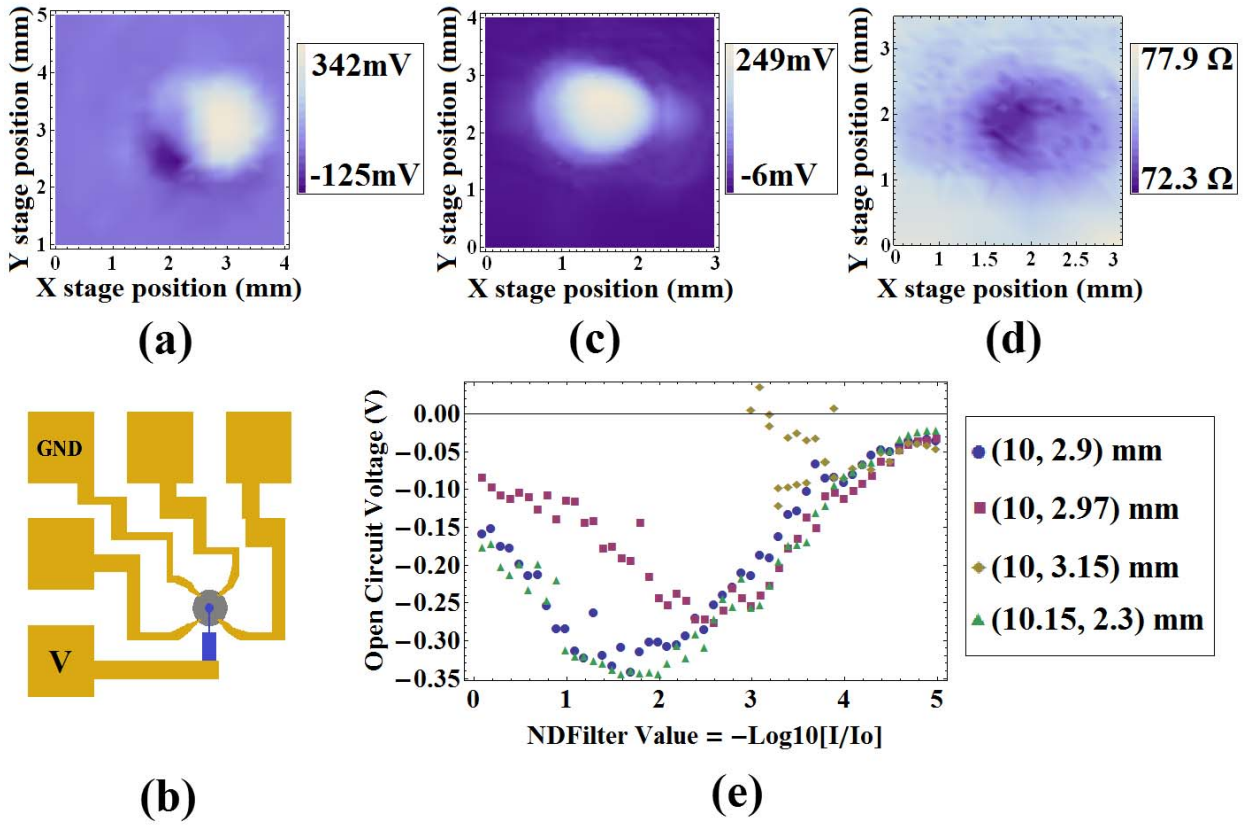

Figure 5.3 Laser rastering across 100 μm EOC sensors V_{oc} (x,y) map of the Schottky interface at I_0, without epoxy (a) and a schematic of sensor's electrical connection (b). (c) V_{oc} (x,y) with epoxy and (d) R_{4pt}(x,y) with epoxy. (e) Intensity dependence of V_{oc} at 4 laser locations.

To elucidate the influence of the Ohmic leads in contact with the mesa floor (insulating GaAs substrate) some devices were fabricated with an opaque epoxy covering the leads except in the nearby vicinity of the sensor while others left the leads unobstructed.

In Fig. 5.3 (a), the unobstructed sensor shows asymmetric features in the V_{oc}(x,y) map that are both positive and negative as compared to the baseline. It is also asymmetric following the locations of the shunt contact and the ground contact. In contrast, the V_{oc} (x,y) map for an epoxied sensor does not display the same asymmetry [see Fig 5.3(b)]. We therefore attribute the lobed features in Fig 5.3(a) to a photovoltaic effect at the leads. Fig. 5.3(c) shows the R_{4pt}(x,y)

map of the epoxied sensor which is symmetric and unaffected by steady state offsets. This behavior is typical for this style of EOC sensor and is present even without the opaque epoxy demonstrating that the four-point EOC measurement senses only the conductivity changes in the active mesa. Figure 5.3(d) shows V_{oc} versus intensity at various laser positions. Further investigation of this aspect will be conducted.

Acknowledgments

This work is supported by the by the US NSF under grant ECCS-0725538, and by the UK EPSRC under grant EP/F065922. SAS is a co-founder of and has a financial interest in PixelEXX a start-up company whose mission is to market imaging arrays.

Note for Thesis: For the benefit of Chapters 5 and 6, Figure 5.2 is an expansion of the figure published in Tran et al. (2012). Figure 5.2 inserted Figure 5.2 (b) where only parts (a) and (c) were included in the publication.

Chapter 6 Photon Induced Asymmetric Resistance Response in Extraordinary Optoconductance Structures

Section 6.1 Introduction

While studying the Schottky barrier behavior of inverse extraordinary optoconductance[42] (I-EOC) and extraordinary optoconductance (EOC) sensors, it was noted that the position of the Gaussian laser beam could induce a positive or negative voltage offset to the current-voltage characteristic curves across the Schottky interface of the sensors as demonstrated in Figure 5.2 (a) and (b). In brief, EOC and IEOC sensors are Ti-GaAs heterostructures constructed from an n-GaAs mesa with four Ohmic contacts evenly spaced around the periphery. Concentric to the mesa is a metal shunt of Ti and the Schottky interface is sandwiched between the two materials parallel to the plane of the sensor (see an example in Figure 5.1). The I-EOC effect (in which resistance is seen to *increase* with intensity) is observed in structures of dimensions less than a micron; sensors of mesa larger or equal to one micron are termed EOC (in which resistance *decreases* with intensity). Further study of the offset effect at the shunt and its impact on EOC measurements is carried out in this work.

Section 6.2 Experimental Methods

Section 6.2.1 Sensor geometry

The sensors studied in this work are 120 μm in diameter, round van der Pauw disks with a shunt metal of 40-70 μm diameter. It should be noted that although the majority of the fifth lead is Ohmic, the shunt and 200 μm tab extending from the shunt to the Ohmic fifth lead were patterned in a single photolithographic step. Therefore, there is a Ti-GaAs interface beneath the

tab as well as the concentric shunt as shown in Figure 6.1. Four sensors were fabricated that were nearly identical except for how they were connected to electrical sources an meters.

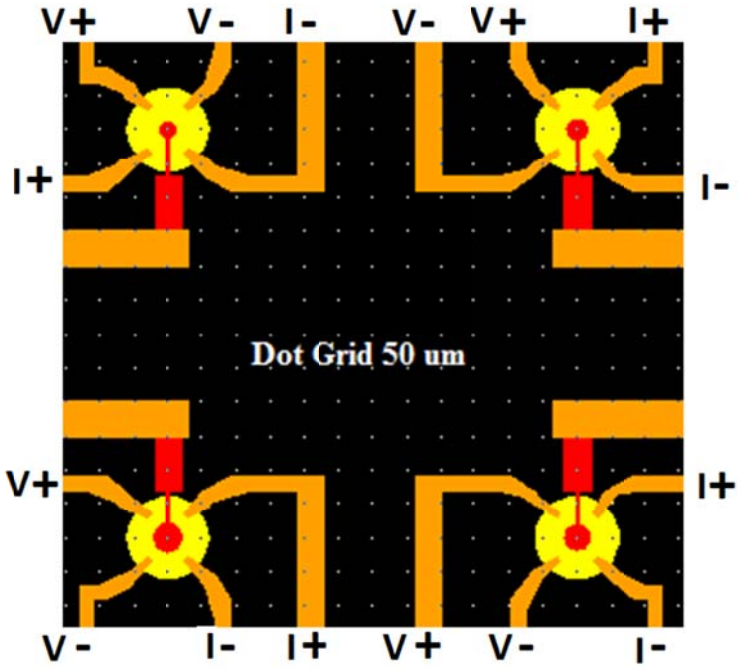

Figure 6.1 Schematic of the sensors and the active (+) and passive (-) contact configuration; red is Ti, yellow is n-GaAs, orange is Au/Ge/Ni, and black is insulating GaAs substrate

Section 6.2.2 Open circuit voltage and sensor resistance

Several parameters were monitored during this experiment. Using an Agilent 34925 MUX card, the four point resistance (R_{4pt}) of the Ti/GaAs heterostructure and a two terminal, open-circuit voltage (V_{oc} →I = 0 nA) across the shunt could be measured on multiple sensors in sequence for a single laser position. Using methods described in chapter 5, from the voltage at high and low polarity of the square wave, V_{high} and V_{low} respectively, two numbers were extracted: the resistance and the photo-induced voltage offset. In this report, we call the DC offset voltage calculated from the four point resistance measurement "V_{off}" to distinguish it from the two point measurement across the shunt, V_{oc}. This is a distinction in name only. Since the

same measured value of V_{off} could be collected separately from the four point configuration with the current source disconnected, it is accurate to think of V_{off} as an open circuit voltage of the Ohmic contacts.

$$R_{4pt} = \frac{V_{high} - V_{low}}{2\,I} \tag{6.1.}$$

$$V_{off} = \frac{V_{high} + V_{low}}{2} \tag{6.2.}$$

By utilizing the computer controlled Agilent switch mainframe, we can compare the R_{4pt} and V_{oc} response of multiple sensors while they were exposed to different local laser intensities from the Gaussian profile.

Section 6.2.3 Optical Apparatus

The laser was an unfocused 5 mW, 632.8 nm HeNe laser with beam waist 1.344±0.018 mm as measured by the razor edge method[43]. The laser was held stationary while the sample stage was moved by two crossed, computer controlled, linear actuators. The 2-D laser rastering maps in Figures 6.3 and 6.4 record the position of the two actuators on the map axes and the measured R_{4pt}, V_{off}, and V_{oc} values as the coloration of the data.

As an optical block, one set of sensors was covered with opaque, black epoxy on the Ohmic leads except in the near vicinity of the sensors, leaving ~ 100 μm or less of lead metal exposed around the mesa. A second set had no such epoxy layer identical to the I-EOC and EOC sensors in which the offset behavior was first noted. Figures 6.1 and 6.2 show the same four devices, but Figure 6.2 shows the approximate covered and exposed areas for each of the four sensors in Figure 6.1.

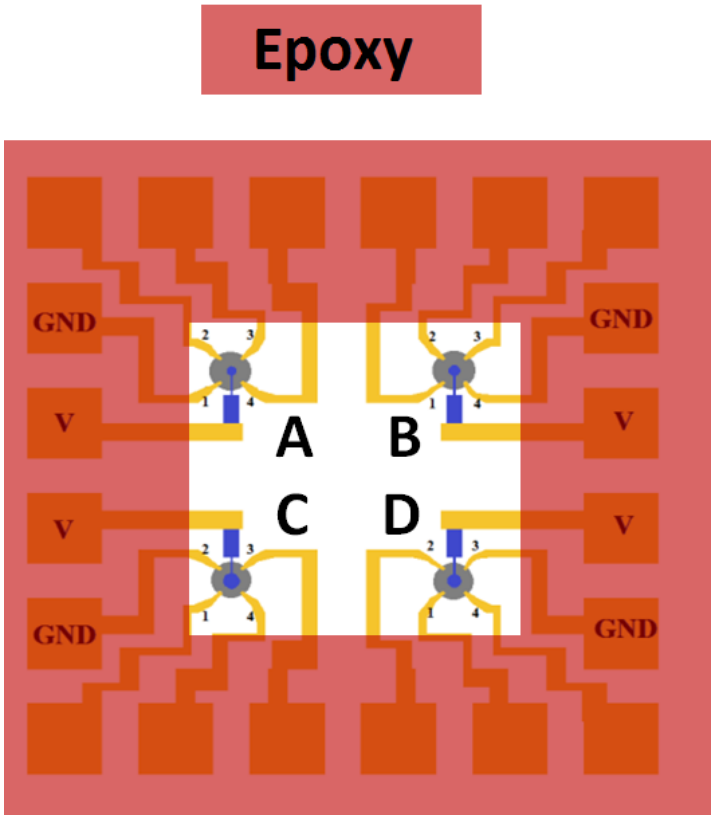

Figure 6.2 Schematic of epoxy covering the wires and identification of the epoxied sensors as "A," "B," "C," and "D"

Section 6.3 Results

Section 6.3.1 Gaussian response

Notice that the V_{oc} of the non-epoxied sensor plotted in Figure 6.3a shows a distinct bi-lobed response and amplitude O($\pm$100mV). The V_{oc} of epoxy-covered sensors shown in Figure 6.3 (b) shows a single-lobed Gaussian response for each of four sensors.

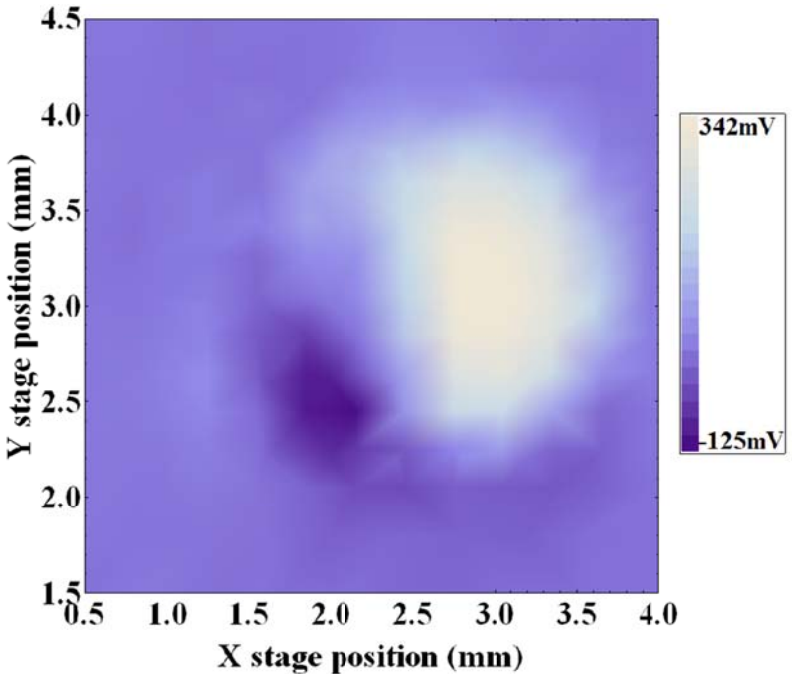

(A)

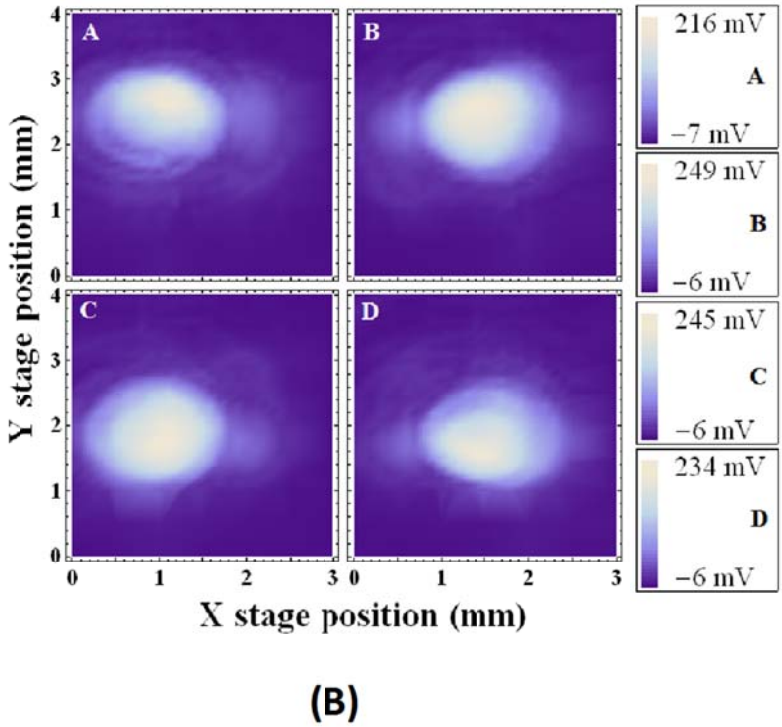

(B)

Figure 6.3 (A) bi-lobed response of open circuit voltage, no epoxy (B) four sensors' single lobed open circuit voltage measured sequentially, with epoxy. Sensor labels A-D correlate to sensor labels given in Figure 6.2.

The epoxy-covered sensors' V_{oc} data (Figure 6.3 (b)) were fitted to a Gaussian,

$$V_{oc}(x,y) = V_0 e^{-((x-x_0)^2+(y-y_0)^2)/2\sigma^2} \quad 6.3.$$

which resulted in a calculated beam waist of $2\sigma_{Voc}$ = 1.852± 0.158 mm. This calculated result is larger than the knife-edge, measured beam waist (1.344±0.018 mm) by approximately the diameter of the area of the exposed sensor and leads (2·100 μm + 120 μm). The four detectors were positioned in a square configuration of 0.6 mm on a side (see dot grid in Figure 6.1 for scale). The fitted location (x_o, y_o) for each detector was used to calculate the average distance between the sensors (0.575±0.123mm).

Fitting the epoxy-covered sensors' R_{4pt} data (Figure 6.4a) to

$$R_{4pt}(x,y) = R_0 e^{-((x-x_0)^2+(y-y_0)^2)/2\sigma^2} \quad 6.4.$$

yielded a calculated beam waist of $2\,\sigma_{4pt}$ = 3.0 ± 0.32 mm, or significantly larger than the two other methods. This could be attributed to a high EOC sensitivity to low-power intensity levels and saturation at high intensities which would overall widen the shape of the Gaussian R_{4pt} response.

Section 6.3.2 Asymmetric response and lead configuration

In Figures 6.4 (a) and 6.4 (b), compare the behavior of sensors A and B as opposed to sensors C and D, (see labels in Figure 6.2). The R_{4pt} Gaussian for sensors A and B have slight asymmetric regions that remain low valued and do not rise with the Gaussian beam profile. Sensors C and D have much higher symmetry in resistance with beam position. Comparing the V_{oc} of the Schottky interface

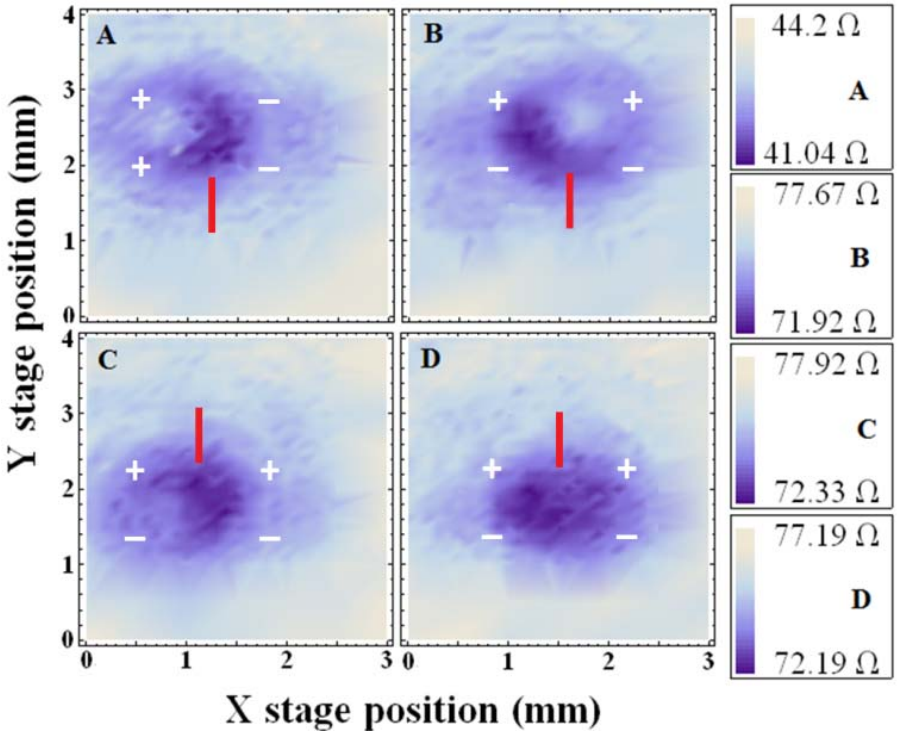

(A)

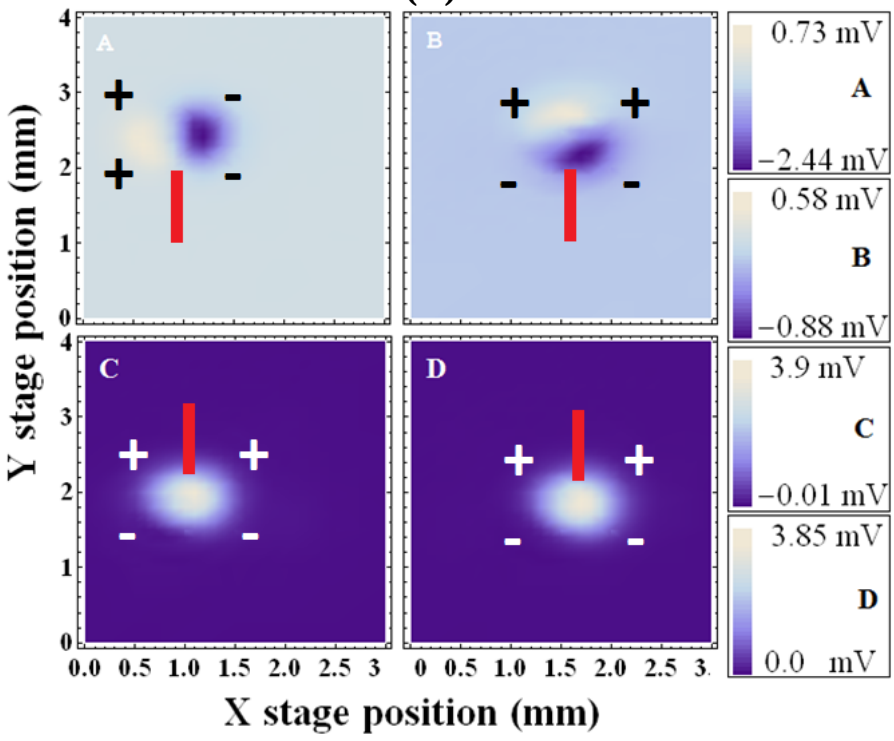

(B)

Figure 6.4 Red line indicates location of a shunt tab,+ indicates active leads, and – indicates ground (A) Laser rastering map: four terminal resistance response (B) Laser rastering map: DC voltage offset of resistance measurement, V_{off}

and V_{off}, the open circuit voltage of the Ohmic interfaces, V_{off} for sensors A and B shows a bi-lobed response similar to the V_{oc} Schottky behavior of the non-epoxy-covered sensor, though of significantly smaller magnitude. A second distinguishing feature is the equivalent size of the two V_{off} lobes, whereas the V_{oc} lobes are distinctly different in size.

Note that the four-point resistance leads were in different orientations with respect to the Ti tab (indicated as a red line overlaid on the data in Figure 6.4). In Figure 6.1, the leads are marked by (I+) for the active contact and (I-) for the grounding contact. The active lead of the current source is "actively" altered between positive and negative current polarization during generation of the square wave. The grounding contact remains grounded for both polarizations of current. The contact labels for the nanovoltmeter are active/reference (V+) and ground (V-). The asymmetries in R_{4pt} and V_{off} in Figure 6.4 correlate to the configurations in which the two active contacts are contiguous around the periphery of the mesa (as in sensors A and B). When the Ti tab and Schottky interface beneath it divide the active contacts, the photon induced responses are symmetric (as in sensors C and D); the same is not true for dividing the ground contacts (as in sensor B).

Section 6.4 Discussion

Section 6.4.1 Lateral photovoltaic effect at Ohmic contacts

The lateral photovoltaic effect[44] arises when an inhomogeneous illumination is incident on a p-n junction. While the transverse (across the junction) photovoltage is the basis for power generation from a photocell, the lateral (parallel to the junction plane) photovoltage was proposed as the basis for a new position-dependent photo detector. Figure 6.5(a) shows a characteristic response across the two Ohmic contacts of the position-sensitive, lateral photovoltaic sensor and Figure 6.5(b) depicts the lateral photovoltaic sensor's design.

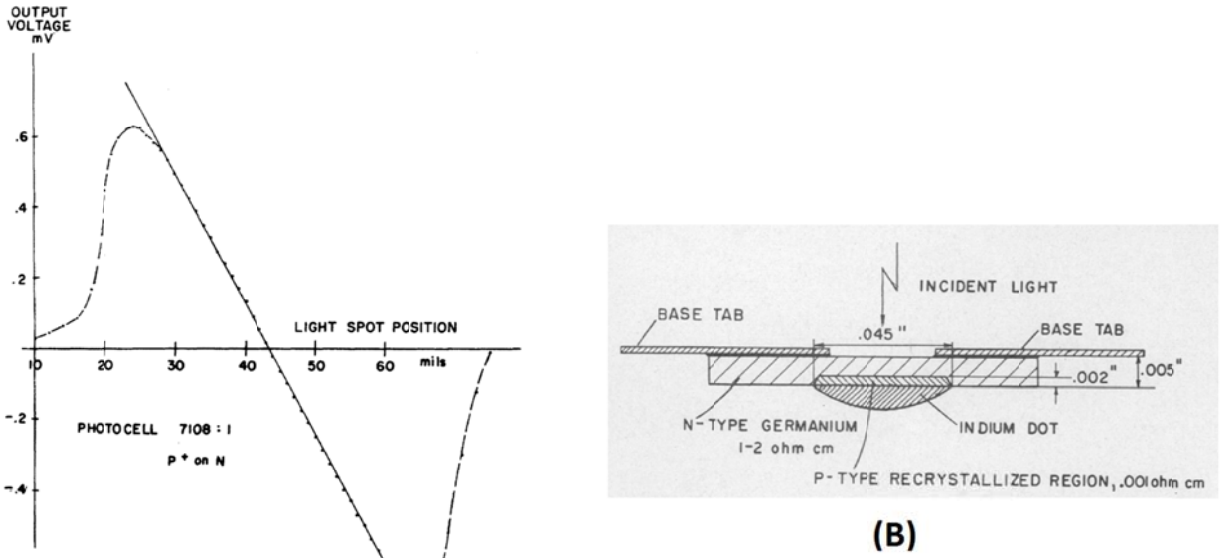

Fig. 15—Experimental response curve. Photocell p^+ on n.

(A)

(B)

Figure 6.5 (A) Plot of the lateral photovoltage induced by scanning illumination inhomogeneity between two Ohmic contacts of the p-n photo detector (B) Lateral photo detector, Schematic of the Germanium substrate, Indium Dot, two Ohmic contacts, and illumination point. From Reference [44]

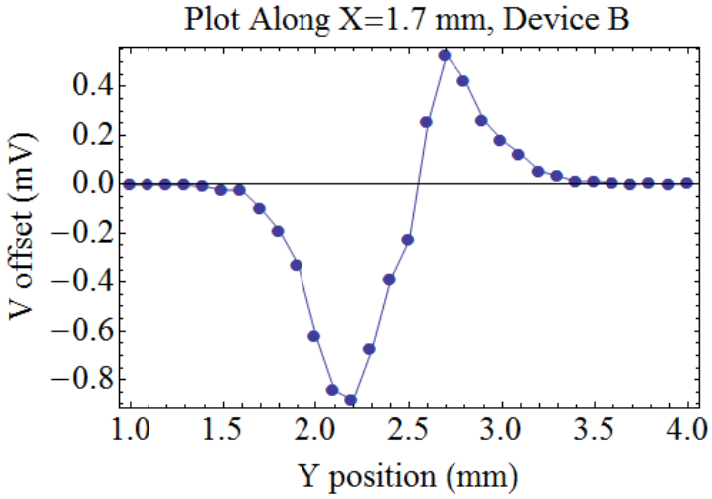

Figure 6.6 Plot of V_{off} data along line X = 1.7 mm for EOC sensor B in Figure 6.3 (d)

Figure 6.6 is a section of V_{off} data (across two of the Ohmic contacts) for epoxied detector B in Figure 6.2. Since the position axes have no intrinsic meaning, the fact that the two graphs 6.5(a) and 6.5(c) are mirror reflections is an artifact of the axes orientation. In magnitude of response and form, they are quite similar. It seems reasonable that the lobed response of the V_{off} is due to non-uniform illumination of the contacts and the GaAs. There are some differences – most obviously that the lateral photo detector is p-n junction based and illuminated through the Ge substrate. Electron-hole pairs are generated and separated along the entire interface and built-in electric field region of the p-n junction discussed in Section 2.4.1 of this thesis. The illumination of the EOC sensors is opposite, on the side of the metal that causes the rectifying junction to form. Although the metal is opaque to light and electron hole pairs can only be expected to be generated around the periphery of the metal mesa rather than along the entire interface, that does not seem to have significantly affected the functional shape of the position dependence.

The effect of the tab removing the bi-lobed lateral photovoltage and replacing it with a simple, positive Gaussian response is currently unexplained. It is possible that the depletion region underneath the tab diverts the photogenerated carriers in such a way that the symmetric Gaussian is the result.

Section 6.4.2 Lateral photovoltage at Schottky contacts

Although two terminal measurements (transverse to the rectifying interface) are not dealt with in Wallmark's lateral photovoltaic effect[44] publication, it seems plausible that a similar non-uniform illumination could cause a static charge distribution to form around the contacts on either side of the Ti-GaAs interface explaining the lobed V_{oc} of the exposed sensor. When the contacts are covered and access to the ground contact is blocked by epoxy, the shape of stable,

static charge distributions is altered as well to eliminate the negative lobe. Within a diffusion length of the edge of the opaque metal, electron-hole charge separation occurs due to the high internal field near the interface. Perhaps when epoxy is applied, perhaps there is not sufficient perimeter exposed for a detectable charge collection.

Section 6.4.3 Asymmetry and sensitivity of R_{4pt} and EOC measurements

Note that the tab introduces an asymmetry into the shape of the EOC sensor that is not present in the standard sensor with a concentric shunt. It is not surprising that this asymmetry in the heterostructure should in turn affect the symmetry of the response to illumination (sensors A and B). Such a response has not been noted previously in standard EOC sensors without a tab. However, it is interesting and deserves further attention to understand exactly what in the orientation of the contacts causes the asymmetry.

It should also be pointed out that the four point resistance response gave the largest calculated beam waist when fitted with the Gaussian profile of the laser beam. This demonstrates that the EOC four point resistance detection mechanism is particularly sensitive to low intensity illumination, more so than the lateral photovoltage of the Ohmic contacts (the beam waist of R_{4pt} = 3*beam waist of V_{off}).

Chapter 7 Extraordinary Electroconductance Sensors as Electrochemical Biosensors

Section 7.1 Expected Change in Electric Field Due to DNA Binding at Sensor Surface: A Calculation of Molecular Detection Lower Limit

It was evident that Extraordinary Electroconductance sensors had a potential application in the detection of bio-molecular concentrations in fluids for lab on a chip diagnostics. Before proceeding with electro chemical detection experiments, studies and modeling of the bio-molecular systems and sensors were performed to determine expected detection limits and viability of the application. Outlined in this section are the parameters for the model from the literature and some simplifying assumptions it employed. Since the primary goal was to establish a lower bound on detection and not to provide calibration of actual measurements, the assumptions may not be physically accurate. For example, when DNA binds to a surface, it can stand on end or lay parallel to the surface or some variation in between. Only the case of a singly connected, on-end DNA strand was considered since it is the limiting case of charges as far away as possible from the sensor while still being bound in place. Any other configuration will only increase the local field.

In previous work in the Solin group, under a system that utilized a parallel plate capacitor configuration to manipulate the electric field, a field resolution of 3.05 V/cm was reported[6]. While it is obvious that a point-like object does not apply a constant electric field on the face of the sensor as in the capacitor configuration, a point object that generates a field larger than 3.05 V/cm at every point on the face would be a reasonable lower limit to detection.

Section 7.1.1 Defining physical system parameters

Section 7.1.1.1 Charge on DNA in solution

The ionization state and molecular conformation of DNA is influenced by the environment that surrounds it. While the structure of DNA and the distribution of charge along the molecule, $\rho(\vec{r})$, can be determined by X-ray crystallographic methods, the DNA sample is typically prepared in a powder crystalline form and is not dissolved in solution. Therefore the distribution of ionized base pairs by loss of a hydrogen ion to the surrounding fluid media, also called deprotonation, is not directly measured by these means. For biological and in vitro experiments, therefore, it is critical to characterize DNA in a biologically relevant environment.

Keyser, et al.[45] use a combination of solid state nanopore technology with a laser optical trap to control DNA position and measure the charge of a double stranded DNA molecule in ionic solutions (potassium chloride) at a range of concentrations (0.02 M–1.0M KCl). DNA is attached to a micro-bead whose position can be manipulated by optical tweezers. A voltage is applied to drive the strand of DNA through the nanopore. The applied bias draws the negatively charged DNA through the pore, but the bead connected to DNA is in the optical trap allowing for position control and a balancing drag force. From the spatial deflection of the bead and the magnitude of measured conductivity change when DNA is blocking ionic flow through the pore, the group measured an average ionization of 0.5 $\pm$0.05 e^-/base pair assuming a base pair spacing of 0.34 nm. The maximum possible deprotonation given DNA's structure would be 2 e^-/base pair. This fractional charge is a result of the calculation and integral used in Keyser's model. A plausible physical origin of this result could be either a probabilistic picture of each base having a 50% chance of ionization which when integrated over the entire strand averages out to 0.5

$\pm$0.05 e^-/base pair. Alternatively, charge screening in the fluid could reduce the effective charge measured per base pair.

Section 7.1.1.2 Charge on Biotin/Streptavidin/Captavidin in solution

Extracted from chicken egg white, avidin is a tetrameric protein (built of four identical sub units). Each unit is made of a 128 amino acid chain with total molecular weight = 4 x 15 kDa. It can bind the vitamin biotin at four sites, one in each unit. Originally, the biotin-avidin binding pair was recognized for its high binding affinity and binding robustness to changes in pH of solution. Later captavidin, an avidin derivative, was developed by Invitrogen™ with similar mid-pH high affinity binding, but with the added feature that it will become unbound from biotin at pH 10. This is a less harsh chemical environment than that required by avidin to release from biotin. Thus a biotinylated surface could be exposed to multiple binding experiments with captavidin removed between each series while leaving the functionalized monolayers (discussed in Section 7.1.1.3) intact. Though the details of the protein modification are unavailable on account of proprietary nature of the product, the literature provided by Invitrogen™ states that "the tyrosine in the biotin-binding site is nitrated" and "all non-nitrated biotin-binding sites of the CaptAvidin biotin binding protein have been pre-blocked with free biotin so that these irreversible sites will not interact with biotinylated molecules"[46] to limit to a one-to-one binding ratio. Since the structure of avidin is well-documented[47] and the additions in captavidin appear to be minimal, avidin was substituted here in the calculation of electric field while captavidin was used in the actual experiments. Another useful avidin derivative is streptavidin, extracted from the actinobacterium Streptomycesa vidinh shown in Figure 7.1. Avidin and captavidin will tend to be positively charged at biological pH 7.4 whereas streptavidin will tend to be negatively charged, making the pair particularly useful for probing the EEC effects in biomolecular

detection. The experimentally determined ionization of avidin and streptavidin at biologically relevant pH is not reported in the literature; it appears to have never been measured experimentally to the author's knowledge.

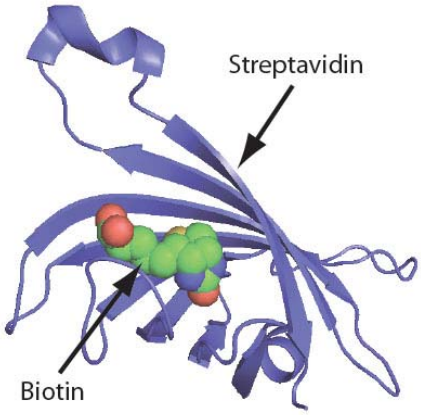

Figure 7.1 The above structure is a streptavidin monomer rather than the tetramer used in the experiments discussed later. The biotin section of probe (spheres) is bound to one of the four monomers in the target, streptavidin, (blue ribbon structure). Image from Integrated DNA Technologies© website.[48] Image is a recreation on modern molecular modeling software of the published work by Weber PC, Ohlendorf DH, et al (1989).[49]

Measurement of deprotonation is unreported in the literature but has been calculated theoretically by such programs as PROPKA[50,51,52,53] and APBS developed by Nathan Baker's research group. PROPKA is a finite element analysis package that can calculate the ionization state of a protein at a particular pH and solve the Poisson-Boltzmann equation to analyze the effect of electrolyte solutions on relevant energies and dipole moments in a protein. A brief development of electrolyte theory, Debye screening, and the Poisson-Boltzmann equation is presented in Section 7.1.4.

The crystal structure of avidin is designated as protein 1AVD in the world wide protein database (wwPDB) and the crystal structure of streptavidin is designated as protein 1STP. Utilizing the architecture provided by PROPKA, De Vico et al.[54] calculated the ionization state

and the net charge on avidin and streptavidin as a function of pH. The plot of charge versus pH from their publication is presented below (Figure 7.2) as well as the linear regression of pH 6.5-8.5 from the supplementary information (Figure 7.3). This linear fit allowed extrapolation of the charges at pH 7.4 as used in our experiments. The net charge of avidin at pH 7.4 is +16.5*e*; the net charge of streptavidin is -8.5*e*, where *e* is the fundamental electric charge, 1.6×10^{-19}C.

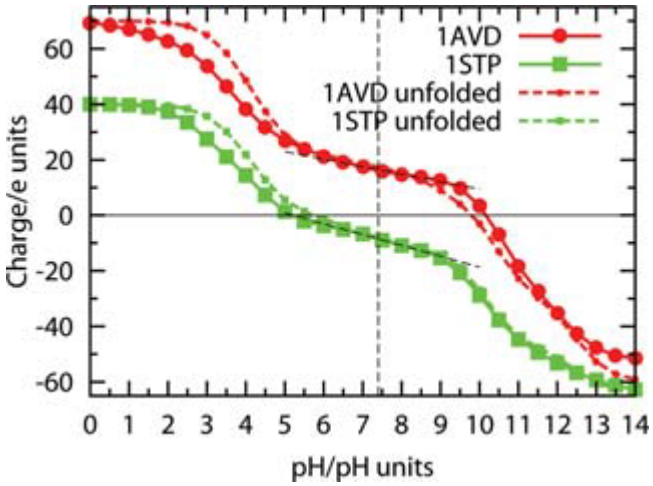

Figure 7.2 Functional dependence of charge on avidin and streptavidin on pH of surrounding solution[54]

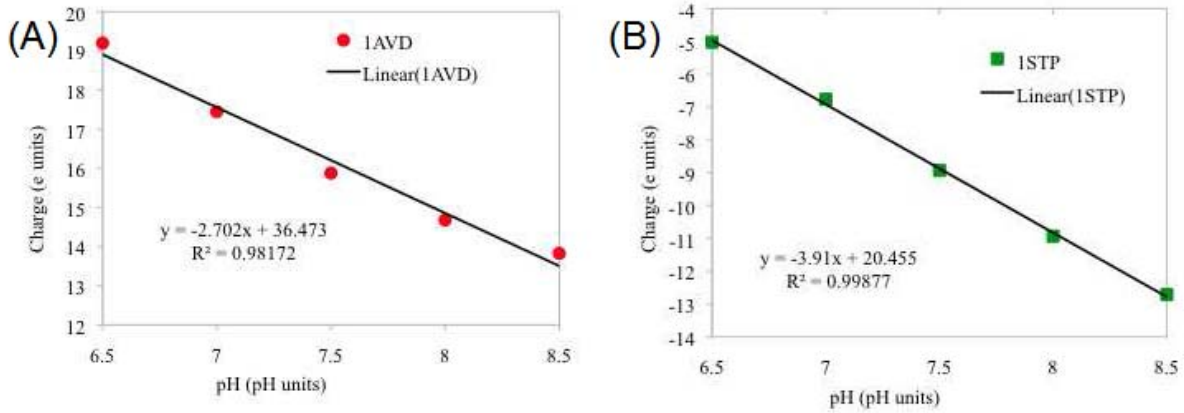

Figure 7.3 Linear regression of charge on (A) avidin and (B) streptavidin as a function of pH of salt solution.[55]

Section 7.1.1.3 Thickness of functionalization and binding site layer

In molecular binding experiments, the molecule fixed on the surface is termed the *probe*, while the molecule introduced in the sample is termed the *target*. There are a large number of well-established probe protocols for attachment to amine (NH_2) groups while the attachment to, for example, oxides is less well-developed. Therefore the process of functionalizing a surface such as aluminum oxide has minimally two components. First, a layer that terminates in NH_2 groups and second, the attachment of the probe layer.

In the first step, the average thickness of a silane layer on silicon dioxide was determined by ellipsometry and X-ray photoelectron spectroscopy in Dorvel, et al.[56] Using a vapor phase deposition method, the group deposited an even, self-assembling monolayer of 3-aminopropyldimethylethoxysilane (APDMS) which resulted in a monolayer 0.8 nm thick (Figure 7.4).

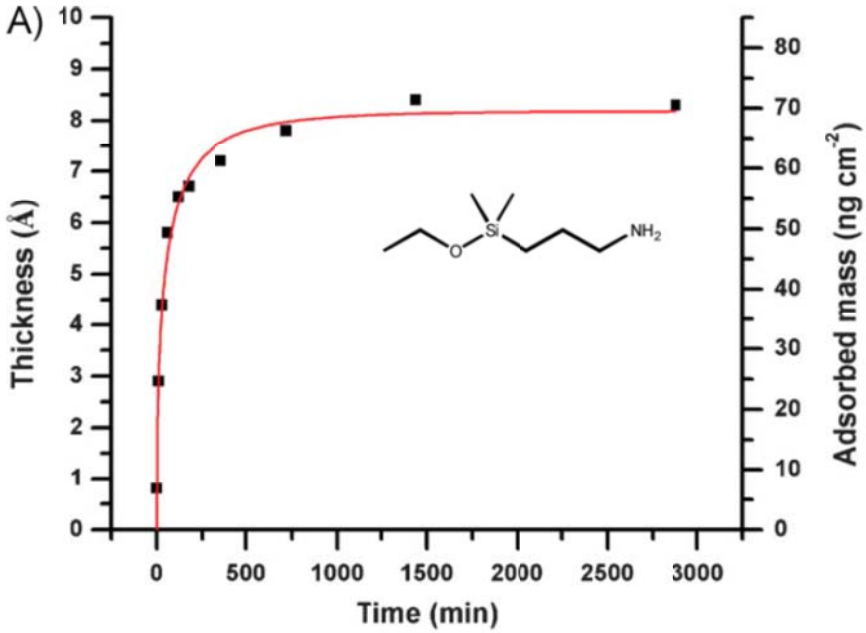

Figure 7.4 From reference [56], Dorvel et al. 2010. The thickness of the self-assembling monolayer and the amount of adsorbed mass is plotted versus vapor exposure time for APDMS. The red line is a fit to the diffusion limited Langmuir equation.

In the second step, the layer of probes is attached to the now densely packed NH_2 groups. Many probes are available for a given biological complex, but in a DNA hybridization experiment, a single strand of DNA that has been unzipped from the complimentary strand is utilized as a probe. Prior to the introduction of an amine-modified DNA probe, the surface is activated by a bath of, for instance, dimethylformamide (DMF), (chemical formula $(CH_3)_2NC(O)H$). The complimentary strand of DNA is then the target in solution and will bind to the single-stranded probe only if the sequences match or are a very near match, typically double base pair mismatch or less. In this case, since the activation molecule DMF is of the same size or smaller than the silane molecule, the total distance from the sensor surface of the tip of the target/probe strands upon binding is of the order of twice the thickness of the silane layer or about 1-2 nm. For such applications 20-40 base pair DNA strands are typical.

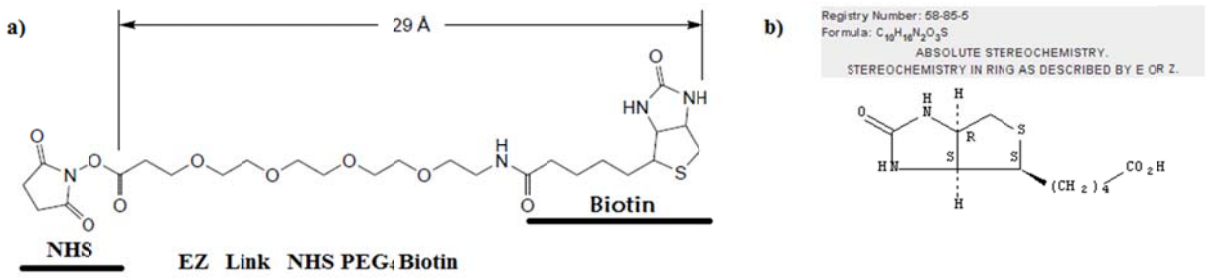

Figure 7.5 a) An example of biotin probe with variable spacer arm available from Thermo Scientific.[57] Figure from chemical information documentation. b) The chemical structure of biotin as defined and pictured by the CAS registry.[58]

If instead, the binding experiment is a protein-based study, such as the biotin-captavidin complex, the spacer shown in Figure 7.5 can be manufactured to be 1-5 nm long while the biotin molecule itself is approximately 1 nm. As shown in Figure 7.1, the biotin molecule is surrounded by the sheet of streptavidin monomer. This implies that the center of a bound captavidin or streptavidin tetramer could be at a distance 1.8-6.8 nm from the oxide surface, adding the silane

and the probe layer thicknesses. More detail on the binding mechanisms can be found in Section 7.2.2.

Section 7.1.1.4 Dielectric Constant for Water

Even for an intrinsically polar molecule, water has an extremely high static dielectric constant at room temperature at $\varepsilon_r \approx 78$. The exact microscopic origin of the high dielectric constant is still an active subject of debate with the most intuitive explanations based upon water's intrinsic electric dipole moment, the high occurrence of hydrogen bonding with local ordering even in the liquid state, and long-range electrostatic effects.[59]

Section 7.1.1.5 Sensor Spatial Dimensions

Since the previous EEC studies were performed in systems where the parallel plate capacitor, laterally constant electric field approximation could be used, this is not the case here. A point-like source with a laterally varying electric field is used instead. Thus it was critical to gauge the magnitude of the field across the entire face of the sensor. This calculation would answer whether the EEC sensors could be expected to detect single-molecule binding events or whether the lower detection threshold was some critical density of bound molecules.

Section 7.1.2 Simple Dielectric Fluid Model for 20, 40 base pair DNA

To estimate the detection limit of our sensors we will model the DNA strand as attached at one end to the functionalization layer deposited on the detector surface with the rest of the base pairs vertically stacked above it (see Figure 7.6). While the DNA strands will most likely fold over and not align perpendicular to the surface, assuming in our model that they are aligned perpendicular to the surface is the worst case scenario for detection. This is because the charge

will be farthest from the detector. Therefore our analysis provides the most conservative estimation on the theoretical detectability limit.

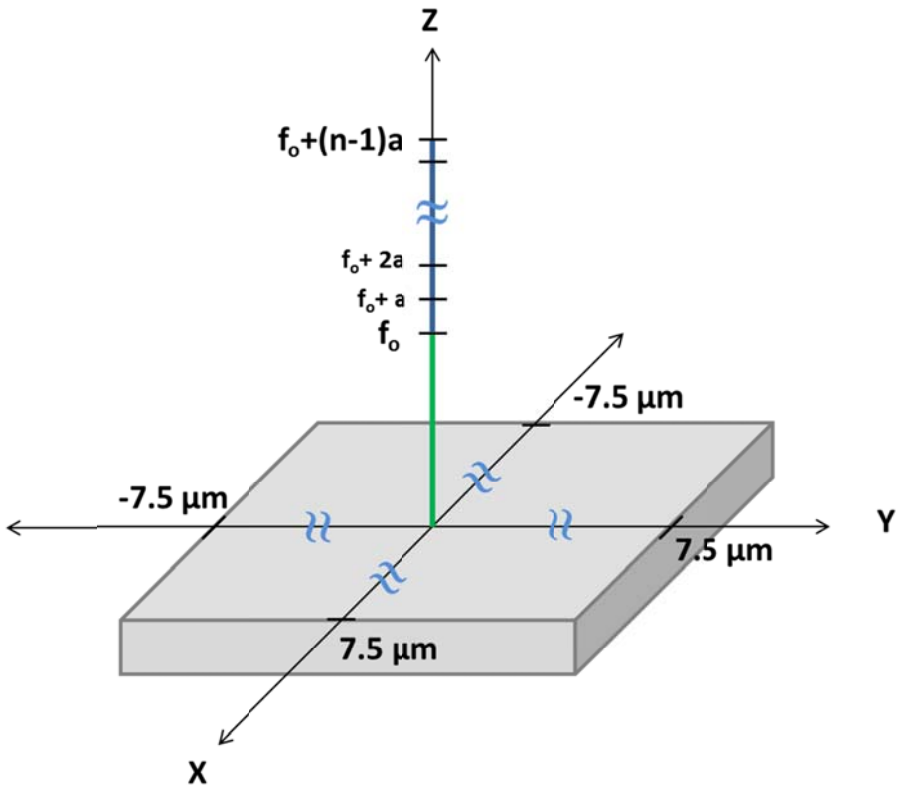

Figure 7.6 The schematic layout for the simple DNA model. The green section of the z-axis indicates the thickness of the functionalization layer, f_o. The tick marks on the z-axis indicate positions of discrete 0.5 e^- charges at each base pair location with spacing, a, for a total of n base pairs. The blue bar indicates the vertical extent of the continuous-charge, smeared distribution.

We consider two simple models for the charge distribution. The first is a straightforward discrete model of n individual 0.5 e^- charges with a base pair spacing of a = 0.34 nm. Obviously 0.5 e^- charges are not meaningful being a fraction of the elementary charge on an electron. Therefore, we modify this distribution by defining a linear charge distribution of density $\lambda = \frac{0.5 \cdot e \cdot n}{(n-1)\, a}$ along the z-axis. This linear distribution has the same net charge spread over the same vertical distance as the discrete model.

To simplify the model, we replaced any monolayers between the layers with dielectric water. A summary of the physical parameters and equations for the two models is presented in Equations 7.1-7.4 and table 7.1. Equations 7.1-7.4 describe the electric potential and the electric field in the sensor plane, that is, at z = 0. Again, see Figure 7.6 for the orientation of the axes.

Table 7.1 Simple DNA Dielectric Fluid Model Parameters

Parameter	**Description**	**Value**
a	DNA base pair spacing	0.34 nm
n	Number of base pairs	20 or 40
k	Coulomb's constant, vacuum	8.988 Nm^2/C^2
$\varepsilon_{r,water}$	Relative static dielectric constant, water	78
$q_{\ base\ pair}$	Charge per base pair	0.5 e = 0.801×10^{-19} C
f_o	Thickness of the functionalization layer	1-2 nm

$$\mathrm{V}_{discrete}(x,y,0) = \frac{k\ q_{base\ pair}}{\varepsilon_{r,water}} \sum_{d=0}^{n-1} \frac{1}{\sqrt{x^2+y^2+(ad+f_o)^2}} \tag{7.1.}$$

$$\vec{\mathrm{E}}_{discrete}(x,y,0) = \frac{k\ q_{base\ pair}}{\varepsilon_{r,water}} \sum_{d=0}^{n-1} \left(\frac{1}{x^2+y^2+(ad+f_o)^2}\right)^{3/2} \begin{Bmatrix} x \\ y \\ ad+f_o \end{Bmatrix} \tag{7.2.}$$

$$\mathrm{V}_{continuous}(x,y,0) = \frac{k}{\varepsilon_{r,water}} \frac{n\ q_{base\ pair}}{(n-1)\ a} \int_{f_o}^{f_o+(n-1)a} \frac{1}{\sqrt{x^2+y^2+z'^2}} dz' \tag{7.3.}$$

$$\vec{\mathrm{E}}_{continuous}(x,y,0) = \frac{k}{\varepsilon_{r,water}} \frac{n\ q_{base\ pair}}{(n-1)\ a} \int_{f_o}^{f_o+(n-1)a} \left(\frac{1}{\sqrt{x^2+y^2+z'^2}}\right)^3 \begin{Bmatrix} x \\ y \\ z' \end{Bmatrix} dz' \tag{7.4.}$$

Two sets of variable values were tested for a low field (at only 20 base pairs and 2 nm functionalization) and high field (at 40 base pairs and 1 nm functionalization). At the origin, the discrete and continuous 20 base pair models vary by 6.8 %, but as one would expect the far-field behaviors converge. The difference in the predicted field from the two models quickly disappears

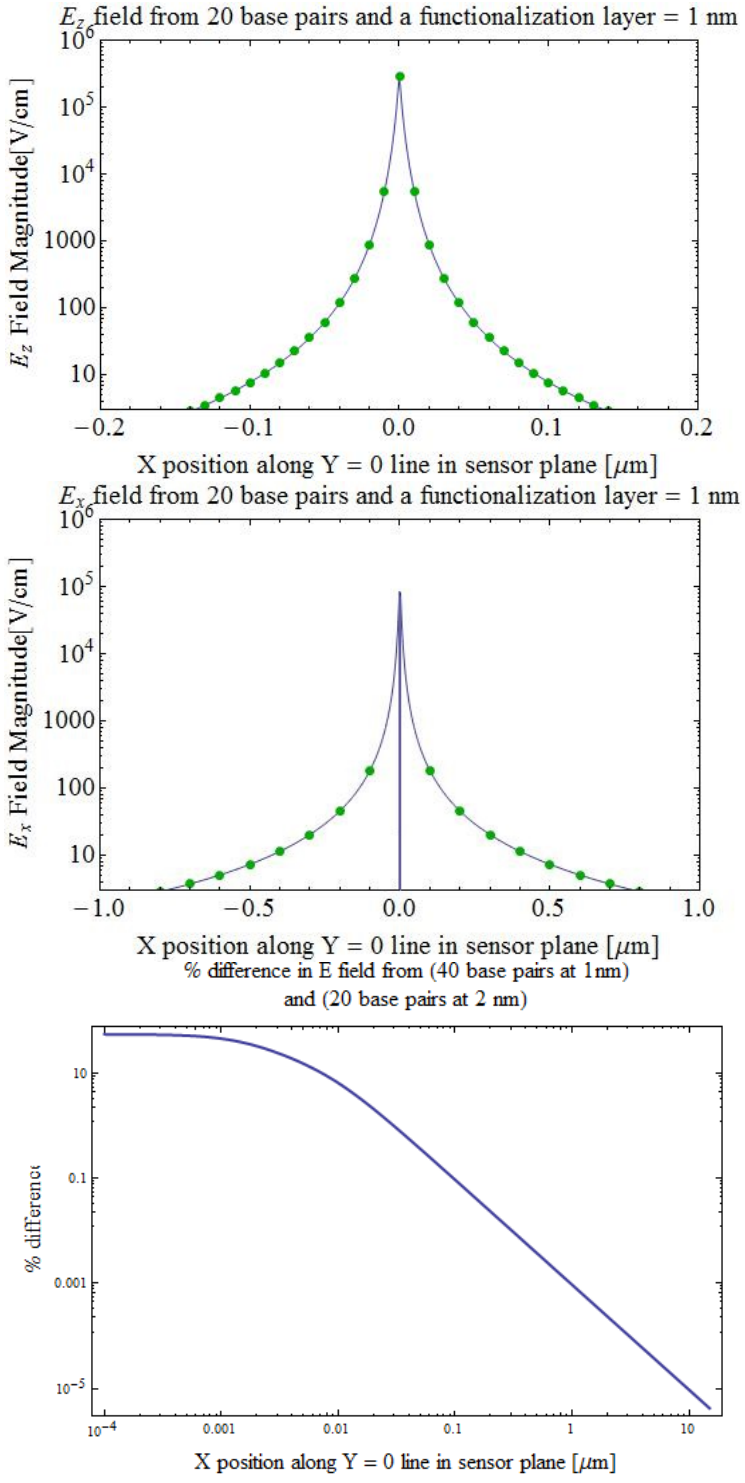

Figure 7.7 Sampled values of the discrete sphere model (green dots) and the smeared, continuous charge distribution model (blue line). (A) Electric field magnitude in Z direction and (B) X direction for n = 20 DNA base pairs attached to a functionalization layer 1 nm thick. In A and B, the lower bound of the E field axis is the detection limit of 3.05 V/cm (C) % difference between E field magnitude due to 40 base pairs at 1nm and 20 base pairs at 2nm

as you move along the face of the sensor, to 0.17% at (10 nm, 0 nm, 0 nm) and to 7.8×10^{-7} % at the sensor's edge (7.5 μm, 0 μm, 0 μm). The results for the discrete and continuous calculations are shown in Figures 7.7 (a) and 7.7 (b) for the magnitude of electric field in the Z and X directions. The x and z components are shown individually since the previous experiments only measured field sensitivity in the direction perpendicular to the sensor (z in this case). The lateral field sensitivity has not yet been established. For simplicity, the lower bound of Figures 7.7(a) and 7.7(b) is the detection limit in the z direction of 3.05 V/cm since the E_x limit is unknown. The E_x field magnitude is zero at the origin (where the field is in z only) and quickly increases in two symmetric lobes that are not resolved on the scale of the x-axis. The difference between the high-field and low-field continuous models is plotted in Figure 7.7 (c). For a 40 base pair strand, the addition of 20 base pairs stacked above the original 20 only changes the field by ~15% near the binding site. The order of magnitude behavior is very similar for all models. The difference between 20 and 40 base pairs is not highly significant at such close functionalization distances. If we establish detection of one DNA type, we can likely expect detection of the other.

Given the extremely high fields at the point of attachment for any of the above models, it is plausible that individual binding events could be detected even though the field falls below the nominal threshold of 3.05 V/cm at the sensor edge.

Section 7.1.3 Simple Dielectric Fluid Model for Biotin and Captavidin

The numerical values for the avidin and streptavidin models outlined in previous sections are shown in Table 7.2. The models are developed as order of magnitude calculations and like the simple DNA model in section 7.1.2, ignore the effects of the self-assembling monolayers or

the ionic fluid on the resulting electric field. In the interest of determining the absolute outer limit for detection, much larger functionalization layers were tested for field strength.

Table 7.2 Simple Protein Dielectric Fluid Model Parameters

Parameter	**Description**	**Value**
q_{avd}	Net charge avidin at pH 7.4	$+16.5e$ = 2.64 x 10^{-18}C
q_{stp}	Net charge streptavidin at pH 7.4	$-8.5e$ = -1.36 x 10^{-18}C
K	Coulomb's constant, vacuum	8.988 Nm^2/C^2
$\varepsilon_{r,water}$	Relative static dielectric constant, water	78
f_o	Thickness of the functionalization layer	1 nm-1.001μm

In the interest of space, only avidin is plotted, since streptavidin's result can be deduced by halving the magnitude of avidin. For both molecules, single binding events may be detectable at a binding height of ~1 nm and perhaps even up to 100 nm as is evident from the electric fields marked with Binding Height 0.001 μm and 0.101 μm in both Figures 7.8 and 7.9. Again, unless otherwise indicated, the lower bound on the electric field magnitude axis is the detection limit. Any field plotted in the figures would be detectable. However, multiple binding events would be necessary to compensate for the decrease in field if the functionalization layer were thicker than 100 nm. The effect is also relatively long range; the fields do not fall below the detection limit until O(1μm) away from the binding site, where O(1μm) is an abbreviation for "on the order of 1 μm." More careful treatment of binding densities and lower limits of detection are presented for the ionic fluid model in Section 7.1.5.

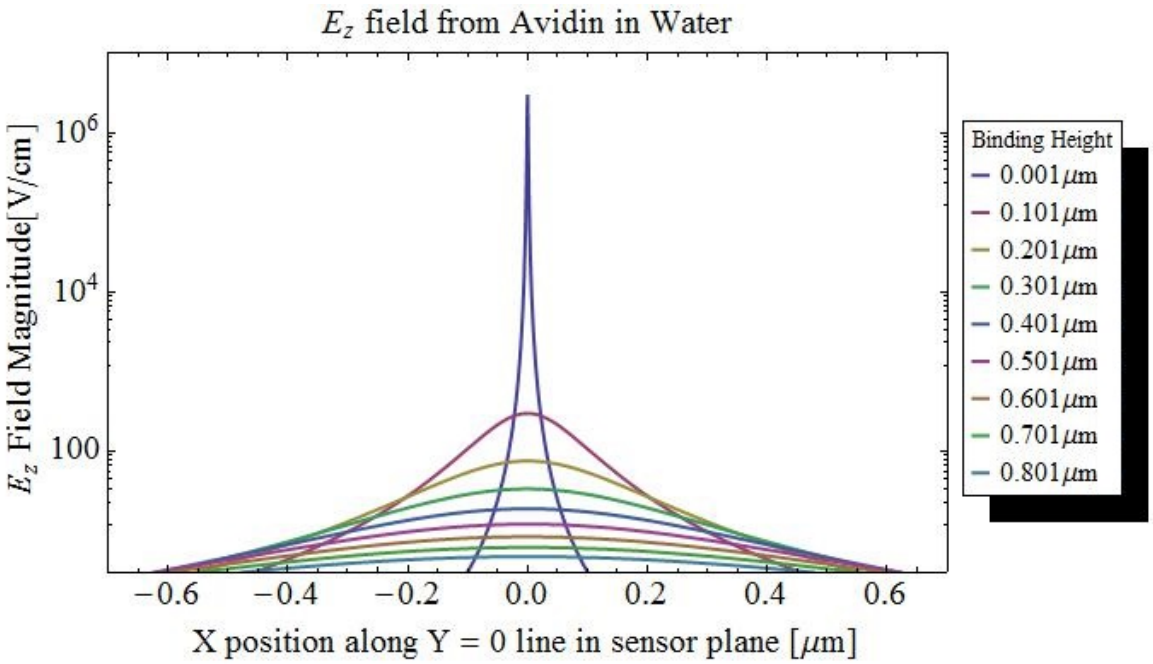

Figure 7.8 Electric field magnitude in Z direction (transverse to interface) along line in sensor plane (x, 0, 0). Avidin modeled as a single charged ion at position (0, 0, Binding Height) in dielectric water.

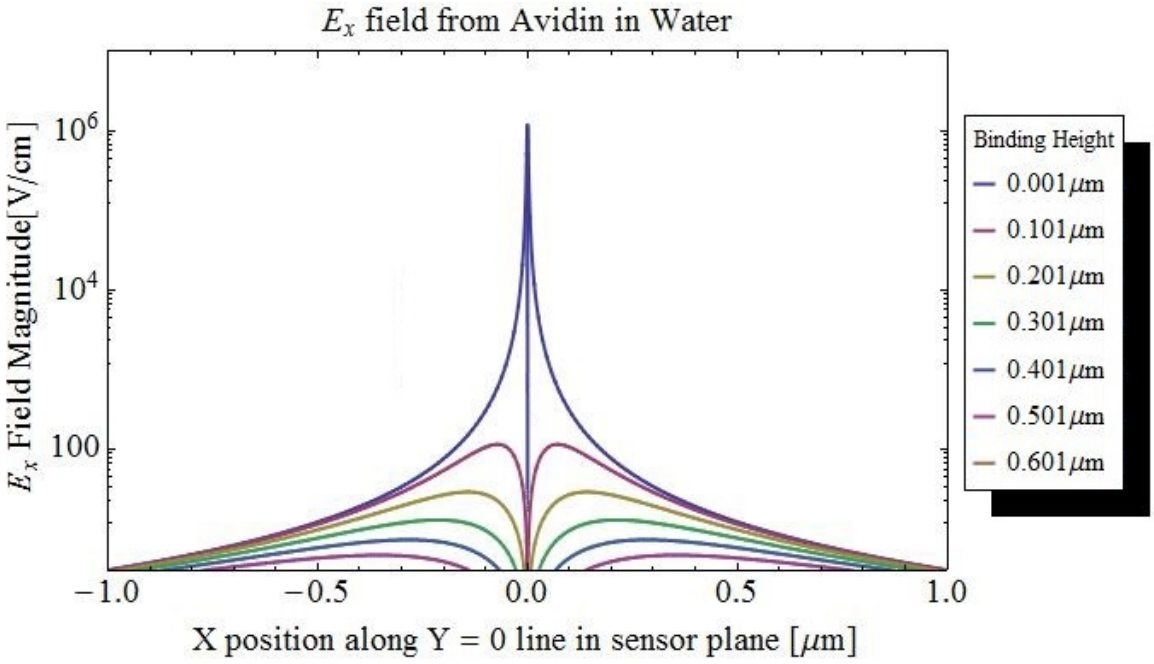

Figure 7.9 Electric field magnitude in X direction (parallel to interface plane) along line in sensor plane (x, 0, 0). Avidin modeled as a single charged ion at position (0, 0, Binding Height) in dielectric water.

Section 7.1.4 Effects of Fluid Ionic Strength and Debye Screening

A slightly more accurate model for the behavior of ionic solutions incorporates charge screening by the Debye-Hückel theory of electrolytes.[60,61] The model is valid for dilute solutions such that the ions can be modeled as hard spheres interacting electrostatically in a continuous, dielectric background media of dielectric constant, ε. The hard shell radius is a parameter that accounts for the fact that there is a set distance of nearest approach for the free ions in the electrolyte. For a protein like avidin, the radius is approximately 4 nm. The electric field at a point "P" in the surrounding space can be expected to be dependent on this quantity since the radius, *a*, will dictate the amount of electrolyte between the central ion and the point, P. A proton will have a smaller radius (~0.05 nm) than a protein with the same charge and the proton will be more significantly shielded. The theory provides a simple description of the tendency for negative ions to cluster around a positive ion in solution and vice versa; Debye-Hückel theory shows it is more likely that an ion will be surrounded by counter-ions. Combining a thermodynamic, Maxwell-Boltzmann dependence of ion density, ρ_i, of ion species *i* on electrostatic potential energy for the nth particle, V_n, with the Poisson equation yields one form of the Poisson-Boltzmann equation:

$$\nabla^2 V_n(\vec{r}) = \frac{-4\pi\rho(\vec{r}_n)}{\varepsilon} = -\frac{4\pi}{\varepsilon}\sum_i \rho_{i,bulk} z_i e \cdot e^{-\frac{z_i e\, V_n}{kT}} \qquad 7.5.$$

where $\rho_{i,bulk}$ is the bulk ion density for ion species *i*, z_i, is the ionization number for ion species *i,* and *e* is the magnitude of the charge of an electron. For instance, a salt solution of sodium chloride, NaCl, would have $z_{Na} = +1, z_{Cl} = -1$ since the electrolyte then is Na^+ and Cl^- ions. The equation as it stands can only be solved numerically. Debye and Hückel outlined a restricted analytical solution by a Taylor expansion of the exponential to the first two terms which

becomes a valid expression at low concentrations. The equation is also simplified by assuming spherical symmetry of ion clustering around the central ion, *n*, making the only functional dependence on *r*, the distance from the central ion. This of course assumes that the ions can be approximated by a continuous distribution and does not treat the ions as discrete particles.

$$\frac{\mathrm{d}^2 V_n}{\mathrm{d}\vec{r}^2} = -\frac{4\pi}{\varepsilon}\sum_i \rho_{i,bulk} z_i e \cdot \left(1 - \frac{z_i e\, V_n}{kT}\right) \tag{7.6.}$$

The first term $\sum_i \rho_{i,bulk} z_i e$ equals 0 for all electrically neutral electrolytes. Thus, the definition of the Debye screening length, K^{-1}, arises from the restricted differential equation, using the spherical Laplacian:

$$\frac{1}{r}\frac{\partial^2 (rV_n)}{\partial r^2} = \frac{4\pi}{\varepsilon}\sum_i \rho_{i,bulk} {z_i}^2 e^2 \cdot \frac{V_n}{kT} = K^2 V_n \tag{7.7.}$$

$$K^2 = \frac{4\pi e^2}{\varepsilon kT} 2I \tag{7.8.}$$

$$I = \frac{1}{2}\sum_i \rho_{i,bulk} {z_i}^2 \tag{7.9.}$$

$$\frac{\partial^2 (rV_n)}{\partial r^2} = K^2 (rV_n) \tag{7.10.}$$

$$rV_n = Ae^{-Kr} + Be^{Kr} \tag{7.11.}$$

Another commonly calculated electrolyte property is the ionic strength, *I*, defined above in Equation (7.9). As one would expect, a higher ionic concentration translates to a higher ionic strength, which in turn implies a large K^2, and thus a very short Debye screening length K^{-1}. The perturbative effect of a charged molecule is damped more swiftly as ionic concentration increases.

Applying the boundary conditions that first, the potential go to zero at infinity, second, the potential and the electric field be continuous at the hard-sphere radius, *a*, and third, that the

potential inside the hard sphere radius is the Coulombic potential of the central ion, the solution for the restricted electrostatic potential outside the hard sphere boundary is

$$V_n(r) = \frac{z_n e^{-K(r-a)}}{r \cdot \varepsilon(aK+1)} \tag{7.12.}$$

This result is self-consistent. Reverting back to a simple dielectric model in which there is no salt in the solution, $\rho_{i,bulk} = K = I = 0$. Then, the electrostatic potential of the central ion *n* is recovered for all space as

$$V_n(r) = \frac{z_n}{r \cdot \varepsilon} \tag{7.13.}$$

The spherical gradient applied to $V_n(r)$ retains only the first term proportional to $\hat{r}$. The electric field is therefore

$$\overrightarrow{E_n}(r) = -\frac{\partial V_n(r)}{\partial r}\hat{r} \tag{7.14.}$$

$$\overrightarrow{E_n}(r) = \left(\frac{z_n e^{-K(r-a)}}{r^2 \cdot \varepsilon(aK+1)} + \frac{z_n K e^{-K(r-a)}}{r \cdot \varepsilon(aK+1)}\right)\ \hat{r} \tag{7.15.}$$

which may also be written

$$\overrightarrow{E_n}(r) = \frac{z_n e^{+Ka}}{\varepsilon(aK+1)}\left(\frac{e^{-Kr}}{r^2} + \frac{K e^{-Kr}}{r}\right)\ \hat{r}$$

by grouping the terms that are dependent on the parameter *r* and not *a*. Substituting *E* into the Poisson-Boltzmann equation (7.5), the spherical, net charge density distribution around atom *n* is

$$\rho_n(r) = -\ \frac{\varepsilon K^2 V_n(r)}{4\pi} = -\ \frac{K^2 z_n e^{-K(r-a)}}{4\pi\, r \cdot (aK+1)} \tag{7.16.}$$

The critical qualitative feature of this equation is that the distribution is proportional to $-z_n$, implying that ions will tend to be surrounded by counter-ions.

Section 7.1.5 Ionic and Dielectric Fluid Model for 20 and 40 base pair DNA

A common salt solution is phosphate buffered saline (PBS) which was used as a baseline measurement in our tests. According to the product information provided by Sigma-Aldrich: "Contents of one pouch, when dissolved in one liter of distilled or deionized water, will yield 0.01 M phosphate buffered saline (NaCl 0.138 M; KCl - 0.0027 M); pH 7.4, at 25 °C."[62] Since this exercise is intended to be an estimation of electric field, it is assumed that the salts are completely ionized, though of course in practice some will bind with the H^+ and OH^- resulting in the pH of 7.4. Paired ions will contribute less to the shielding being overall neutral or weak dipoles. Assuming full ionization will overestimate the ionic strength and underestimate the Debye screening length. Table 7.3 summarizes the variables of the model.

Table 7.3 DNA Ionic, Dielectric Fluid Model Parameters

Parameter	**Description**	**Value**
a	DNA base pair spacing	0.34 nm
n	Number of base pairs	20 or 40
k	Coulomb's constant, vacuum	8.988 Nm^2/C^2
$\varepsilon_{r,water}$	Relative static dielectric constant, water	78
$q_{\ base\ pair}$	Charge per base pair	0.5 e = 0.801×10^{-19} C
f_o	Thickness of the functionalization layer	1-2 nm
ρ_K, ρ_{Cl}	Ionic density from 0.0027 M KCl	0.0027 M
ρ_{Na}, ρ_{Cl}	Ionic density from 0.138 M NaCl	0.138 M
ρ_{H+}	H density from pH 7.4	$10^{-7.4}$ M
ρ_{OH-}	OH density from pH 7.4	$10^{-6.6}$ M
a_{Bohr}	Bohr radius, used for hard sphere potential	$0.529\ \ 10^{-10}$ m
Z_i	All ions are singly charged	± 1

Given the concentrations of ions in 10 mM PBS and assuming that they are fully ionized, the Debye screening length is 0.81 nm. To demonstrate the sensitivity to ionic strength and shielding, Figure 7.10 shows the electric field at the origin (0, 0, 0) from a proton at a fixed location (0, 0, 5nm) for a range of concentrations. The hard shell radius of the proton was set to

the classical Bohr radius for a Hydrogen atom. As demonstrated in the development of the electrolyte equations, the concentration of zero on the axis is equal to the simple electrostatic field in a dielectric medium (Equation 7.13), a system like those of Section 7.1.2 and Section 7.1.3. When the concentration is above 44 mM, the electric field from the proton is effectively masked from any possibility of detection. At 10 mM PBS, the concentration used in our experiments, the 0.81 nm screening length has decreased the field magnitude of a proton to 1/66 its salt-free value. Recall, that the proton's position at 5 nm is 6.2 screening lengths from the origin on the sensor surface.

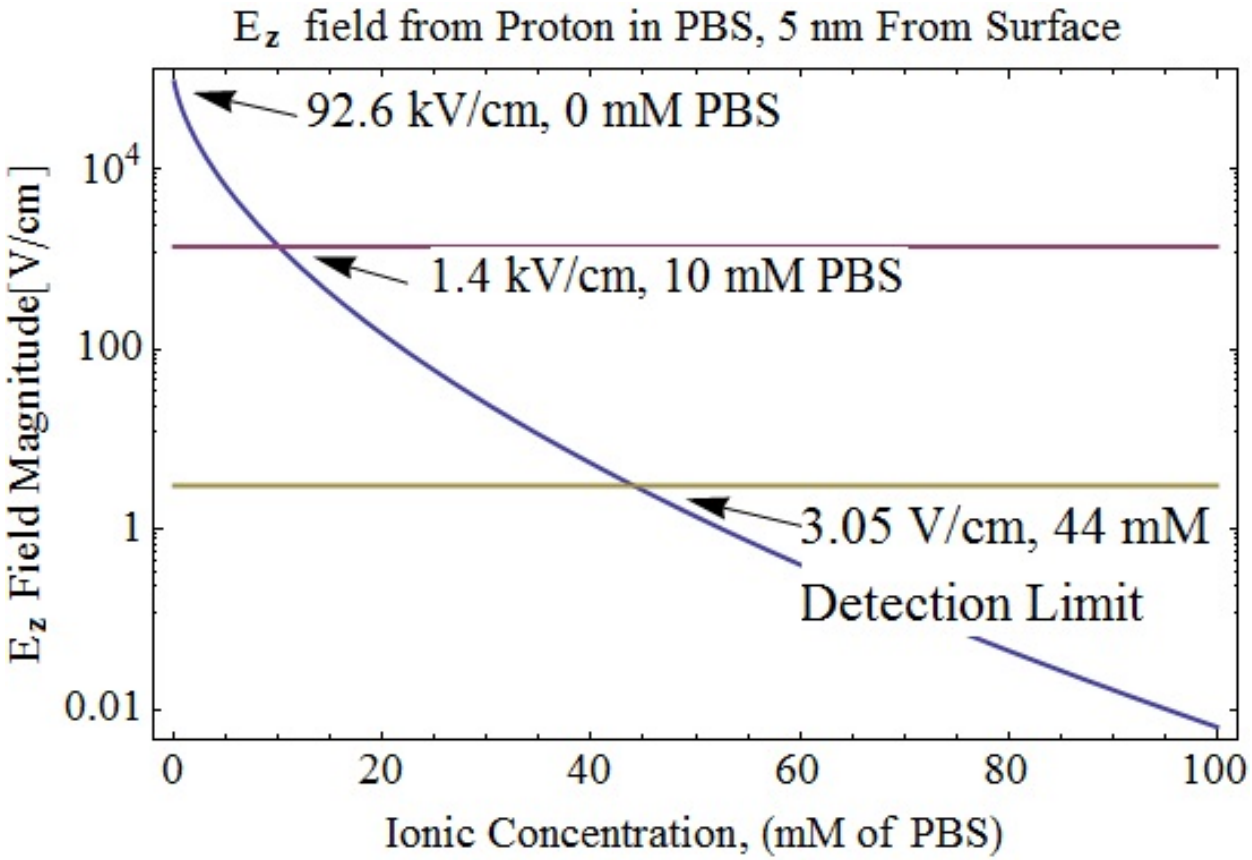

Figure 7.10 Functional dependence of electric field in Z direction at the origin from a proton at a fixed location (0, 0, 5nm) on the concentration of PBS. This demonstrates signal quenching due to ionic shielding. The highlighted values are: 0 mM PBS (no salt, equivalent to the simple dielectric), 10 mM PBS (the concentration used in the following experiments), and 44 mM PBS (at detection limit)

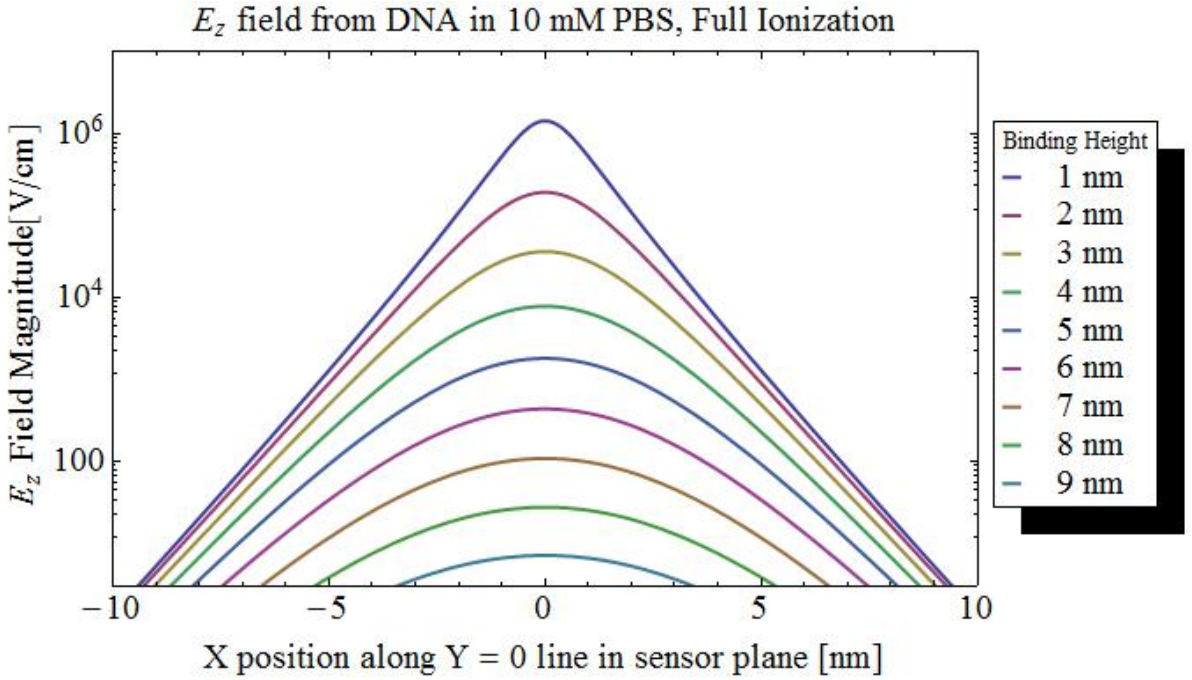

(A)

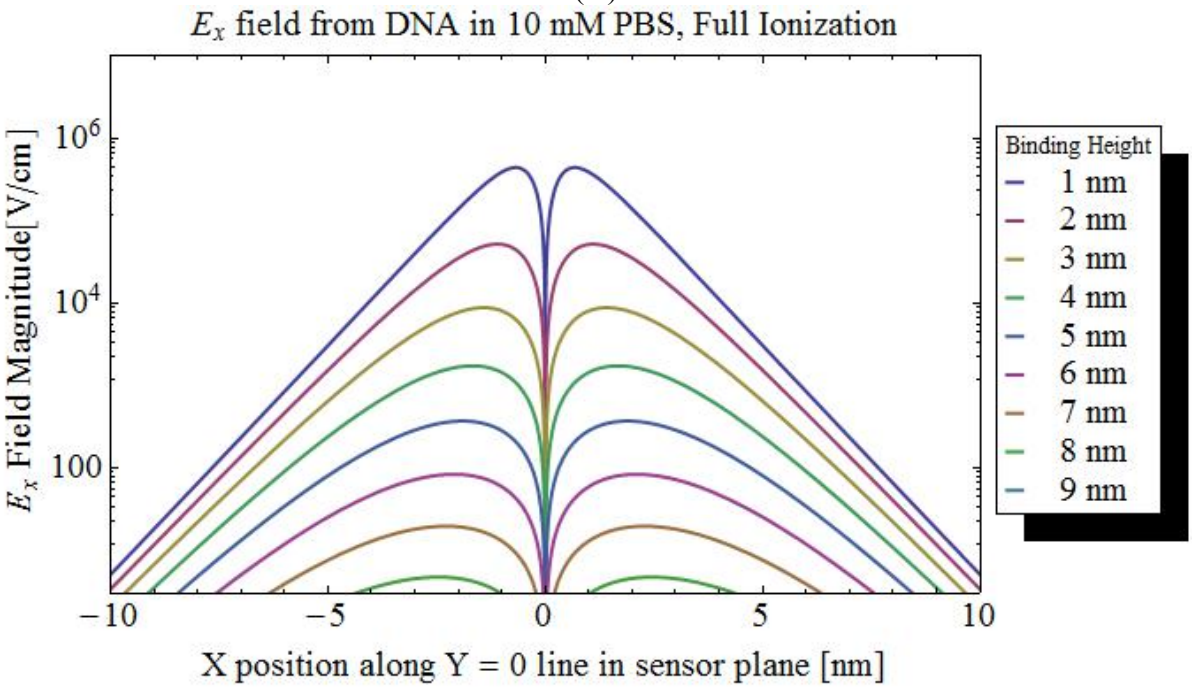

(B)

Figure 7.11 Functional dependence of electric field (A) in the Z and (B) in the X directions from a 20 base pair DNA strand under identical parameters to the discrete model of section 7.1.2 but with the introduction of 10mM concentration of PBS. This figure also demonstrates signal quenching due to functionalization layer thickness (increasing binding height).

In addition to assuming fully ionized salts, the model also ignores the effects of other strands of DNA. In addition, and perhaps most critically, the effects of neighboring base pairs are ignored. The solution for electric field derived in Equation (7.15) assumed a single ion at the center of a spherically symmetric distribution of counter-ions. This electric field is applied at each discrete DNA base pair position in a superposition of electric fields. In reality of course, the neighboring base pairs would alter the ability of the counter-ions to congregate around the central ionized base pair.

Recall that the criterion for detection is a field of 3.05 V/cm across the face of the 15 μm sensor. Note that the long-range interaction is significantly damped in Figure 7.11 (a) and (b). The ions cause the field to fall below the detection limit on O(10 nm) from the binding site whereas in Figure 7.7 (a) and (b) the range was O(1 μm). Given a functionalization layer of 2 nm, the results of the DNA calculation in dielectric indicate that a minimum density of one DNA strand bound every 1 μm^2 would be sufficient coverage to generate a field larger than 3.05 at all points in space on the sensor face (~100 bound/sensor). The ionic shielding calculation indicates that one DNA strand every 20nm x 20nm = 400 nm^2 (~10^6 bound/ detector) would be required to achieve a field of 3.05 or more at every point on the sensor face.

This is the first application of an EEC sensor for detection of a point-like source and laterally varying field. The magnitude of the fields at the binding site can be much higher than was tested previously in the Solin group with external electric field biasing by capacitor plates. Therefore it is difficult to say with certainty what the necessary coverage and binding density would be. If instead of the criterion that the absolute value of the field be greater than 3 V/cm at every point, we require the average field across the face of the detector to be greater than 3 V/cm, by numerical integration of the field function on a square with sides 2*d centered at the

origin, we find in Figure 7.12 that the average field from a single strand of DNA at 1 nm falls below the detection limit O(1 μm) from the sensor. Assuming a spacing of 2 μm between bound DNA strands at a height of 1 nm, ~ 40/sensor would meet detection criteria or half that of the unshielded, nonionic solution. Some intermediate density between the highly shielded and unshielded cases is the most probable outcome.

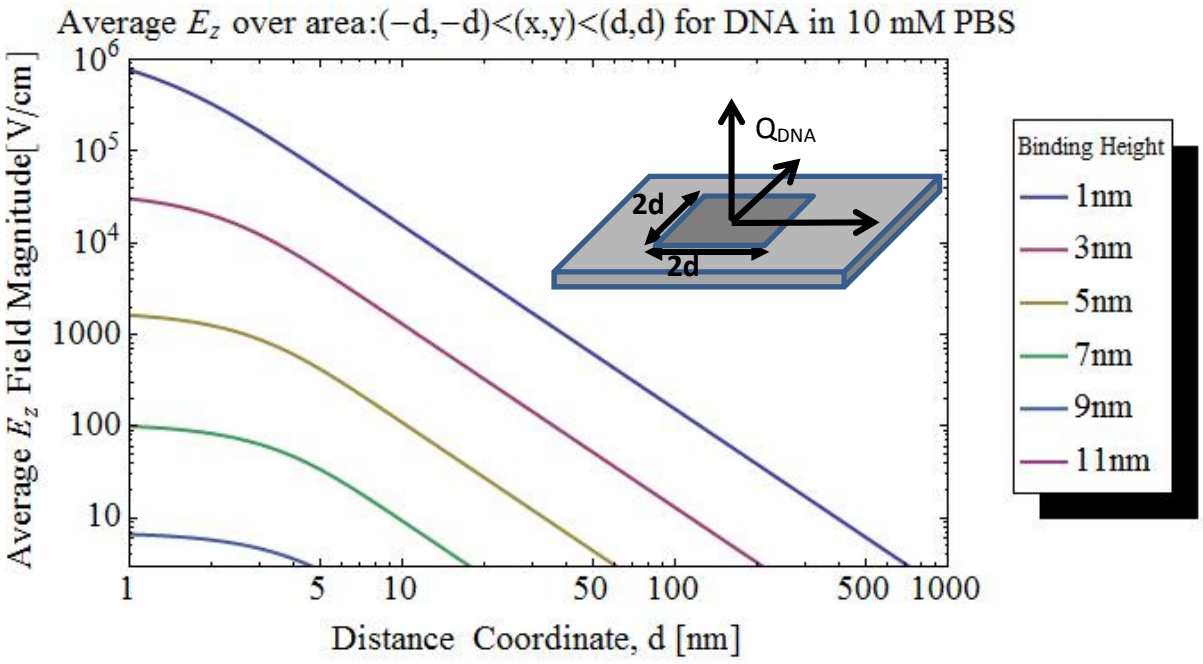

Figure 7.12 The average field in the Z direction for 20 base pair DNA at various binding heights as a function of *d* (which dictates the integrated area). The lower bound of the field axis is 3.05 V/cm. Note that 11 nm is below the limit and is off the range of this plot.

Section 7.1.6 Ionic and Dielectric Fluid Model for Biotin and Streptavidin

Since the buffer is identical in this case, the Debye screening length is still 0.81 nm. Also, since avidin and streptavidins' electric fields will have the same shape with the scale of charge, only avidin results are presented. Table 7.4 summarized the parameters of the model. Results for

both the ion hard-shell radius of ~ 0.05 nm (as a "worst case scenario" of high shielding) and avidin's hard-shell radius of 4 nm are included.

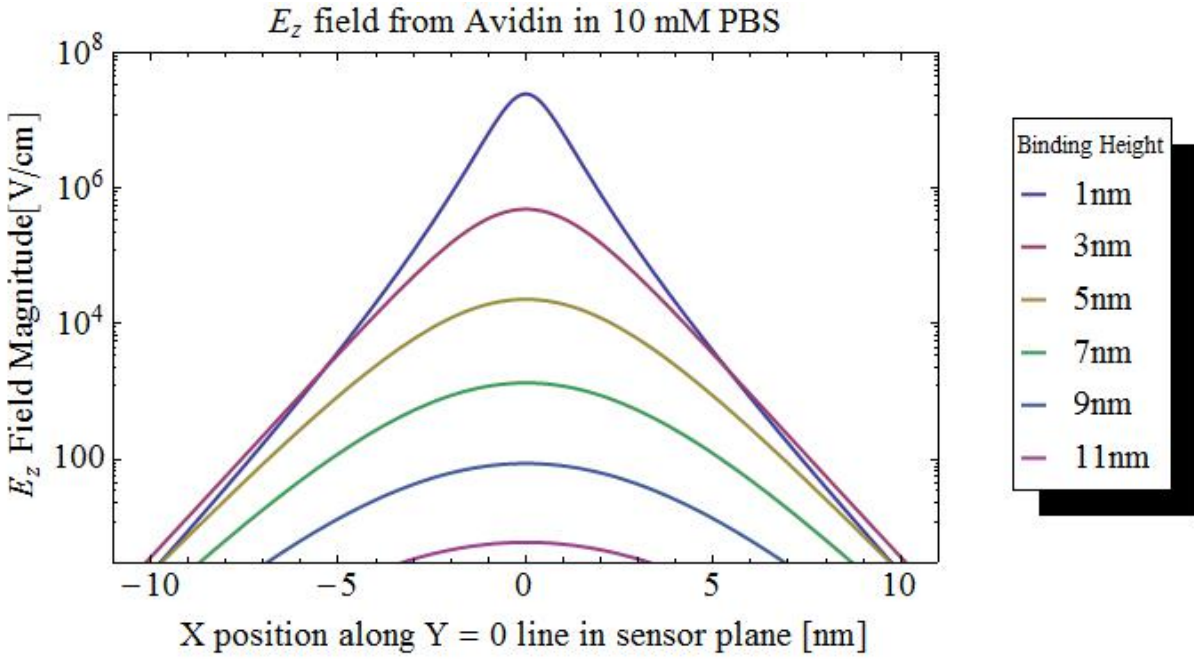

(A)

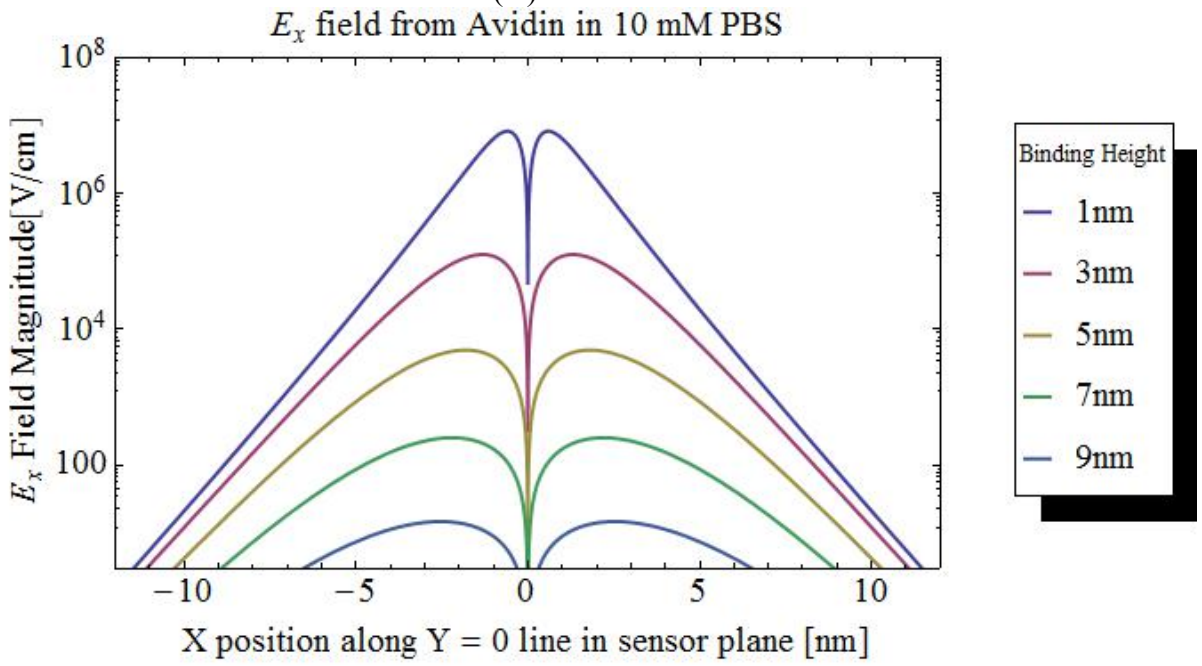

(B)

Figure 7.13 Functional dependence of electric field (A) in the Z direction (B) in the X direction from avidin with parameters identical to the dielectric model of section 7.1.3 but with the

introduction of 10mM concentration of PBS and a_{Bohr}. This figure also demonstrates signal quenching due to functionalization layer thickness (increasing binding height).

Table 7.4 Avidin Ionic, Dielectric Fluid Model Parameters

Parameter	**Description**	**Value**
q_{avd}	Net charge avidin at pH 7.4	$+16.5e$ = 2.64 x 10^{-18}C
q_{stp}	Net charge streptavidin at pH 7.4	$-8.5e$ = -1.36 x 10^{-18}C
K	Coulomb's constant, vacuum	8.988 Nm^2/C^2
$\varepsilon_{r,water}$	Relative static dielectric constant, water	78
f_o	Thickness of the functionalization layer	1 nm-21nm
ρ_K, ρ_{Cl}	Ionic density from 0.0027 M KCl	0.0027 M
ρ_{Na}, ρ_{Cl}	Ionic density from 0.138 M NaCl	0.138 M
ρ_{H+}	H density from pH 7.4	$10^{-7.4}$ M
ρ_{OH-}	OH density from pH 7.4	$10^{-6.6}$ M
a_{Bohr}	Bohr radius, used for hard sphere potential	0.529 10^{-10} m
a_{avidin}	Avidin protein radius, used for hard sphere potential	4 10^{-9} m
z_i	All ions are singly charged	± 1

Similar to the ionic DNA result, the detection limit for avidin's field at a PBS of 10 mM as in Figure 7.13 (a) is reached on O(10 nm) from the binding site, indicating a higher binding density is needed for detection. At 13 nm functionalization layer thickness the signal is decreased entirely to below the detection threshold.

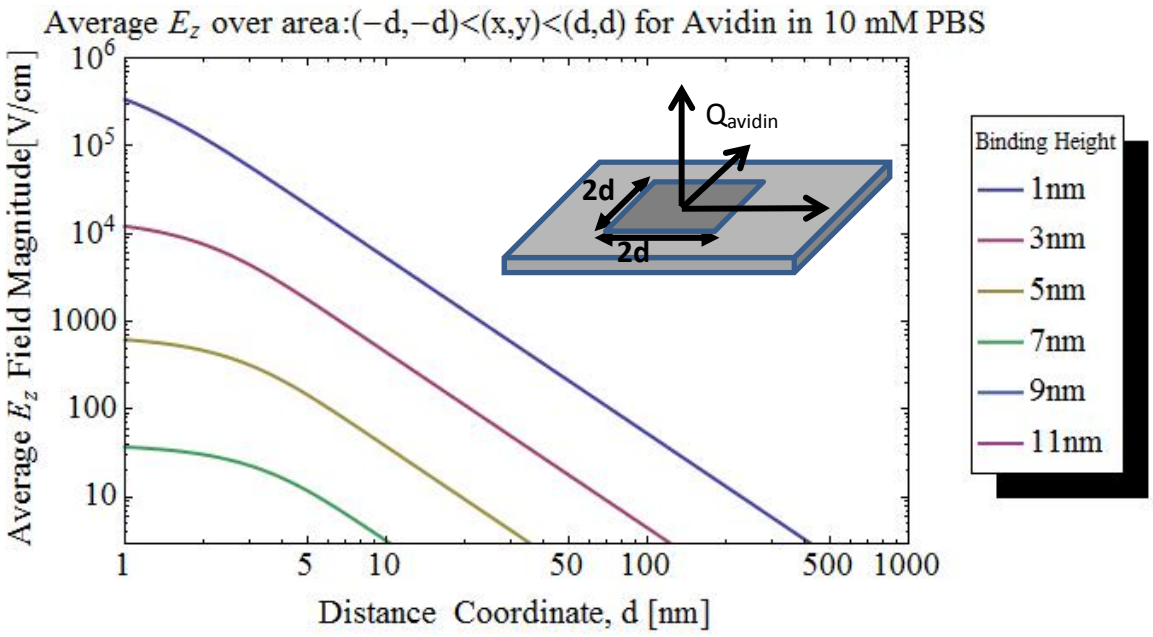

Figure 7.14 The averaged electric field in the Z direction for 10 mM PBS and aBohr. The spacing of proteins would be every 2*d*. The lower bound of the field axis is 3.05 V/cm. Note that 9 and 11 nm are below the limit and are off the range of this plot.

The average electric field for the minimum binding distance of captavidin (2 nm in Figure 7.14) indicates that the lowest density of protein needed for detection would be every ~200 nm x 200 nm (~5600/sensor). Assuming that the EEC detectors are also sensitive to a lateral, E_x and E_y sensitivity, a lower number bound per sensor to achieve a signal is possible.

If the hard-shell radius of avidin (a_{avidin}) is used, no electrolyte ions are present in the space $a_{Bohr} < r < a_{avidin}$ which somewhat reduces the shielding effects of the worst case scenario in Figures 7.13-14. However, the model is not highly sensitive to the difference in *a* on these length scales as can be seen in Figure 7.15. The change in the electric field from equation 7.15 is a factor of ~23 or

$$\frac{23\, e^{+Ka_{Bohr}}}{(a_{Bohr}K+1)} \approx \frac{e^{+Ka_{avidin}}}{(a_{avidin}K+1)} \qquad 7.17.$$

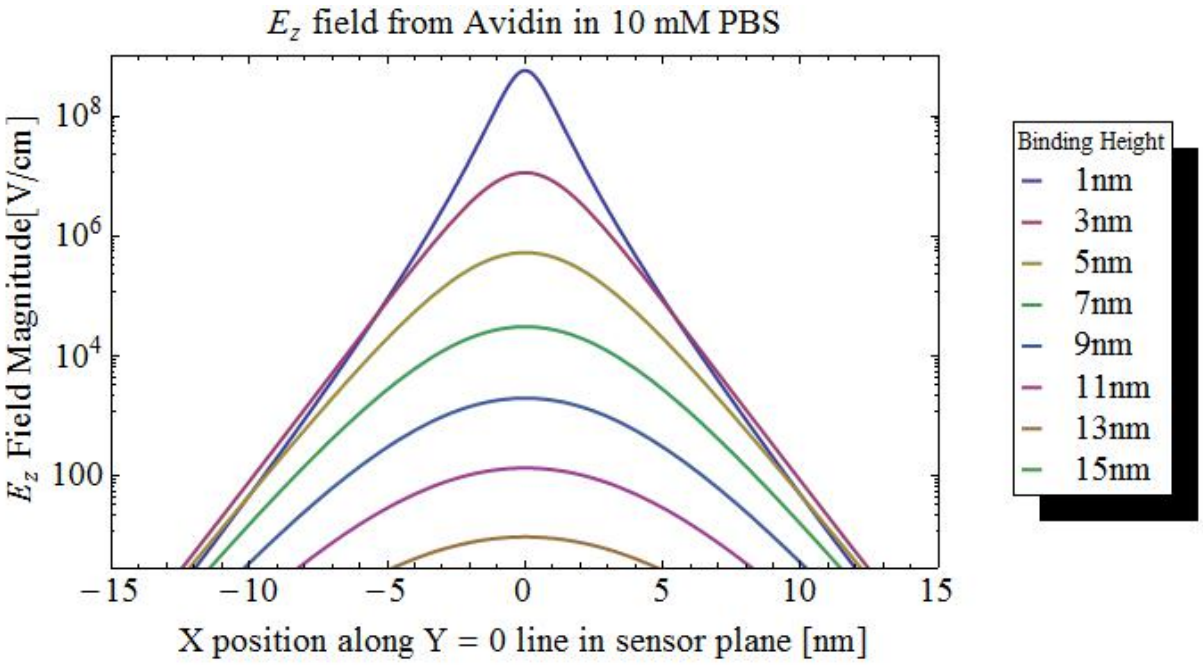

(A)

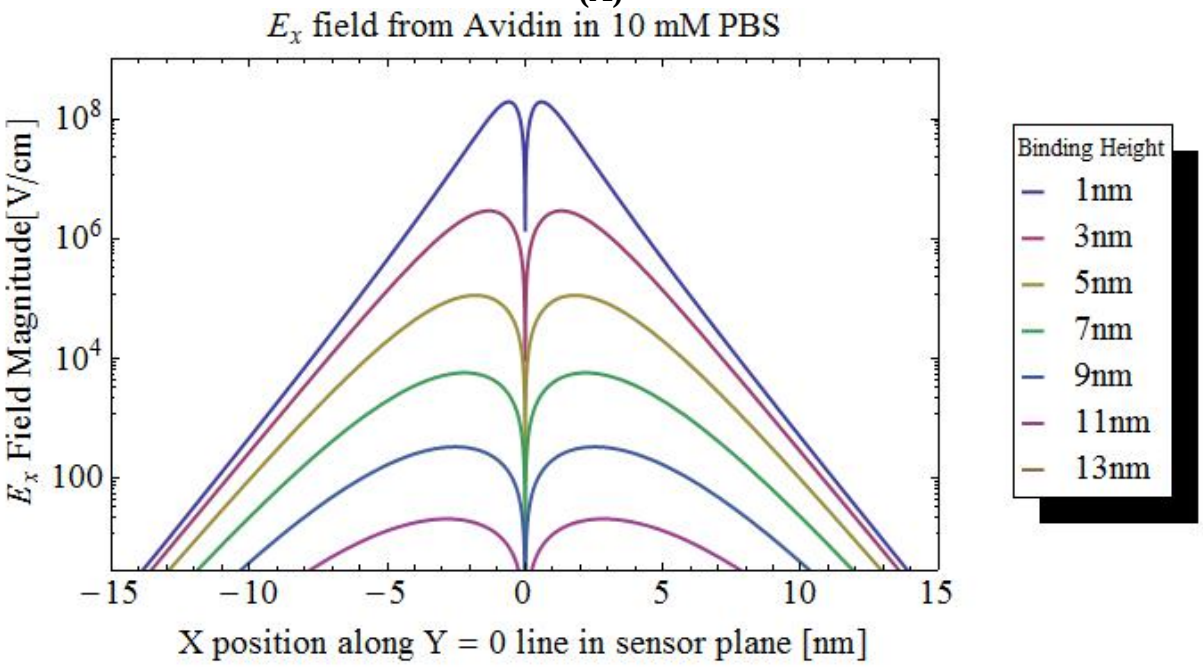

(B)

Figure 7.15 **Electric field magnitude** in the z direction (A) and the x direction (B) **from avidin in 10 mM PBS and aavidin. Notice that binding distance of 13 nm is below the 3 V/cm threshold and is off the range of the plots.**

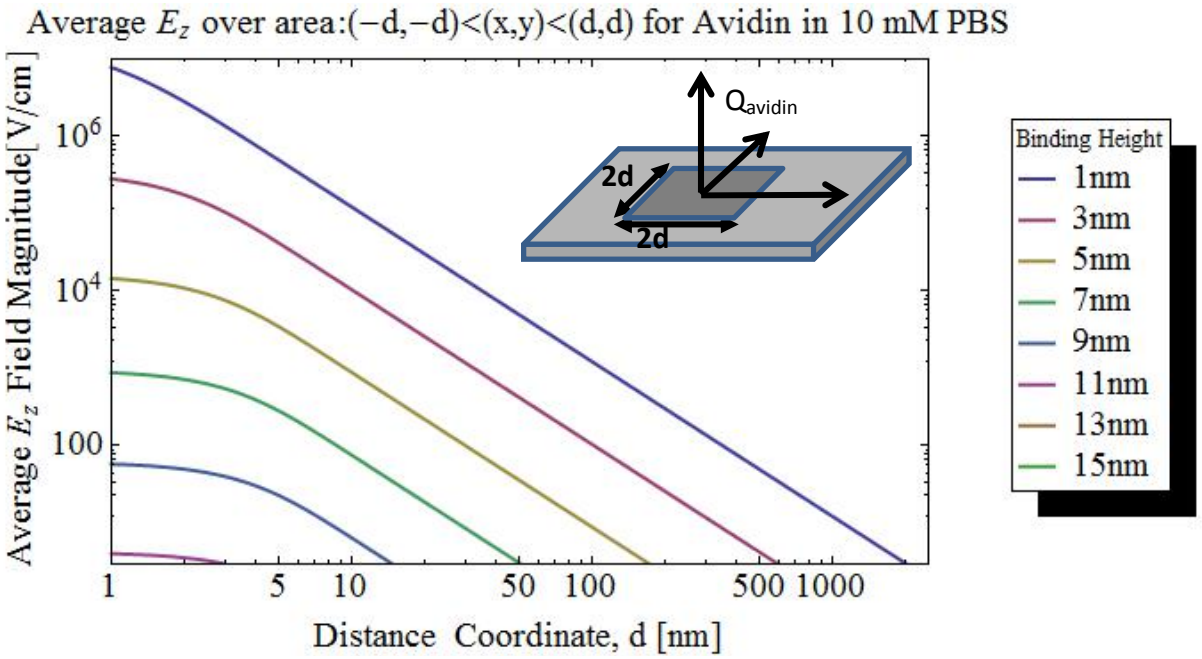

Figure 7.16 **Averaged electric field** in the z direction from a**vidin in 10 mM PBS** and $\mathbf{a_{avidin}}$**.** To estimate necessary binding density, proteins would be bound every 2*d*. Binding heights 13 nm and 15 nm are below the detectable range.

The average electric field for the avidin in Figure 7.16 indicates that at a binding height of 3nm a binding density of 1 avidin/0.25μm^2 and a binding height 5 nm, a minimum binding density of 1 avidin/0.04 μm^2.

Reducing the ionic concentration of course amplifies the signal. Since as was mentioned, some ions may be expected to bind in solution and not contribute to shielding, a second concentration at 1/10th of the experimentally used value was included. As can be seen in Figure 7.17 at a thickness of 6 nm, shielding damps the field to below the detection limit on O(25 nm) from the binding site. This would reduce the required binding density to 1 avidin/2500 nm^2. This is approximately ¼ the density required by the 10 mM solution shown in Figure 7.15 (a).

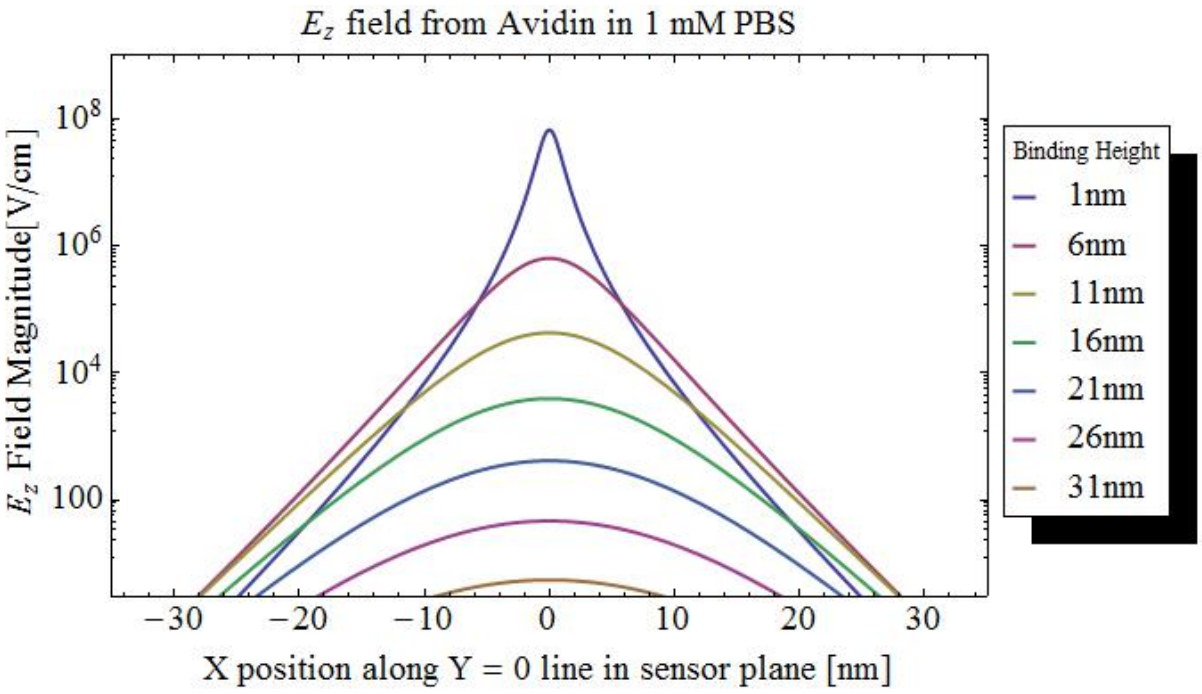

Figure 7.17 Functional dependence of electric field from avidin with parameters identical to the dielectric model of section 7.1.3 but with the introduction of 1 mM concentration of PBS, or 1/10 that used in experiment and a_{avidin}. This figure also demonstrates signal quenching due to functionalization layer thickness (increasing binding height).

Section 7.2 Fabrication Process and Experimental Methods

Section 7.2.1 Sensor Design Parameters

The physical structure of the EEC sensors is similar to what was broadly described in Chapter 3.1.2 when the overview of the fabrication procedure was presented. The specific design variation used in the biochemical detection experiment is summarized here.

All sensors were fabricated from a single GaAs wafer with a lattice matched, Si-doped epilayer, 100 nm thick, at a dopant concentration of $N_D = 4x10^{17}$ cm^{-3}. The same shunt materials of n-GaAs/TiAu were used to form the Schottky interfaces and annealed GaAs/AuGeNi formed the four Ohmic contacts. The square mesas were 15 μm laterally, while the shunts were designed to have a patterned width of 7.5 μm. Due to undercutting of photoresist and image reversal processes outlined in the photolithographic projection Section of Chapter 3.1.2.2, the patterned shunts had an actual width in the range of 8-10 μm and with the rounded corners visible in the photographs of Figure 7.18. The sensors were fabricated in three styles: bare (without shunt), with shunt (four leads), and with shunt connected to an added contact accessing the interface (five leads). Using atomic layer deposition, the sensors were covered in 200 atomic layers of amorphous aluminum oxide (Al_2O_3) for a film approximately 18 nm thick. The oxide layer served as electrical isolation of the sensors from the functionalization layers and the biomolecule containing liquid droplets.

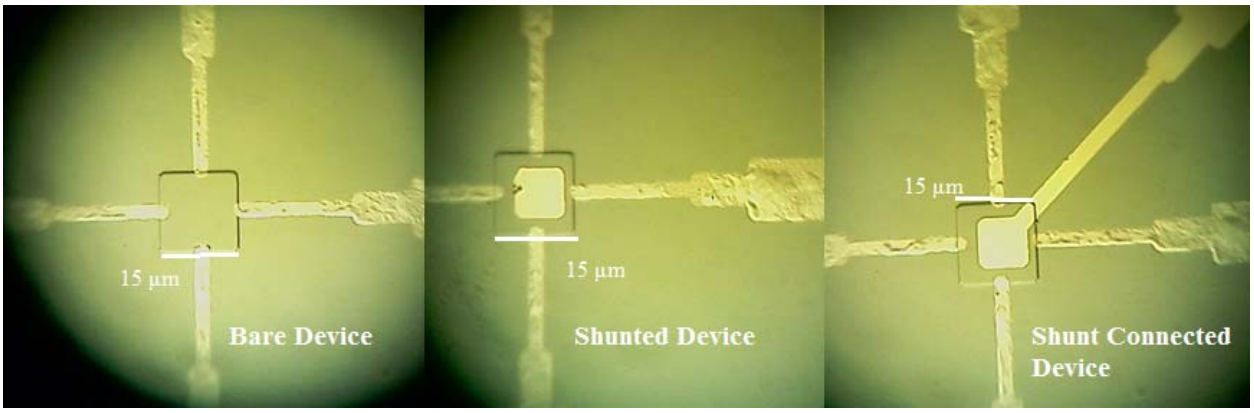

Figure 7.18 The above sensor photographs were taken by camera through a microscope objective under 100x magnification.

Section 7.2.2 Functionalization of Aluminum Oxide

The sensors were washed in methanol for 5-10 seconds to remove any contaminants on the surface and then dried in an oven under convecting air for one or more hours at 70°C. This removed the methanol and any adsorbed water molecules from humidity in the air off the aluminum oxide surface. Oxygen gas at a pressure of 275 mTorr and a power of 55W in a SPI Plasma Prep II (Model 11050AB) was applied for 20 seconds while the feedback was manually adjusted until the plasma struck. The struck plasma was then applied for an additional 18 seconds. The oxygen plasma serves the dual purpose of cleaning the aluminum oxide and activating the surface for silane attachment by ionization of oxygen groups. The samples were transferred to a gaseous nitrogen flow environment and bathed in a solution of 3-aminopropylmethyldiethoxysilane (APMDES, pictured in Figure 7.19(a)) in dry toluene (20 mL toluene and 0.2 mL silane for 1% dilution) for 10 minutes to coat the surface with $–NH_2$ terminated groups. The sensors were rinsed with toluene and baked in the oven for 30 minutes at 70°C. A homogeneous solution of Methyl-polyethylene glycol$_4$-*N*-Hydroxysuccinimide Ester (Methyl-PEG$_4$-NHS Ester, hereafter called PEG$_4$, pictured in Figure 7.19(b)) and EZ Link NHS-PEG$_4$-Biotin (hereafter called PEG$_4$-biotin, pictured in Figure 7.19(c)) from ThermoScientific

was prepared in a solution of dimethyl sulfoxide (DMSO). The amine terminators were biotinylated by submersion in a 1:8 solution of PEG_4:PEG_4-biotin linkers at room temperature for a minimum of one hour. The linkers attach to the amine groups by release of the *N*-Hydroxysuccinimide (NHS) group (pictured in Figure 7.20). This 1:8 ratio controls the surface density of biotin molecules. Approximately one of every nine amine ($–NH_2$) groups will link a biotin and eight of nine amine groups will be methyl terminated ($–CH_3$) which is non-reactive and blocks binding to the avidin family. The general schematic of the attachment is depicted in Figure 7.21 and some details provided in the caption.

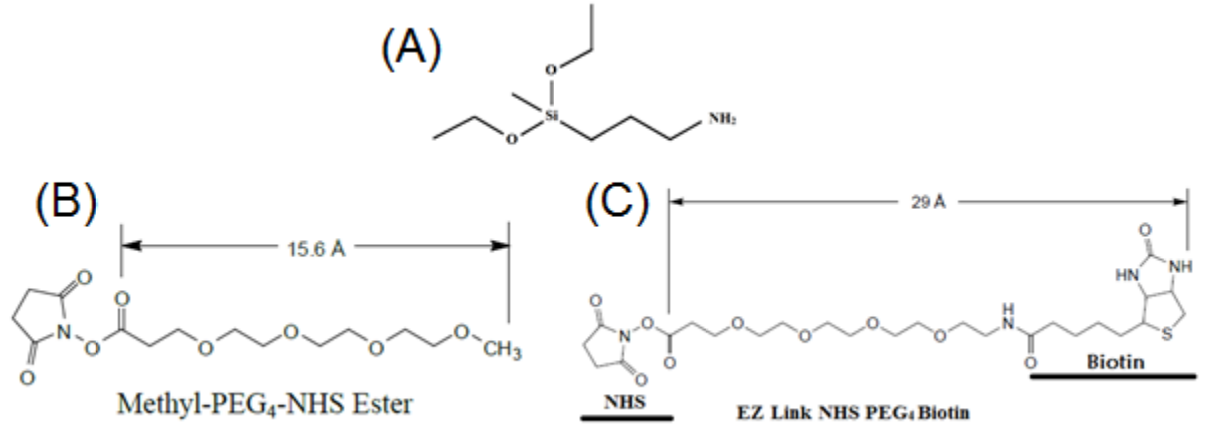

Figure 7.19 (A) Structure of APMDES (B) PEG_4, Ref[63] (C) PEG_4-biotin, Ref[57]

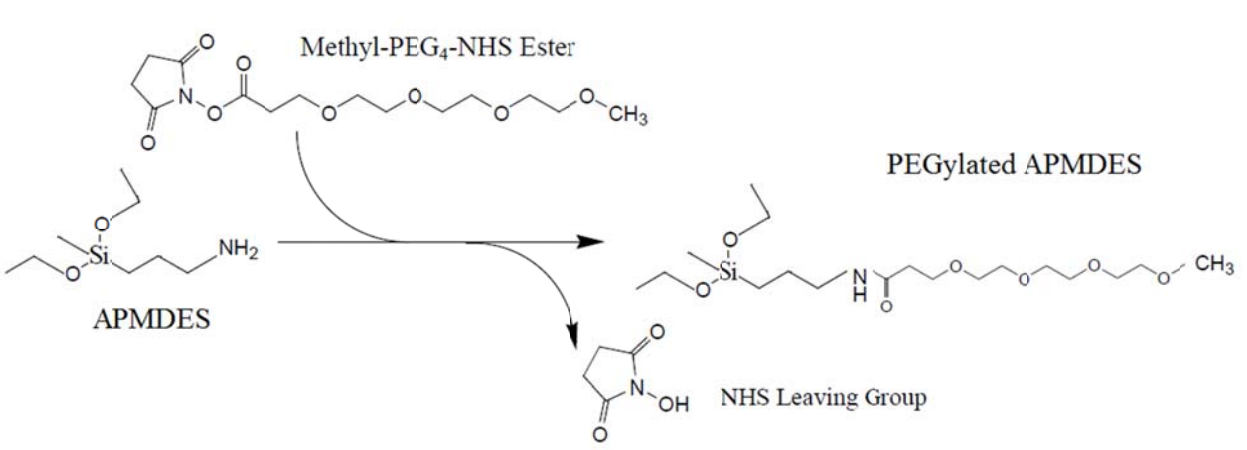

Figure 7.20 Schematic of reaction attaching PEG_4 and PEG_4-biotin to amine group of APMDES. Adapted from the structures provided by ThermoScientific and Gelest molecular data sheets.

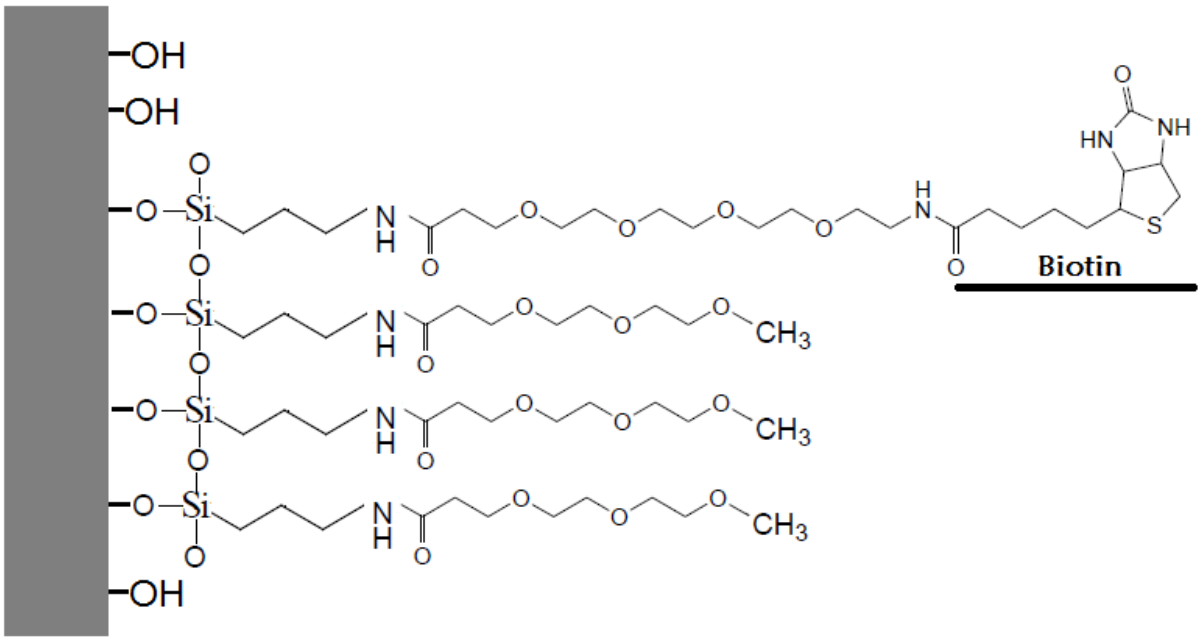

Figure 7.21 Schematic of attached APMDES, PEG_4 and PEG_4-biotin on aluminum oxide. This is a proposed attachment outcome. Documentation of the attachment mechanism for APMDES to oxide surfaces has not been proposed in published literature, to the author's knowledge. The chemical changes that occur at the oxide surface for a dimethyl silane (DMS) are a substitution of carbon for available oxygen at the surface and from neighboring silanes. However, it is unconfirmed whether the two carbons in the ethyl groups of diethyl silane, APM(DES), such as we used would detach differently than the single carbon methyl groups of APMDMS. The figure demonstrates an APMDMS-like attachment.

Section 7.2.3 Dilution Curve and Protein Binding Experiment

After functionalization, the sensors were mounted in an in-house, custom constructed experimental box that shielded the sensors from exterior noise sources and light. Each sensor could be accessed individually by a computer controlled multiplexing mainframe (Agilent 34980A mainframe and 34925A MUX card). When the sensors were exposed to a chemical droplet, and the cover of the box replaced, a Labview program automatically sampled the resistance of each sensor in a cyclic rotation. The multiplexing mainframe also allowed for the flexibility to take a four point measurement or two pairs of two point measurements. During a two point measurement, the two unused Ohmic contacts were open wires, disconnected by way

of open switches at the multiplexing mainframe, and left floating. Also, during all resistance measurements the shunt wire (fifth lead) should one exist, is floating and not directly accessed by the equipment. Details of the connection configuration are overlaid on the device photographs in Figure 7.22.

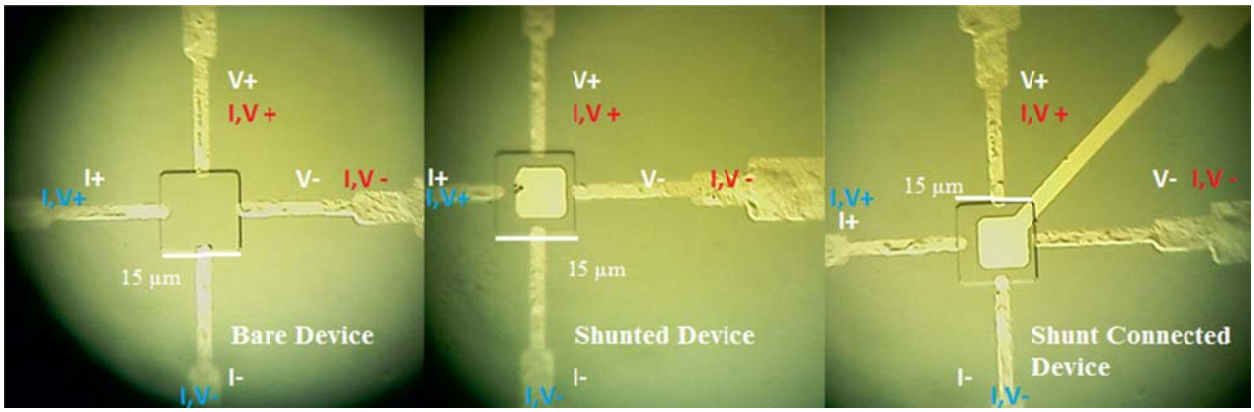

Figure 7.22 Detector photographs with measurement configuration overlaid. White (I,V) = Four Point Resistance, Red (I,V) = Two Point Resistance, A, Blue (I,V) = Two Point Resistance, B

The competitive binding assay involves two stages. First, the biotin-covered sensor surface is washed in phosphate buffered saline (PBS) as a baseline, followed by successively higher concentrations of captavidin and biotin in solution. Since the captavidin and the biotin are mixed in the vial and the reaction dynamics are very swift, all available biotin binding sites will be blocked by the free biotin in solution. Few to no binding sites will be available for binding to the biotin on the sample surface. This section of the assay tests the sensitivity of the sensors to changing ionic concentration of the solution with increasing captavidin concentration. The final captavidin/biotin solution is removed and the sample is soaked in PBS until the initiation of the second stage.

The second stage of the assay begins again with a PBS baseline wash. Then, increasing concentrations of pure captavidin with unblocked binding sites are applied to the sensors. In the

second sequence, sensitivity to binding events at the sensor surface is expected in addition to the sensitivity to ionic concentration.

In both stages the concentration increases by a factor of ten at each chemical droplet, called a “serial dilution curve”. To test for a consistent response to a particular concentration, more than one droplet of the same concentration may have been applied.

Section 7.3 Experimental Results

Section 7.3.1 Characterization of Sensors

After fabrication, the five lead EEC 15 μm sensors were characterized to test the Schottky interfaces. Figure 7.23 is an example connection diagram.

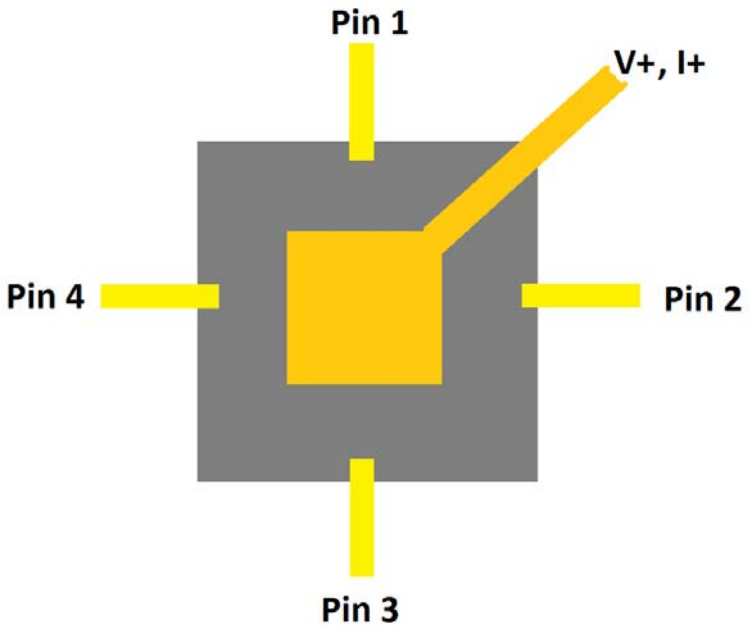

Figure 7.23 Shunt connected device with Ohmic, ground pins identified for the I-V characteristic curves and the fifth lead the positive reference

The results are shown below in Figure 7.24, rotating which Ohmic contact was grounded. For the most part, the different Ohmic contacts have such identical behavior that the curves lay

directly one on top of the other, with the exception of sensor 1. However, several sensors did not perform to design specifications. The shunts of several sensors (devices 1 and 3 in Figure 7.24) were Ohmic in nature and that there was no barrier to overcome to traverse the interface. This could be due to three types of causes: first, misalignment of the shunt metal from the center of the sensor such that the Ohmic contact metal and the shunt metal are in direct physical contact, second, a contaminant in the shunt interface acting as a dopant that alters the available energy levels and lowers the effective barrier between the GaAs semiconducting crystal energy levels and the Fermi level of the titanium, or third, no contaminant, but atomic diffusion across the interface such that the materials no longer sustain an abrupt interface, which also degrades the energy barrier. Since it appears that multiple ground pins all yield Ohmic interface behavior, the first type, physical contact with the leads, is less likely.

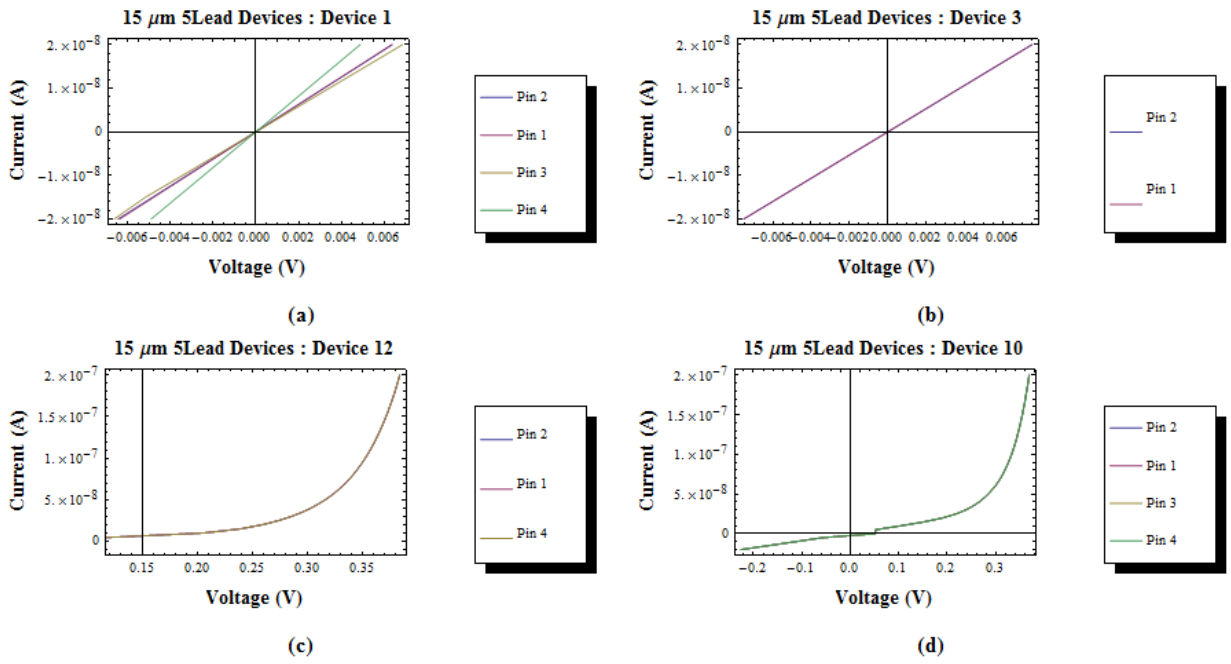

Figure 7.24 Current-Voltage behavior across Schottky interface of five-lead sensors after fabrication.

There had been a delay of some months before the protein experiments were performed, therefore the five-lead sensor interfaces were tested again in the week prior to the initiation of experiments. It was evident that sensor 10 interface had also degraded over time, most likely due to atomic diffusion (Figure 7.25(d)).

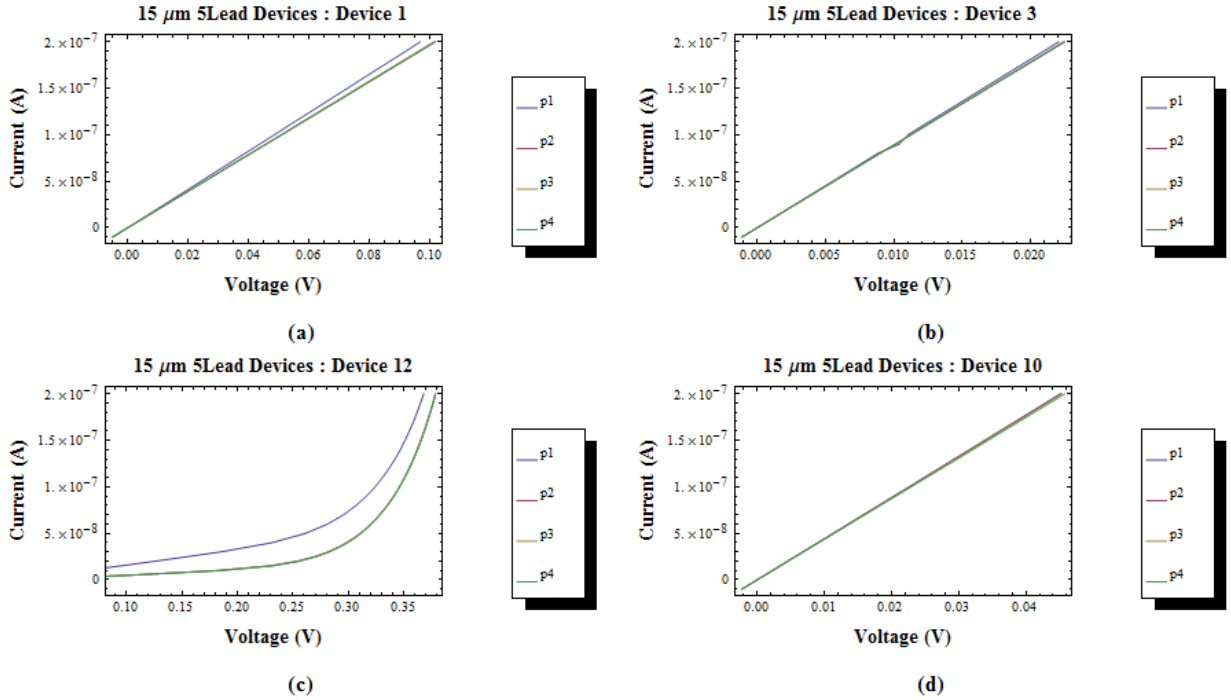

Figure 7.25 Current-Voltage behavior across Schottky interface of five-lead sensors prior to functionalization and captavidin competitive assay.

It should also be noted that the leads in the last remaining active interface (sensor 12) are no longer identical in behavior. Pin 1 deviated from the other three contacts, indicating the degradation was on the part of the Ohmic contact and not at the Schottky interface. Although many of the shunt interfaces were not the intended Schottky type, biological experiments were performed for proof of principle behavior, discussed in the following section. After the experiments, three leads of sensor 12 were intact, while the fourth had degraded to Ohmic which would of course still compromise performance. It is not clear at precisely what point in time sensor 12 should be considered degraded at the interface.

Section 7.3.2 Captavidin Serial Dilution Curve and Protein Binding Experiment

Section 7.3.2.1 Results – Bare Device Binding Signal

Figure 7.26 shows the bare sensor four point behavior. The percent change in resistance from the resistance at time zero aligns multiple sensors on the same vertical axis for comparison of different sensors in the same subcategory of type and electrical connection for measurement (see Figure 7.22 in methods Section 7.2.3 for configuration). It also compares each sensor to itself. Each sensor is its own standard to minimize distinctions of fabrication etc. between sensors.

$$\%\ change = \ 100 * \frac{R(t) - R(t_0)}{R(t_0)} \qquad 7.18.$$

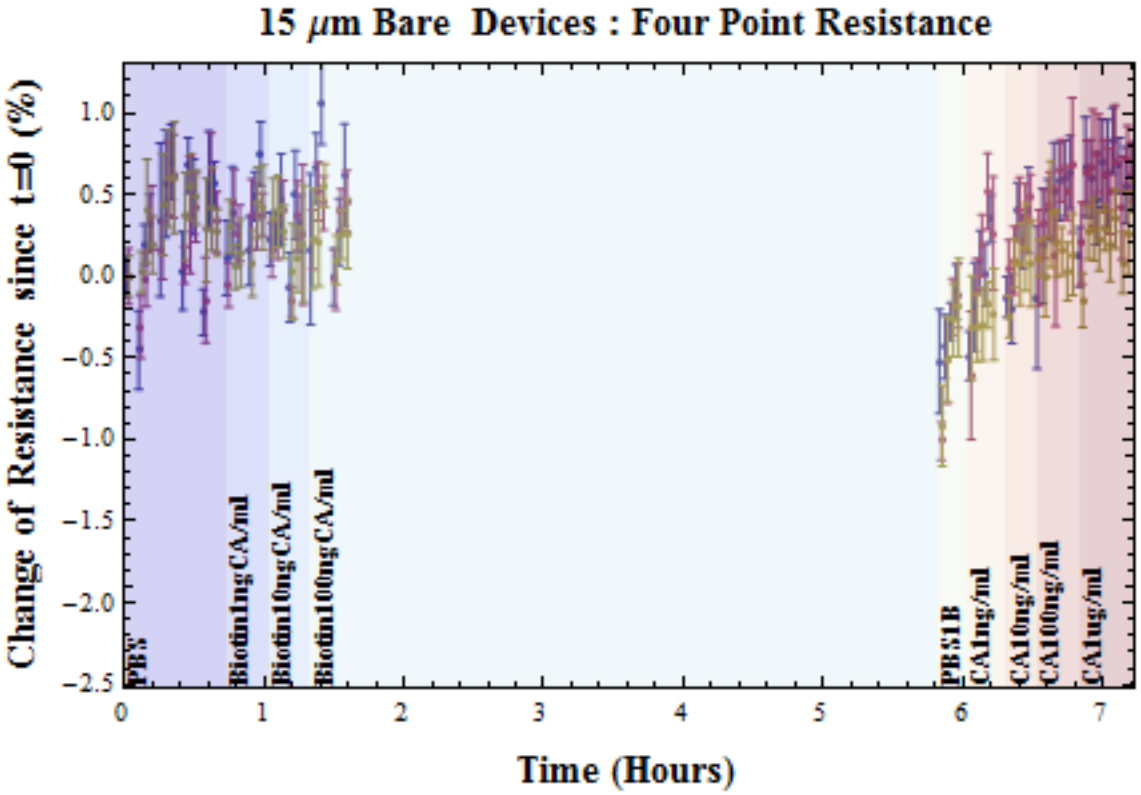

Figure 7.26 Four point resistance of three bare devices (pink, yellow, blue data with error bars). Time 0-1.5 hours shows the competitive binding assay of captavidin. Time 5.8-7.4 hours shows the serial dilution of captavidin and the distinct response to bound proteins. The color bars are marked with the biochemical droplet label applied at a particular point in time.

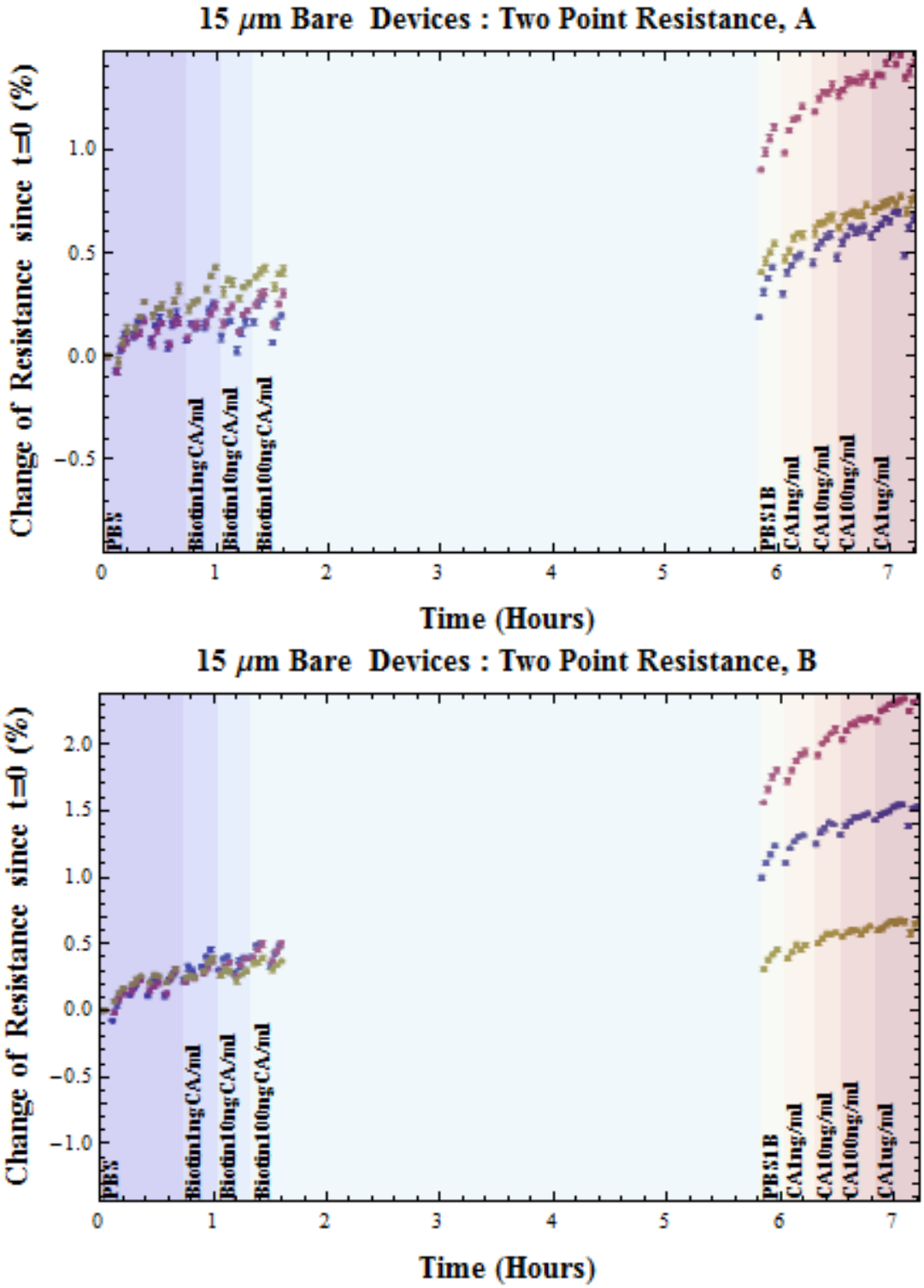

Figure 7.27 Two point resistance configuration (A) and (B) of three bare devices (pink, yellow, blue data with error bars) for the competitive binding assay and the serial dilution of captavidin. The color bars are marked with the biochemical droplet name.

The agreement between the sensors for the first series of competitive binding in Figures 7.26 and 7.27(a-b) is generally very good. In fact, the sensors agree so well in Figure 7.26 that the data of two detectors (pink, yellow) nearly obscure the data of the third (blue). This indicates the stability and self-consistency of the sensors to the changing ionic environment with increasing captavidin/biotin concentration in the fluid. The functionalized layers and the aluminum oxide appear to protect the sensors well from electrically shorting to the fluid.

After exposure to free captavidin at t = 6 hours, subsequent captavidin binding to the sensor surface causes an increase in resistance in the bare EEC sensors. The slope of the percent change in resistance is highest in the four point measurements. From this data, it is clear that not only are EEC sensors a viable physical geometry for a biochemical detector, but also that the four point measurement technique shows promise for high sensitivity (steep change in signal with small variations in concentration). By monitoring changes in the conductivity of the mesa alone, eliminating contact effects, the EEC sensor's four point response is due to a confined local environment, one with high spatial resolution. Thus small changes in charge concentration near the detector have a significant impact on the conductivity.

A comment on the signal to noise ratio in Figures 7.26 and 7.27(a-b) is called for at this point. The four point resistance is expected to be significantly less than the two point resistances since contact resistance is eliminated from the measurement. Also, the voltage sensing contacts are farther away from the source contacts in a four point measurement, lowering the local current density, the measured voltage, and the resulting resistance. Therefore, although the absolute error from noise is roughly the same number in Ohms between two point and four point measurements, the noise affects the smaller four point signal much more significantly. That is, the SNR for four point measurement was worse than for two point.

Whereas the four point resistance data for the bare EEC sensors were in good agreement with one another, the captavidin binding and surface charge density increase reveal distinguishing features and variation in sensitivity between sensors in the two point measurements. The offset and the slope of resistance were not identical between sensors or even between the two pairs of leads on the same sensor. A possible explanation of this is discussed in Section 7.3.2.4. Here, it is sufficient to point out that although the magnitude of the resistance was large leading to a small SNR, the two point data as it stands could not be utilized to predict the concentration of fluid – every sensor behaved differently. Until the sensors show a consistent repeatability, the behavior cannot be used as a standard for detection. The two point responses could be utilized for a *qualitative* test of binding. However, the inconsistencies would disallow its use in making *quantitative* statements about surface charge densities. The four point method was highly self-consistent across three distinct bare detectors, allowing calibration of signal change with a specific surface charge binding density.

Section 7.3.2.2 Results – Shunted Device Binding Signal

In Figures 7.28-29, the results from the 5 lead and 4 lead EEC sensors are less definitive with respect to binding signal. The four point signal in particular is lost below the SNR as well as other issues discussed in Sections 7.3.2.4 and 7.3.2.5.

Figures 7.28 (a-b) demonstrate a lack of sensitivity to captavidin binding in shunted four point measurements. The behavior is consistent regardless of what was applied chemically. The four lead EEC sensors' two point configuration shows two detectors (blue, yellow data in Figure 7.29) that behave in a similar manner to one another and to the bare devices. The sensor plotted as pink shows a deviance from the other four lead EEC sensors, particularly in the (B) electrical

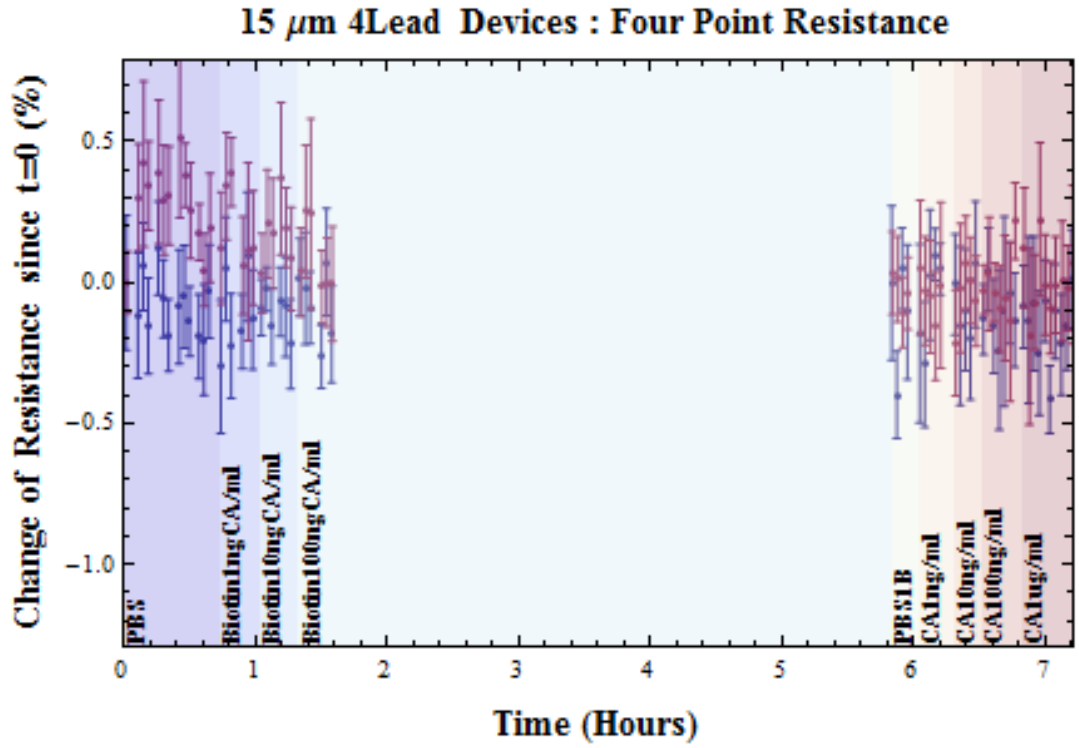

(A)

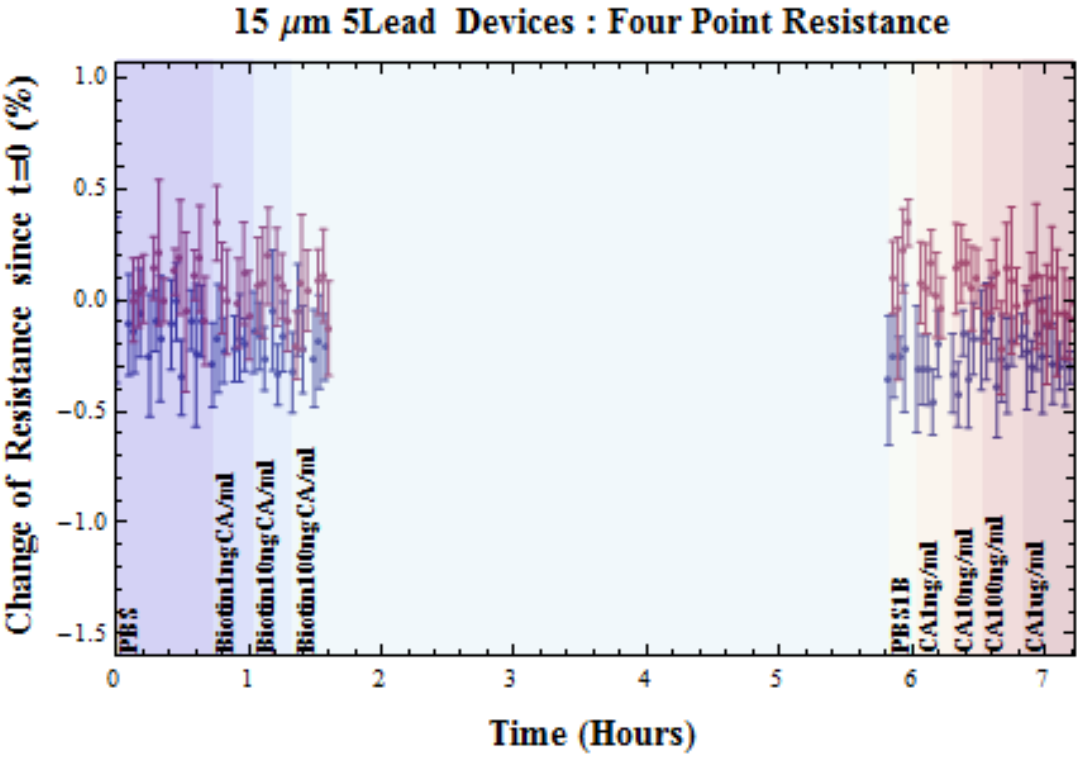

(B)

Figure 7.28 Four point resistance configuration for four lead (A) and five lead (B) sensors for the competitive binding assay and the serial dilution of captavidin. The color bars are marked with the biochemical droplet name.

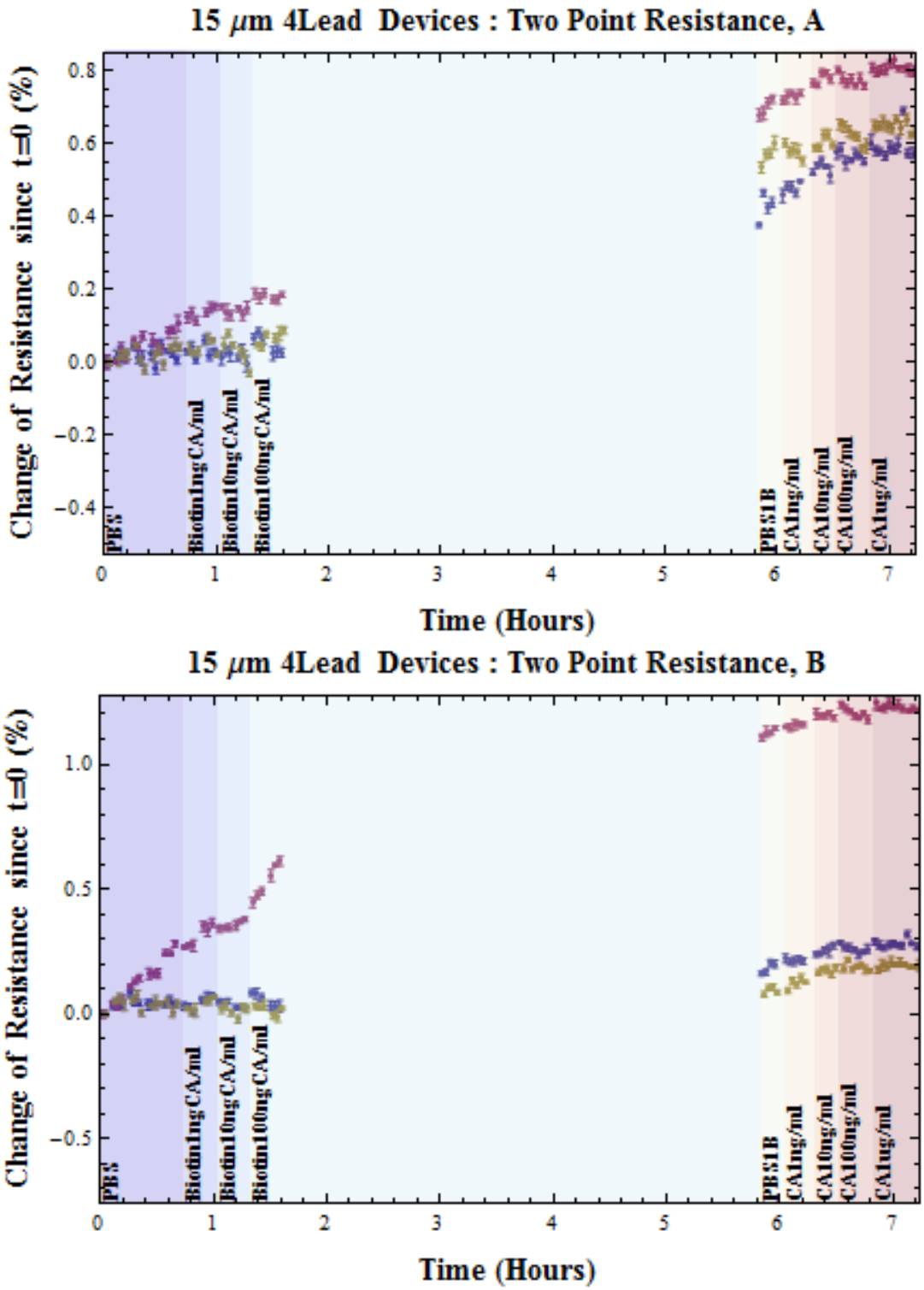

Figure 7.29 Four lead sensors: Two point resistance configuration (A) and (B) for the competitive binding assay and the serial dilution of captavidin. The color bars are marked with the biochemical droplet name.

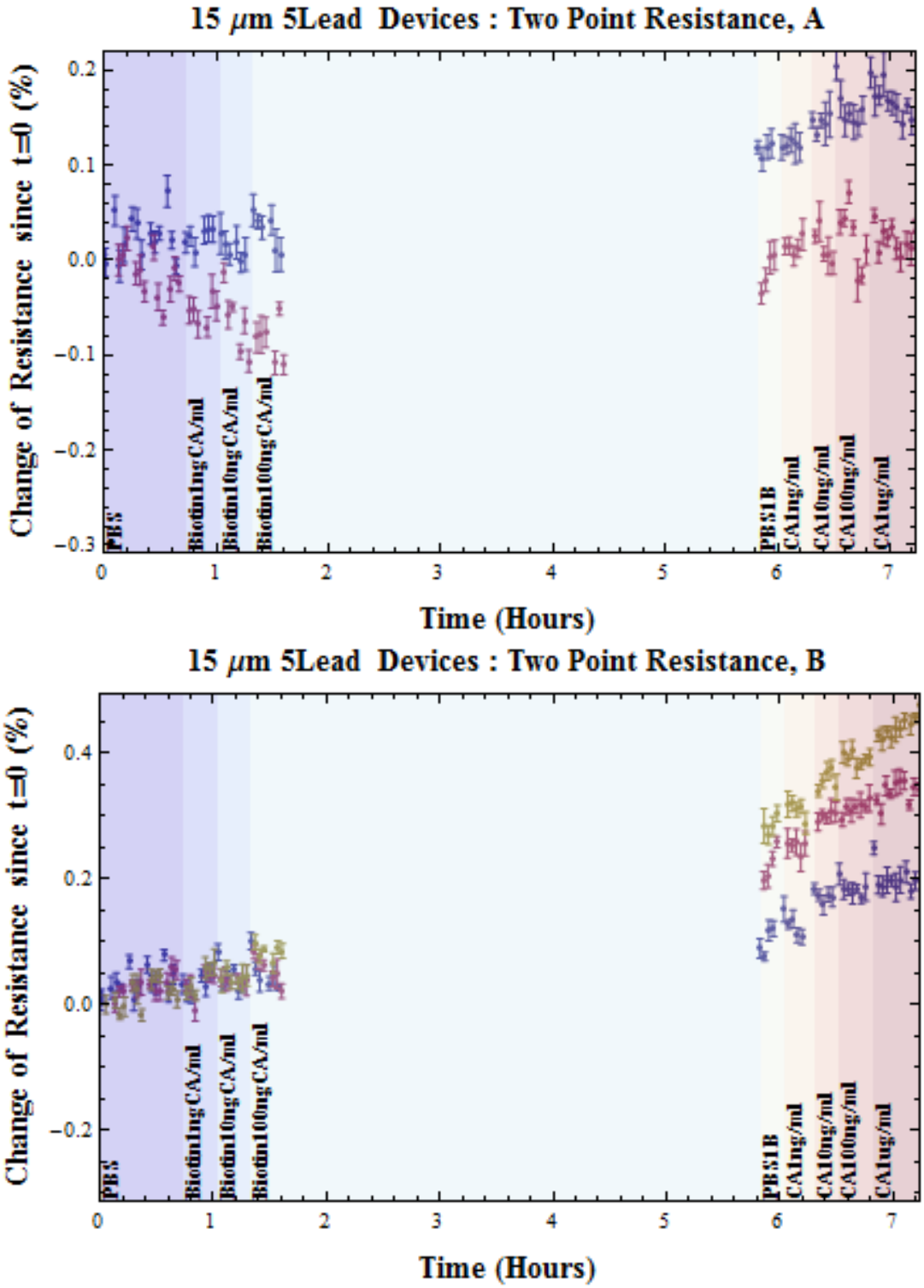

Figure 7.30 Five lead sensors: Two point resistance configuration (A) and (B) for the competitive binding assay and the serial dilution of captavidin. The color bars are marked with the biochemical droplet name.

configuration. A five lead EEC sensor suffered damage to the wires during functionalization which is the reason that there are only two devices for configuration (A) in Figure 7.30 and for the four point data in Figure 7.28(b).

Section 7.3.2.3 Calculations of Sensitivity

The slopes from a linear fit of the competitive assay and a linear fit of the binding assay data in Figures 7.26-30 are extracted as the parameter that characterizes each component of the experiment. The two assays were separated and a percent change in resistance was calculated individually for both sets (that is to say, t = 0 for the second sequence was at 5.8 hours). Further details of the calculations are provided in the appendix. Then, the slope of the response for each style of sensor is plotted in Figure 7.31. Nominally, this is the sensitivity of the sensor to the change in concentration. However, since the concentration changed by powers of ten with each droplet, sensitivity is defined as

$$sensitivity = \frac{change\ in\ resistance\ in\ \%}{log10[concentration]} \tag{7.19.}$$

In Figure 7.31, typically the slopes of the second assay with binding to the surface (red) are larger than those of the competitive assay with minimal binding (blue), particularly for the bare devices. That is, the sensors are generally more sensitive to binding than to ions. The change in resistance was greater for bound proteins. Also the four point sensitivity to binding for bare sensors is significantly higher than any other configuration.

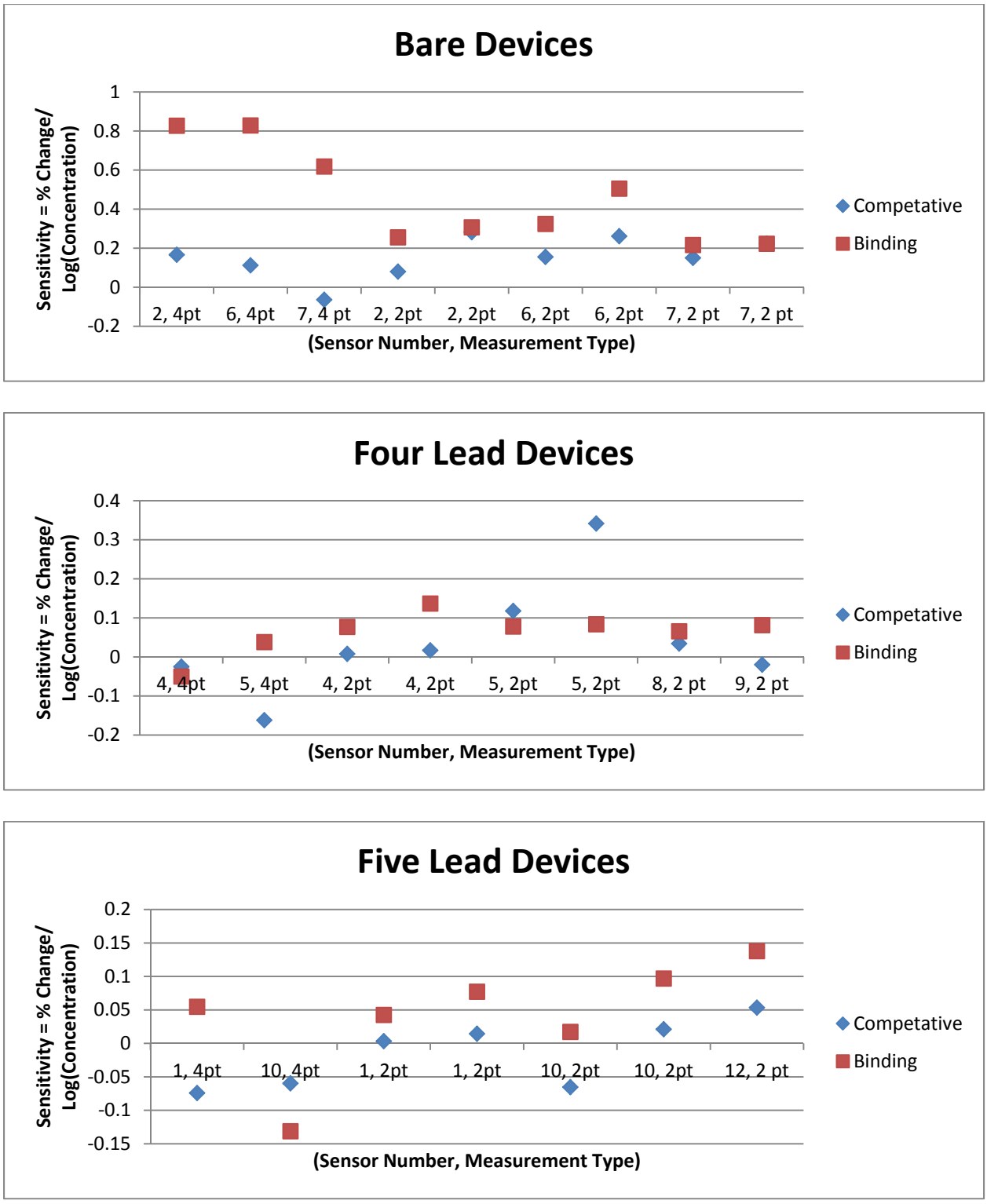

Figure 7.31 Overview of Sensitivity. The blue data is the first sequence, competitive assay, with minimal binding, while the red data of each graph is the second assay, with binding to the surface.

Section 7.3.2.4 Two-Point versus Four-Point: Discussion

When an EEC sensor is configured for two point detection, the system becomes similar to that of an ion sensitive field effect transistor[64] (ISFET). In an ISFET, the source and drain are patterned in the substrate plane, while the ionic fluid serves the function of the gate. A voltage-biasing probe in the fluid may also be employed to directly manipulate the fluid like a traditional FET gate. The bare devices, lacking the layer of metal that is the shunt, are the most similar to an ISFET of the EEC sensors when operated in a two point configuration, with only the addition of the second set of floating Ohmic contacts. However, a critical weakness of a method that employs only two contacts, such as a source and drain is evident in the inconsistent behavior of the sensors two point data's offsets and slopes.

The dispersion in sensitivity of two-point measurements seen in Figures 7.27, 7.28, and 7.30 has several possible origins. First, physical variations of the lead patterning alignment exist. Asymmetry in placement could lead to a different overall resistance, the effects of which are eliminated by the four point methods. Second, a variation in the biological monolayers and binding site densities in the regions near the contacts could also exist.

This second origin warrants some further discussion and development. Deposition of silanes in the solution phase as was done in this experiment by submersion of the aluminum oxide in a 1% concentration of APMDES in toluene is the easiest method to implement and the solution phase is commonly used to attach silanes of many variations to oxide surfaces.[65,66] However, it has also been shown to be an inconsistent method of self-assembling monolayer deposition. In fact, solution phase deposition of APMDES has been shown to have monolayers interspersed with large aggregated areas of silane multilayers, much thicker than the desired monolayer.[67] Recently, deposition of silanes by various vapor phase methods such as mild

vacuum[67] to increase evaporation or mild heat[56] to increase vapor pressure have been demonstrated to result in consistent monolayers of silane. Such vapor phase methods were unnecessary at the first development of silane-oxide protocol since the applications were in fluorescent microscopy and protein purification. Both these applications depend only upon the density of amine terminators on the surface and not on the thickness of the layer. The orientation of the molecules and propensity to self-assemble with the amine terminator exposed were more critical criteria to achieve. Now, as the field has expanded into biochemical sensing and electrochemical signal transduction, the development of reliable, monolayer films has been the focus.

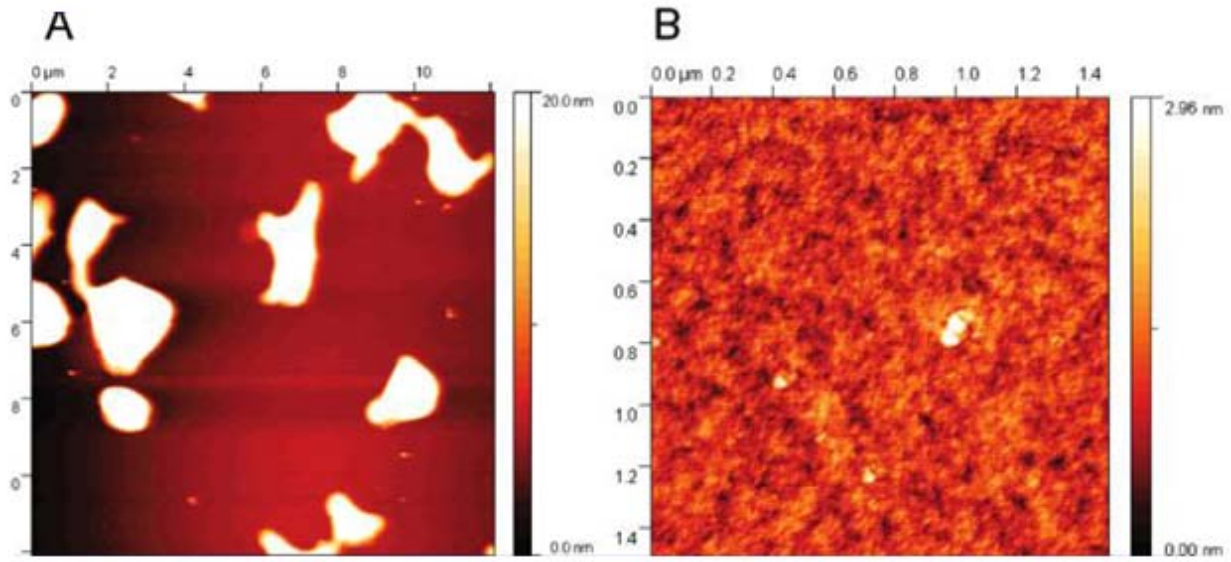

Figure 7.32 Atomic force microscopy image of APMDES layers deposited on silicon dioxide by (A) solution phase in 1% toluene (B) vapor phase deposition at ~125 Torr. From Anderson, et al. (2008)[67]

In Figure 7.32 (a), notice the micron-scale white regions of multilayers of APMDES surrounded by the black and red monolayer and bilayer regions. It should be noted that the white regions are off the scaled axis and could be as thick as several microns. At minimum they are 20 nm (see scale bar of Figure 7.32 (a)) which is approximately 7 times the thickness of the layers

achieved by vapor phase deposition (see scale bar of Figure 7.32 (b)). Should an aggregation occur on an EEC sensor, the cross sectional area of the multilayer region is also a significant fraction of the area of the 15 μm x 15 μm sensor mesa.

Our group confirmed deposition of silanes and biotin linkers by fluorescence microscopy in the protocol development and chemical selection phase of the project. However, that method does not give any information about the thicknesses of the layers, only the presence and density of active amine groups.

The four point method intentionally measures only the conductivity change in the mesa itself by eliminating influences of the leads and contacts. It is possible that thick silane layers separated the binding sites from the sensors reducing the expected signal. On the other hand, two-point measurements not only measure the conductivity changes in the mesa, but also any induced voltages along the traces and contacts. This significantly increases the effective sensing area to be much larger than the aggregate areas. Although we did not expect the induced response in a long strip of metal to be as large as that of the sensor itself, it is possible that the two point measurements, like an ISFET, pick up the cumulative effect of the binding events above the leads and the device. That is potentially the origin of the sensitivity of the two point measurements and the distribution of offsets in the resistance. The position of an aggregated, multilayer region obviously could not be controlled. The total area of monolayer and of strongest binding signal could be very inconsistent between sensors and even between leads on the same sensor.

While it is likely that altering the functionalization procedure will result in a consistent film and therefore consistent two-point sensitivity between independent sensors, the four point measurement on bare devices was consistent even in an environment when other configurations

were not. This demonstrates a fundamental advantage of reliable, *quantitative* calibration of EEC sensors under the traditional EXX method of measurement. Also, we may propose from the result of Figure 7.26 that it is unlikely that an aggregation was positioned near any of the bare detector mesas. The devices behaved too similarly to suspect one of having a different effective sensing area.

Section 7.3.2.5 Bare versus Shunted: Discussion

The bare EEC sensors generally show the highest sensitivity and are the only EEC sensors to demonstrate a four point resistance signal larger than the noise of the measurement. The shunted EEC sensors' four point data show no response to environmental conditions. In understanding this result, there are several key points to consider.

First, recall that the EEC sensors showed degraded Schottky interfaces that were instead Ohmic. The floating, Ohmic shunt interface should not affect the electric field of the bound surface charge. The field will be nulled inside the shunt, but due to the charge redistribution inside the metal and the metal's non-zero equipotential at the semiconductor boundary, the electric field should be largely transferred to the GaAs without modification. If the shunt were grounded, then shielding from the metal layer would block the electric field transduction to the semiconductor by setting the voltage of the metal equipotential surface to zero and allowing for charge to leach off to earth ground.

Second, if the bare sensor mesa and the shunted sensor mesa were identical, the response to electric field should also be identical. Recall that sensor 10 demonstrated degradation of the interface over time due to diffusion across the interface. Since the response to binding was significantly diminished for sensors with the shunt interface from those sensors without a shunt, it is likely that contaminant or diffused ions have increased the donor and the electron carrier

concentration in the shunted mesas. This increase in carriers in turn increases the propensity for static charge buildup in the mesa, a decrease in the Thomas-Fermi screening length, and maintains a high concentration of conducting free carriers which are screened from the effects of the external field.

Third, if the shunt/mesa interfaces were in fact Schottky, rather than Ohmic, the depletion region would have been highly sensitive to changes in the electric field and consequently so would the conductivity.

Fourth, if the shunt metal itself is shielding the mesa directly below the shunt by some mechanism rather than the transduction discussed above in the first point, the effective sensing area is only that exposed GaAs mesa around the periphery which is significantly smaller than the area of a bare EEC sensor. To conclude, the four-point response of the shunted sensors was eliminated and it is reasonable that the quenched four-point signal is due at least in part to diffusion in the GaAs and an increase in majority carriers in the mesa. However, we have clearly demonstrated that a biological, captavidin binding signal exists in the bare devices.

Section 7.3.3 Streptavidin Serial Dilution Curve

Section 7.3.3.1 Temperature Fluctuations and Evaporative Cooling

Experiments with streptavidin were also carried out on a second set of sensors. The four point resistance results demonstrated a high sensitivity to temperature changes due to the evaporative cooling of the chemical droplets. As mentioned above for the captavidin competitive binding assay, the experimental method used a 1-10 uL droplet centered on the 1mm x 1mm area on which the sensors are patterned. The sensors are at room temperature, as was the fluid. The effects of evaporation can also be seen in the captavidin assays, but are significantly less

pronounced which is why the subject is treated with the following exemplar bare sensor in Figure 7.33.

It should also be noted that two droplets of the same chemical were applied to study the repeatability and stability to a particular concentration. The first droplet was removed by syringe before the second was applied. Thus, for each labeled color bar in Figure 7.33 there are two saw-tooth like traces correlating with the application of two separate droplets, with the exception of the PBS baseline in which there were three droplets and three corresponding down spikes.

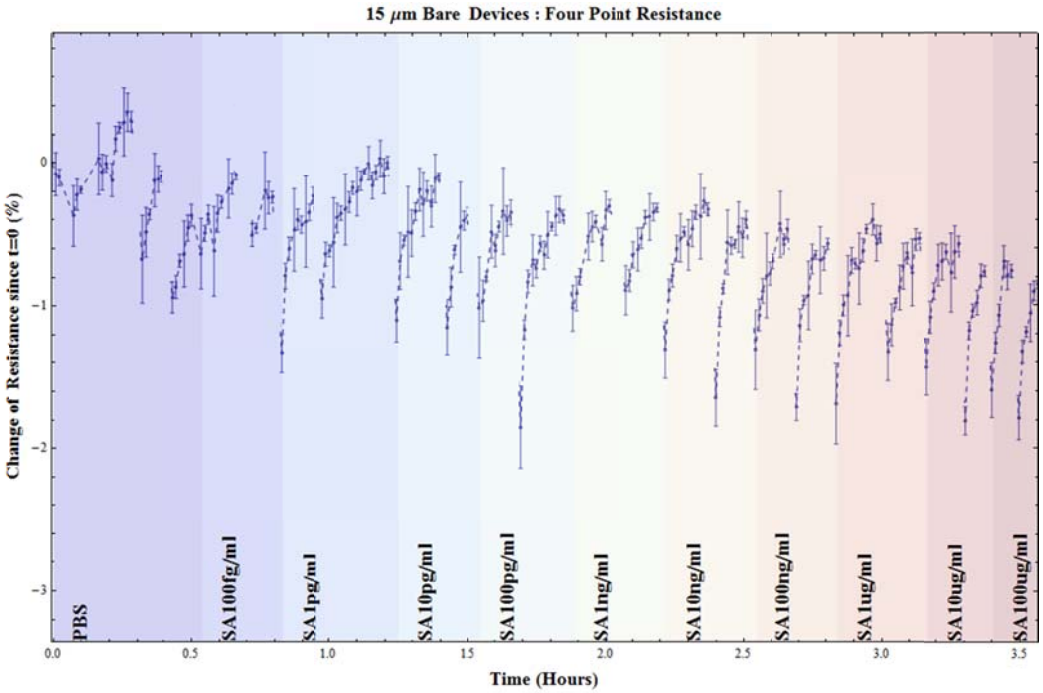

Figure 7.33 Example of four point resistance response from a bare sensor undergoing a streptavidin dilution curve. Two droplets of each chemical were applied correlating to the two downward spikes in each color bar. The dashed lines connecting the data points of a droplet are meant as a guide for the eye only.

Recall that in this temperature regime, the resistance of a semiconductor has an exponential dependence on temperature, since thermal excitations across the band gap from the valence band and from impurity levels will have a Boltzmann-like probability distribution. When a semiconductor is heated, more thermal excitations into the conduction band can occur and the

resistance will decrease. Inversely, when the semiconductor is cooled, thermal excitations are less likely and the carrier concentration in the conduction band will decrease, increasing the resistance. Thus, the data in Figure 7.33 demonstrates a warmer drop at initial contact (highest volume) by the decrease in resistance. Since the droplet cools as the more energetic (hotter) molecules evaporate from the droplet surface, the resistance can be seen to increase until the next room temperature droplet is applied.

This data supports a change of method used in our experiments. The current work has moved away from droplets to larger volumes of fluid, such that an even temperature "heat bath" will exist across multiple measurements of the same chemical concentration and noise from an evaporating droplet's changing temperature may be eliminated.

As it is also evident, what minimal change there is in the four point resistance has a generally downward trend. This could be due to binding of the negatively-charged streptavidin to the sensor surface. This result is the compliment of the positively-charged, captavidin experiments in which the bare sensors' four-point binding signal showed a positive trending slope. However, the result is not definitive as there were clearly experimental issues that could be improved upon. Until a more robust experiment is performed, the opposite direction of the data trend is mentioned here with a possible, but unconfirmed, cause of protein binding.

Concluding statements

In this thesis, we demonstrate that EXX sensors are a promising class of heterostructures for detection in multiple applications.

In Chapter 4, the I-EOC sensor was shown to be a high Specific Detectivity, room temperature optical detector. The transition from ballistic to diffusive transport through the I-EOC heterostructure results in dynamic sensors which show promise for commercial and industrial applications. Imaging arrays constructed from the VLSI compatible I-EOC sensors would have a spatial resolution unparalleled by those in use today.

In the captavidin binding experiments described in Chapter 7, the detected four-point signal from bare sensors establishes at a proof of principle level that we have the capability to perform successful functionalization and binding experiments. These preliminary results indicate that the EEC sensor geometry is well-suited to transducing an electrochemical binding signal in the consistency between the four point data from independent sensors. In addition to the promise of reliable, *quantitative* calibration, the sensitivity of bare, four point data was shown to be the highest EEC sensitivity, higher than two point configurations. In the captavidin experiment, we also demonstrate the negative result that highly-doped mesas coupled with Ohmic interfaces are not more sensitive than a bare interface with a lower doping concentration. While this was not the intended goal of the original design, it confirms previous understanding of how the shunted EEC sensors function. Fundamental to a sensitive shunted EEC sensor is an intact Schottky interface which is why historically the EEC sensor was the first to have a rectifying interface after the development of EMR, EPC, and EOC. It will be left to later work to lower the signal to noise ratio, to establish definitively the thickness of the silane layers, and to demonstrate the increased sensitivity of Schottky-based sensors to a captavidin binding experiment.

Appendix

Simple DNA Model

In[1]:=
```
k = 8.9875517*^9 ; (* Coulomb's constant for vaccuum 1/4πεo, Units: N m^2 /C^2 *)
ϵ = 78; (* Relative static dielectric constant for water: unitless*)
a = 0.34*^-9; (* DNA base pair spacing Units: m *)
dnaq = -0.5; (* Charge on a single base pair *)
qe = 1.602*^-19; (* electron charge Units: C *)
n = 20;
```

Convert to (0.01 V/cm) = V/m to gain the final integral funciton.

■ Electric Field

In[7]:=
```
EfieldDiscrete3D[x_, y_, fo_, n_] :=
  0.01 Evaluate[qe dnaq (k/ϵ) Sum[1/Sqrt[x^2 + y^2 + (a d + fo)^2]^3, {d, 0, n-1}] {x, y, a d + fo}];

EfieldDiscreteX[x_, y_, fo_, n_] := 0.01 Evaluate[qe dnaq (k/ϵ) Sum[x/Sqrt[x^2 + y^2 + (a d + fo)^2]^3, {d, 0, n-1}]];

EfieldDiscreteZ[x_, y_, fo_, n_] := 0.01 Evaluate[qe dnaq (k/ϵ) Sum[(a d + fo)/Sqrt[x^2 + y^2 + (a d + fo)^2]^3, {d, 0, n-1}]];

EfieldIntegral00[z_, n_] := Evaluate[Assuming[z > 0, (qe dnaq n)/((n - 1) a) (k/ϵ) Integrate[1/(r + z)^2, {r, 0, (n-1) a}]]];

EfieldVector[x_, y_, z_, n_] :=
  Evaluate[Assuming[{x ∈ Reals, y ∈ Reals, z > 0},
    (qe dnaq n)/((n - 1) a) (k/ϵ) Integrate[1/Sqrt[x^2 + y^2 + (r + z)^2]^3 {x, y, r + z}, {r, 0, (n-1) a}]]];

EfieldIntegral3D[x_, y_, z_, n_] :=
  If[x == y == 0, {0, 0, 0.01 EfieldIntegral00[z, n]}, 0.01 EfieldVector[x, y, z, n]];

EfieldIntegralX[x_, y_, z_, n_] := If[x == y == 0, 0, 0.01 EfieldVector[x, y, z, n][[1]]]
EfieldIntegralZ[x_, y_, z_, n_] :=
  If[x == y == 0, 0.01 EfieldIntegral00[z, n], 0.01 EfieldVector[x, y, z, n][[3]]];

fontsize = 20;
Needs["PlotLegends`"]
```

```
Show[LogPlot[Norm[EfieldIntegral3D[x 1*^-6, 0, fo, n]],
  {x, -15, 15}, PlotRange → {{-15, 15}, {5*^-3, 1*^6}}, PlotPoints → 100],
 ListLogPlot[Table[{x, Norm[EfieldDiscrete3D[x 1*^-6, 0, fo, n]]}, {x, -15, 15}],
  PlotStyle → Directive[Darker[Green], PointSize[Large]]], Frame → True,
 LabelStyle → Directive[20, FontFamily → "Times"], FrameLabel →
  {Style["X position along Y = 0 line in sensor plane [μm]", fontsize],
   Style["E Field Magnitude [V/cm]", fontsize], Style["E field from " <>
     ToString[n] <> " base pairs and a functionalization layer = " <>
     ToString[fo 1*^9] <> " nm", fontsize]}, ImageSize → 550]
```

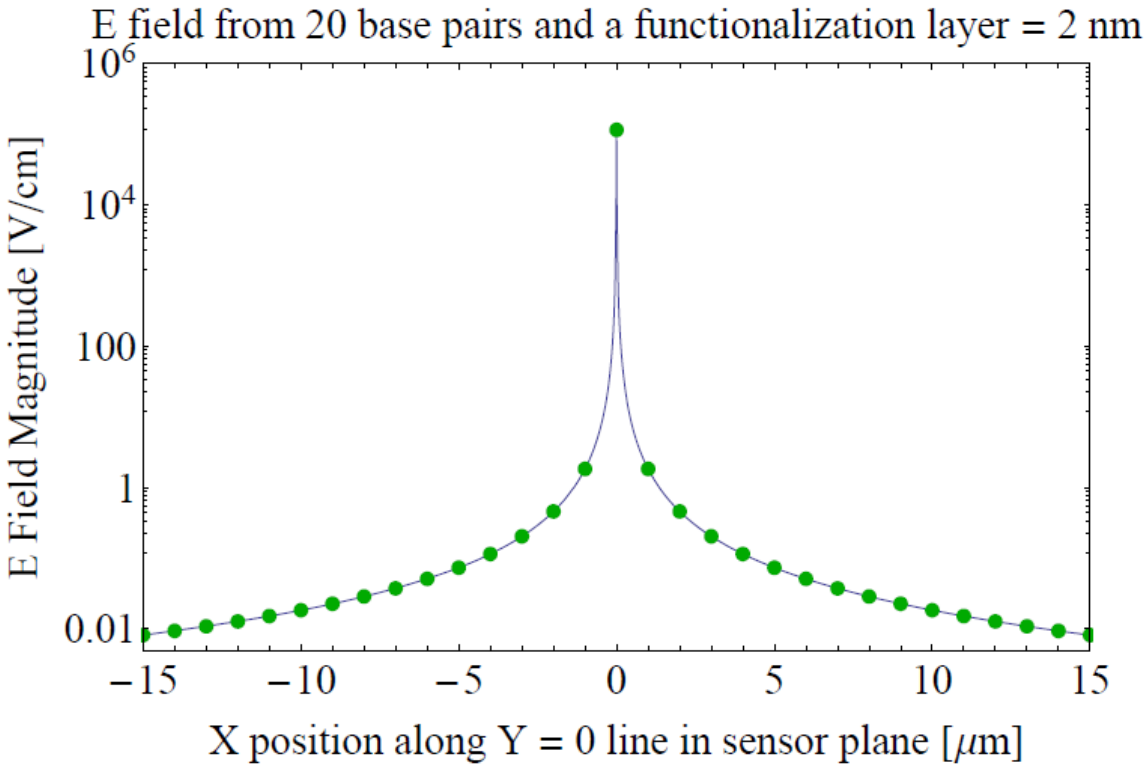


```
fontsize = 16;
```

```
LogLogPlot[
 100
  (Norm[EfieldIntegral3D[x 1*^-6, 0, 0.5 fo, 40]] -
     Norm[EfieldIntegral3D[x 1*^-6, 0, fo, 20]]) /
   Norm[EfieldIntegral3D[x 1*^-6, 0, 0.5 fo, 40]], {x, 10^-4, 15}, PlotPoints → 100,
 Frame → True, PlotStyle → Thick,
 FrameLabel → {Style["X position along Y = 0 line in sensor plane [μm]", fontsize],
   Style["% difference", fontsize],
   Style[Column[{"% difference in E field from (40 base pairs at 1nm)",
      "and (20 base pairs at 2 nm)"}, Center], fontsize]}, ImageSize → 500]
```

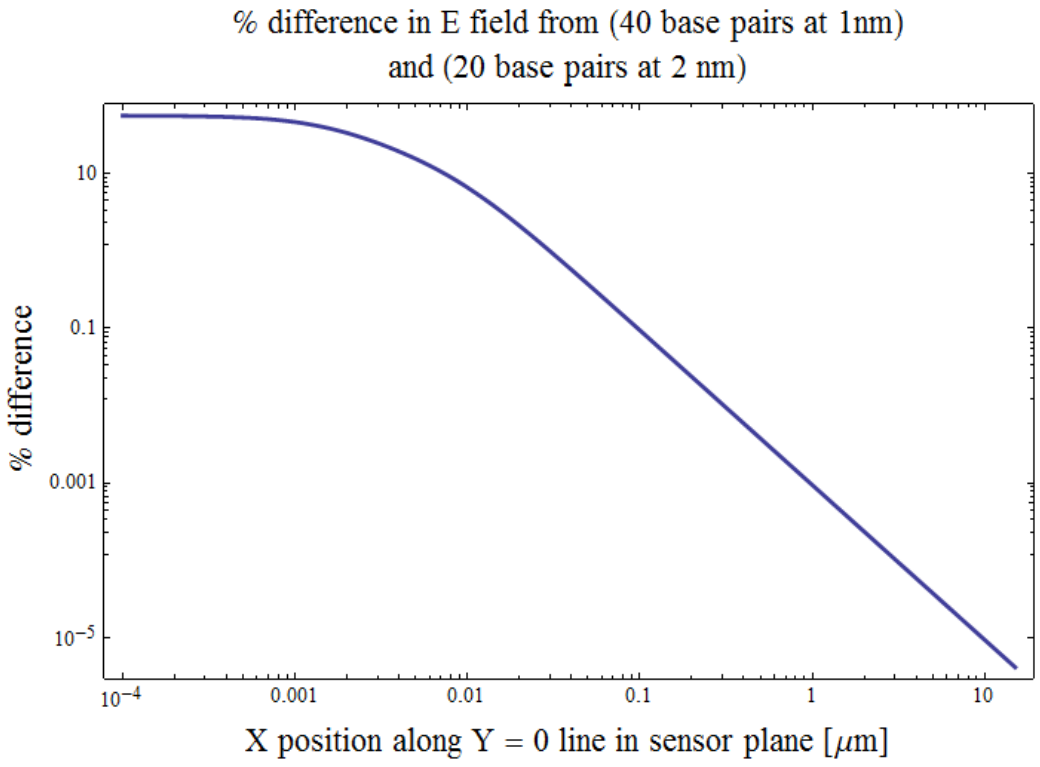


```
Show[LogPlot[Abs[EfieldIntegralZ[x 1*^-6, 0, fo, n]], {x, -15, 15},
  PlotRange → {{-15, 15}, {5*^-7, 1*^6}}, PlotPoints → 100],
 ListLogPlot[Table[{x, Abs[EfieldDiscreteZ[x 1*^-6, 0, fo, n]]}, {x, -15, 15}],
  PlotStyle → Directive[Darker[Green], PointSize[Large]]], Plot[3.05, {x, -15, 15}],
 Frame → True, LabelStyle → Directive[20, FontFamily → "Times"],
 FrameLabel → {Style["X position along Y = 0 line in sensor plane [μm]", fontsize],
   Style["E_z Field Magnitude [V/cm]", fontsize],
   Style["E_z field from " <> ToString[n] <>
     " base pairs and a functionalization layer = " <> ToString[fo 1*^9] <> " nm",
    fontsize]}, ImageSize → 550]
```

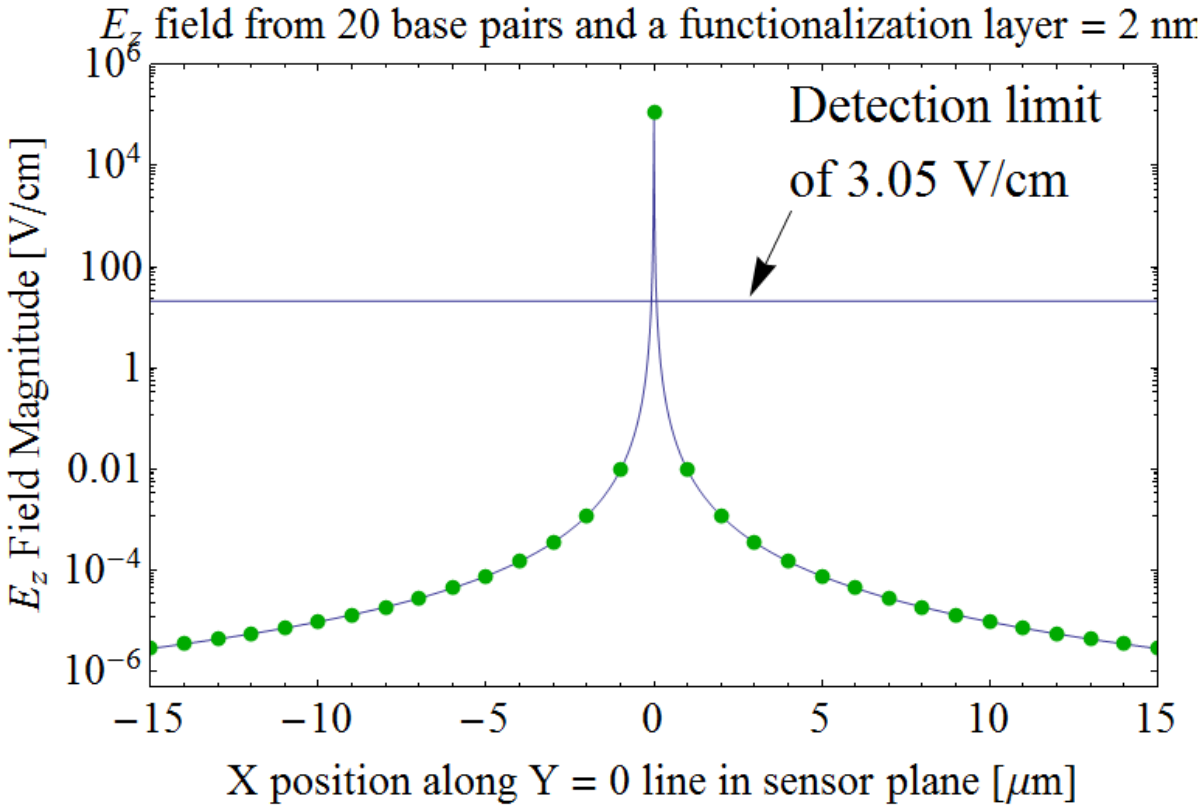
E_z field from 20 base pairs and a functionalization layer = 2 nm
Detection limit
of 3.05 V/cm
E_z Field Magnitude [V/cm]
10^6
10^4
100
1
0.01
10^{-4}
10^{-6}
−15
−10
−5
0
5
10
15
X position along Y = 0 line in sensor plane [μm]

```
Show[LogPlot[Abs[EfieldIntegralZ[x 1*^-6, 0, fo, n]], {x, -15, 15},
  PlotRange → {{-0.2, 0.2}, {3, 1*^6}}, PlotPoints → 100 000],
 ListLogPlot[Table[{x, Abs[EfieldDiscreteZ[x 1*^-6, 0, fo, n]]}, {x, -15, 15, 0.01}],
  PlotStyle → Directive[Darker[Green], PointSize[Large]]], Frame → True,
 LabelStyle → Directive[20, FontFamily → "Times"],
 FrameLabel → {Style["X position along Y = 0 line in sensor plane [μm]", fontsize],
   Style["Ez Field Magnitude [V/cm]", fontsize],
   Style["Ez field from " <> ToString[n] <>
     " base pairs and a functionalization layer = " <> ToString[fo 1*^9] <> " nm",
    fontsize]}, ImageSize → 550]
```

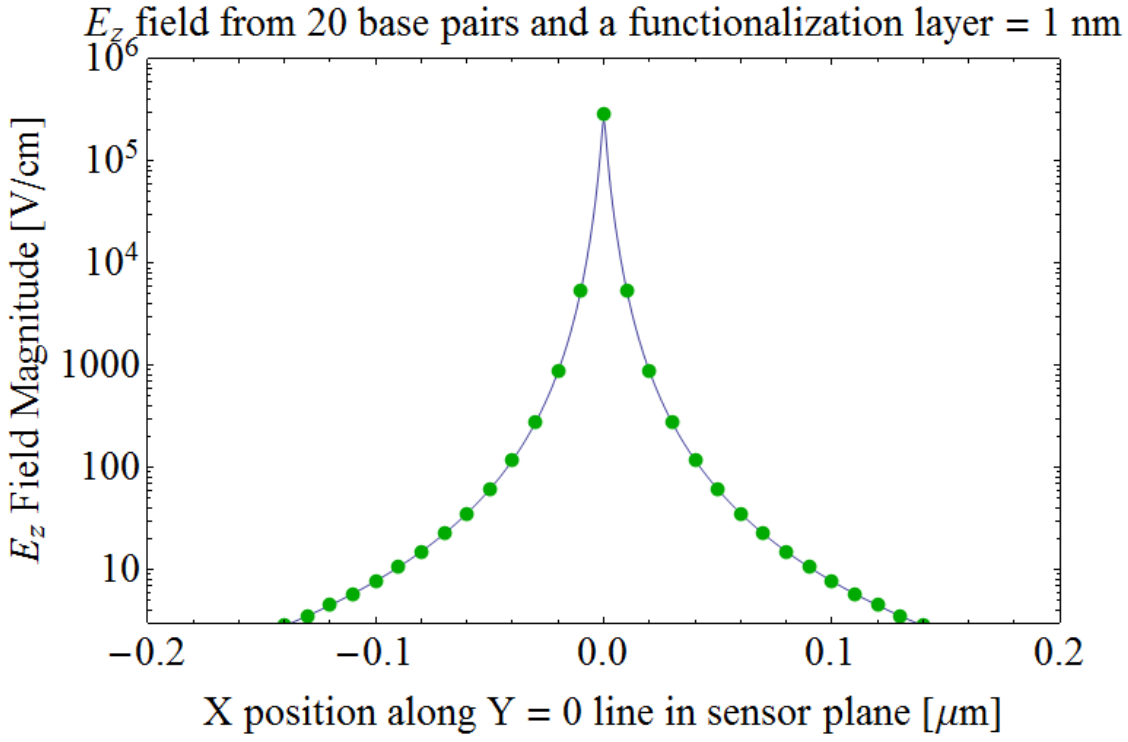


```
Show[LogPlot[Abs[EfieldIntegralX[x 1*^-6, 0, fo, n]], {x, -2, 2},
  PlotRange → {{-1, 1}, {3, 1*^6}}, PlotPoints → 100 000],
 ListLogPlot[Table[{x, Abs[EfieldDiscreteX[x 1*^-6, 0, fo, n]]}, {x, -2, 2, 0.1}],
  PlotStyle → Directive[Darker[Green], PointSize[Large]]], Frame → True,
 LabelStyle → Directive[20, FontFamily → "Times"],
 FrameLabel → {Style["X position along Y = 0 line in sensor plane [μm]", fontsize],
   Style["Ex Field Magnitude [V/cm]", fontsize],
   Style["Ex field from " <> ToString[n] <>
     " base pairs and a functionalization layer = " <> ToString[fo 1*^9] <> " nm",
    fontsize]}, ImageSize → 550]
```

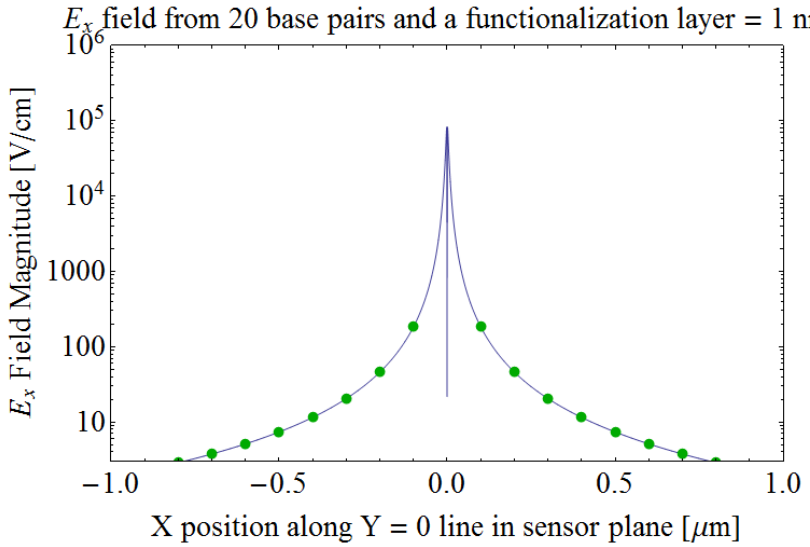

Simple Protein Model

- **Calculate net charge**

```
pH = 7.4;
qstp = -3.91 * pH + 20.455 (* charge in # of el on streptavidin *)
qavd = -2.702 * pH + 36.473 (* charge in # of el on avidin *)
el = 1.6*^-19; (* charge of an electron Units: Coulombs *)
k = 8.9875517*^9 ; (* Coulomb's constant for vaccuum 1/4πεo, Units: N m^2 /C^2 *)
ϵ = 78; (* Relative static dielectric constant for water: unitless*)
Needs["PlotLegends`"]
```

```
-8.479
```

```
16.4782
```

Charges in Coulombs

- **Magnitude of electric field from point charge at (0,0,z) along line in plane (x,0,0) for range -X<x<X, converted to units of V/cm**
- **Plot for Avidin**

```
fontsize = 20;
```

- **Electric field magnitude in all directions - absolute magnitude**
- **Electric field magnitude in Z direction**

```
{f1, f2, fstep} = {1, 801, 100};
x1 = 0.7;
LogPlot[Evaluate[Table[Abs[EfieldZ[qavd, x, z]], {z, f1 10^-9, f2 10^-9, fstep 10^-9}]],
 {x, -x1, x1}, PlotRange → {{-x1, x1}, {3, 1*^7}},
 PlotLegend → (Style[Text[# <> "μm"], 16] & /@ ToString /@ Range[0.001 f1, 0.001 f2, 0.001 fstep]),
 LegendSize → {0.3, 0.7}, LegendPosition → {0.8, -.3}, LegendLabel → Style["Binding Height", 14],
 Frame → True, PlotStyle → Thick,
 FrameLabel → {Style["X position along Y = 0 line in sensor plane [μm]", fontsize],
   Style["Ez Field Magnitude [V/cm]", fontsize],
   Style["Ez field from Avidin in Water", fontsize]},
 LabelStyle → Directive[fontsize, FontFamily → "Times"], ImageSize → 700]
```

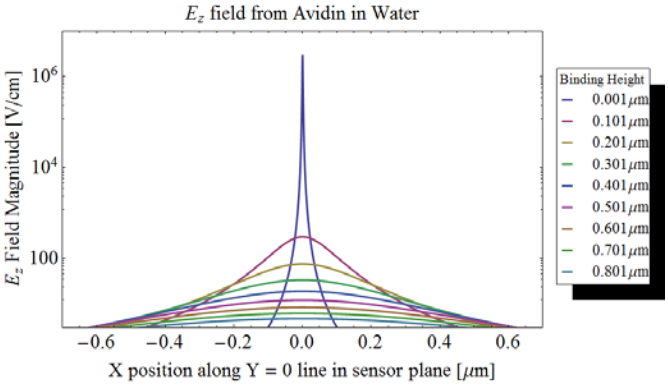

■ **Electric field magnitude in X direction**

```
{f1, f2, fstep} = {1, 601, 100};
x1 = 1;
LogPlot[Evaluate[Table[Abs[EfieldX[qavd, x, z]], {z, f1 10^-9, f2 10^-9, fstep 10^-9}]],
 {x, -x1, x1}, PlotRange → {{-x1, x1}, {3, 1*^7}},
 PlotLegend → (Style[Text[# <> "μm"], 16] & /@ ToString /@ Range[0.001 f1, 0.001 f2, 0.001 fstep]),
 LegendSize → {0.3, 0.7}, LegendPosition → {0.8, -.3}, LegendLabel → Style["Binding Height", 14],
 Frame → True, PlotStyle → Thick,
 FrameLabel → {Style["X position along Y = 0 line in sensor plane [μm]", fontsize],
   Style["Ex Field Magnitude [V/cm]", fontsize],
   Style["Ex field from Avidin in Water", fontsize]},
 LabelStyle → Directive[fontsize, FontFamily → "Times"], ImageSize → 700]
```

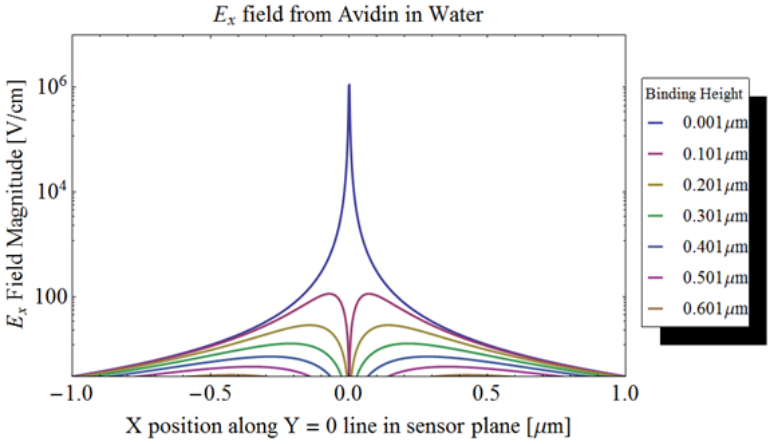

Notice that the 0.001 um line is not plotted as Ex = 0 at the origin. The equation evaluates correctly at the origin, but *Mathematica* is not sampling a high enough number of points close to the origin to demonstrate the behavior of 0.001um correctly. This is altered in the next figure.

```
EfieldX[qavd, 0, 10^-9]
```

```
0.
```

```
{f1, f2, fstep} = {1, 501, 100};
x1 = 1;
```

```
LogPlot[Evaluate[Table[Abs[EfieldX[qavd, x, z]], {z, f1 10^-9, f2 10^-9, fstep 10^-9}]],
 {x, -x1, x1}, PlotRange → {{-x1, x1}, {3, 1*^7}}, PlotPoints → 100 000,
 PlotLegend → (Text[# <> "μm"] & /@ ToString /@ Range[0.001, 1.001, 0.1]), LegendSize → {0.3, 0.7},
 LegendPosition → {0.8, -.3}, LegendLabel → "Binding Height", Frame → True, PlotStyle → Thick,
 FrameLabel → {Style["X position along Y = 0 line in sensor plane [μm]", fontsize],
   Style["E_x Field Magnitude [V/cm]", fontsize],
   Style["E_x field from Avidin in Water", fontsize]},
 LabelStyle → Directive[fontsize, FontFamily → "Times"], ImageSize → 700]
```

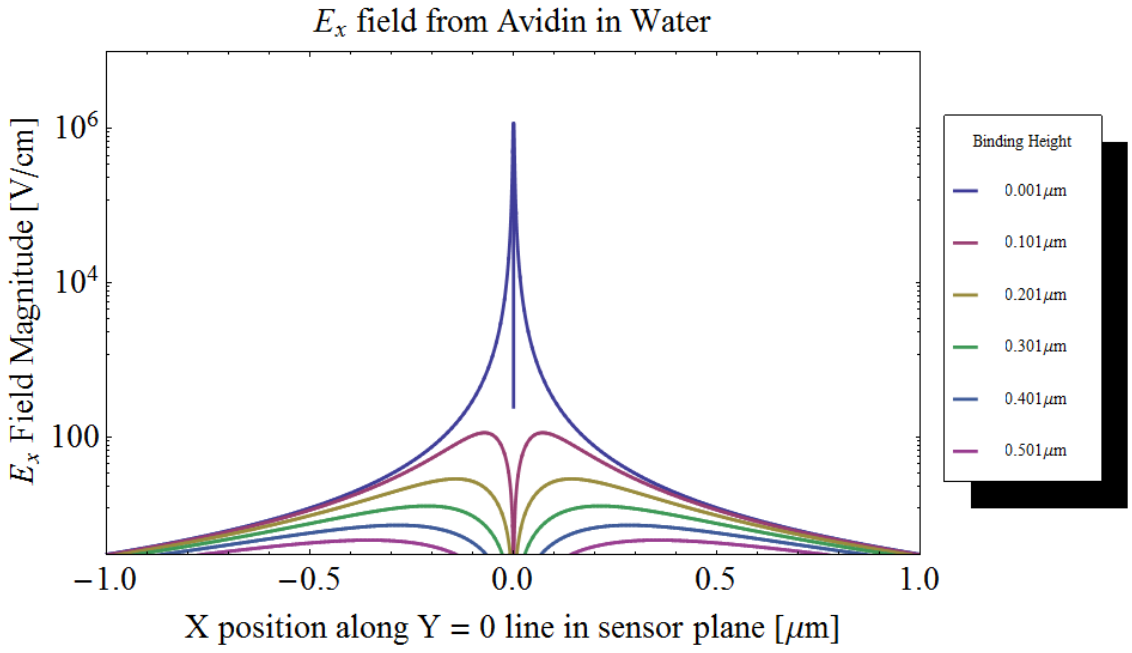

■ **Plot for Streptavidin**

Ionic DNA Model

Calculate net charge

```
Needs["PlotLegends`"]

k = 8.9875517*^9 ; (* Coulomb's constant for vaccuum 1/4πεo, Units: N m^2 /C^2 *)
ϵ = 78; (* Relative static dielectric constant for water: unitless*)
a = 0.34*^-9; (* DNA base pair spacing Units: m *)
dnaq = -0.5; (* Charge on a single base pair *)
n = 20;
el = 1.6*^-19; (* charge of an electron Units: Coulombs *)
ϵr = 78; (* Relative static dielectric constant for water: unitless*)
ϵo = 8.854*^-12 ; (*  vaccuum permitivity, Units: C2/(CV m) *)
aBohr = 0.529*^-10; (*  Bohr Radius,
test value for the hard shell model of atom Unit: meters *)
kbT = 1.3806488*^-23 (273 + 25); (* m2 kg s-2 *)
Na = 6.022*^23; (* Avogadros Number #/mol *)
```

Magnitude of electric field from point charge at (0, 0, z) along line in plane (x, 0, 0) for range -X<x<X, converted to units of V/cm

```
Ion[p_] := 0.5 Total[p];

K[p_] := el Sqrt[1000 Na 2 Ion[p] / (ϵo ϵr kbT)]

p1 = {0.0027, 0.138, 10^(-7.4), 0.0027, 0.138, 10^(-6.6)};

Eionic[r_, a_, q_, p_] := 0.01 (q el Exp[-K[p] (r - a)] / (r r ϵo ϵr (a K[p] + 1)) + q el K[p] Exp[-K[p] (r - a)] / (r ϵo ϵr (a K[p] + 1)))
```

Above : Factor of 0.01 converts V/m to V/cm.

Equations

```
EfieldDiscreteIons[x_, fo_, aBohr_, q_, p_] :=
  Sum[{x, a d + fo} / Sqrt[x^2 + (a d + fo)^2] Eionic[Sqrt[x^2 + (a d + fo)^2], aBohr, q, p], {d, 0, n-1}];

EfieldDiscreteIonsZ[x_, y_, fo_, aBohr_, q_, p_] :=
  Sum[a d + fo / Sqrt[x^2 + y^2 + (a d + fo)^2] Eionic[Sqrt[x^2 + y^2 + (a d + fo)^2], aBohr, q, p], {d, 0, n-1}];

EfieldDiscreteIonsX[x_, y_, fo_, aBohr_, q_, p_] :=
  Sum[x / Sqrt[x^2 + y^2 + (a d + fo)^2] Eionic[Sqrt[x^2 + y^2 + (a d + fo)^2], aBohr, q, p], {d, 0, n-1}]
```

1/K is the Debye Screening length for 1 M PBS in meters.

```
1 / K[p1]
```

8.09309×10^{-10}

```
fo = 10^-9;
Eionic[5 fo, aBohr, 1, 0 p1]
Eionic[5 fo, aBohr, 1, 4.4 p1]
```

```
92 671.4
```

```
3.0718
```

■ **Average field in Z direction over areas**

```
{x1, x2, xstep} = {10^-9, 1001 × 10^-9, 10 × 10^-9};
{f1, f2, fstep} = {1, 11, 2};
data =
  Table[
   {xi 10^9, NIntegrate[Evaluate[EfieldDiscreteIonsZ[x, y, z 10^-9, aBohr, 0.5, p1]] / (4 xi xi),
     {x, xi, -xi}, {y, xi, -xi}, MaxPoints → 40 000]}, {z, f1, f2, fstep}, {xi, x1, x2, xstep}];

ListLogLogPlot[data, Joined → True,
 PlotLegend → (Style[Text[# <> "nm"], 20] & /@ ToString /@ Range[f1, f2, f3]),
 LegendSize → {0.3, 0.7}, LegendPosition → {0.9, -.3}, LegendLabel → Style["Binding Height", 14],
 Frame → True, PlotStyle → Thick, PlotRange → {{x1 10^9, x2 10^9}, {3, 1*^6}},
 FrameLabel → {Style["Distance  Coordinate, d [nm]", fontsize],
   Style["Average Ez Field Magnitude [V/cm]", fontsize],
   Style["Average Ez over area:(-d,-d)<(x,y)<(d,d) for DNA in 10 mM PBS", fontsize]},
 LabelStyle → Directive[fontsize, FontFamily → "Times"], ImageSize → 700]
```

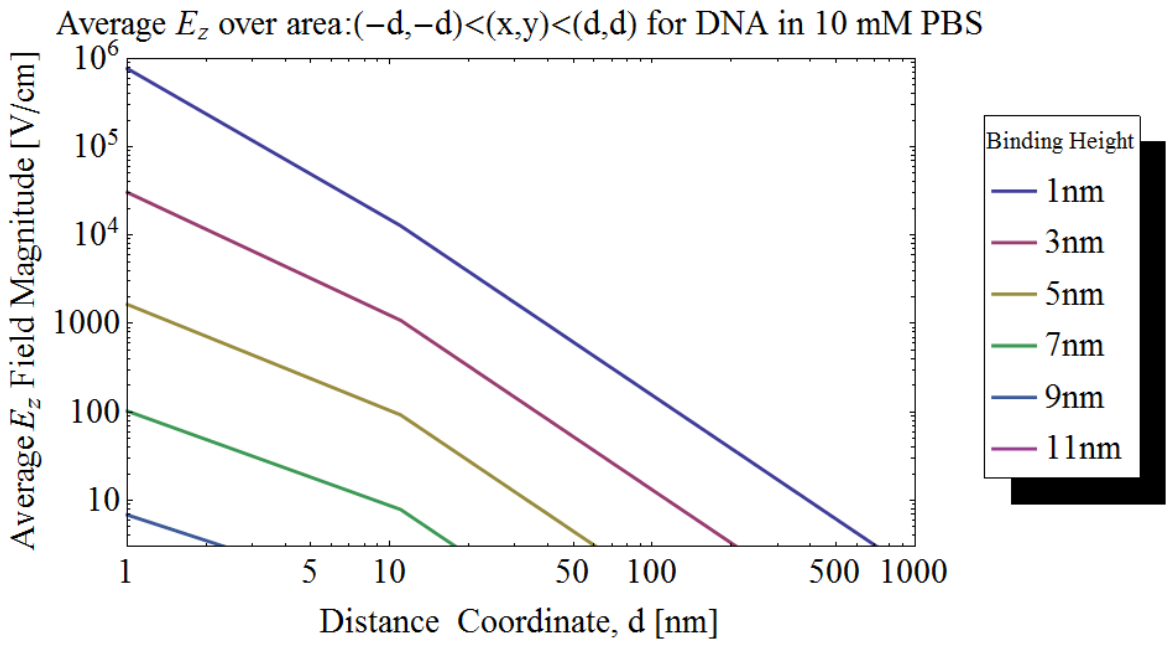

■ **Effect of Ionic Strength at origin - demonstrate screening**

```
fontsize = 20;
fo = 10^-9;
LogPlot[{Eionic[5 fo, aBohr, 1, 0.1 d p1], Eionic[5 fo, aBohr, 1, p1], 3.05}, {d, 0, 100},
 Frame → True, PlotStyle → Thick, PlotRange → All,
 FrameLabel → {Style["Ionic Concentration, (mM of PBS)", fontsize],
   Style["E Field Magnitude [V/cm]", fontsize],
   Style["E field from Proton in PBS, 5 nm From Surface", fontsize]},
 LabelStyle → Directive[fontsize, FontFamily → "Times"], ImageSize → 550]
```

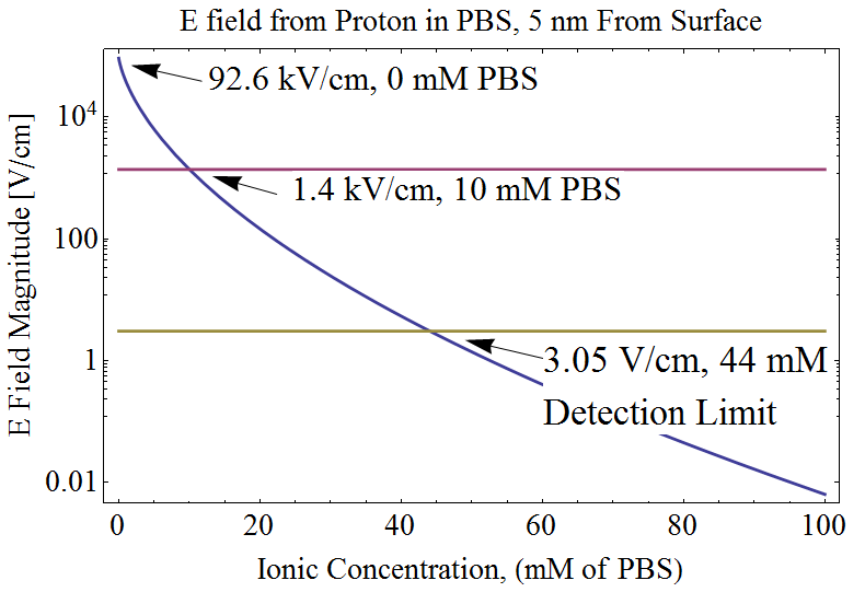

■ **Avidin - E field magnitude, all directions**

```
fontsize = 20;
{f1, f2, f3} = {1, 21, 4};
x1 = 20;
LogPlot[
 Evaluate[Table[Norm[EfieldDiscreteIons[x*10^-9, z, aBohr, 0.5, p1]],
   {z, f1*10^-9, f2*10^-9, f3*10^-9}]], {x, -x1, x1}, PlotRange → {{-x1, x1}, {5*^-10, 1*^8}},
 PlotLegend → (Text[# <> "nm"] & /@ ToString /@ Range[f1, f2, f3]), LegendSize → {0.3, 0.7},
 LegendPosition → {0.9, -.3}, LegendLabel → "Binding Height", Frame → True, PlotStyle → Thick,
 FrameLabel → {Style["X position along Y = 0 line in sensor plane [nm]", fontsize],
   Style["E Field Magnitude [V/cm]", fontsize],
   Style["E field from DNA in 10 mM PBS, Full Ionization", fontsize]},
 LabelStyle → Directive[fontsize, FontFamily → "Times"], ImageSize → 700]
```

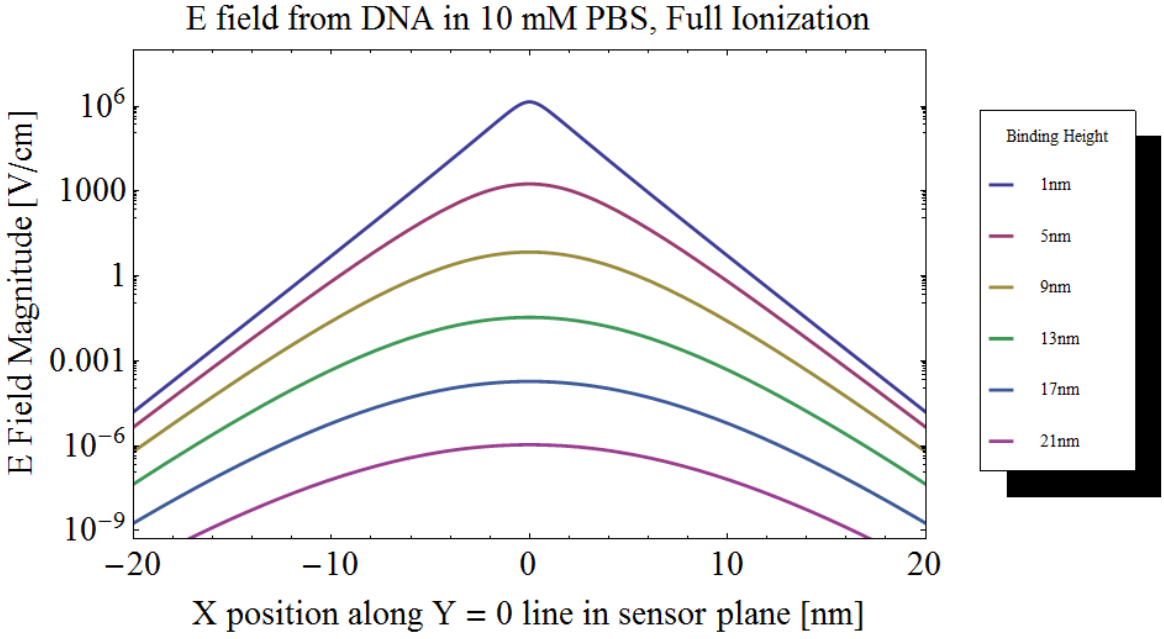

```
fontsize = 20;
{f1, f2, f3} = {1, 9, 2};
x1 = 11;
LogPlot[
 Evaluate[Table[Norm[EfieldDiscreteIons[x * 10^-9, z, aBohr, 0.5, p1]],
   {z, f1 * 10^-9, f2 * 10^-9, f3 * 10^-9}]], {x, -x1, x1}, PlotRange → {{-x1, x1}, {3, 1*^7}},
 PlotLegend → (Text[# <> "nm"] & /@ ToString /@ Range[f1, f2, f3]), LegendSize → {0.3, 0.7},
 LegendPosition → {0.9, -.3}, LegendLabel → "Binding Height", Frame → True, PlotStyle → Thick,
 FrameLabel → {Style["X position along Y = 0 line in sensor plane [nm]", fontsize],
   Style["E Field Magnitude [V/cm]", fontsize],
   Style["E field from DNA in 10 mM PBS, Full Ionization", fontsize]},
 LabelStyle → Directive[fontsize, FontFamily → "Times"], ImageSize → 700]
```

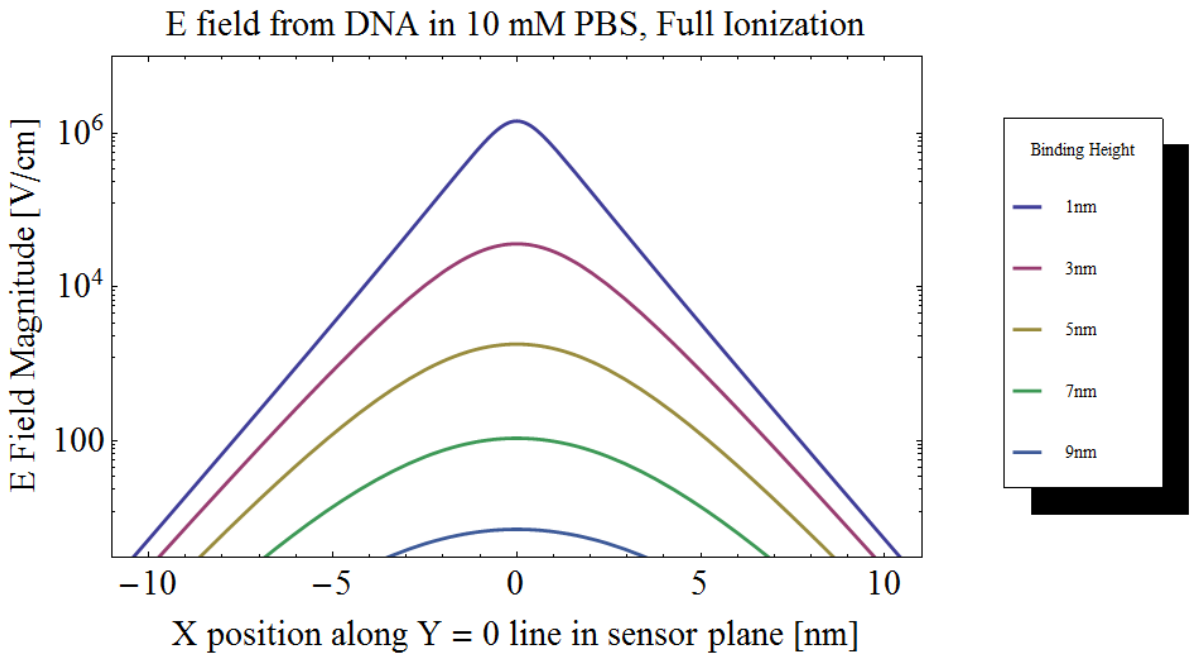


```
EfieldDiscreteIonsZ[0 * 10^-9, 0, 10^-9, aBohr, 0.5, p1]
```

1.42533×10^{6}

```
EfieldDiscreteIons[0 * 10^-9, 10^-9, aBohr, 0.5, p1]
```

$\{0., 1.42533 \times 10^{6}\}$

■ **Avidin - E field magnitude - Z direction only**

```
{f1, f2, f3} = {1, 11, 1};
x1 = 20;
fontsize = 20;
LogPlot[Evaluate[Table[Abs[EfieldDiscreteIonsZ[x * 10^-9, 0, z, aBohr, 0.5, p1]],
   {z, f1 * 10^-9, f2 * 10^-9, f3 * 10^-9}]], {x, -x1, x1}, PlotRange → {{-x1, x1}, {5*^-10, 1*^7}},
 PlotLegend → (Text[# <> "nm"] & /@ ToString /@ Range[f1, f2, f3]), LegendSize → {0.3, 0.7},
 LegendPosition → {0.9, -.3}, LegendLabel → "Binding Height", Frame → True, PlotStyle → Thick,
 FrameLabel → {Style["X position along Y = 0 line in sensor plane [nm]", fontsize],
   Style["Ez Field Magnitude [V/cm]", fontsize],
   Style["Ez field from DNA in 10 mM PBS, Full Ionization", fontsize]},
 LabelStyle → Directive[fontsize, FontFamily → "Times"], ImageSize → 700]
```

```
{f1, f2, f3} = {1, 9, 1};
x1 = 10;
fontsize = 20;
LogPlot[Evaluate[Table[Abs[EfieldDiscreteIonsZ[x * 10^-9, 0, z, aBohr, 0.5, p1]],
   {z, f1 * 10^-9, f2 * 10^-9, f3 * 10^-9}]], {x, -x1, x1}, PlotRange → {{-x1, x1}, {3.05, 1*^7}},
 PlotLegend → (Style[Text[# <> " nm"], 20] & /@ ToString /@ Range[f1, f2, f3]),
 LegendSize → {0.3, 0.7}, LegendPosition → {0.8, -.3}, LegendLabel → Style["Binding Height", 14],
 Frame → True, PlotStyle → Thick,
 FrameLabel → {Style["X position along Y = 0 line in sensor plane [nm]", fontsize],
   Style["Ez Field Magnitude [V/cm]", fontsize],
   Style["Ez field from DNA in 10 mM PBS, Full Ionization", fontsize]},
 LabelStyle → Directive[fontsize, FontFamily → "Times"], ImageSize → 700]
```

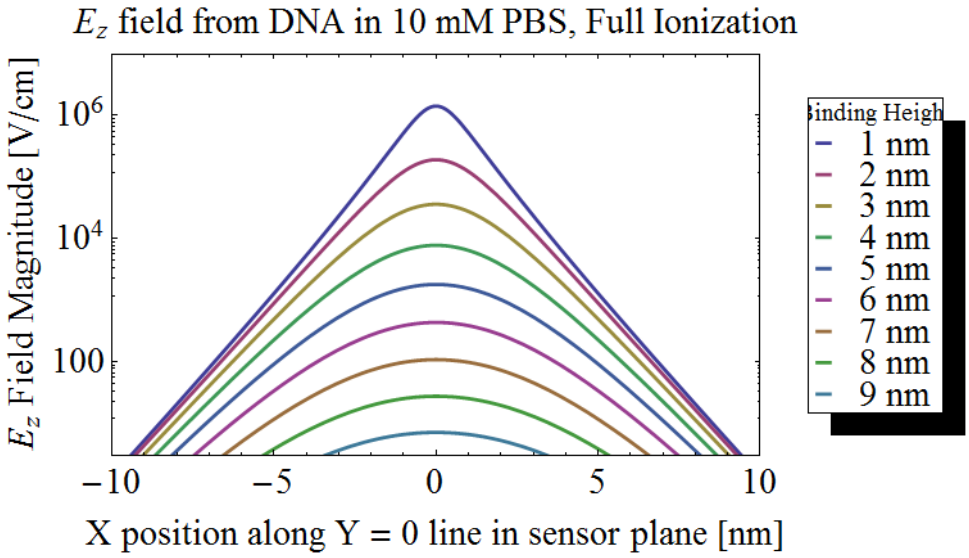

■ **Avidin - E field magnitude - X direction only**

```
{f1, f2, f3} = {1, 9, 1};
x1 = 10;
fontsize = 20;
LogPlot[Evaluate[Table[Abs[EfieldDiscreteIonsX[x * 10^-9, 0, z, aBohr, 0.5, p1]],
   {z, f1 * 10^-9, f2 * 10^-9, f3 * 10^-9}]], {x, -x1, x1}, PlotRange → {{-x1, x1}, {3.05, 1*^7}},
 PlotLegend → (Style[Text[# <> " nm"], 20] & /@ ToString /@ Range[f1, f2, f3]),
 LegendSize → {0.3, 0.7}, LegendPosition → {0.8, -.3}, LegendLabel → Style["Binding Height", 14],
 Frame → True, PlotStyle → Thick,
 FrameLabel → {Style["X position along Y = 0 line in sensor plane [nm]", fontsize],
   Style["E_x Field Magnitude [V/cm]", fontsize],
   Style["E_x field from DNA in 10 mM PBS, Full Ionization", fontsize]},
 LabelStyle → Directive[fontsize, FontFamily → "Times"], ImageSize → 700]
```

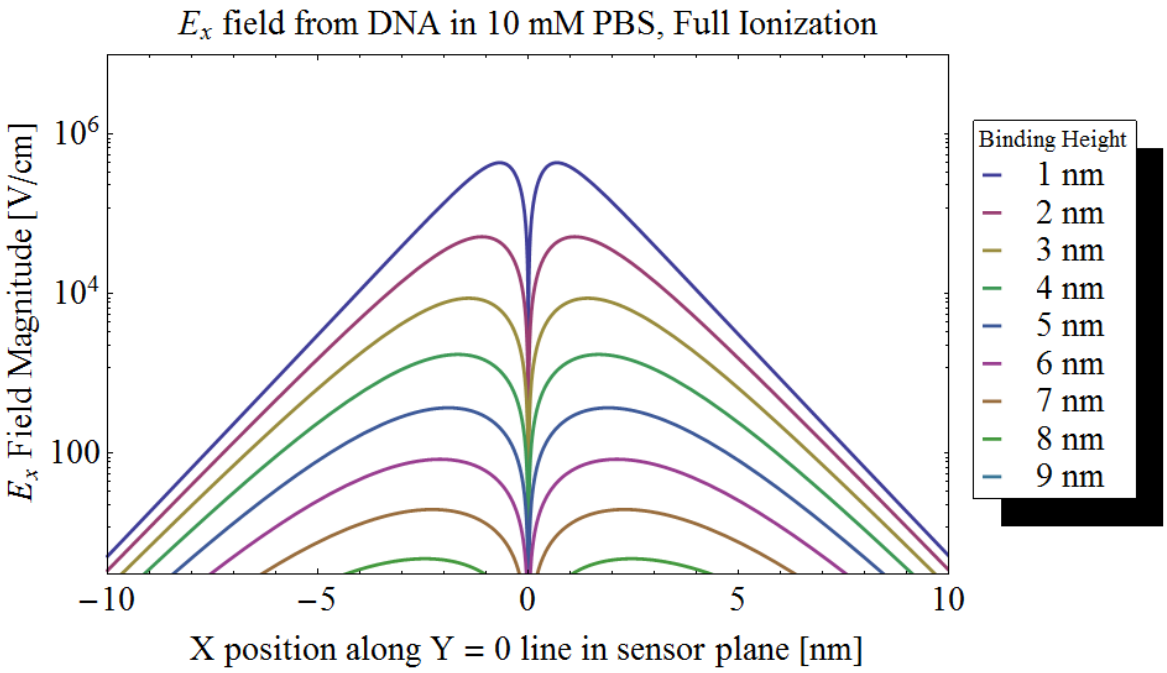

Ionic Protein Model

■ Calculate net charge

```
Needs["PlotLegends`"]

pH = 7.4;
qstp = -3.91 * pH + 20.455 (* charge in # of el on streptavidin *)
qavd = -2.702 * pH + 36.473 (* charge in # of el on avidin *)
el = 1.6*^-19; (* charge of an electron Units: Coulombs *)
εo = 8.854*^-12 ; (*  vaccuum permitivity, Units: C2/(CV m) *)
εr = 78.5; (* Relative static dielectric constant for water: unitless*)
kbT = 1.3806488*^-23 (273 + 25); (* m2 kg s-2 *)
aBohr = 0.529*^-10; (*  Bohr Radius,
test value for the hard shell model of atom Unit: meters *)
Na = 6.022*^23; (* Avogadros Number #/mol *)
```

- **Magnitude of electric field from point charge at (0, 0, z) along line in plane (x, 0, 0) for range -X<x<X, converted to units of V/cm**

```
Ion[p_] := 0.5 Total[p];

K[p_] := el Sqrt[1000 Na Abs[2 Ion[p] / (eo er kbT)]]

Clear[K]

p1 = {0.0027, 0.138, 10^(-7.4), 0.0027, 0.138, 10^(-6.6)};

1 / K[0.1 p1]
```

2.56745×10^{-9}

```
1 / K[p1]
```

8.11898×10^{-10}

Below: Factor of 0.01 converts V/m to V/cm.

```
Eionic[r_, a_, q_, p_] := 0.01 (q el Exp[-K[p] (r - a)] / (r r eo er (a K[p] + 1)) + q el K[p] Exp[-K[p] (r - a)] / (r eo er (a K[p] + 1)));
EionicX[r_, x_, a_, q_, p_] := 0.01 x / r (q el Exp[-K[p] (r - a)] / (r r eo er (a K[p] + 1)) + q el K[p] Exp[-K[p] (r - a)] / (r eo er (a K[p] + 1)));
EionicZ[r_, z_, a_, q_, p_] := 0.01 z / r (q el Exp[-K[p] (r - a)] / (r r eo er (a K[p] + 1)) + q el K[p] Exp[-K[p] (r - a)] / (r eo er (a K[p] + 1)));

fontsize = 20;

Evaluate[EionicZ[Sqrt[x x + y y + z z], z 10^-9, aBohr, 0.5, p1]]
```

$$\frac{1}{\sqrt{x^2 + y^2 + z^2}}\, 1. \times 10^{-11}\, z \left(\frac{1.08061 \times 10^{-10}\, e^{-1.23168 \times 10^9 \left(-5.29 \times 10^{-11} + \sqrt{x^2+y^2+z^2}\right)}}{x^2 + y^2 + z^2} + \frac{0.133096\, e^{-1.23168 \times 10^9 \left(-5.29 \times 10^{-11} + \sqrt{x^2+y^2+z^2}\right)}}{\sqrt{x^2 + y^2 + z^2}} \right)$$

■ **Average field in Z direction over areas**

```
{x1, x2, xstep} = {0, 3, 0.01};
{f1, f2, fstep} = {1, 11, 2};

data =
  Table[
   {10^xi, NIntegrate[Evaluate[EionicZ[Sqrt[x x + y y + z z 10^-18], z 10^-9, aBohr, 0.5, p1]] /
       (4 × 10^(2 (xi - 9))), {x, 10^(xi - 9), -10^(xi - 9)}, {y, 10^(xi - 9), -10^(xi - 9)},
     MaxPoints → 40 000]}, {z, f1, f2, fstep}, {xi, x1, x2, xstep}];

ListLogLogPlot[data, Joined → True,
 PlotLegend → (Style[Text[# <> "nm"], 20] & /@ ToString /@ Range[f1, f2, fstep]), LegendSize → {0.3, 0.7},
 LegendPosition → {0.9, -.3}, LegendLabel → Style["Binding Height", 14], Frame → True,
 PlotStyle → Thick, PlotRange → {{x1 10^9, x2 10^9}, {3, 1*^6}},
 FrameLabel → {Style["Distance  Coordinate, d [nm]", fontsize],
   Style["Average Ez Field Magnitude [V/cm]", fontsize],
   Style["Average Ez over area:(-d,-d)<(x,y)<(d,d) for Avidin in 10 mM PBS", fontsize]},
 LabelStyle → Directive[fontsize, FontFamily → "Times"], ImageSize → 700]
```

56]=

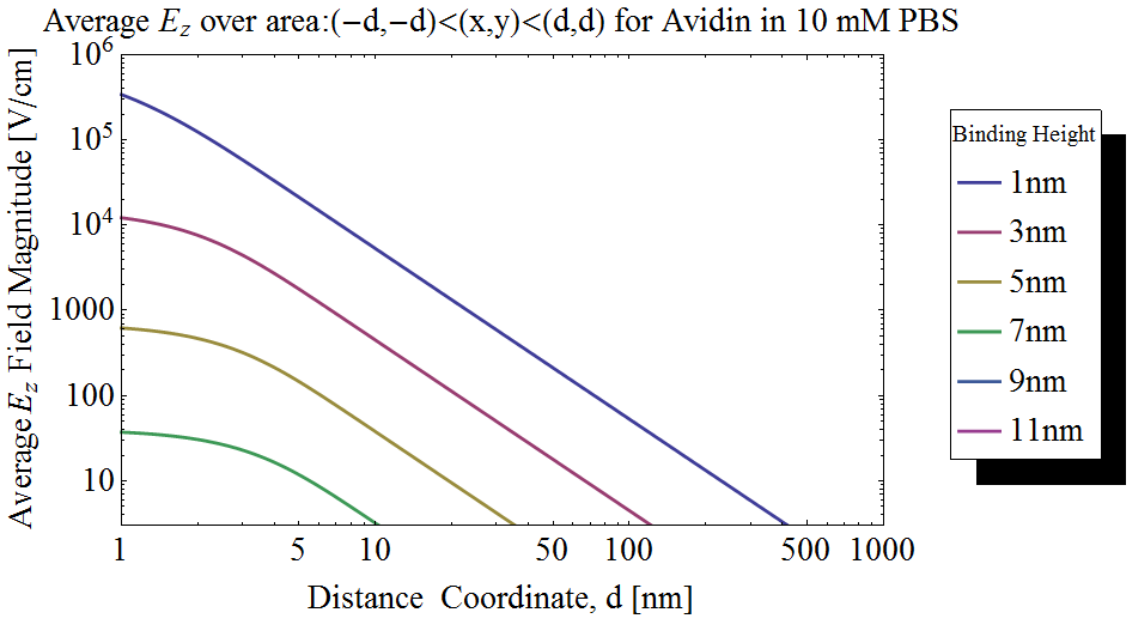

■ **E field magnitude all directions - absolute magnitude**

```
LogPlot[Evaluate[Table[Eionic[Sqrt[x x (10^-18) + z z], aBohr, qavd, p1], {z, 1*^-9, 21*^-9, 4*^-9}]],
 {x, -20, 20}, PlotRange → {{-20, 20}, {5*^-8, 1*^8}},
 PlotLegend → (Text[# <> "nm"] & /@ ToString /@ Range[1, 21, 4]), LegendSize → {0.3, 0.7},
 LegendPosition → {0.9, -.3}, LegendLabel → "Binding Height", Frame → True, PlotStyle → Thick,
 FrameLabel → {Style["X position along Y = 0 line in sensor plane [nm]", fontsize],
   Style["E Field Magnitude [V/cm]", fontsize],
   Style["E field from Avidin in 10 mM PBS", fontsize]},
 LabelStyle → Directive[fontsize, FontFamily → "Times"], ImageSize → 700]
```

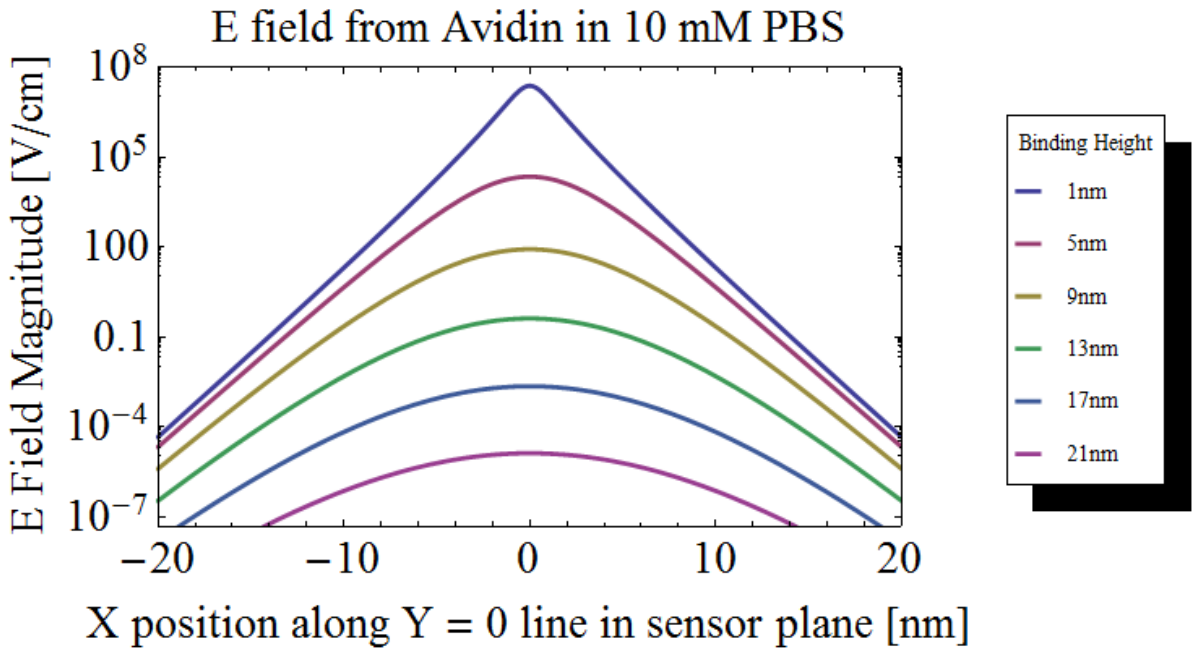

■ **E field magnitude Z direction only**

```
fontsize = 20;
{f1, f2, f3} = {1, 11, 2};
x1 = 11;
LogPlot[Evaluate[Table[Norm[EionicZ[Sqrt[x x (10^-18) + z z], z, aBohr, qavd, p1]],
   {z, f1 * 10^-9, f2 * 10^-9, f3 * 10^-9}]], {x, -x1, x1}, PlotRange → {{-x1, x1}, {3, 1*^8}},
 PlotLegend → (Style[Text[# <> "nm"], 20] & /@ ToString /@ Range[f1, f2, f3]),
 LegendSize → {0.3, 0.7}, LegendPosition → {0.9, -.3}, LegendLabel → Style["Binding Height", 14],
 Frame → True, PlotStyle → Thick,
 FrameLabel → {Style["X position along Y = 0 line in sensor plane [nm]", fontsize],
   Style["E_z Field Magnitude [V/cm]", fontsize],
   Style["E_z field from Avidin in 10 mM PBS", fontsize]},
 LabelStyle → Directive[fontsize, FontFamily → "Times"], ImageSize → 700]
```

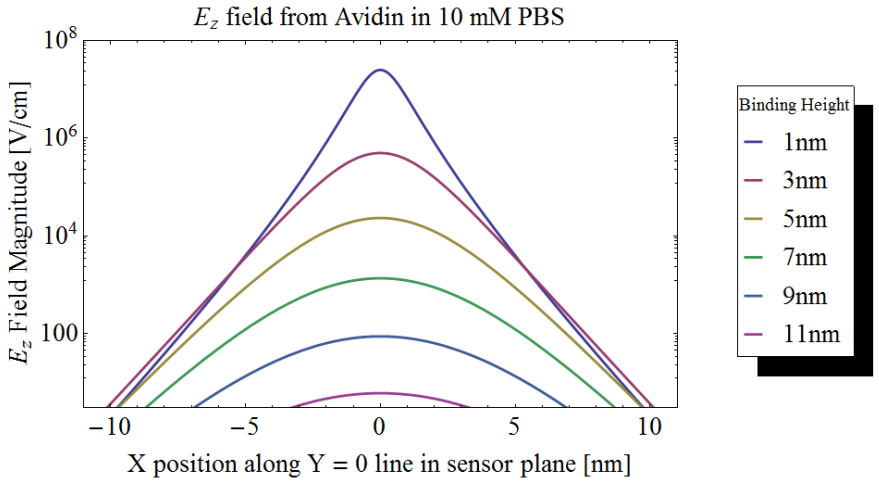

```
fontsize = 20;
{f1, f2, f3} = {1, 11, 2};
x1 = 30;
LogPlot[Evaluate[Table[Norm[EionicZ[Sqrt[x x (10^-18) + z z], z, aBohr, qavd, 0.1 p1]],
   {z, f1*10^-9, f2*10^-9, f3*10^-9}]], {x, -x1, x1}, PlotRange → {{-x1, x1}, {3, 1*^8}},
 PlotLegend → (Style[Text[# <> "nm"], 20] & /@ ToString /@ Range[f1, f2, f3]),
 LegendSize → {0.3, 0.7}, LegendPosition → {0.8, -.3}, LegendLabel → Style["Binding Height", 14],
 Frame → True, PlotStyle → Thick,
 FrameLabel → {Style["X position along Y = 0 line in sensor plane [nm]", fontsize],
   Style["Ez Field Magnitude [V/cm]", fontsize],
   Style["Ez field from Avidin in 1 mM PBS", fontsize]},
 LabelStyle → Directive[fontsize, FontFamily → "Times"], ImageSize → 700]
```

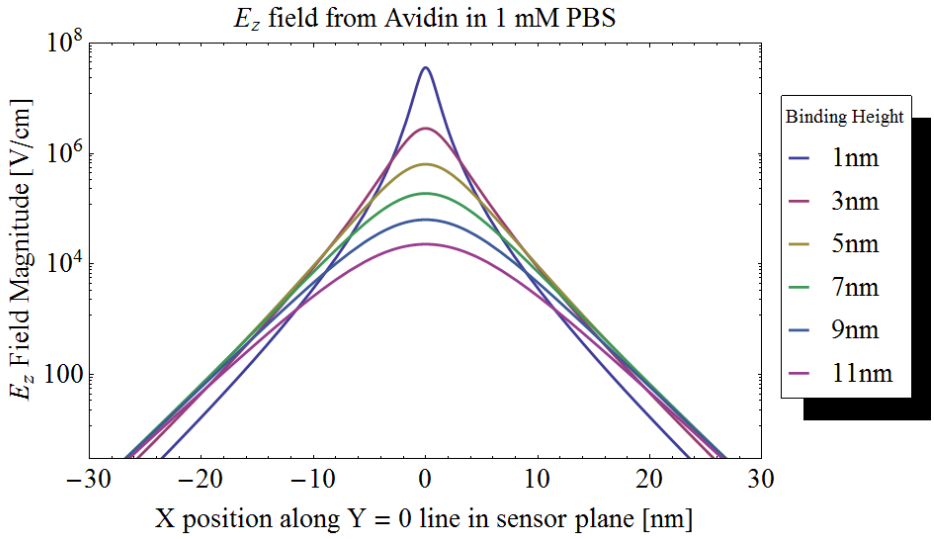

■ **E field magnitude X direction only**

```
fontsize = 20;
{f1, f2, f3} = {1, 9, 2};
x1 = 12;
LogPlot[
 Evaluate[Table[Norm[EionicX[Sqrt[x x (10^-18) + z z], x (10^-9), aBohr, qavd, p1]],
   {z, f1*10^-9, f2*10^-9, f3*10^-9}]], {x, -x1, x1}, PlotRange → {{-x1, x1}, {3, 1*^8}},
 PlotLegend → (Style[Text[# <> "nm"], 20] & /@ ToString /@ Range[f1, f2, f3]),
 LegendSize → {0.3, 0.7}, LegendPosition → {0.9, -.3}, LegendLabel → Style["Binding Height", 14],
 Frame → True, PlotStyle → Thick,
 FrameLabel → {Style["X position along Y = 0 line in sensor plane [nm]", fontsize],
   Style["Ex Field Magnitude [V/cm]", fontsize],
   Style["Ex field from Avidin in 10 mM PBS", fontsize]},
 LabelStyle → Directive[fontsize, FontFamily → "Times"], ImageSize → 700]
```

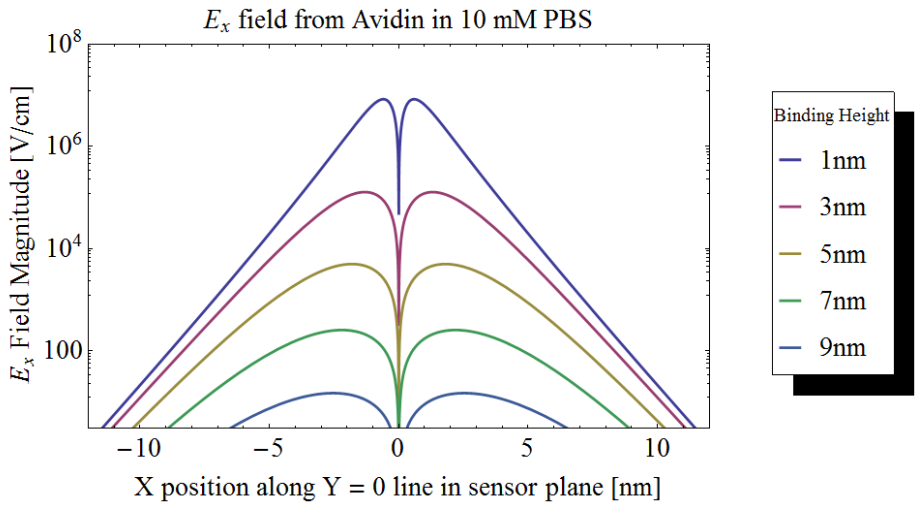


```
fontsize = 20;
{f1, f2, f3} = {1, 11, 2};
x1 = 30;
LogPlot[
 Evaluate[Table[Norm[EionicX[Sqrt[x x (10^-18) + z z], x (10^-9), aBohr, qavd, 0.1 p1]],
   {z, f1 * 10^-9, f2 * 10^-9, f3 * 10^-9}]], {x, -x1, x1}, PlotRange → {{-x1, x1}, {3, 1*^8}},
 PlotLegend → (Text[# <> "nm"] & /@ ToString /@ Range[f1, f2, f3]), LegendSize → {0.3, 0.7},
 LegendPosition → {0.9, -.3}, LegendLabel → "Binding Height", Frame → True, PlotStyle → Thick,
 FrameLabel → {Style["X position along Y = 0 line in sensor plane [nm]", fontsize],
   Style["E_x Field Magnitude [V/cm]", fontsize],
   Style["E_x field from Avidin in 1 mM PBS", fontsize]},
 LabelStyle → Directive[fontsize, FontFamily → "Times"], ImageSize → 700]
```

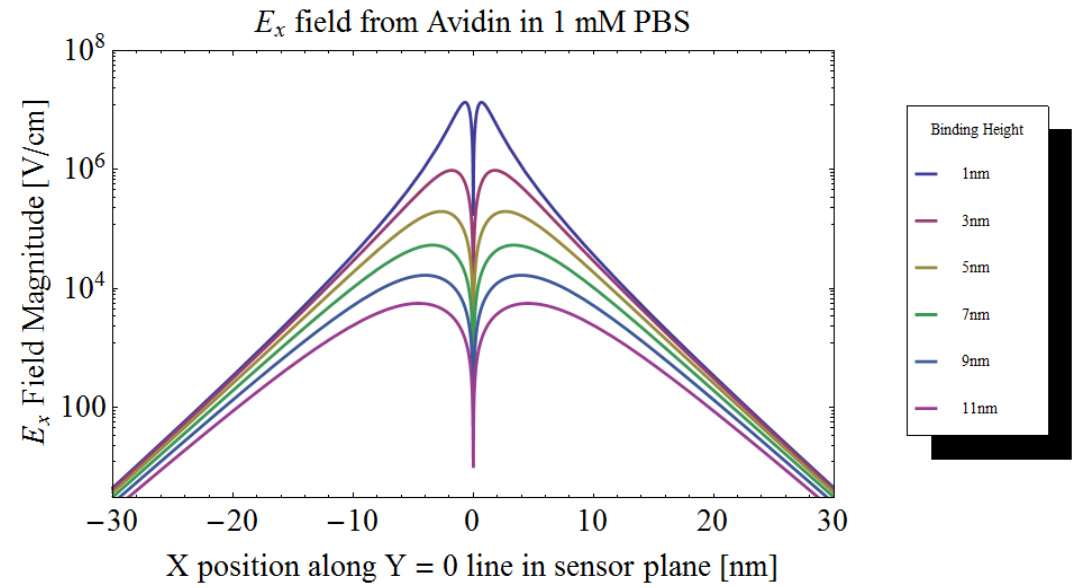

Define Data manipulation functions, Load Data

```
<< "ErrorBarPlots`"
dir = Table[NotebookDirectory[] <> "S1." <> str <> ".E3.averages.dat",
   {str, {" 1", " 2", " 4", " 5", " 6", " 7", "10.corrected", " 8", " 9", "12"}}];
type = {" 5Lead ", " Bare ", " 5Lead ", " 4Lead ", " 4Lead ", " Bare ", " Bare ",
   " 4Lead ", " 4Lead ", " 5Lead ", " Bare ", " 5Lead "};
part[data_] := Module[{in = data, out, imax = (Dimensions[data][[2]] - 3) / 7},
   out = Table[in[[1 ;;, Flatten[{Range[1, 3], Range[3 + i, 9 + i]}]]], {i, 1, 7 imax, 7}]];
numactive = 10;
indiv =
  Flatten[
   Table[Map[(Join[#1[[1 ;; 6]], {DateDifference["14:50:39.01", #1[[7]], "Hour"][[1]]}, #1[[8 ;; 10]]] &),
     part[Import[dir[[i]]]], {2}], {i, 1, numactive}], 1];
bypins[indiv_] := GatherBy[indiv, #[[1, 5]] &];
bydev[indiv_] := GatherBy[indiv, #[[1, 2]] &];
bytype[indiv_] := GatherBy[indiv, type[[#[[1, 2]]]] &];
bytypepin[indiv_] := GatherBy[indiv, {type[[#[[1, 2]]]] &, #[[1, 5]] &}];
bytime[data_] := GatherBy[data, #[[7]] ≤ 5 &];
scaled[in_] := Module[{out}, out = in; out[[All, 9]] = out[[All, 9]] 100 / in[[1, 9]] - 100;
   out[[All, 10]] = out[[All, 10]] 100 / in[[1, 9]]; out ];
errindiv[in_] :=
  Module[{out}, out = in; out[[All, 10]] = Map[{#[[1 ;; 2]], ErrorBar[#[[3]]]} &, in[[All, {7, 9, 10}]]];
   out ];
deleteoutlier[in_, limit_] := Module[{out}, out = in; Select[out, Abs[#[[9]]] < limit &] ];
eqnindiv[in_] := Module[{out = in, data = in[[All, {7, 9}]]}, out[[All, 10]] = Fit[data, {1, x}, x]; out ];
```

Check Data - View sorting

```
Clear[pins]

pins = bypins[indiv];

t = bytype[indiv];

t[[1]]

Dimensions /@ t

{{7}, {9, 62, 10}, {8, 62, 10}}
```

This demonstrates the format of a single data point in the .dat file written by Labview. indiv[[1,1]] = indiv[[device imported first,first row of data]]
Column Categories are : {Chip ID, device ID, Chemical droplet name, type of electrical configuration, numeric code for electric config, date, time in hours since start of experiement, current supplied in (nA), resistance average of 10 measurements (Ohms), resistance standard deviaiton of 10 measurements (Ohms)}
Labview saved only one value that incorporated both the date and the timestamp. *Mathematica* interperets this single colum at two separate columns.

```
indiv[[1, 1]]

{S1, 1, PBS1., p12Vp34I, 1234, 04/16/2012, -0.00163889, 50., 273.071, 1.01638}

indiv[[1, 1]] // Length

10
```

Define Plotting Functions and Options

```
Clear[y, pin]

newtitle[b_] := Switch[b, "p12Vp34I", "Four Point Resistance", "p34Delta",
  "Two Point Resistance, A", "p12Delta", "Two Point Resistance, B"]
frame[data_] :=
  FrameLabel → (Text[StyleForm[#, FontSize → 14, FontWeight -> "Bold"]] & /@
     {"Time (Hours)", "Change of Resistance since t=0 (%)",
      "15 μm" <> type[[data[[1, 2]]]] <> " Devices : " <> newtitle[data[[1, 4]]]});
gridlabel[x_, y_, data_] :=
  Graphics[
   Text[StyleForm[Which[StringTrim[#[[1]], ("1." | ".")] == "PBS", StringTrim[#[[1]], ("1." | ".")],
         StringTrim[#[[1]], ("1." | ".")] == "PBS1B", StringTrim[#[[1]], ("1." | ".")], True,
         StringTrim[#[[1]], ("1." | ".")] <> "/ml"], FontSize → 10, FontWeight -> "Bold"],
      {#[[2]] + x, y}, {-1, 0}, {0, 1}] & /@
    Select[(#[[1, {3, 7}]] & /@ GatherBy[data, #[[3]] &]),
     Not[StringMatchQ[#[[1]], RegularExpression[".*[2-9].*"]]] &]];
range[plot_, y_] :=
 Module[
  {auto = AbsoluteOptions[ErrorListPlot[plot, Axes → False, ImageSize → {450, 300}], PlotRange][[
     1, 2]]}, auto[[2, 1]] = auto[[2, 1]] - y (auto[[2, 2]] - auto[[2, 1]]); auto]
time[data_, start_] :=
  Module[
   {out =
     Differences[
      Append[Select[(#[[1, {3, 7}]] & /@ GatherBy[data, #[[3]] &]),
        Not[StringMatchQ[#[[1]], RegularExpression[".*[2-9].*"]]] &][[All, 2]], 7.4]]},
   If[start == 0, out, Prepend[out, start]]] ;
rect[y_, data_, start_] := {#, y} & /@ time[data, start];
gridlabel[0, 0, indiv[[1]]]
time[indiv[[1]], 0]
time[indiv[[1]], 6]
```

PBS
Biotin1ngCA/ml
Biotin10ngCA/ml
Biotin100ngCA/ml
PBS1B
CA1ng/ml
CA10ng/ml
CA100ng/ml
CA1ng/ml

```
{0.729928, 0.309731, 0.290728, 4.49532, 0.211464, 0.268458, 0.217289, 0.3056, 0.573125}

{6, 0.729928, 0.309731, 0.290728, 4.49532, 0.211464, 0.268458, 0.217289, 0.3056, 0.573125}
```

Plot Data No Curve Fitting

```
indivscaled = scaled /@ indiv;
indivscalederr = errindiv /@ indivscaled;

pics =
  Map[
   Show[ErrorListPlot[#[[All, All, 10]], Axes → False, ImageSize → {450, 300}, Frame → True,
      frame[#[[1]]], PlotRange → range[#[[All, All, 10]], .55]],
     RectangleChart[rect[3, indiv[[1]], 0], ChartBaseStyle → EdgeForm[None],
      ChartStyle → {Opacity[.2], "ThermometerColors"}, BarSpacing → None],
     RectangleChart[rect[-3, indiv[[1]], 0], ChartBaseStyle → EdgeForm[None],
      ChartStyle → {Opacity[.2], "ThermometerColors"}, BarSpacing → None],
     gridlabel[0.1, range[#[[All, All, 10]], .55][[2, 1]], indiv[[1]]] &, bytypepin[indivscalederr],
    {2}];

Column[Flatten[pics]]
```

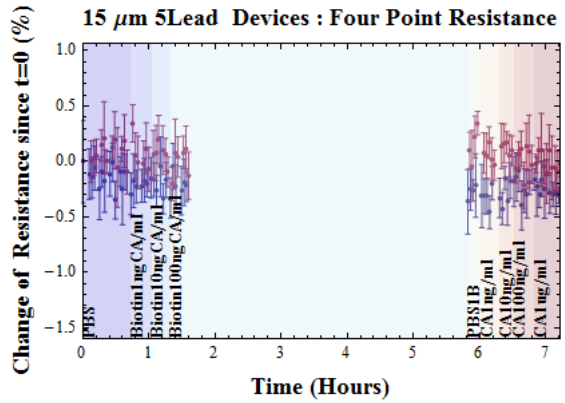

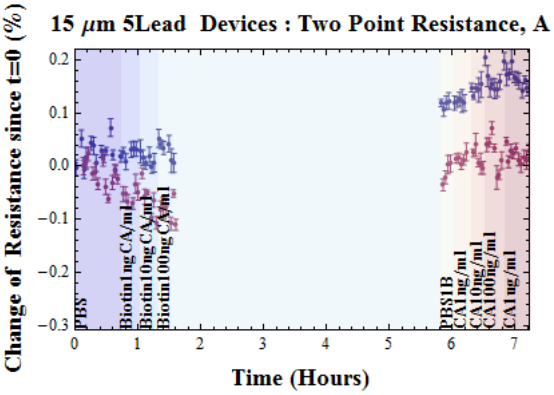

Plot Data with Linear Curve Fitting

```
bytimedata = bytime /@ indiv;
indivscaledCABiotin = deleteoutlier[#, 5] & /@ scaled /@ bytimedata[[All, 1]];
indivscaledCABinding = deleteoutlier[#, 5] & /@ scaled /@ bytimedata[[All, 2]];
indivscalederrCABinding = errindiv /@ indivscaledCABinding;
indivscalederrCABiotin = errindiv /@ indivscaledCABiotin;
eqnsCABiotin = eqnindiv /@ indivscaledCABiotin;
eqnsCABinding = eqnindiv /@ indivscaledCABinding;

eqnsCABiotin[[1, 1, {2, 4, 10}]]
```

```
{1, p12Vp34I, -0.113492 - 0.0742047 x}
```

```
dat1 = indivscaledCABiotin[[1]];
dat2 = indivscaledCABinding[[1]];

picsCABiotin =
  Map[
   Show[ErrorListPlot[#[[All, All, 10]], Axes → False, ImageSize → {450, 300}, Frame → True,
      frame[#[[1]]], PlotRange → range[#[[All, All, 10]], .55]],
     Plot[Evaluate[Fit[#[[All, {7, 9}]], {1, x}, x] & /@ #], {x, 0, 7.5}, Axes → False,
      ImageSize → {450, 300}, PlotRange → range[#[[All, All, 10]], .55]],
     RectangleChart[rect[3, dat1, 0], ChartBaseStyle → EdgeForm[None],
      ChartStyle → {Opacity[.2], "ThermometerColors"}, BarSpacing → None],
     RectangleChart[rect[-3, dat1, 0], ChartBaseStyle → EdgeForm[None],
      ChartStyle → {Opacity[.2], "ThermometerColors"}, BarSpacing → None],
     gridlabel[0.05, range[#[[All, All, 10]], .55][[2, 1]], dat1]] &, bytypepin[indivscalederrCABiotin],
   {2}];

Column[Flatten[picsCABiotin]]
```

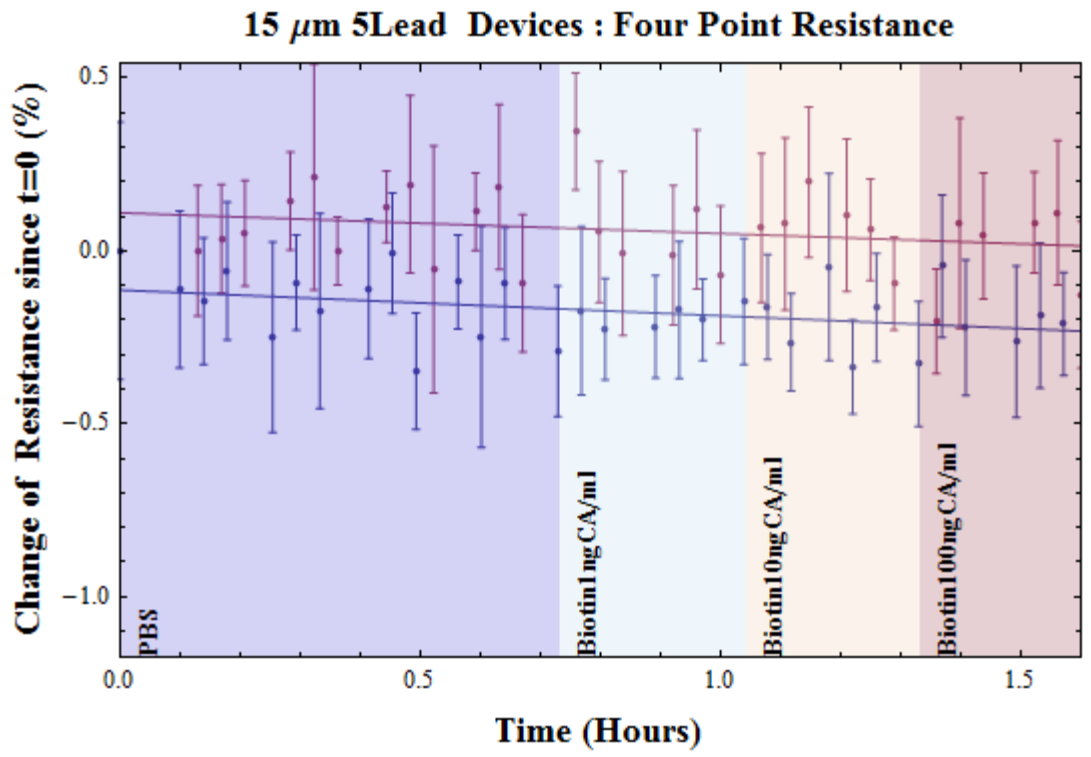
15 μm 5Lead Devices : Four Point Resistance
Change of Resistance since t=0 (%)
0.5
0.0
−0.5
−1.0
PBS
Biotin1ngCA/ml
Biotin10ngCA/ml
Biotin100ngCA/ml
0.0
0.5
1.0
1.5
Time (Hours)

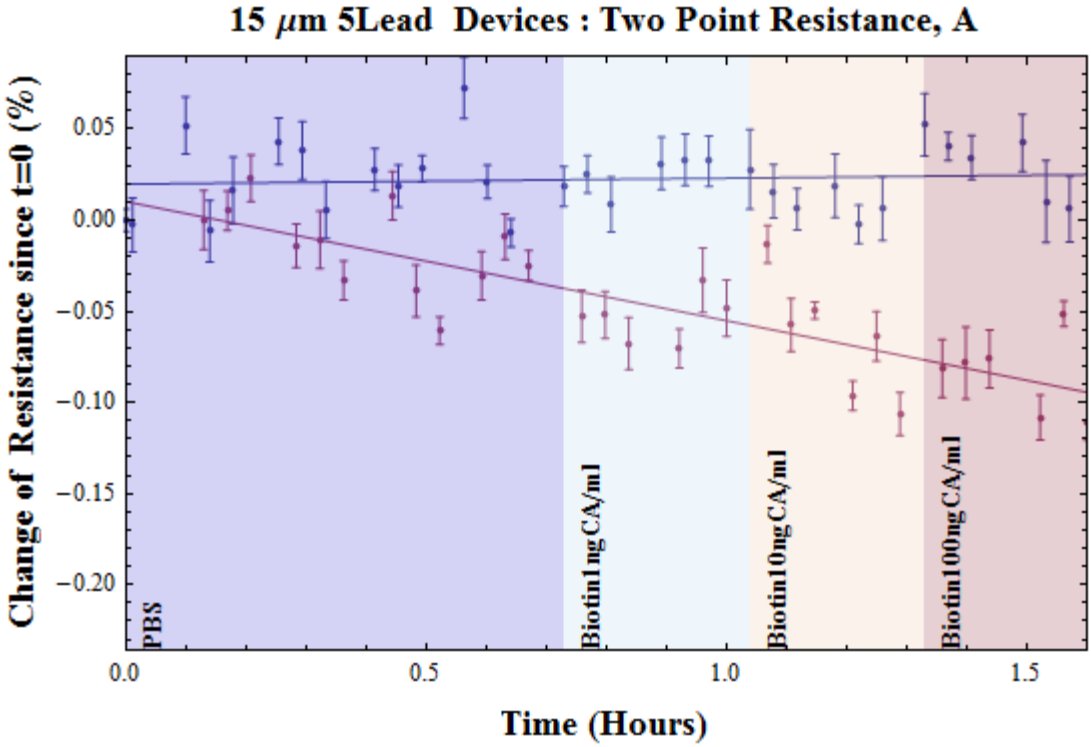
15 μm 5Lead Devices : Two Point Resistance, A
Change of Resistance since t=0 (%)
0.05
0.00
−0.05
−0.10
−0.15
−0.20
PBS
Biotin1ngCA/ml
Biotin10ngCA/ml
Biotin100ngCA/ml
0.0
0.5
1.0
1.5
Time (Hours)

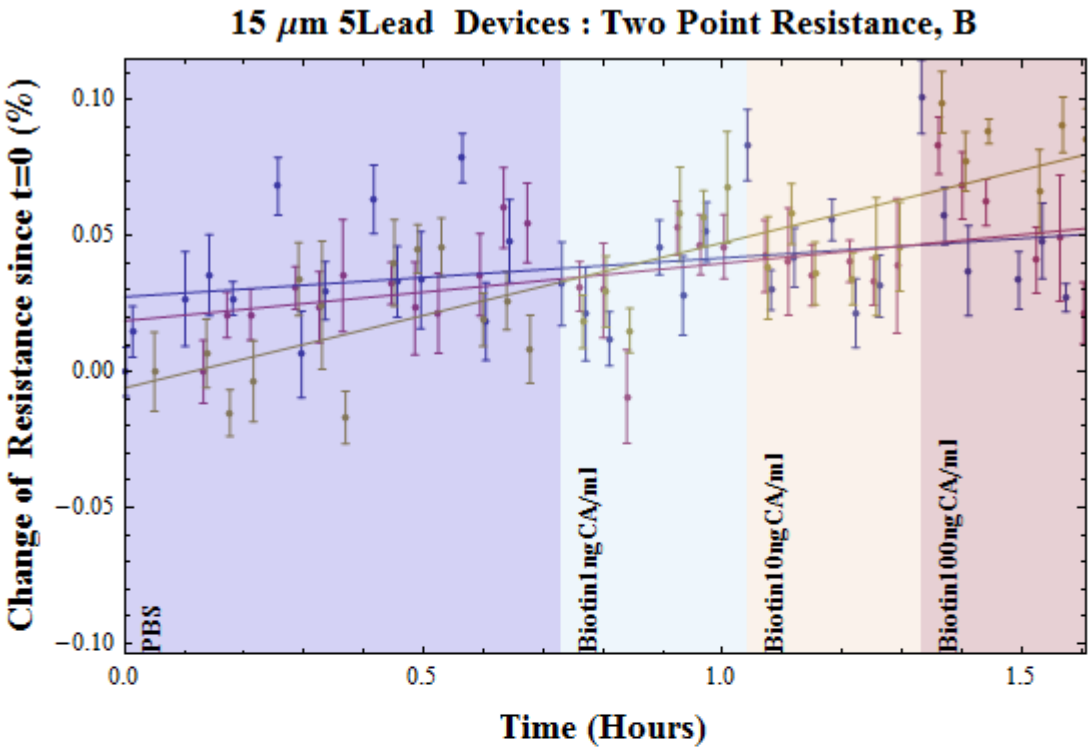
15 μm 5Lead Devices : Two Point Resistance, B
Change of Resistance since t=0 (%)
0.10
0.05
0.00
−0.05
−0.10
0.0
0.5
1.0
1.5
PBS
Biotin1ngCA/ml
Biotin10ngCA/ml
Biotin100ngCA/ml
Time (Hours)

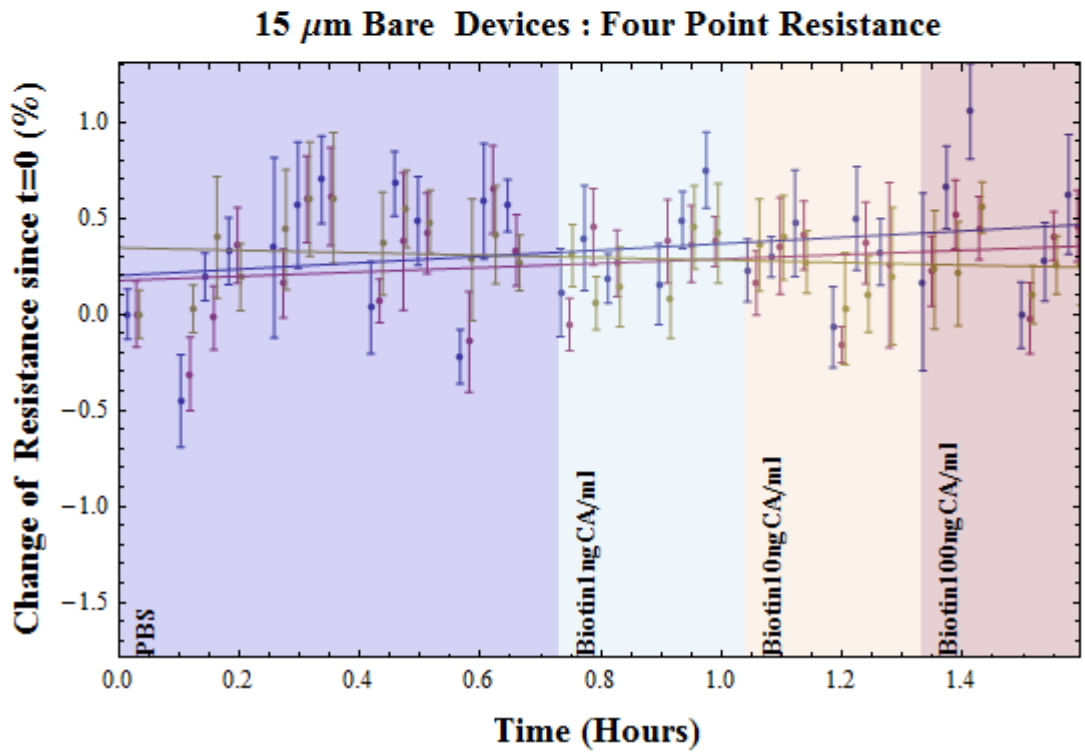
15 μm Bare Devices : Four Point Resistance
Change of Resistance since t=0 (%)
1.0
0.5
0.0
−0.5
−1.0
−1.5
0.0
0.2
0.4
0.6
0.8
1.0
1.2
1.4
PBS
Biotin1ngCA/ml
Biotin10ngCA/ml
Biotin100ngCA/ml
Time (Hours)

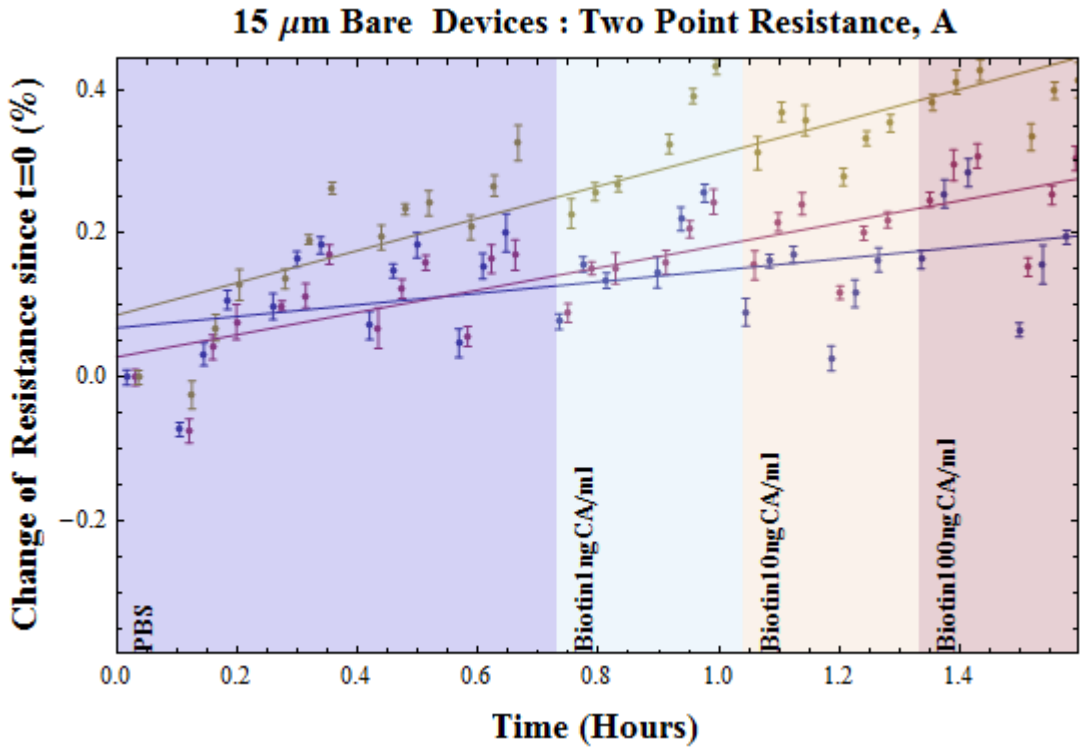
15 μm Bare Devices : Two Point Resistance, A
Change of Resistance since t=0 (%)
0.4
0.2
0.0
−0.2
PBS
Biotin1ngCA/ml
Biotin10ngCA/ml
Biotin100ngCA/ml
0.0
0.2
0.4
0.6
0.8
1.0
1.2
1.4
Time (Hours)

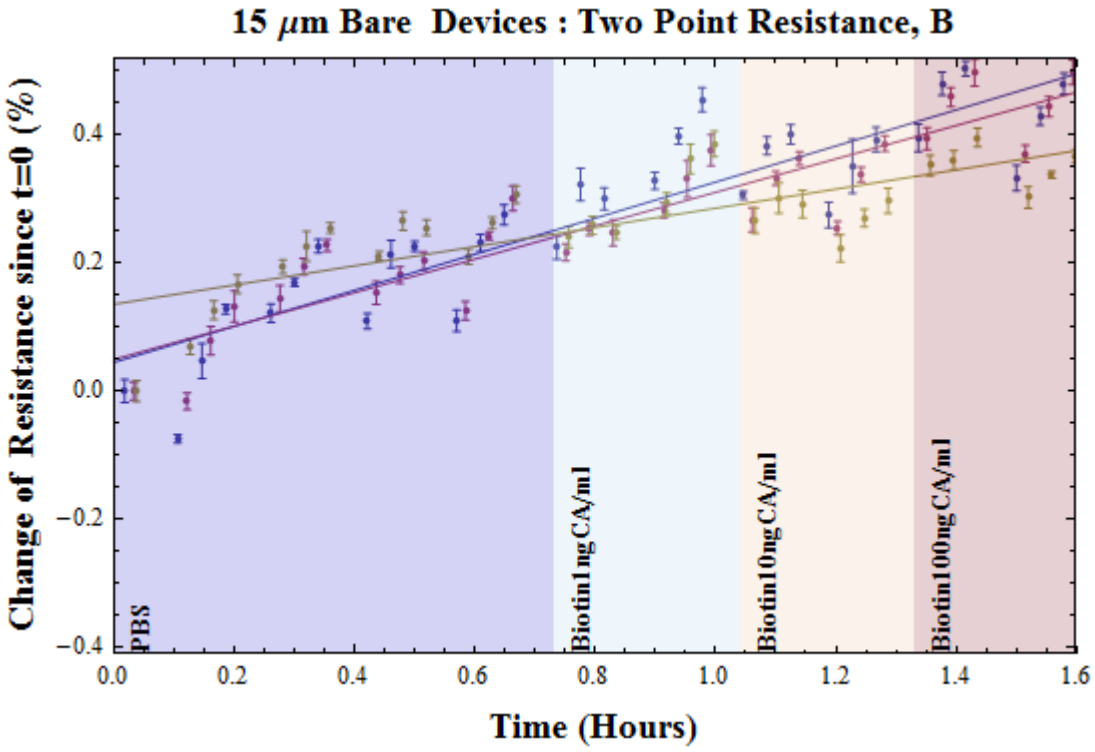
15 μm Bare Devices : Two Point Resistance, B
Change of Resistance since t=0 (%)
0.4
0.2
0.0
−0.2
−0.4
PBS
Biotin1ngCA/ml
Biotin10ngCA/ml
Biotin100ngCA/ml
0.0
0.2
0.4
0.6
0.8
1.0
1.2
1.4
1.6
Time (Hours)

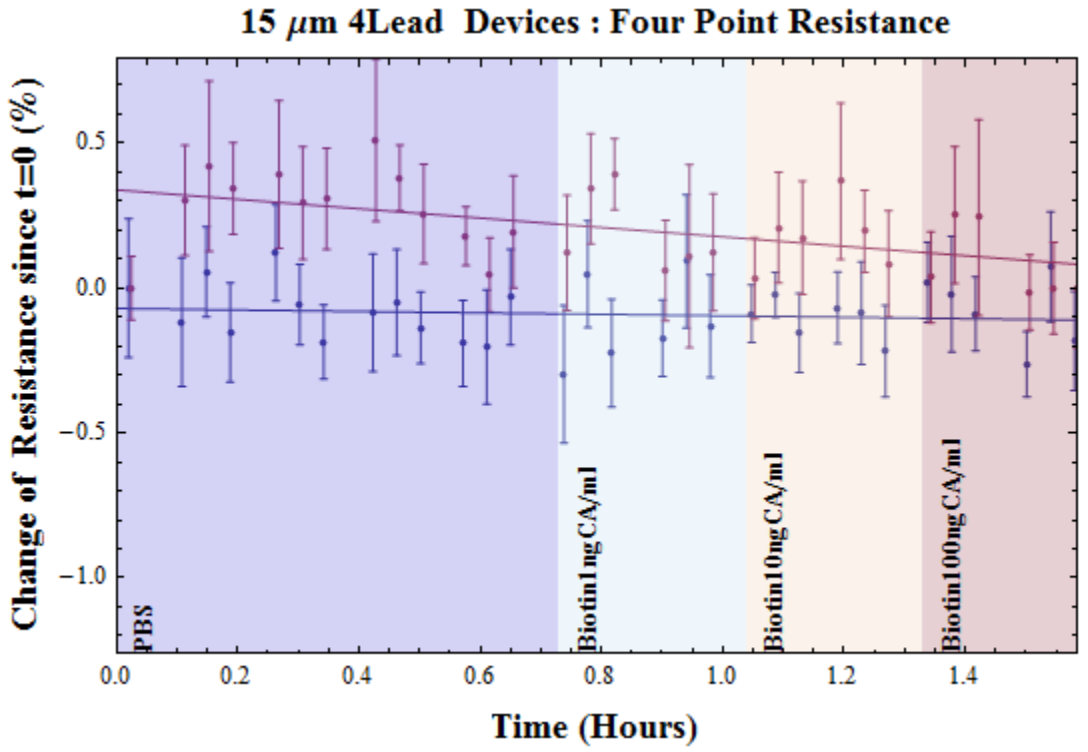
15 μm 4Lead Devices : Four Point Resistance
Change of Resistance since t=0 (%)
0.5
0.0
−0.5
−1.0
PBS
Biotin1ngCA/ml
Biotin10ngCA/ml
Biotin100ngCA/ml
0.0
0.2
0.4
0.6
0.8
1.0
1.2
1.4
Time (Hours)

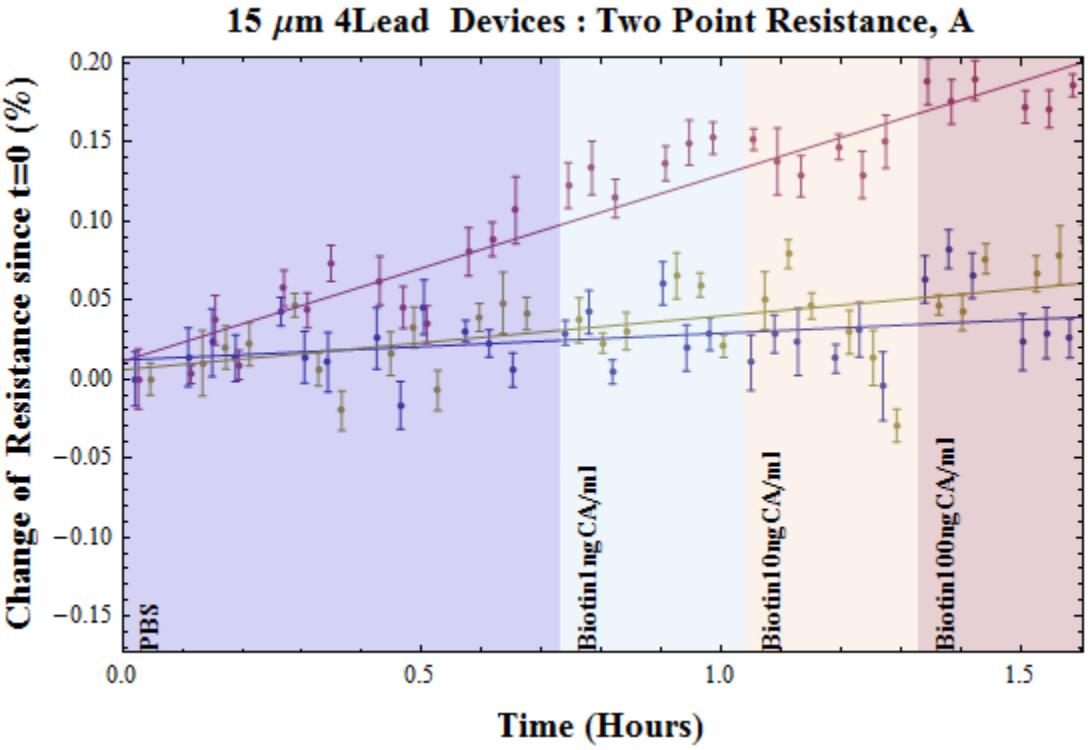
15 μm 4Lead Devices : Two Point Resistance, A
Change of Resistance since t=0 (%)
0.20
0.15
0.10
0.05
0.00
−0.05
−0.10
−0.15
PBS
Biotin1ngCA/ml
Biotin10ngCA/ml
Biotin100ngCA/ml
0.0
0.5
1.0
1.5
Time (Hours)

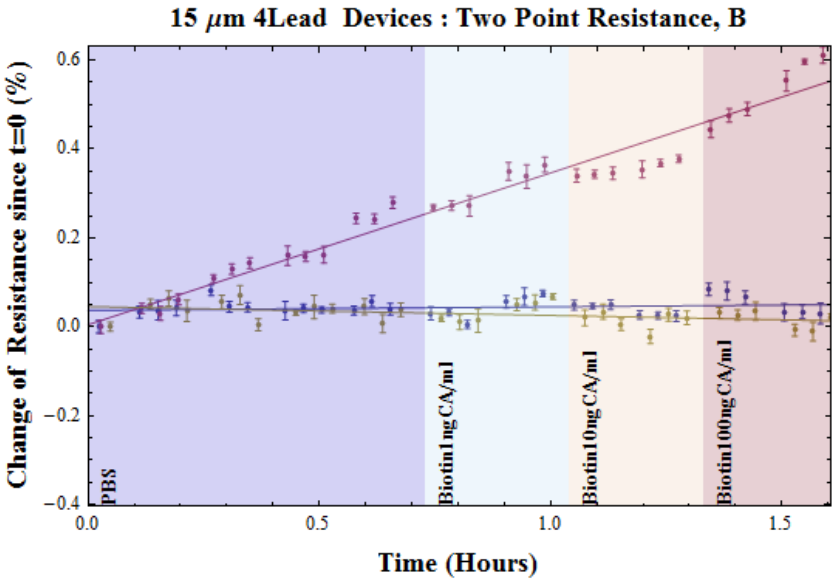


```
picsCABinding =
  Map[
   Show[ErrorListPlot[#[[All, All, 10]], Axes → False, ImageSize → {450, 300}, Frame → True,
     frame[#[[1]]], PlotRange → range[#[[All, All, 10]], .55]],
    Plot[Evaluate[Fit[#[[All, {7, 9}]], {1, x}, x] & /@ #], {x, 0, 7.5}, Axes → False,
     ImageSize → {450, 300}, PlotRange → range[#[[All, All, 10]], .55]],
    RectangleChart[rect[3, dat2, dat2[[1, 7]]], ChartBaseStyle → EdgeForm[None],
     ChartStyle → {Opacity[.2], "ThermometerColors"}, BarSpacing → None],
    RectangleChart[rect[-3, dat2, dat2[[1, 7]]], ChartBaseStyle → EdgeForm[None],
     ChartStyle → {Opacity[.2], "ThermometerColors"}, BarSpacing → None],
    gridlabel[0.05, range[#[[All, All, 10]], .55][[2, 1]], dat2]] &,
   bytypepin[indivscalederrCABinding], {2}];

Column[Flatten[picsCABinding]]
```

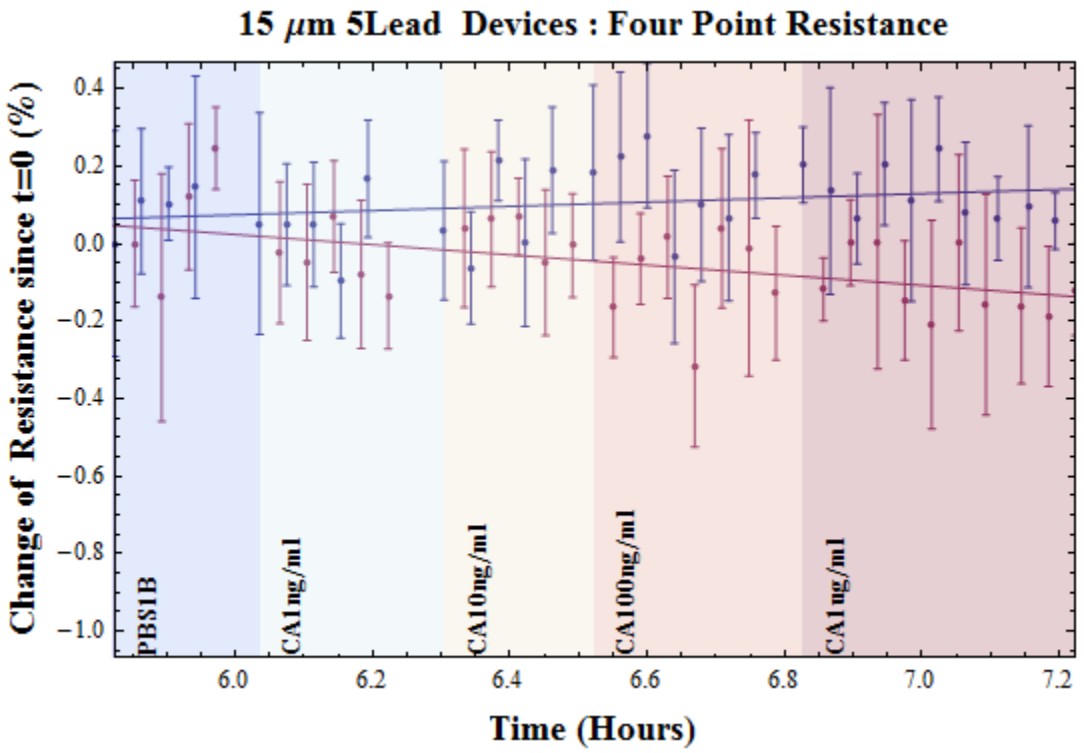
15 μm 5Lead Devices : Four Point Resistance
Change of Resistance since t=0 (%)
0.4
0.2
0.0
−0.2
−0.4
−0.6
−0.8
−1.0
PBS1B
CA1ng/ml
CA10ng/ml
CA100ng/ml
CA1ng/ml
6.0
6.2
6.4
6.6
6.8
7.0
7.2
Time (Hours)

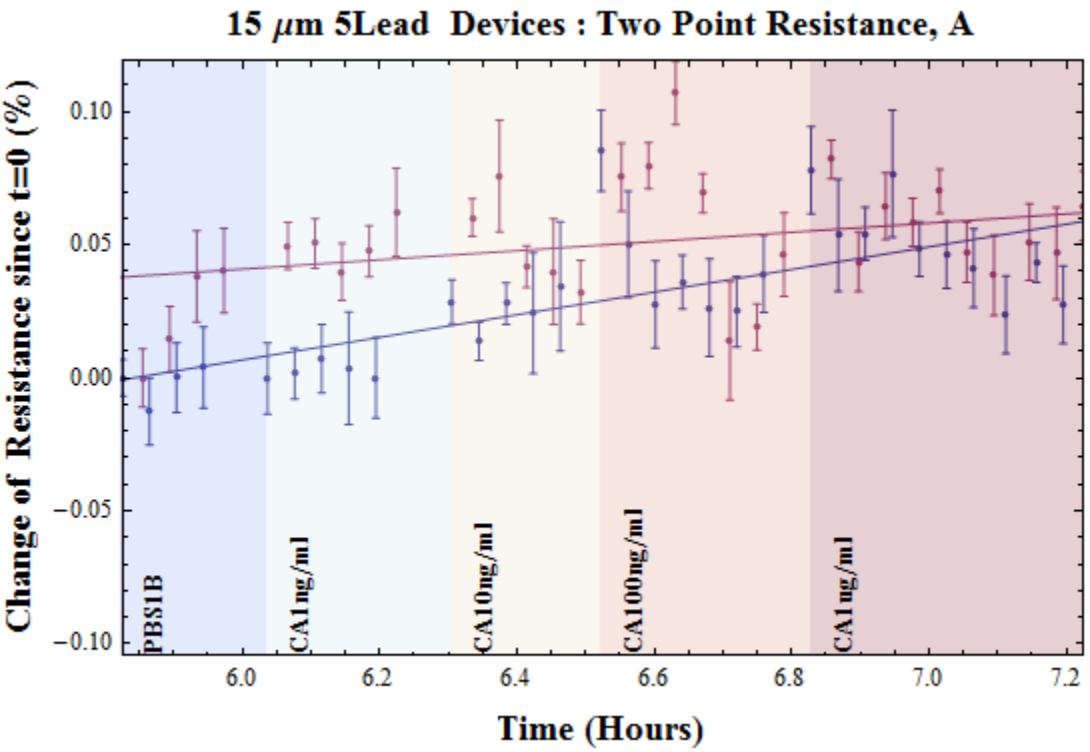
15 μm 5Lead Devices : Two Point Resistance, A
Change of Resistance since t=0 (%)
0.10
0.05
0.00
−0.05
−0.10
PBS1B
CA1ng/ml
CA10ng/ml
CA100ng/ml
CA1ng/ml
6.0
6.2
6.4
6.6
6.8
7.0
7.2
Time (Hours)

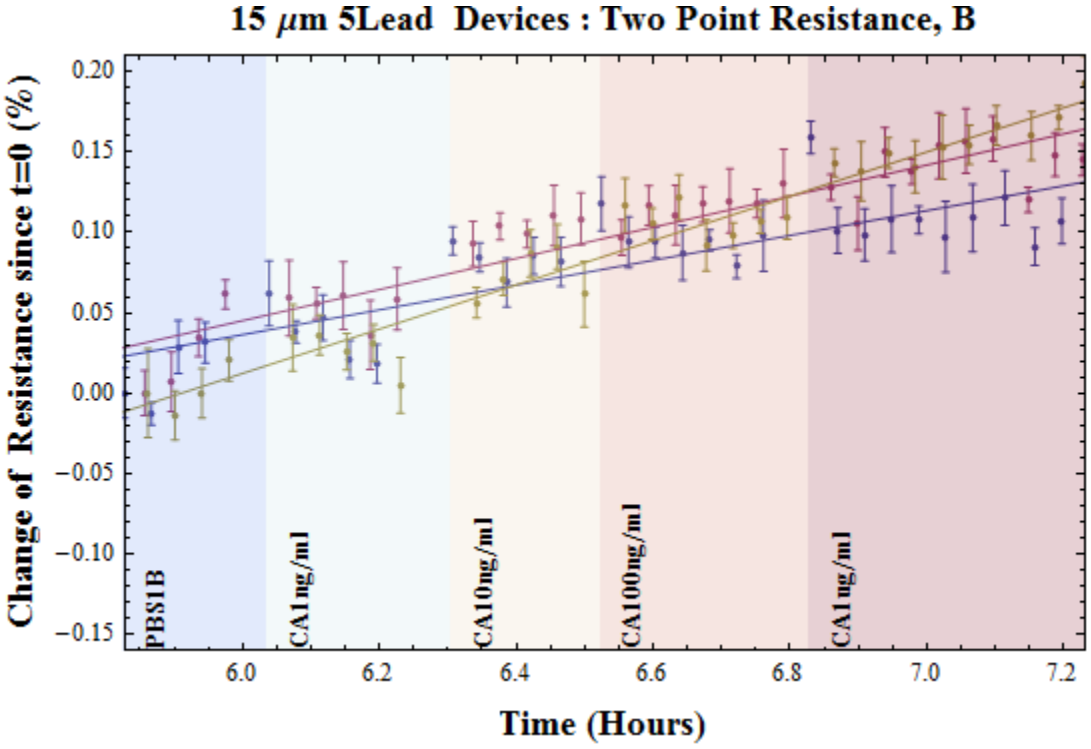
15 μm 5Lead Devices : Two Point Resistance, B
Change of Resistance since t=0 (%)
0.20
0.15
0.10
0.05
0.00
−0.05
−0.10
−0.15
PBS1B
CA1ng/ml
CA10ng/ml
CA100ng/ml
CA1ug/ml
6.0
6.2
6.4
6.6
6.8
7.0
7.2
Time (Hours)

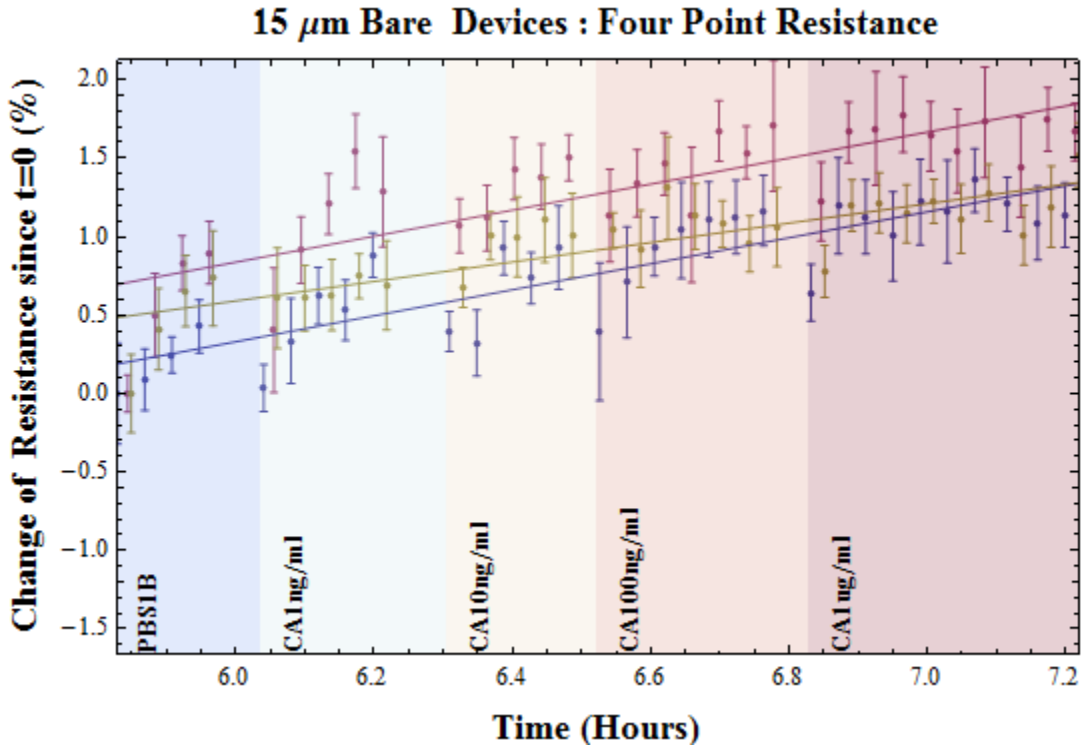
15 μm Bare Devices : Four Point Resistance
Change of Resistance since t=0 (%)
2.0
1.5
1.0
0.5
0.0
−0.5
−1.0
−1.5
PBS1B
CA1ng/ml
CA10ng/ml
CA100ng/ml
CA1ug/ml
6.0
6.2
6.4
6.6
6.8
7.0
7.2
Time (Hours)

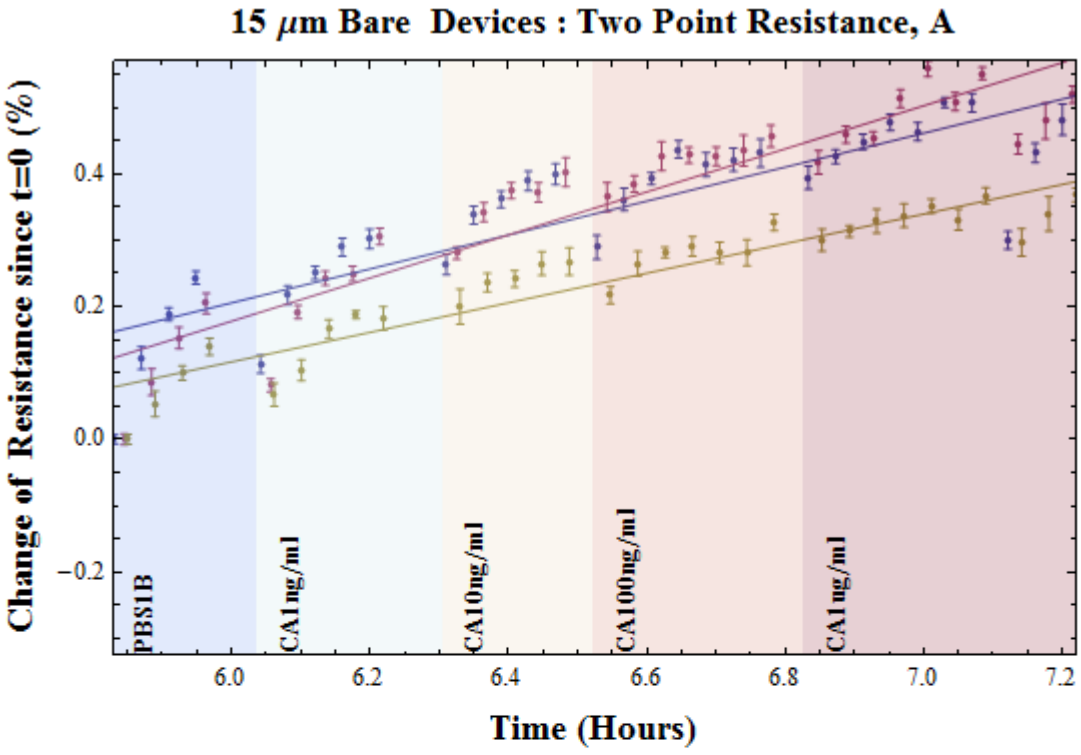
15 μm Bare Devices : Two Point Resistance, A
Change of Resistance since t=0 (%)
0.4
0.2
0.0
−0.2
PBS1B
CA1ng/ml
CA10ng/ml
CA100ng/ml
CA1ug/ml
6.0
6.2
6.4
6.6
6.8
7.0
7.2
Time (Hours)

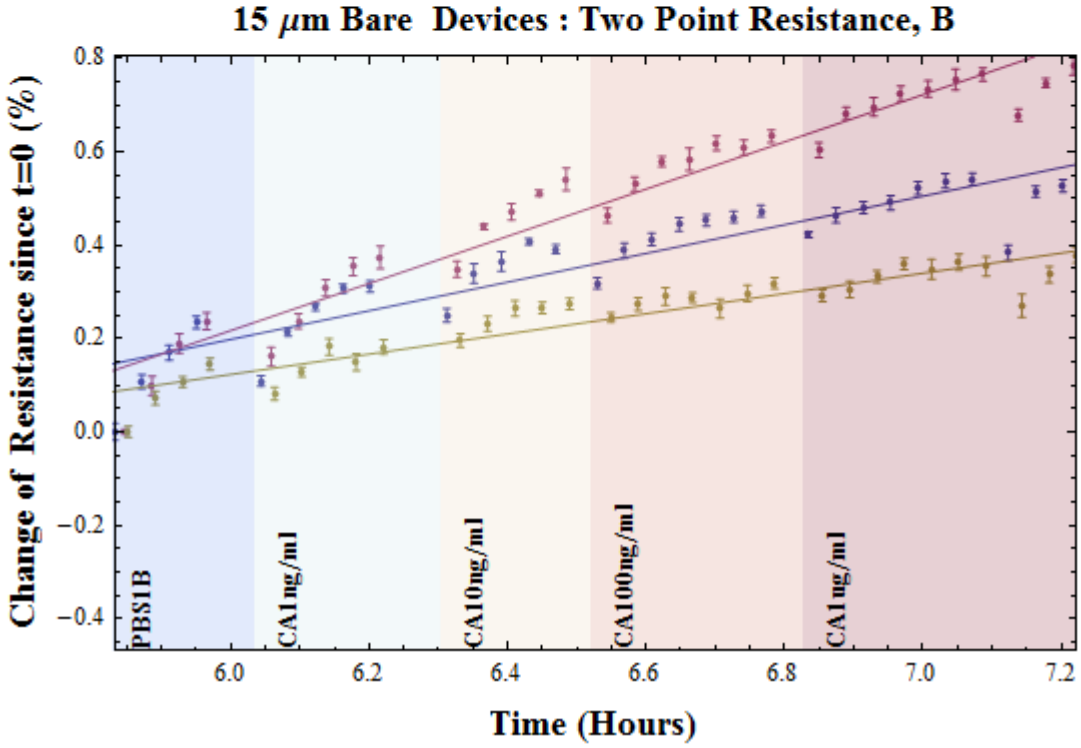
15 μm Bare Devices : Two Point Resistance, B
Change of Resistance since t=0 (%)
0.8
0.6
0.4
0.2
0.0
−0.2
−0.4
PBS1B
CA1ng/ml
CA10ng/ml
CA100ng/ml
CA1ug/ml
6.0
6.2
6.4
6.6
6.8
7.0
7.2
Time (Hours)

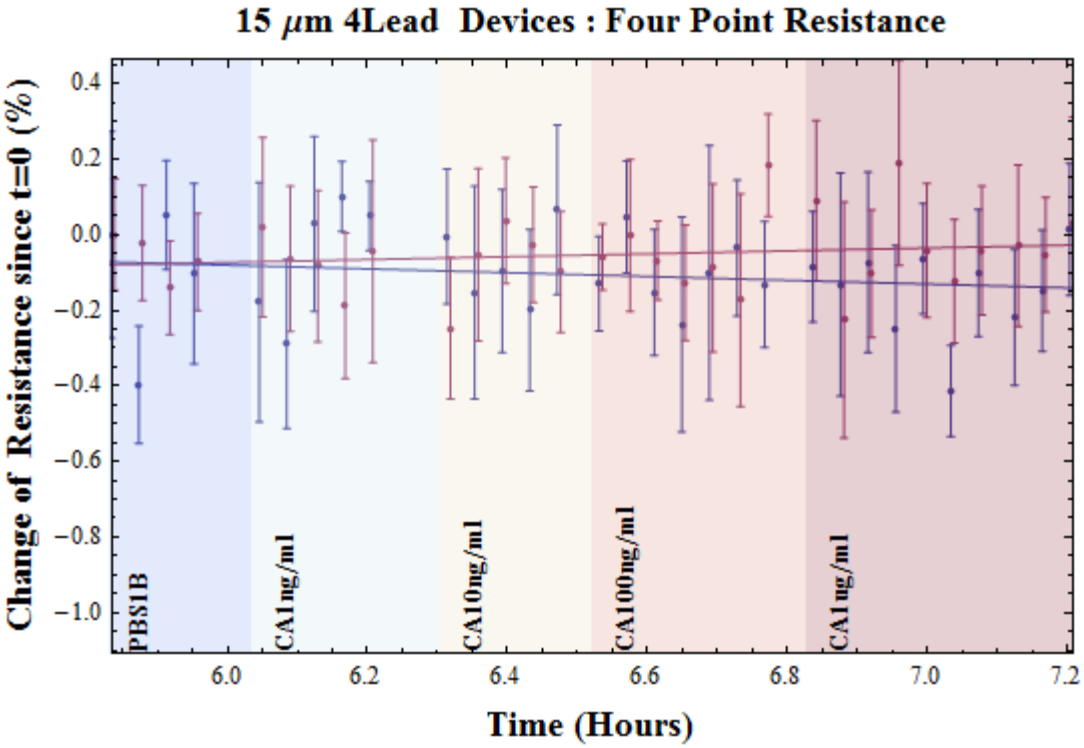
15 μm 4Lead Devices : Four Point Resistance
Change of Resistance since t=0 (%)
0.4
0.2
0.0
−0.2
−0.4
−0.6
−0.8
−1.0
PBS1B
CA1ng/ml
CA10ng/ml
CA100ng/ml
CA1ug/ml
6.0
6.2
6.4
6.6
6.8
7.0
7.2
Time (Hours)

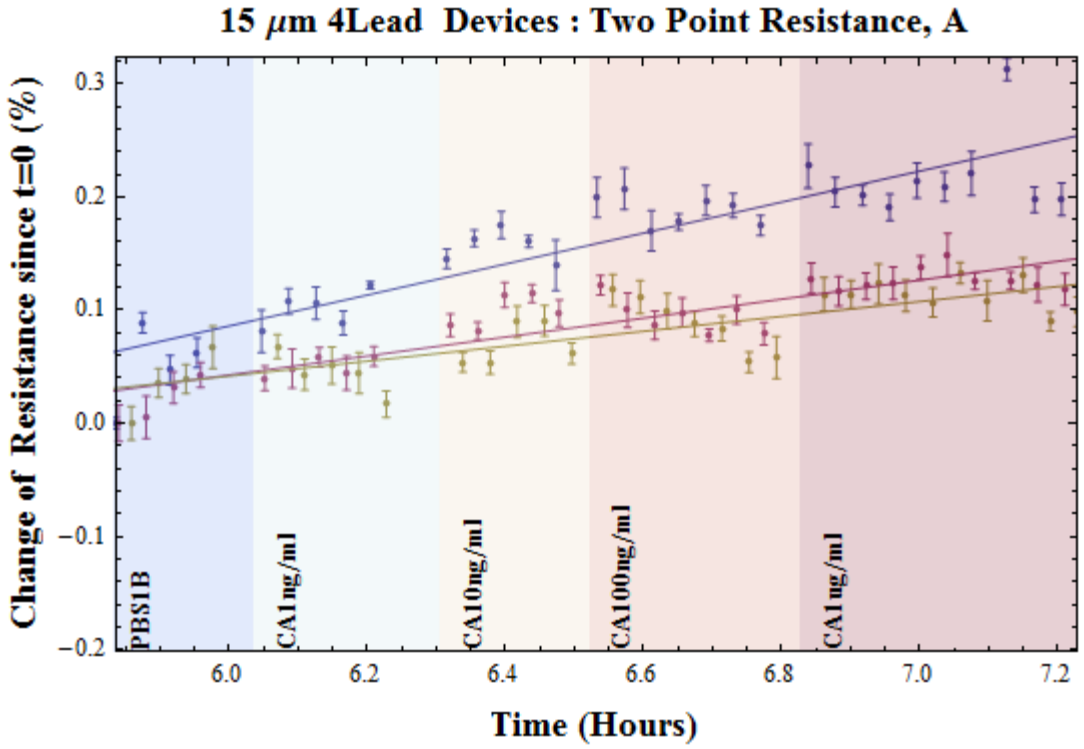
15 μm 4Lead Devices : Two Point Resistance, A
Change of Resistance since t=0 (%)
0.3
0.2
0.1
0.0
−0.1
−0.2
PBS1B
CA1ng/ml
CA10ng/ml
CA100ng/ml
CA1ug/ml
6.0
6.2
6.4
6.6
6.8
7.0
7.2
Time (Hours)

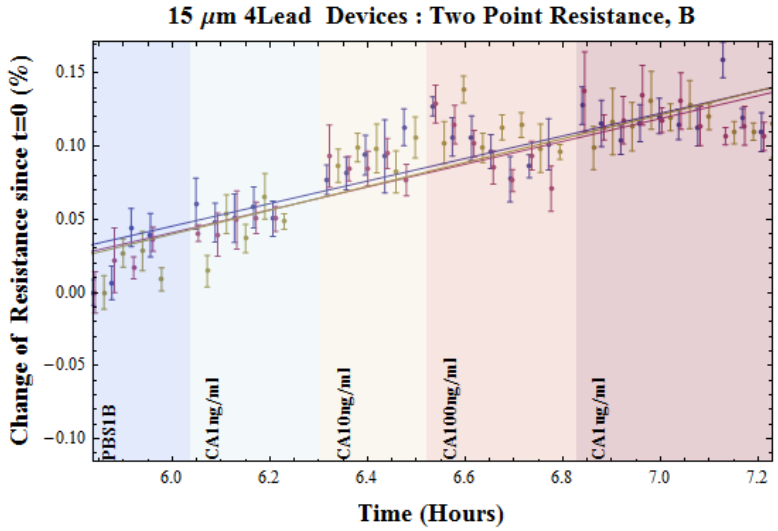


```
Join[
  SortBy[GatherBy[{type[#[[1]]], newtitle[#[[2]]], #[[3, 2]] /. x → 1} & /@
      eqnsCABiotin[[All, 1, {2, 4, 10}]], First], #[[2]] &][[All, All, 3]],
  SortBy[GatherBy[{type[#[[1]]], newtitle[#[[2]]], #[[3, 2]] /. x → 1} & /@
      eqnsCABinding[[All, 1, {2, 4, 10}]], First], #[[2]] &][[All, All, 3]]] // Dimensions
```

```
{6}
```

```
a = {{{0, 8}, {-.3, .9}}, {{0, 10}, {-.3, .9}}, {{0, 9}, {-.3, .9}}};
tf = {{2, 6}, {3, 7}, {2, 8}};
```

```
twofour[b_] := Switch[b, "p12Vp34I", "Four Point Resistance", "p34Delta",
  "Two Point Resistance", "p12Delta", "Two Point Resistance"]
```

```
title[data_] :=
  FrameLabel → (Text[StyleForm[#, FontSize → 18, FontWeight -> "Bold"]] & /@
     {"", "Sensitivity = Change of Resistance (%) / Log10[Concetration]",
      "Sensitivity of 15 μm " <> data <> " Devices "});
```

```
biotin = Map[SortBy[#, #[[2]] &] &,
   GatherBy[{type[#[[1]]], twofour[#[[2]]], #[[3, 2]] /. x → 1} & /@ eqnsCABiotin[[All, 1, {2, 4, 10}]],
    First], {1}];
binding = Map[SortBy[#, #[[2]] &] &,
   GatherBy[{type[#[[1]]], twofour[#[[2]]], #[[3, 2]] /. x → 1} & /@ eqnsCABinding[[All, 1, {2, 4, 10}]],
    First], {1}];
```

```
biotinnum = Map[SortBy[#, #[[2]] &] &,
   GatherBy[{type[#[[1]]], twofour[#[[2]]], #[[1]], #[[3, 2]] /. x → 1} & /@ eqnsCABiotin[[All, 1, {2, 4, 10}]],
    First], {1}];
bindingnum = Map[SortBy[#, #[[2]] &] &,
   GatherBy[{type[#[[1]]], twofour[#[[2]]], #[[1]], #[[3, 2]] /. x → 1} & /@
     eqnsCABinding[[All, 1, {2, 4, 10}]], First], {1}];
```

```
Grid /@ biotinnum[[All, All]]
```

```
{{5Lead  Four Point Resistance  1  -0.0742047
  5Lead  Four Point Resistance 10  -0.0598083
  5Lead   Two Point Resistance  1   0.00323604
  5Lead   Two Point Resistance  1   0.0143455 ,
  5Lead   Two Point Resistance 10  -0.0653777
  5Lead   Two Point Resistance 10   0.0211843
  5Lead   Two Point Resistance 12   0.0534838},

 {Bare  Four Point Resistance 2   0.166006
  Bare  Four Point Resistance 6   0.112257
  Bare  Four Point Resistance 7  -0.0641147
  Bare   Two Point Resistance 2   0.0799769
  Bare   Two Point Resistance 2   0.281831 ,
  Bare   Two Point Resistance 6   0.154963
  Bare   Two Point Resistance 6   0.261127
  Bare   Two Point Resistance 7   0.149981
  Bare   Two Point Resistance 7   0.223682},

 {4Lead  Four Point Resistance 4  -0.0250442
  4Lead  Four Point Resistance 5  -0.162054
  4Lead   Two Point Resistance 4   0.00787841
  4Lead   Two Point Resistance 4   0.0169772 }
  4Lead   Two Point Resistance 5   0.117801  }
  4Lead   Two Point Resistance 5   0.341819
  4Lead   Two Point Resistance 8   0.0340471
  4Lead   Two Point Resistance 9  -0.0198424}
```

```
Grid /@ bindingnum[[All, All]]
```

```
{{5Lead  Four Point Resistance  1   0.0546837
  5Lead  Four Point Resistance 10  -0.131131
  5Lead   Two Point Resistance  1   0.0425289
  5Lead   Two Point Resistance  1   0.0771881 ,
  5Lead   Two Point Resistance 10   0.0172875
  5Lead   Two Point Resistance 10   0.0968834
  5Lead   Two Point Resistance 12   0.137791},

 {Bare  Four Point Resistance 2  0.827578
  Bare  Four Point Resistance 6  0.828927
  Bare  Four Point Resistance 7  0.618665
  Bare   Two Point Resistance 2  0.255763
  Bare   Two Point Resistance 2  0.306767 ,
  Bare   Two Point Resistance 6  0.324485
  Bare   Two Point Resistance 6  0.505164
  Bare   Two Point Resistance 7  0.216559
  Bare   Two Point Resistance 7  0.222698},

 {4Lead  Four Point Resistance 4  -0.0501268
  4Lead  Four Point Resistance 5   0.0379988
  4Lead   Two Point Resistance 4   0.0770474
  4Lead   Two Point Resistance 4   0.136862 }
  4Lead   Two Point Resistance 5   0.0779442 }
  4Lead   Two Point Resistance 5   0.0837673
  4Lead   Two Point Resistance 8   0.0658745
  4Lead   Two Point Resistance 9   0.081566}
```

References

1 Solin, S. A., et al. "Enhanced room-temperature geometric magnetoresistance in inhomogeneous narrow-gap semiconductors." *Science* 289.5484 (2000): 1530-1532.

2 Solin, S. A., et al. "Nonmagnetic semiconductors as read-head sensors for ultra-high-density magnetic recording." *Applied Physics Letters* 80.21 (2002): 4012-4014.

3 Rowe, A. C. H., D. R. Hines, and S. A. Solin. "Enhanced room-temperature piezoconductance of metal–semiconductor hybrid structures." *Applied physics letters* 83.6 (2003): 1160-1162.

4 Wieland, K. A., et al. "Experimental measurement and finite-element modeling of extraordinary optoconductance in GaAs-In metal-semiconductor hybrid structures." *Physical Review B* 73.15 (2006): 155305.

5 Wang, Yun, et al. "Extraordinary electroconductance in metal-semiconductor hybrid structures." Applied physics letters 92.26 (2008): 262106-262106.

6 Newaz, A. K. M., et al. "Transport measurements and analytical modeling of extraordinary electrical conductance in Ti-GaAs metal-semiconductor hybrid structures." *Physical Review B* 79.19 (2009): 195308.

7 G. Burns, Solid State Physics, Chapter 10, 1985

8 Bloch, "Über die quantenmechanik der elektronen in kristallgittern (About the quantum mechanics of electrons in crystal lattices)," Z. Physik, vol. 52, p. 555 (1928).

9 R. de L. Kronig and W. G. Penney, "Quantum Mechanics of Electrons in Crystal Lattices," Proc. Roy. Soc. A 130, 499 (1931).

10 M. L. Cohen and T. K. Bergstresser, "Band structures and pseudopotential form factors for fourteen semiconductors of the diamond and zinc-blende structures", Phys. Rev. 141, 789, 1966

11 J. R. Chelikowsky and M. L. Cohen, Phys. Rev. B, 14, 556 (1976).

12 G. Burns, Solid State Physics, Chapter 10 Section 16, 1985 or S. M. Sze, Physics of Semiconductor Devices 2nd Ed., Chapter 1 Section 4, 1981

13 R. A. Swalin, Thermodynamics of Solids 2nd Ed., Section 13.1, 1962

14 S. M. Sze, Physics of Semiconductor Devices 2nd Ed., Chapter 1 Section 5, 1981

15 G. Burns, Solid State Physics, Chapter 11 Section 9, 1986

16 G. Burns, Solid State Physics, Chapter 10 Section 17, 1986

17 Sinha, A. K., et al. "n-GaAs Schottky diodes metallized with Ti and Pt/Ti." Solid-State Electronics 19.6 (1976): 489-492.

18 S. M. Sze, Physics of Semiconductor Devices 2nd Ed., Chapter 1 Section 5, 1981

19 Kulkarni, A. K., and J. T. Lukowski. "Effect of annealing process parameters on the properties of AuGe ohmic contacts to GaAs." Journal of applied physics59.8 (1986): 2901-2904.

20 van der Pauw, L. J. "A method of measuring specific resistivity and Hall effect of discs of arbitrary shape." (1958).

21 A. Vaseashta and D, Dimova-Malinovska, Science and Technology of Advanced Materials 6, 312 (2005).

22 K. Fife, , A. E. Gamal, and H.-S. P. Wong, *IEEE Int. Electron Devices Meeting-IEDM'07*, 986 (2007).

23 M. Law, D.J. Sirbuly, J.C. Johnson, J. Goldberger, R.J. Saykally, P. Yang, *Science* **305**, 1269, (2004)
24 M.J. Chou, D.C. Tsui, and G. Weimann, *Appl. Phys. Lett.* **47**, 609 (1985).
25 H. Nakanishi, K. J. M. Bishop, B. Kowalczyk, A. Nitzan, E.A. Weiss, K. V. Tretiakov, M. M. Apodaca, R. Klajn, J. F. Stoddart, BA Grzybowski, *Nature* **460** 371 (2009).
26 M. Heiblum, M. I. Nathan, D. C. Thomas, and C. M. Knoedler, *Phys. Rev. Lett*. **55**, 2200 (1985).
27 A.M. Gilbertson, A.K.M. Newaz, Woo-Jin Chang, R. Bashir, S.A. Solin, and L.F. Cohen, *Appl. Phys. Lett.* **95**, 012113 (2009).
28 S. M. Sze, *Physics of Semiconductor Devices, 2nd ed*. (Wiley-Interscience, New York, 1981) pp. 793-795.
29 D. L.Rode, and S. Knight, *Phys. Rev.* **B 3**, 2534 (1971).
30 J. T. Wallmark, *Proc. IRE* **45,** 474 (1957).
31 K. A. Wieland, Yun Wang, L. R. Ram-Mohan, S. A. Solin, and A. M. Girgis, *Appl. Phys. Lett.* **88**, 052105 (2006).
32 U. Strauss, W. W. Ruhle, and K. Kohler, *Appl. Phys. Lett.* **62**, 55 (1993).
33 See supplementary material at [*URL will be inserted by AIP*] for a derivation of the photoinduced carrier density.
34 R. de Picciotto, H.L. Stormer, L.N. Pfeiffer, K.W. Baldwin, and K.W. West, *Nature* **411**, 51 (2001).
35 J.R. Hays, A.F. Levi, and W. Wiegman, *Phys. Rev. Lett.* **54**, 1570 (1985).
36 S. Datta, in "Electronic Transport in Mesoscopic Systems" ed. by H. Ahmed, M. Pepper and A. Broers (Cambridge University Press, 1995).
37 R. Lipperheide, T. Weis and U. Wille, *J. Phys. Condens. Matter* **13**, 3347 (2001).
38 M. Shaban, K Nomoto, S. Izumi, and T. Yoshitake, *App. Phys. Lett.* **94**, 222113 (2009).
39 A. Van Der Ziel, *Noise in Solid State Devices and Circuits*, (Wiley, New York, 1986).
40 G. N. Lu, J. M. Galvan, C. Jeloyan, G. Goumy, and V. Marcoux, *Mat. Sci. and Eng.* **C21**, 203 (2002).
41 K. H. Lee, R. W. Chuang, P. C. Chang, S. J. Chang, Y. C. Wang, C. L. Yu, J. C. Lin, and S. L. Wu*, Journal of Electrochem. Soc.* 155, H959 (2008).
42 Newaz, A. K. M., et al. "A nanoscale Ti/GaAs metal-semiconductor hybrid sensor for room temperature light detection." *Applied physics letters* 97.8 (2010): 082105-082105.
43 Suzaki, Yasuzi, and Atsushi Tachibana. "Measurement of the μm sized radius of Gaussian laser beam using the scanning knife-edge." *Applied Optics* 14.12 (1975): 2809-2810.
44 Wallmark, J. Torkel. "A new semiconductor photocell using lateral photoeffect."*Proceedings of the IRE* 45.4 (1957): 474-483.
45 Keyser, et al. "Direct Force Measurements on DNA in Solid-State Nanopore," *Nature Physics*, (July, 2006) Vol. 2, pp. 473-477
46 Invitrogen, "CaptAvidin Biotin-Binding Protein Product Information," Item C-21385, http://tools.invitrogen.com/content/sfs/manuals/mp21385.pdf
47 Pugliese, Luisa, et al. "Three-dimensional structure of the tetragonal crystal form of egg-white avidin in its functional complex with biotin at 2.7 A resolution." *Journal of molecular biology* 231.3 (1993): 698.
48 http://www.idtdna.com/pages/decoded/decoded-articles/core-concepts/decoded/2012/09/20/which-biotin-modification-to-use-

49 Weber PC, Ohlendorf DH, et al "Structural origins of high-affinity biotin binding to streptavidin." (1989) *Science*, 243:85–88.

50 Hui Li, Andrew D. Robertson, and Jan H. Jensen "Very Fast Empirical Prediction and Interpretation of Protein pKa Values" *Proteins*, 2005, 61, 704-721.

51 Delphine C. Bas, David M. Rogers, and Jan H. Jensen "Very Fast Prediction and Rationalization of pKa Values for Protein-Ligand Complexes" *Proteins*, 2008, 73, 765-783.

52 Mats H.M. Olsson, Chresten R. Søndergard, Michal Rostkowski, and Jan H. Jensen "PROPKA3: Consistent Treatment of Internal and Surface Residues in Empirical pKa predictions" *Journal of Chemical Theory and Computation*, 2011 7 (2), 525-537

53 Chresten R. Søndergaard, Mats H.M. Olsson, Michaz Rostkowski, and Jan H. Jensen "Improved Treatment of Ligands and Coupling Effects in Empirical Calculation and Rationalization of pKa Values" *Journal of Chemical Theory and Computation*, 2011 7 (7), 2284-2295

54 De Vico, Luca, et al. "Quantifying signal changes in nano-wire based biosensors." *Nanoscale* 3.2 (2011): 706-717.

55 Supplementary information for publication: De Vico, Luca, et al. "Quantifying signal changes in nano-wire based biosensors." *Nanoscale* 3.2 (2011): 706-717.

56 Dorvel, et al. "Vapor Phase Deposition of Monofunctional Alkoxysilanes for Sub-Nanometer-Level Biointerfacing on Silicon Oxide Surfaces", *Adv. Funct. Mater*. 2010, 20, 87-95. DOI: 10.1002/adfm.200901688

57 Thermo Scientific Catalog and Chemical Product Information www.piercenet.com product ID 21330: EZ-Link PEG4-Biotin

58 CAS Registry Number: 58-85-5

59 Sharma, Manu, Raffaele Resta, and Roberto Car. "Dipolar correlations and the dielectric permittivity of water." *Physical review letters* 98.24 (2007): 247401.

60 P. Debye and E. Hückel "The theory of electrolytes. I. Lowering of freezing point and related phenomena" (1923). *Physikalische Zeitschrift* 24: 185–206.

61 T.L. Hill, "An Introduction to Statistical Thermodynamics," Ch. 18, Dover Publications Inc, New York, (1986)

62 Sigma-Aldrich product number P3813 SIGMA – Phosphate Buffered Saline, powder, pH 7.4

63 Thermo Scientific Catalog and Chemical Product Information www.piercenet.com product ID 22342: MS(PEG)4

64 Lee, Chang-Soo, Sang Kyu Kim, and Moonil Kim. "Ion-sensitive field-effect transistor for biological sensing." *Sensors* 9.9 (2009): 7111-7131.

65 Moon, Joong Ho, et al. "Absolute surface density of the amine group of the aminosilylated thin layers: ultraviolet-visible spectroscopy, second harmonic generation, and synchrotron-radiation photoelectron spectroscopy study." *Langmuir* 13.16 (1997): 4305-4310.

66 Moon, Joong Ho, et al. "Formation of uniform aminosilane thin layers: an imine formation to measure relative surface density of the amine group." *Langmuir* 12.20 (1996): 4621-4624.

67 Anderson, Aaron S., et al. "Functional PEG-modified thin films for biological detection." *Langmuir* 24.5 (2008): 2240-2247.